

*SIMULTANEOUS SIZING, LAYOUT AND  
TOPOLOGY OPTIMIZATION FOR  
BUCKLING AND POSTBUCKLING OF  
STIFFENED PANELS*



**Sheng Chu**

**Cardiff School of Engineering**

**Cardiff University**

**This thesis is being submitted in partial fulfilment of the requirements for the  
degree of Doctor of Philosophy**

**September 2022**

Simultaneous Sizing, Layout and Topology Optimization for Buckling and Postbuckling of Stiffened Panels – Sheng Chu – September 2022

## ABSTRACT

This thesis aims to develop a computational scheme for simultaneous sizing, layout and topology optimization for buckling and postbuckling of stiffened panels. Many efforts have been made using structural optimization techniques to improve the buckling and postbuckling behaviours of stiffened panels, focusing on sizing and layout optimization. Stiffener internal topologies have however, received little attention for optimization. This reduces the design space that can be searched, and consequently limits the potential improvement in structural performance. In this thesis, a level-set-based topology optimization parameterization is developed, enabling the simultaneous optimization of the thicknesses of the skin and stiffeners, and stiffener layout and internal topologies.

The simultaneous sizing, layout and topology optimization for buckling of panels stiffened with straight stiffeners is investigated for the first time. Numerical investigations demonstrate the effectiveness of the proposed method. The benefit of simultaneously conducting sizing, layout and topology optimization for the design of stiffened panels is also demonstrated. Since stiffness is commonly considered in the topology optimization field, the difference between buckling-driven and stiffness-driven designs is investigated and discussed. Besides buckling, stress is another critical failure criterion of stiffened panels. The proposed method is extended to stiffened panel design under both stress and buckling constraints.

The simultaneous sizing, layout and topology optimization for postbuckling of panels with straight stiffeners is investigated for the first time. The proposed method is extended to postbuckling optimization. The out-of-plane skin deformation and the load-carrying capability are considered to access the postbuckling behaviours of stiffened panels. Compared with buckling optimization, postbuckling optimization can provide a design with more promising postbuckling behaviours of interest.

The design of panels with curved stiffeners is investigated. The level-set-based method is extended to simultaneously optimize both stiffener curves and internal topologies. Numerical investigations demonstrate and validate the proposed method for simultaneous layout and topology optimization of curved stiffened panels. Compared with panels with straight stiffeners, curved stiffened panels have the potential to result in lighter weight designs.

## ACKNOWLEDGEMENTS

This thesis represents not only my research work at the keyboard, but it is also a milestone in my life. Undertaking this Ph.D. has been a truly life-changing experience for me, and it would not have been possible to finish it without the support and guidance that I received from many people, especially during this challenging period due to Covid-19.

First and foremost, I would like to express my sincere gratitude to my supervisor, Prof. H. Alicia Kim, not only for all her scientific advice and suggestions on how to do research, but also for many insightful discussions as well as all the “hard” questions on my research helping me to become a “real” researcher. My skills in research, communication and writing were all improved. These would benefit me throughout my life.

I would also like to express my deepest gratitude to my another supervisor, Prof. Carol Featherston, for giving encouragement and sharing her expertise in the thin-walled structures field and insightful suggestions with me, which incentivised me to widen my research from various perspectives.

Many thanks also to Prof. David Kennedy, for his guidance. He was always there for discussions about anything that I was unsure about.

I am also very grateful to all my colleagues, i.e., Scott Townsend, Andreas Neofytou, Renato Picelli, Xiaoyi Zhou, Kang Gao, Ayan Haldar, Alessia Prato and Zeyang Li at Cardiff University, and Carolina Jarequie, Douglas de Aquino Castro, Zongliang Du, Sandilya Kambampati, Lei Li, Hayoung Chung, Jaeyub Hyun, Eliana Bortot, Hesaneh Kazemi, Alex Guibert, Charles Mish and Brianna MacNider at the University of California San Diego, who have helped and supported me in many ways. It was a great time we worked together.

Last but not the least, I would like to thank all my family members for always believing in me and encouraging me to follow my dreams, for unconditional support for all my decisions, and for helping in whatever way they could, especially after Covid-19 occurred and daily lives were affected in many ways.

# LIST OF PUBLICATIONS AND CONFERENCES

## Journal Papers

- S. Chu, C. Featherston, D. Kennedy, H.A. Kim, Postbuckling topology optimization of stiffened panels: challenges and insights, to be submitted.
- S. Chu, S. Townsend, C. Featherston, H.A. Kim, Exploring optimal topologies of stiffened panels under buckling constraints, to be submitted.
- S. Chu, C. Featherston, H.A. Kim, Design of stiffened panels for stress and buckling via topology optimization, *Structural and Multidisciplinary Optimization*, 64 (2021) 3123-3146.
- S. Chu, S. Townsend, C. Featherston, H.A. Kim, Simultaneous layout and topology optimization of curved stiffened panels, *AIAA Journal*, 59 (2021) 2768-2783.

## Conference Proceedings

- S. Chu, S. Townsend, C. Featherston, H.A. Kim, Simultaneous size, layout and topology optimization of stiffened panels under buckling constraints, in: *AIAA Scitech 2021 Forum*, 2021, pp. 1894.
- S. Chu, S. Townsend, C. Featherston, H.A. Kim, Simultaneous layout and topology optimization of curved stiffened panels, in: *AIAA Aviation 2020 Forum*, 2020, pp. 3144. (2nd Place in the 2020 AIAA Multidisciplinary Design Optimization Student Paper Competition)

## Conference Presentations

- S. Chu, C. Featherston, D. Kennedy, H.A. Kim, Postbuckling Optimization of Stiffened Panels via Topological Design, *WCCM-APCOM 2022*, 31 July - 5 August, 2022, Virtual Event.
- S. Chu, C. Featherston, D. Kennedy, H.A. Kim, Challenges in topology optimization for postbuckling of stiffened panels, *ASMO-UK 12/ASMO-Europe 1/ ISSMO*, 18-19 July, 2022, Leeds, UK.

- S. Chu, C. Featherston, H.A. Kim, Simultaneous size, layout and topology optimization of stiffened panels under stress and buckling constraints, WCSMO-14, 13-18 June, 2021, Virtual Event.
- S. Chu, S. Townsend, C. Featherston, H.A. Kim, Simultaneous size, layout and topology optimization of stiffened panels under buckling constraints, AIAA Scitech 2021 Forum, 11–15 & 19–21 January, 2021, Virtual Event.
- S. Chu, S. Townsend, C. Featherston, H.A. Kim, Simultaneous layout and topology optimization of curved stiffened panels, AIAA Aviation 2020 Forum, June 15-19, 2020, Virtual Event. (2nd Place in the 2020 AIAA Multidisciplinary Design Optimization Student Paper Competition)

# CONTENTS

<b>1 INTRODUCTION.....</b>	<b>1</b>
<b>2 LITERATURE REVIEW.....</b>	<b>4</b>
2.1 DESIGN OPTIMIZATION FOR BUCKLING AND STRESS OF STIFFENED PANELS.....	4
2.2 DESIGN OPTIMIZATION FOR POSTBUCKLING OF STIFFENED PANELS .....	9
2.3 TOPOLOGY OPTIMIZATION .....	12
2.3.1 <i>Buckling-based Topology Optimization.....</i>	<i>12</i>
2.3.2 <i>Stress-based Topology optimization .....</i>	<i>13</i>
2.3.3 <i>Topology optimization for stiffened panel design.....</i>	<i>14</i>
<b>3 SIMULTANEOUS SIZING, LAYOUT AND TOPOLOGY OPTIMIZATION OF PANELS WITH STRAIGHT STIFFENERS UNDER BUCKLING CONSTRAINTS.....</b>	<b>18</b>
3.1 STIFFENED PANEL MODEL .....	19
3.1.1 <i>Layout Description.....</i>	<i>19</i>
3.1.2 <i>Topology Description.....</i>	<i>21</i>
3.1.3 <i>Sizing Description .....</i>	<i>23</i>
3.1.4 <i>Finite Element Model.....</i>	<i>24</i>
3.2 PROBLEM FORMULATION AND OPTIMIZATION METHOD .....	26
3.2.1 <i>Problem Formulation.....</i>	<i>26</i>
3.2.2 <i>Sensitivity Analysis.....</i>	<i>27</i>
3.2.3 <i>Optimization Algorithm.....</i>	<i>32</i>
3.3 NUMERICAL EXAMPLES .....	34

3.3.1 Stiffened Panel under Shear Loading .....	34
3.3.2 Stiffened Panel under Combined Shear and Compression .....	45
3.3.3 Stiffened Panel under a Concentrated Load .....	47
3.4 CONCLUSIONS .....	52
<b>4 SIMULTANEOUS SIZING, LAYOUT AND TOPOLOGY OPTIMIZATION OF PANELS WITH STRAIGHT STIFFENERS UNDER STRESS AND BUCKLING CONSTRAINTS.....</b>	<b>54</b>
4.1 STIFFENED PANEL MODEL .....	55
4.1.1 Geometric Model.....	55
4.1.2 Finite Element Model.....	56
4.2 PROBLEM FORMULATION AND OPTIMIZATION METHOD .....	64
4.2.1 Problem Formulation.....	64
4.2.2 Sensitivity Analysis.....	66
4.2.3 Optimization Algorithm.....	70
4.3 NUMERICAL EXAMPLES .....	71
4.3.1 Stiffened Panel under Compression and Shear.....	72
4.3.2 Stiffened Panel under Compression, Shear and Bending .....	79
4.4 CONCLUSIONS .....	84
<b>5 SIMULTANEOUS SIZING, LAYOUT AND TOPOLOGY OPTIMIZATION FOR POSTBUCKLING OF PANELS WITH STRAIGHT STIFFENERS .....</b>	<b>86</b>
5.1 STIFFENED PANEL MODEL AND POSTBUCKLING ANALYSIS .....	87
5.1.1 Geometric Model.....	88
5.1.2 Finite Element Model.....	89

5.1.3 <i>Postbuckling Analysis</i> .....	91
5.2 OPTIMIZATION FORMULATIONS .....	96
5.2.1 <i>Optimization Formulations for Stiffened Panels under Displacement Loading</i> .....	97
5.2.2 <i>Optimization Formulations for Stiffened Panels under Force Loading</i> .....	98
5.3 OPTIMIZATION ALGORITHM AND SENSITIVITY ANALYSIS .....	99
5.3.1 <i>Sensitivity Analysis for the Optimization of Stiffened Panels under Displacement Loading</i> .....	100
5.3.2 <i>Sensitivity Analysis for the Optimization of Stiffened Panels under Force Loading</i> .....	103
5.4 NUMERICAL EXAMPLES .....	105
5.4.1 <i>Stiffened panel loaded by Shear Displacement</i> .....	105
5.4.2 <i>Stiffened Panel Loaded by a Shear Load</i> .....	140
5.4.3 <i>Stiffened Panel Loaded by Compression and Shear Loads</i> .....	145
5.5 CONCLUSION .....	149
<b>6 SIMULTANEOUS LAYOUT AND TOPOLOGY OPTIMIZATION OF PANELS WITH CURVED STIFFENERS CONSIDERING BUCKLING</b> .....	<b>151</b>
6.1 CURVED STIFFENED PANEL MODEL .....	152
6.1.1 <i>Layout Description</i> .....	152
6.1.2 <i>Topology Description</i> .....	155
6.1.3 <i>Finite Element Model</i> .....	157
6.2 PROBLEM FORMULATION AND OPTIMIZATION METHOD .....	159
6.2.1 <i>Problem Formulation</i> .....	159
6.2.2 <i>Sensitivity Analysis</i> .....	160

6.2.3 Optimization Algorithm.....	164
6.3 NUMERICAL EXAMPLES .....	166
6.3.1 Mass Minimization with Buckling Constraint.....	166
6.3.2 Critical Buckling Load Factor Maximization with Mass Constraint.....	175
6.3.3 Comparison with the Optimization of Panels with Straight Stiffeners .....	177
6.4 CONCLUSIONS .....	181
<b>7 CONCLUSIONS AND FURTHER WORK.....</b>	<b>183</b>
7.1 SUMMARY AND MAIN CONTRIBUTIONS .....	183
7.2 SUGGESTIONS FOR FURTHER WORK.....	189
<b>8 REFERENCES.....</b>	<b>191</b>

## LIST OF TABLES

Table 3.1 Solution times and optimization results for the design of a stiffened panel under shear loading, using different numbers of buckling modes. ....	41
Table 3.2 Comparison of the optimized results under shear loading, employing different initial designs. ....	44
Table 3.3 Comparison of the optimized results under shear loading, using different kinds of optimization.....	45
Table 3.4 Comparison of the optimized results under combined shear and compression, employing initial designs with different numbers of stiffeners.....	47
Table 3.5 Comparison of the optimized results under combined shear and compression, employing initial designs with 11 stiffeners but different stiffener spacing.....	48
Table 3.6 Initial designs under a concentrated load, considering different optimization problems with or without skin thickness optimization and employing initial designs with different numbers of stiffeners. ....	50
Table 3.7 Comparison of optimized designs under a concentrated load, considering different optimization problems with or without skin thickness optimization and employing initial designs with different numbers of stiffeners.....	51
Table 4.1 Comparison of the optimized results with different stress constraints and without a stress constraint. ....	76
Table 4.2 Comparison of the optimized results with different buckling constraints. ....	79
Table 4.3 Comparison of the optimized results using different kinds of optimization with $\sigma_{\text{upper\_bound}} = 427.5 \text{ MPa}$ and $\lambda_{\text{lower\_bound}} = 1$ . ....	79
Table 4.4 Comparison of the optimized results with different $p$ in the $p$ -norm stress function. ....	84
Table 5.1 Objective and constraints for different postbuckling optimizations. ....	96
Table 5.2 Comparison of the initial and optimized designs of the stiffened panel under the design shear displacement $u_d = 1.25 \text{ mm}$ . ....	109

Table 5.3 Comparison of the optimization results of minimizing $P_{w,skin}$ employing different imperfections, for the stiffened panel under the design shear displacement $u_a = 1.25$ mm.....	112
Table 5.4 Comparison of the $P_{w,skin}$ value of the structures at the $i$ -th iterations, employing the imperfections at the $i$ -th and $(i-1)$ -th iterations in the analysis, for the optimized designs at the 68th-73rd iterations of minimizing $P_{w,skin}$ under the design shear displacement $u_a = 1.25$ mm.....	116
Table 5.5 Comparison of the initial and optimized designs of the stiffened panel under the design shear displacement $u_a = 5$ mm. ....	119
Table 5.6 Comparison of analysis results of the optimized design of minimizing $P_{w,skin}$ , employing imperfections with different directions and amplitudes in the analysis, for the stiffened panel under the design shear displacement $u_a = 5$ mm.....	121
Table 5.7 Comparison of the optimized designs at the 22nd-24th iterations of minimizing $P_{w,skin}$ , for the stiffened panel under the design shear displacement $u_a = 5$ mm. ....	123
Table 5.8 Comparison of the optimized designs at the 101st-104th iterations of minimizing $P_{w,skin}$ , for the stiffened panel under the design shear displacement $u_a = 5$ mm. ....	126
Table 5.9 Comparison of the optimized designs at the 192nd-193rd iterations of minimizing $P_{w,skin}$ , for the stiffened panel under the design shear displacement $u_a = 5$ mm. ....	128
Table 5.10 Comparison of the optimized designs at the 208th-210th iterations of minimizing $P_{w,skin}$ , for the stiffened panel under the design shear displacement $u_a = 5$ mm. ....	129
Table 5.11 Comparison of the optimized results with and without the use of symmetry control, for the stiffened panel under the design shear displacement $u_a = 5$ mm.	136
Table 5.12 Comparison of the optimized designs of the stiffened panel under the shear load.....	144

Table 5.13 Comparison of the optimized designs of the stiffened panel under the compression and shear loads.....	149
--	-----

## LIST OF FIGURES

Figure 3.1 Illustration of updating the stiffener layout using the control mesh: (a) a sample stiffened panel; (b) the initial stiffened panel and control mesh; (c) the updated stiffened panel and control mesh.....	19
Figure 3.2 Illustration of updating the FE mesh using free-form mesh deformation with the control mesh: (a) the initial FE and control meshes; (b) the updated FE and control meshes.....	20
Figure 3.3 Illustration of the stiffener internal topologies represented by the level set functions: (a) the LSFs corresponding to the three stiffeners respectively, their zero level sets and level set meshes; (b) stiffener layout and topologies; (c) the volume fraction fields, zero level sets and undeformed FE meshes corresponding to the three stiffeners; (d) the deformed FE mesh and corresponding physical density field. ....	21
Figure 3.4 Illustration of the computation of the volume fraction field on an undeformed FE mesh: (a) the structural boundary approximated by straight lines; (b) computation of the intersection between the element boundary and the zero level set; (c) computation of the elemental volume fraction.....	23
Figure 3.5 Illustration of the thickness distribution of the stiffened panel: (a) thicknesses for each stiffener and the skin; (b) the elemental thickness distribution on the FE mesh; (c) the geometric model of the stiffened panel, with its thickness distribution, stiffener layout and topologies. ....	24
Figure 3.6 Illustration of the pressure application. ....	24
Figure 3.7 Illustration of the computation of the term $\partial v_j / \partial \Phi_{n,b}$ : the structural boundary and material distribution (a) before perturbation; (b) after perturbation.....	31
Figure 3.8 Flowchart of the proposed method. ....	34
Figure 3.9 Loading and boundary conditions for the design of a stiffened panel under shear loading. ....	35
Figure 3.10 Initial design with 7 vertical stiffeners, $m = 0.855$ kg, and its first 4 buckling modes under shear loading, $\lambda_1 = 1.141$ , $\lambda_2 = 1.459$ , $\lambda_3 = 1.702$ , $\lambda_4 = 1.903$ . ....	35

Figure 3.11 Optimized design, $m = 0.356$ kg, and its first 4 buckling modes under shear loading, $\lambda_1 = 1.010$ , $\lambda_2 = 1.017$ , $\lambda_3 = 1.021$ , $\lambda_4 = 1.024$ .....	36
Figure 3.12 Convergence curve of the mass for the design of the stiffened panel under shear loading. ....	37
Figure 3.13 Convergence curves of the buckling load factors for the design of the stiffened panel under shear loading.....	38
Figure 3.14 First buckling modes from the 201st to the 210th iterations for the design of the stiffened panel under shear loading.....	38
Figure 3.15 First 50 buckling modes in 201st and 202nd iterations for the design of the stiffened panel under shear loading.....	39
Figure 3.16 Geometries of the optimized designs under shear loading, using different numbers of buckling modes. ....	40
Figure 3.17 Optimized designs under shear loading, employing initial designs with different thickness distributions. ....	42
Figure 3.18 Optimized designs under shear loading, employing initial designs with different stiffener layouts. ....	42
Figure 3.19 Optimized designs under shear loading, employing initial designs with different stiffener topologies. ....	43
Figure 3.20 Optimized designs under shear loading, employing initial designs with different thickness distributions, stiffener layouts and topologies.....	43
Figure 3.21 Optimized designs under shear loading, using different kinds of optimization.....	44
Figure 3.22 Loading and boundary conditions for the design of a stiffened panel under combined shear and compression.....	45
Figure 3.23 Initial and optimized designs under combined shear and compression, employing initial designs with different numbers of stiffeners.....	46

Figure 3.24 Initial and optimized designs under combined shear and compression, employing initial designs with 11 stiffeners but different stiffener spacing. ....	48
Figure 3.25 Loading and boundary conditions for the design of a stiffened panel under a concentrated load. ....	48
Figure 3.26 Initial and optimized designs under a concentrated load, considering different optimization problems with or without skin thickness optimization and employing initial designs with different numbers of stiffeners. ....	50
Figure 4.1 Illustration of how to construct and update the geometric model of a sample stiffened panel: (a) the initial stiffened layout; (b) the updated stiffened layout; (c) the initial LSFs and their zero level set for the internal topologies of the stiffeners; (d) the updated LSFs and their zero level set for the internal topologies of the stiffeners; (e) the initial layout and internal topologies of the stiffeners; (f) the updated layout and internal topologies of the stiffeners; (g) the initial thickness distribution; (h) the updated thickness distribution; (i) the initial geometric model; (j) the updated geometric model. ....	56
Figure 4.2 Illustration of updating the finite element mesh using the free-form mesh deformation method with control mesh: (a) the initial finite element and control meshes; (b) top view of the initial finite element and control meshes; (c) the updated finite element and control meshes; (d) top view of the updated finite element and control meshes. ....	57
Figure 4.3 Loading and boundary conditions for the design of a stiffened panel under combined compression and shear.....	58
Figure 4.4 Panel with the undeformed FE mesh, and its stress distribution at the middle surface and first four buckling modes under combined compression and shear, $\sigma_{vm,m,max} = 426.12$ MPa, $\lambda_1 = 0.1154$ , $\lambda_2 = 0.1717$ , $\lambda_3 = 0.2828$ , $\lambda_4 = 0.4191$ .....	58
Figure 4.5 Panel with the FE mesh using the free-form mesh deformation method with control mesh, and its stress distribution at the middle surface and first four buckling modes under combined compression and shear, $\sigma_{vm,m,max} = 400.91$ MPa, $\lambda_1 = 0.1154$ , $\lambda_2 = 0.1717$ , $\lambda_3 = 0.2828$ , $\lambda_4 = 0.4191$ . ....	59

Figure 4.6 Illustration of updating the finite element mesh using the modified free-form mesh deformation method with control mesh: (a) the initial finite element and control meshes; (b) top view of the initial finite element and control meshes; (c) the updated finite element and control meshes; (d) top view of the updated finite element and control meshes. ....	60
Figure 4.7 Panel with the FE mesh using the modified free-form mesh deformation method with control mesh, and its stress distribution at the middle surface and first four buckling modes under combined compression and shear, $\sigma_{vm,m,max} = 424.60$ MPa, $\lambda_1 = 0.1154$ , $\lambda_2 = 0.1717$ , $\lambda_3 = 0.2828$ , $\lambda_4 = 0.4192$ . ....	61
Figure 4.8 Physical density field: (a) initial; (b) updated. ....	62
Figure 4.9 Illustration of the application of pressure. ....	63
Figure 4.10 Flowchart of the level set based stiffened panel optimization method.....	71
Figure 4.11 Initial design with seven vertical stiffeners, $m = 0.826$ kg, and its stress distributions and first four buckling modes under combined compression and shear, $\sigma_{vm,b,max} = 375.5$ MPa, $\sigma_{vm,m,max} = 387.1$ MPa, $\sigma_{vm,t,max} = 401.9$ MPa, $\lambda_1 = 3.822$ , $\lambda_2 = 4.767$ , $\lambda_3 = 5.395$ , $\lambda_4 = 5.700$ . ....	72
Figure 4.12 Optimized design ( $\sigma_{upper\_bound} = 427.5$ MPa and $\lambda_{lower\_bound} = 1$ ), $m = 0.507$ kg, and its stress distributions and first four buckling modes under combined compression and shear, $\sigma_{vm,b,max} = 398.9$ MPa, $\sigma_{vm,m,max} = 411.2$ MPa, $\sigma_{vm,t,max} = 427.3$ MPa, $\lambda_1 = 1.001$ , $\lambda_2 = 1.013$ , $\lambda_3 = 1.038$ , $\lambda_4 = 1.119$ . ....	73
Figure 4.13 Convergence curves: (a) mass; (b) $p$ -norm stress function and maximum stresses at the bottom, middle and top surfaces; (c) buckling load factors. ....	74
Figure 4.14 Optimized design ( $\sigma_{upper\_bound} = 356$ MPa and $\lambda_{lower\_bound} = 1$ ), $m = 0.594$ kg, and its stress distributions and first four buckling modes under combined compression and shear, $\sigma_{vm,b,max} = 330.7$ MPa, $\sigma_{vm,m,max} = 341.6$ MPa, $\sigma_{vm,t,max} = 356.0$ MPa, $\lambda_1 = 1.007$ , $\lambda_2 = 1.152$ , $\lambda_3 = 1.304$ , $\lambda_4 = 1.399$ . ....	75
Figure 4.15 Optimized design ( $\sigma_{upper\_bound} = 513$ MPa and $\lambda_{lower\_bound} = 1$ ), $m = 0.443$ kg, and its stress distributions and first four buckling modes under combined	

compression and shear,  $\sigma_{vm,b,max} = 481.4$  MPa,  $\sigma_{vm,m,max} = 495.3$  MPa,  $\sigma_{vm,t,max} = 512.9$  MPa,  $\lambda_1 = 1.004$ ,  $\lambda_2 = 1.007$ ,  $\lambda_3 = 1.013$ ,  $\lambda_4 = 1.052$ ..... 75

Figure 4.16 Optimized design (without stress constraint and  $\lambda_{lower\_bound} = 1$ ),  $m = 0.341$  kg, and its stress distributions and first four buckling modes under combined compression and shear,  $\sigma_{vm,b,max} = 696.1$  MPa,  $\sigma_{vm,m,max} = 722.1$  MPa,  $\sigma_{vm,t,max} = 757.5$  MPa,  $\lambda_1 = 1.001$ ,  $\lambda_2 = 1.006$ ,  $\lambda_3 = 1.018$ ,  $\lambda_4 = 1.024$ ..... 76

Figure 4.17 Optimized design ( $\sigma_{upper\_bound} = 427.5$  MPa and  $\lambda_{lower\_bound} = 2$ ),  $m = 0.528$  kg, and its stress distributions and first four buckling modes under combined compression and shear,  $\sigma_{vm,b,max} = 395.7$  MPa,  $\sigma_{vm,m,max} = 409.3$  MPa,  $\sigma_{vm,t,max} = 427.4$  MPa,  $\lambda_1 = 2.006$ ,  $\lambda_2 = 2.017$ ,  $\lambda_3 = 2.029$ ,  $\lambda_4 = 2.035$ ..... 77

Figure 4.18 Optimized design ( $\sigma_{upper\_bound} = 427.5$  MPa and  $\lambda_{lower\_bound} = 3$ ),  $m = 0.552$  kg, and its stress distributions and first four buckling modes under combined compression and shear,  $\sigma_{vm,b,max} = 398.3$  MPa,  $\sigma_{vm,m,max} = 411.0$  MPa,  $\sigma_{vm,t,max} = 427.4$  MPa,  $\lambda_1 = 3.018$ ,  $\lambda_2 = 3.032$ ,  $\lambda_3 = 3.046$ ,  $\lambda_4 = 3.056$ ..... 78

Figure 4.19 Optimized design using different kinds of optimization with  $\sigma_{upper\_bound} = 427.5$  MPa and  $\lambda_{lower\_bound} = 1$ : (a) sizing optimization; (b) sizing and layout optimization; (c) topology optimization; (d) sizing and topology optimization; (e) layout and topology optimization. .... 78

Figure 4.20 Loading and boundary conditions for the design of a stiffened panel under combined compression, shear and bending..... 80

Figure 4.21 Initial design with seven vertical stiffeners,  $m = 0.826$  kg, and its stress distributions and first four buckling modes under combined compression, shear and bending,  $\sigma_{b,max} = 268.7$  MPa,  $\sigma_{m,max} = 182.6$  MPa,  $\sigma_{t,max} = 323.4$  MPa,  $\lambda_1 = 1.485$ ,  $\lambda_2 = 3.449$ ,  $\lambda_3 = 3.866$ ,  $\lambda_4 = 4.618$ ..... 80

Figure 4.22 Optimized design with  $p = 6$ ,  $m = 0.458$  kg, and its stress distributions and first four buckling modes under combined compression, shear and bending. .... 81

Figure 4.23 Optimized design with  $p = 8$ ,  $m = 0.454$  kg, and its stress distributions and first four buckling modes under combined compression, shear and bending. .... 81

Figure 4.24 Optimized design with $p = 10$ , $m = 0.453$ kg, and its stress distributions and first four buckling modes under combined compression, shear and bending. ....	82
Figure 4.25 Optimized design with $p = 12$ , $m = 0.448$ kg, and its stress distributions and first four buckling modes under combined compression, shear and bending. ....	82
Figure 4.26 Optimized design with $p = 18$ , $m = 0.443$ kg, and its stress distributions and first four buckling modes under combined compression, shear and bending. ....	83
Figure 4.27 Optimized design with $p = 24$ , $m = 0.444$ kg, and its stress distributions and first four buckling modes under combined compression, shear and bending. ....	83
Figure 5.1 Illustration of the geometric and FE models of a sample stiffened panel. ....	88
Figure 5.2 Illustration of applying a pressure loading. ....	91
Figure 5.3 Procedure for the geometrically nonlinear analysis, employing a modified automatic load incrementation scheme. ....	93
Figure 5.4 Design of a stiffened panel loaded by shear displacement: (a) loading and boundary conditions; (b) force diagram. ....	105
Figure 5.5 Initial design of the stiffened panel loaded by shear displacement. ....	106
Figure 5.6 Optimized designs of the stiffened panel under the design shear displacement $u_a = 1.25$ mm. ....	108
Figure 5.7 Equilibrium paths for the initial and optimized designs of the stiffened panel under the design shear displacement $u_a = 1.25$ mm. ....	108
Figure 5.8 Displacement configurations of the optimized design minimizing $P_{w,skin}$ , employing different imperfections in the analysis, for the stiffened panel under the design shear displacement $u_a = 1.25$ mm. ....	110
Figure 5.9 Equilibrium paths and comparison of the optimized design minimizing $P_{w,skin}$ , employing different imperfections in the analysis, for the stiffened panel under the design shear displacement $u_a = 1.25$ mm. ....	110

Figure 5.10 Optimization results of minimizing $P_{w,skin}$ employing different imperfections, for the stiffened panel under the design shear displacement $u_a = 1.25$ mm. ....	111
Figure 5.11 Convergence history curves of the optimization minimizing $P_{w,skin}$ employing positive imperfections with an amplitude of $20 \mu\text{m}$ , for the stiffened panel under the design shear displacement $u_a = 1.25$ mm. ....	114
Figure 5.12 Employed imperfection and displacement configurations of the optimized designs at the 66th-73rd iterations of minimizing $P_{w,skin}$ employing positive imperfections with an amplitude of $20 \mu\text{m}$ , for the stiffened panel under the design shear displacement $u_a = 1.25$ mm. ....	114
Figure 5.13 Equilibrium paths of the optimized designs at the 66th-73rd iterations of minimizing $P_{w,skin}$ employing positive imperfections with an amplitude of $20 \mu\text{m}$ , for the stiffened panel under the design shear displacement $u_a = 1.25$ mm. ....	115
Figure 5.14 Comparison of displacement configurations of the structures at the $i$ -th iterations, employing the imperfections at the $i$ -th and $(i-1)$ -th iterations in analysis, for the optimized designs at the 68th-73rd iterations of minimizing $P_{w,skin}$ under the design shear displacement $u_a = 1.25$ mm. ....	115
Figure 5.15 Optimized designs of the stiffened panel under the design shear displacement $u_a = 5$ mm. ....	118
Figure 5.16 Equilibrium paths for the initial and optimized designs of the stiffened panel under the design shear displacement $u_a = 5$ mm. ....	119
Figure 5.17 Displacement configurations of the optimized design of minimizing $P_{w,skin}$ , employing imperfections with different directions and amplitudes in the analysis, for the stiffened panel under the design shear displacement $u_a = 5$ mm. ....	120
Figure 5.18 Equilibrium paths for the optimized design of minimizing $P_{w,skin}$ , employing imperfections with different directions and amplitudes in the analysis, for the stiffened panel under the design shear displacement $u_a = 5$ mm. ....	121
Figure 5.19 Convergence history curves of the optimization minimizing $P_{w,skin}$ , for the stiffened panel under the design shear displacement $u_a = 5$ mm. ....	122

Figure 5.20 Employed imperfections and displacement configurations of the optimized designs at the 22nd-24th iterations of minimizing $P_{w,skin}$ , for the stiffened panel under the design shear displacement $u_a = 5$ mm. ....	122
Figure 5.21 Equilibrium paths for the optimized designs at the 22nd-24th iterations of minimizing $P_{w,skin}$ , for the stiffened panel under the design shear displacement $u_a = 5$ mm.....	123
Figure 5.22 Employed imperfections and displacement configurations of the optimized designs at the 101st-104th iterations of minimizing $P_{w,skin}$ , for the stiffened panel under the design shear displacement $u_a = 5$ mm. ....	125
Figure 5.23 Equilibrium paths for the optimized designs at the 101st-104th iterations of minimizing $P_{w,skin}$ , for the stiffened panel under the design shear displacement $u_a = 5$ mm.....	126
Figure 5.24 Employed imperfections and displacement configurations of the optimized designs at the 192nd-193rd iterations of minimizing $P_{w,skin}$ , for the stiffened panel under the design shear displacement $u_a = 5$ mm. ....	127
Figure 5.25 Equilibrium paths for the optimized designs at the 192nd-193rd iterations of minimizing $P_{w,skin}$ , for the stiffened panel under the design shear displacement $u_a = 5$ mm.....	128
Figure 5.26 Employed imperfections and displacement configurations of the optimized designs at the 208th-210th iterations of minimizing $P_{w,skin}$ , for the stiffened panel under the design shear displacement $u_a = 5$ mm. ....	128
Figure 5.27 Equilibrium paths for the optimized designs at the 208th-210th iterations of minimizing $P_{w,skin}$ , for the stiffened panel under the design shear displacement $u_a = 5$ mm.....	129
Figure 5.28 Comparison of the optimized designs of minimizing $P_{w,skin}$ employing positive and negative imperfections, for the stiffened panel under the design shear displacement $u_a = 5$ mm. ....	131

Figure 5.29 Equilibrium paths for the optimized designs of minimizing $P_{w,skin}$ employing positive and negative imperfections, for the stiffened panel under the design shear displacement $u_a = 5$ mm. ....	131
Figure 5.30 Convergence history curves of the optimization maximizing $F_{r,total}$ , for the stiffened panel under the design shear displacement $u_a = 5$ mm. ....	132
Figure 5.31 Employed imperfections and displacement configurations of the optimized designs at the 16th-19th iterations of maximizing $F_{r,total}$ , for the stiffened panel under the design shear displacement $u_a = 5$ mm. ....	133
Figure 5.32 Equilibrium paths and comparison of the optimized designs at the 16th-19th iterations of maximizing $F_{r,total}$ , for the stiffened panel under the design shear displacement $u_a = 5$ mm. ....	133
Figure 5.33 Convergence study for the optimized designs at the 19th-23rd iterations of maximizing $F_{r,total}$ , for the stiffened panel under the design shear displacement $u_a = 5$ mm. ....	134
Figure 5.34 Illustration of symmetry control. ....	135
Figure 5.35 Comparison of the optimized results with and without the use of symmetry control, for the stiffened panel under the design shear displacement $u_a = 5$ mm. ....	136
Figure 5.36 Illustration of the algorithm for minimizing the applied displacement at a design load under displacement loading. ....	137
Figure 5.37 Procedure for the geometrically nonlinear analysis, combined with the bisection method. ....	138
Figure 5.38 Optimized design minimizing the applied displacement at the design load $F_d = 1.5 \times 10^5$ N, for the stiffened panel under the design shear displacement. ...	140
Figure 5.39 Loading and boundary conditions for the design of a stiffened panel loaded by a shear load. ....	141
Figure 5.40 Initial designs with (a) 3 stiffeners and (b) 7 stiffeners, for the design of the stiffened panel under the shear load. ....	142

Figure 5.41 Optimized designs of the stiffened panel under the shear load, employing the 3-stiffener initial design. ....	142
Figure 5.42 Optimized designs of the stiffened panel under the shear load, employing the 7-stiffener initial design. ....	143
Figure 5.43 Equilibrium paths for the optimized designs of the stiffened panel under the shear load. ....	143
Figure 5.44 Loading and boundary conditions for the design of a stiffened panel loaded by compression and shear loads. ....	146
Figure 5.45 Optimized designs of the stiffened panel under the compression and shear loads, employing the 3-stiffener initial design. ....	147
Figure 5.46 Optimized designs of the stiffened panel under the compression and shear loads, employing the 7-stiffener initial design. ....	148
Figure 5.47 Equilibrium paths for the optimized designs of the stiffened panel under the compression and shear loads. ....	148
Figure 6.1 Sample curved stiffened panel and its control and FE meshes: (a) geometric model; (b) control and FE meshes. ....	153
Figure 6.2 Illustration of the curved stiffener layout represented by the LSF: (a) the LSF, the zero level set and the level set mesh for the initial structure; (b) the LSF, the zero level set and the control mesh wireframe for the initial structure; (c) the initial control mesh wireframe and the FE mesh; (d) the LSF, the zero level set and the level set mesh for the updated structure; (e) the LSF, the zero level set and the control mesh wireframe for the updated structure; (f) the updated control mesh wireframe and the FE mesh.....	153
Figure 6.3 Illustration of how to construct the geometric and FE models of a sample curved stiffened panel using LSFs: (a) the LSF representing the stiffener curves, its zero level set and level set mesh; (b)-(d) the LSFs corresponding to the three stiffeners respectively, their zero level sets and level set meshes; (e) the deformed FE mesh; (f)-(h) the volume fraction fields, zero level sets and undeformed FE	

meshes corresponding to the three stiffeners; (i) the deformed FE mesh and corresponding physical density field; (j) the geometric model. .... 156

Figure 6.4 Illustration of the application of pressure: (a) an example with the undeformed FE mesh; (b) an example with the deformed FE mesh. .... 158

Figure 6.5 Illustration of how to compute the term of  $\partial y_i / \partial \Phi_{l,b}$ : (a) the zero level set before perturbation and the level set mesh; (b) the zero level set and the corresponding control mesh before perturbation; (c) the zero level set after perturbation; (d) the control mesh, deformed in accordance with the change of the zero level set after perturbation. .... 162

Figure 6.6 Flowchart of the proposed method for the design of curved stiffened panels. .... 166

Figure 6.7 Loading and boundary conditions for the design of a stiffened panel under shear loading. .... 168

Figure 6.8 Initial design with 7 vertical stiffeners,  $m = 0.855$  kg, and its first 6 buckling modes under shear loading,  $\lambda_1 = 1.141$ ,  $\lambda_2 = 1.459$ ,  $\lambda_3 = 1.702$ ,  $\lambda_4 = 1.903$ ,  $\lambda_5 = 2.089$ ,  $\lambda_6 = 2.155$ . .... 169

Figure 6.9 Optimized design for mass minimization with buckling constraints, considering the initial design with 7 vertical stiffeners,  $m = 0.563$  kg, and its first 6 buckling modes under shear loading,  $\lambda_1 = 1.008$ ,  $\lambda_2 = 1.077$ ,  $\lambda_3 = 1.102$ ,  $\lambda_4 = 1.122$ ,  $\lambda_5 = 1.246$ ,  $\lambda_6 = 1.256$ . .... 170

Figure 6.10 Optimized design without the layout optimization for mass minimization with buckling constraints, considering the initial design with 7 vertical stiffeners,  $m = 0.594$  kg, and its first 6 buckling modes under shear loading,  $\lambda_1 = 1.000$ ,  $\lambda_2 = 1.039$ ,  $\lambda_3 = 1.064$ ,  $\lambda_4 = 1.170$ ,  $\lambda_5 = 1.182$ ,  $\lambda_6 = 1.293$ . .... 170

Figure 6.11 Initial design with 8 vertical stiffeners,  $m = 0.905$  kg, and its first 6 buckling modes under shear loading,  $\lambda_1 = 1.364$ ,  $\lambda_2 = 1.744$ ,  $\lambda_3 = 2.027$ ,  $\lambda_4 = 2.255$ ,  $\lambda_5 = 2.412$ ,  $\lambda_6 = 2.522$ . .... 172

Figure 6.12 Optimized design for mass minimization with buckling constraints, considering the initial design with 8 vertical stiffeners,  $m = 0.564$  kg, and its first 6

buckling modes under shear loading, $\lambda_1 = 1.002$ , $\lambda_2 = 1.061$ , $\lambda_3 = 1.119$ , $\lambda_4 = 1.190$ , $\lambda_5 = 1.248$ , $\lambda_6 = 1.253$ . .....	172
Figure 6.13 Initial design with 9 vertical stiffeners, $m = 0.955$ kg, and its first 6 buckling modes under shear loading, $\lambda_1 = 1.667$ , $\lambda_2 = 2.134$ , $\lambda_3 = 2.475$ , $\lambda_4 = 2.731$ , $\lambda_5 = 2.837$ , $\lambda_6 = 3.046$ . .....	173
Figure 6.14 Optimized design for mass minimization with buckling constraints, considering the initial design with 9 vertical stiffeners, $m = 0.565$ kg, and its first 6 buckling modes under shear loading, $\lambda_1 = 1.008$ , $\lambda_2 = 1.058$ , $\lambda_3 = 1.108$ , $\lambda_4 = 1.196$ , $\lambda_5 = 1.298$ , $\lambda_6 = 1.316$ . .....	173
Figure 6.15 Initial design with 11 vertical stiffeners, $m = 1.056$ kg, and its first 6 buckling modes under shear loading, $\lambda_1 = 3.153$ , $\lambda_2 = 3.2322$ , $\lambda_3 = 3.2325$ , $\lambda_4 = 3.848$ , $\lambda_5 = 3.992$ , $\lambda_6 = 4.193$ . .....	174
Figure 6.16 Optimized design at 1500th iteration for mass minimization with buckling constraints, considering the initial design with 11 vertical stiffeners, $m = 0.562$ kg, and its first 6 buckling modes under shear loading, $\lambda_1 = 1.006$ , $\lambda_2 = 1.047$ , $\lambda_3 = 1.099$ , $\lambda_4 = 1.145$ , $\lambda_5 = 1.163$ , $\lambda_6 = 1.216$ . .....	174
Figure 6.17 Optimized design at 2500th iteration for mass minimization with buckling constraints, considering the initial design with 11 vertical stiffeners, $m = 0.559$ kg, and its first 6 buckling modes under shear loading, $\lambda_1 = 1.003$ , $\lambda_2 = 1.085$ , $\lambda_3 = 1.142$ , $\lambda_4 = 1.163$ , $\lambda_5 = 1.220$ , $\lambda_6 = 1.254$ . .....	175
Figure 6.18 Optimized design for critical buckling load factor maximization with a mass constraint, considering the initial design with 7 vertical stiffeners, $m = 0.563$ kg, and its first 6 buckling modes under shear loading, $\lambda_1 = 1.000$ , $\lambda_2 = 1.060$ , $\lambda_3 = 1.094$ , $\lambda_4 = 1.119$ , $\lambda_5 = 1.210$ , $\lambda_6 = 1.242$ . .....	176
Figure 6.19 Comparison of the geometries of the optimized designs in Figs. 6.9 (blue, $m = 0.563$ kg and $\lambda_1 = 1.008$ ) and 6.18 (red, $m = 0.563$ kg and $\lambda_1 = 1.000$ ). .....	176
Figure 6.20 Optimized design without the layout optimization for critical buckling load factor maximization with a mass constraint, considering the initial design with 7 vertical stiffeners, $m = 0.563$ kg, and its first 6 buckling modes under shear loading, $\lambda_1 = 0.691$ , $\lambda_2 = 0.717$ , $\lambda_3 = 0.805$ , $\lambda_4 = 0.823$ , $\lambda_5 = 0.884$ , $\lambda_6 = 0.958$ . .....	177

Figure 6.21 Optimized design with straight stiffeners for mass minimization with buckling constraints, considering the initial design with 7 vertical stiffeners,  $m = 0.557$  kg, and its first 6 buckling modes under shear loading,  $\lambda_1 = 1.001$ ,  $\lambda_2 = 1.012$ ,  $\lambda_3 = 1.014$ ,  $\lambda_4 = 1.022$ ,  $\lambda_5 = 1.070$ ,  $\lambda_6 = 1.162$ . ..... 178

Figure 6.22 Optimized design with curved stiffeners for mass minimization with  $p$ -norm buckling, stiffener spacing and element distortion constraints, considering the initial design with 7 vertical stiffeners,  $m = 0.563$  kg, and its first 6 buckling modes under shear loading,  $\lambda_1 = 1.007$ ,  $\lambda_2 = 1.065$ ,  $\lambda_3 = 1.083$ ,  $\lambda_4 = 1.119$ ,  $\lambda_5 = 1.237$ ,  $\lambda_6 = 1.244$ . ..... 179

Figure 6.23 Optimized design with curved stiffeners for mass minimization with buckling constraints, considering the optimized design with straight stiffeners in Fig. 6.21 as the initial design,  $m = 0.554$  kg, and its first 6 buckling modes under shear loading,  $\lambda_1 = 1.002$ ,  $\lambda_2 = 1.118$ ,  $\lambda_3 = 1.140$ ,  $\lambda_4 = 1.150$ ,  $\lambda_5 = 1.203$ ,  $\lambda_6 = 1.241$ . ..... 180

Figure 6.24 Comparison of postbuckling behaviours between the optimized design with curved stiffeners in Fig. 6.23 and the optimized design with straight stiffeners in Fig. 6.21. .... 181

# 1 INTRODUCTION

Stiffened panel structures, which are usually assembled from thin plates and additional reinforcing structural members called stiffeners, are widely used in aircraft applications, such as the fuselage and wings, due to their high stiffness-to-weight and strength-to-weight ratios. However, they are prone to buckling under flight loads and hence their load-carrying capability is strongly influenced by stability issues. Inevitably, this leads to stiffened panel design bringing buckling phenomena into consideration.

Most of the existing stiffened panel designs have been based on experimental research and the experience of designers. This usually leads to over-design to ensure the safety and reliability of structures. The growing use of high-performance composite structures has further motivated the development of optimization for the design of stiffened panels to improve their buckling capability. Topology optimization is one of the structural optimization methods with the greatest degree of design freedom. It can help with determining the best possible shapes and material distributions for the prescribed objective by redistributing material within a given design domain. This is achieved by discretizing the design domain where material can potentially exist in the form of finite elements, and then adding, removing and redistributing material within these elements. These elements can take the form of thin plates or solid blocks, with 3D brick elements providing a more generalized although more computationally expensive solution. In Aage et al. [1] for example, stiffness-based topology optimization was used to produce an optimum full-scale aircraft wing design using brick elements. To obtain a design allowing for details of the order of those found in existing wing structures which are essentially made up of plates and beams, 1.1 billion 3D elements were required to

## **Simultaneous Sizing, Layout and Topology Optimization for Buckling and Postbuckling of Stiffened Panels**

discretize the entire wing. Although only linear elasticity was considered for optimization for three load cases, up to 5 days of computing time on 8000 CPUs were needed to obtain the optimized design.

For a stiffened panel, the more relevant, but challenging design criterion is buckling, usually requiring a time-consuming structural analysis. This puts a severe limitation on the application of topology optimization parametrizing the design space with 3D brick elements. It is well-known that for a stiffened panel, 2D plate and shell elements are much more efficient and accurate. This thesis presents a topology optimization parameterization for panels stiffened with straight stiffeners, enabling the simultaneous optimization of the thicknesses of the skin and stiffeners, and stiffener layout and internal topologies, employing plate and shell elements for computational efficiency and accuracy. The weight minimization of stiffened panels under buckling constraints is investigated. Since stiffened panels are also prone to stress-fracture/yield under flight loads, stress is another important design criterion. The weight minimization of stiffened panels under stress and buckling constraints is also investigated.

It is well-known however that stiffened panels can carry loads several times and even higher than the critical buckling load. Therefore, stiffened panels can be designed to work in the postbuckling field beyond the critical buckling load, offering significant potential for further structural weight reductions. This thesis extends the proposed method to optimize the postbuckling behaviour of stiffened panels with straight stiffeners.

Kapania et al. [2] introduced curvilinearly stiffened panels and showed that they have the potential to result in lighter weight designs than straight stiffened panels under particular design loads. In this thesis, the proposed method is extended to design panels stiffened with curved stiffeners as well, focusing on the development of a method to manipulate the stiffener layout, with curved members allowed. Simultaneous layout and topology optimization of stiffened panels is investigated.

The thesis is organized as follows: Chapter 2 presents a literature review of design optimization for buckling, stress and postbuckling of stiffened panels. This is followed by a discussion about the topology optimization of stiffened panel design as well as buckling- and stress-based topology optimization. The main challenges and objectives that this thesis aims to address are outlined. Chapter 3 presents simultaneous sizing,

## **Chapter 1: Introduction**

layout and topology optimization of panels with straight stiffeners under buckling constraints. Chapter 4 presents simultaneous sizing, layout and topology optimization of panels with straight stiffeners under both stress and buckling constraints. Chapter 5 presents simultaneous sizing, layout and topology optimization of panels with straight stiffeners considering postbuckling. Simultaneous layout and topology optimization of panels with curved stiffeners considering buckling is described in Chapter 6. In Chapters 2 to 6, the optimization methodology, problem definition, numerical examples, discussions for the method and optimized results, and conclusions are all included for each optimization. Chapter 7 presents overall conclusions and future works.

## 2 LITERATURE REVIEW

This chapter presents a literature review focusing on the design optimization of stiffened panels considering buckling, stress and postbuckling. Works on topology optimization for stiffened panel design and buckling- and stress-based topology optimization are also presented. Based on the outcomes of this review and considering the need to study the postbuckling topology optimization of stiffened panels which has not been investigated so far, the main challenges and objectives that this thesis aims to address are outlined.

### 2.1 Design Optimization for Buckling and Stress of Stiffened Panels

Stiffened panels constitute one of the most common components in aerospace structures, such as the fuselage and wings of aircraft, due to their high stiffness-to-weight and strength-to-weight ratios. However, they are prone to fail due to buckling or high stress. Therefore, in the design and optimization of stiffened panels, buckling and stress are the two most important design criteria.

Since Bedair [3] investigated the effect of stiffener location on structural stability noting that the size of a stiffener influences its optimal location, many research works in which stiffened panels are designed for maximum buckling performance, or for minimum weight whilst ensuring structural performance in relation to buckling and stress, have been conducted using sizing and layout optimization, to determine the best thickness distribution on the skin and stiffeners, the stiffener number and the best orientation, spacing and placement for each stiffener, as well as the optimal curvature for curved

stiffeners [2, 4-11]. Kapania et al. [2] investigated both panels with straight and curvilinear stiffeners. NURBS (Non-Uniform Rational B-Splines) were used to represent stiffener curves. The problem of mass minimization subject to buckling and stress constraints was investigated. Both the thickness of the skin and the cross-sectional sizes of the stiffeners were considered as design variables, as well as the design parameters in the NURBS to manipulate the orientation, spacing, location, and curvature of the stiffeners. In this work, the layout optimization of the stiffeners was conducted by manually updating one or two design parameters in the NURBS. Therefore, the allowed number of design variables for the layout optimization was limited. Continuing this research on curvilinearly stiffened panels, a framework, EBF3PanelOpt, was developed for their design optimization [9, 10, 12]. In EBF3PanelOpt, both the panel size and shape could be specified, through the panel thickness, stiffener thickness, and stiffener height as sizing quantities, with the stiffener curve represented through the coordinates of two end-points and a control point in a third order uniform rational B-spline. The problem of minimizing the mass of the stiffened panel with constraints imposed on global buckling, von Mises stress and crippling or local failure of the stiffeners was investigated, employing Genetic Algorithm (GA) or Particle Swarm Optimization (PSO). The number of stiffeners has also been taken as the design variable in some works. Locatelli et al. [13] investigated the parameterization of curvilinear spars and ribs inside a wing structure, where the number and placement of the stiffeners were optimized. Following this work, Stanford et al. [14] presented the aeroelastic sizing and layout design of a wingbox, where the structural mass was minimized under stress, buckling and manufacturing (stiffener thickness and aspect ratio) constraints. A nested optimization was employed. Specifically, the number and placement of the ribs and skin stiffeners were optimized within the outer level using a global optimizer, with the sizes of all components in the wingbox optimized within the inner level using a gradient-based optimizer. De et al. [15] developed an optimization framework for the internal structure of aircraft wings with curvilinear spars and ribs, where the weight and flutter velocity of the wing were optimized under buckling and stress constraints. The parameterization of curvilinear spars and ribs in [13] was modified, where spars and ribs which did not start at the leading-edge spar and end at the trailing-edge spar, could be generated. The number, location, and curvature of the stiffening members could be optimized, as well as the thicknesses of the panel and stiffening members, using PSO.

## Simultaneous Sizing, Layout and Topology Optimization for Buckling and Postbuckling of Stiffened Panels

In the aforementioned works when layout optimization, or both discrete (the number of spars, ribs, and stiffeners) and continuous (sizing variables and the rest of the layout variables such as stiffener spacing and parameters manipulating B-Splines representing stiffener curves) variables were included in the optimization, gradient-free optimization techniques such as GAs, PSO, and Response Surface Approaches (RSA), were used. Though these optimization problems can be effectively solved using gradient-free optimization techniques, this family of algorithms is computationally expensive. To alleviate this issue, the improvement in gradient-free optimization techniques and the application of approximate analyses have been investigated. For example, Nagendra et al. [4] investigated the minimum weight design of a stiffened composite panel with a centrally located hole, by optimizing ply thicknesses in the panel and stiffener laminates, and the stiffener height. Constraints were imposed on the buckling load and the maximum strain near the hole. Structural optimization of stiffened panels often involves multiple local optima with comparable performance, making it suitable for GAs which allow designers to obtain multiple candidate designs. However, the cost of a GA search is generally high, often requiring thousands or more of structural analyses. To address this, Nagendra et al. [5] made several changes to the GA to reduce the computational cost and improve its reliability. Compared with the optimized design by [4] using a continuous optimization procedure, the weights of the optimized designs using GA optimization were decreased by about 8%. However, the use of detailed finite element models for global optimization remains unaffordable in many cases due to the high computational cost of the structural analysis. Considerations of computational cost often dictate the use of simplified models in structural optimization, for example using a simple finite strip model. Following the works [4, 5], experimental and analytical studies were conducted to test the validity of the buckling and failure analysis on the optimized stiffened panels, so as to obtain a good understanding of the difference between analytical and experimental results [16, 17]. Approximate analyses were also investigated by Vitali et al. [18, 19], providing reasonably accurate estimates efficiently and allowing the many thousands of structural analyses needed for global optimization to be performed. In the work by Vitali et al. [18], a crack propagation constraint was used as an example to demonstrate the feasibility of combining multi-fidelity models to obtain accurate results at a low computational cost. For the EBF3PanelOpt, kriging approximation in conjunction with GA was also employed to improve the computational efficiency [10].

It is also known that gradient-free algorithms like GAs scale poorly with an increasing number of design variables. When sizing and shape variables are included, they need to be restricted to a small and diluted set of parameters. Decreasing the number of design variables in an optimization and applying gradient-free algorithms combined with gradient-based optimization have been investigated to address this issue. For example, in EBF3PanelOpt [9] apart from the skin thickness as a design variable, six further design variables were required for each uniform cross-section blade-stiffener, namely, two for the end-points and two for the control point manipulating the third order uniform rational B-spline, and two for height and thickness. Therefore, the number of design variables was six times the number of stiffeners, in addition to the one design variable for the skin. It was recommended that a maximum of six stiffeners, namely 37 design variables, should be used during the optimization using EBF3PanelOpt [9]. To decrease the number of layout design variables, linked shape parameterization based on the B-spline curves in [13] was proposed, where only six design variables were required to define a set of spars and ribs. Specifically, one design variable represented the number of spars and ribs; two design variables were used to define the position of the line where the control points were placed; three design variables were used to define the spacing of the start, control, and end points of B-spline curves. Continuing this work, by employing an extended design space and mapping technology, the linked shape parameterization was modified to allow the generation of spars and ribs which did not start at the leading-edge spar and end at the trailing-edge spar in [15]. Decreasing the number of sizing design variables was also investigated in [15]. The panel thicknesses were optimized during the optimization, while the thicknesses of the stiffeners were related to the panel thicknesses and determined by empirical formulas. Due to the large number of design variables in the optimization of composite stiffened panels, Herencia et al. [20] presented a two-step optimization strategy combining a gradient-based method and a GA. In the first step of the two-step optimization scheme, gradient-based optimization optimized the lamination parameters; while in the second step, the GA was used to identify the lay-ups for a super-stiffener's laminates. To solve issues, i.e., the high computational cost and the limited number of design variables, Stanford et al. [14] developed a nested optimization to simultaneously handle wingbox rib and skin stiffener layout design with a mixed-integer surrogate infill optimizer, as well as a spatially detailed set of component sizing design variables with a gradient-based sizing optimizer. Even so, the total number of design variables considered in this work was still around one hundred.

## Simultaneous Sizing, Layout and Topology Optimization for Buckling and Postbuckling of Stiffened Panels

It is noted that in all the aforementioned works, the internal topology of each stiffener was predetermined and has not been considered for optimization. This causes a reduced design space to be able to be searched, and consequently limits the performance improvement.

Unlike sizing and shape optimization, topology optimization can be conducted at the concept design stage where information on structural geometry and topology is unknown, offering a design method with the highest degree of design freedom. Since the pioneering work of Bendsøe and Kikuchi [21], different topology optimization methods, such as the solid isotropic material with penalization (SIMP) method [22-24], the level set method (LSM) [25-28] and the evolutionary approach [29, 30] have been developed. Generally, it parameterizes the design space with small continuum material units, i.e., 3D brick elements, and is able to achieve the structure with the optimal performance by adding, removing and redistributing material on these units. However, because of this parameterization with 3D brick elements, it is challenging to enforce a plate-based stiffened panel configuration in the resulting solution and typically it requires an extremely fine mesh [1]. For a stiffened panel, 2D plate and shell elements are preferred as they are much more efficient and accurate. In Stanford et al. [31] and Townsend and Kim [32], topology optimization was applied to the design of stiffened panels using 2D plate elements. The internal topologies of the stiffeners were optimized using the SIMP and level set methods, respectively. However, the optimizations were conducted with fixed thickness distribution and stiffener layout. The design space was therefore, still limited, unable to vary the stiffener thicknesses and layout as well as the skin thickness.

Until now, the design of stiffened panels simultaneously optimizing the thickness distribution of the whole structure and the layout and internal topologies of the stiffeners, has not been investigated. The main reason for this is that one cannot expect a reliable convergence when applying gradient-free optimization approaches to this optimization problem due to the large number of design variables in topology optimization, from thousands to billions, and even higher. Meanwhile, there is still no effective gradient-based optimization method to handle the simultaneous sizing, layout and topology optimization.

It is noted that, in contrast to traditional panels stiffened with straight stiffeners, Kapania et al. [2] introduced curvilinearly stiffened panels and showed that they have the potential to result in lighter weight designs. In this work, mass minimization subject to buckling and stress constraints was investigated. NURBS were used to represent the stiffener curves. The effects of orientation, spacing, location, and curvature of curvilinear stiffeners on the optimized designs were explored, and the optimized designs with curvilinear stiffeners were compared with those with straight stiffeners. A curvilinear placement of stiffeners tended to provide a slightly better design than straight stiffeners though it was not always guaranteed. It has been observed that many local optima exist for this problem, and panels with either curvilinear stiffeners or straight stiffeners can be the global optimum. Following this research on curvilinearly stiffened panels, B-Splines were used for the representation of stiffener curves in lots of stiffened panel optimization works, i.e., BF3PanelOpt [9, 10, 12], and spar/rib optimization in a wingbox in [13-15]. However, for the B-Spline curves, they do not pass through all the control points, leading to the convenience of using the locations of control points to describe a stiffener curve. An additional step is often needed to ensure that the described stiffener is located within the skin. Zhao et al. [33] utilized a Hobby spline to parameterize stiffener curves, since it allows a curve to pass through all the control points and therefore, it is easier to make sure that the described stiffener is located within the skin. In these works, however, the stiffener curves are limited by the pre-specified curvilinear functions, whether B-Spline or Hobby spline curves are used, as well as the optimization design space.

## 2.2 Design Optimization for Postbuckling of Stiffened Panels

It is well-known that stiffened panels can carry loads several times higher than the critical buckling load. Therefore, stiffened panels can be designed to work in the postbuckling field well beyond the critical buckling load, offering the potential for further structural weight reductions.

Many research works for the design of stiffened panels considering postbuckling behaviour have focused on sizing optimization [34, 35], i.e., optimizing the sizes of the skin and stiffeners, as well as the angles of the stacking sequence for composite stiffened panels [36, 37]. Arendsen et al. [38] investigated the optimization for weight minimization of stiffened panels, by optimizing the height of a stiffener or the thickness of a sublaminates. Constraints were imposed on the ratio of the prebuckling to

## Simultaneous Sizing, Layout and Topology Optimization for Buckling and Postbuckling of Stiffened Panels

postbuckling strains, global buckling load and prebuckling stiffness. Liguori et al. [37] presented the postbuckling optimization of a variable angle tow composite wingbox. The out-of-plane displacement of the wingbox with the “worst-case” imperfection was minimized, where the “worst-case” imperfection was defined as the one resulting in the largest out-of-plane displacement among all possible imperfections. Strains and tip displacement were constrained by adding a penalty term to the objective function when any constraint was not satisfied. The angles of the stacking sequence were optimized, employing an integer-based GA and a Monte Carlo Algorithm. In some works, the stiffener number and panel lay-up have also been considered for optimization. Bisagni and Lanzi [39] investigated postbuckling optimization for composite stiffened panels subjected to compression loads. The numbers of layers in the skin and stiffeners, side dimensions of the stiffeners and the number of stiffeners were optimized. The optimization problem was formulated to minimize the structural weight, subject to constraints on critical buckling and collapse loads, and pre-buckling stiffness, employing GA with neural networks. Rikards et al. [40] investigated the optimization design for weight minimization of stiffened composite shells. Constraints were imposed on critical buckling and collapse loads, and prebuckling and postbuckling stiffness of the stiffened shell, where the ratio of collapse load to first critical load was selected by a designer, and the selection of the ratio of the prebuckling and postbuckling stiffness depended on the design requirement, i.e., strong or mild stiffness reduction in the postbuckling stage. The surrogate models employing the experimental design and response surface methodology were built for the optimization. The design variables included the thicknesses of the layers in the skin and stringers and the height and number of stringers. Lanzi and Giavotto [41] studied multi-objective optimization for the design of composite stiffened panels in the postbuckling regime. Multiple objectives, i.e., weight minimization, critical buckling load maximization, and collapse load maximization were considered with/without a constraint on the ratio between collapse and buckling loads. The design variables included the number of stiffeners and their dimensions, and lay-up variables describing the stacking sequences of the panel skin and of the stiffeners. The optimization was based on GA with global approximation strategies. Kang and Kim [42] investigated the minimum weight design of compressively loaded composite stiffened panels for a given design strength in the postbuckling regime. In this work, the skin size and the number of stiffeners were fixed during the optimization; stiffener locations and dimensions, and the numbers of skin and stiffener plies were

taken as design variables and optimized using a modified GA with a parallel computing scheme. Since the postbuckling optimization problem is highly nonlinear and non-convex, and in most of the above-mentioned works both discrete and continuous variables are included in the optimization, gradient-free optimization techniques such as GA, were usually used. As it has been discussed for the buckling and stress optimization of stiffened panels, the main disadvantage of this family of algorithms is that they require a very high number of function evaluations compared to gradient-based algorithms. Therefore, an optimization procedure based on GA coupled with a global approximation strategy, such as neural networks [43, 44], Radial Basis Functions [45, 46] and Kriging method [47, 48], or coupled with a parallel computing scheme, are usually employed.

The topologies of stiffened panels, including stiffener layout (locations and orientations) and internal topologies however, have not been considered for postbuckling optimization. One of the main reasons for this is that these gradient-free algorithms scale poorly with an increasing number of design variables and topology optimization usually requires a large number of design variables.

For a stiffened panel, bifurcation-type buckling usually occurs, accompanied by the loss of in-plane stiffness in the postbuckling regime as well as increasing out-of-plane deformation of the skin. This can cause a sharp drop in load-carrying capability and the growth of out-of-plane displacements of the skin can reduce the performance of the stiffened panel. For example, the aerodynamic characteristics of a wing surface can be affected by large out-of-plane deformation of the skin. Therefore, depending on the application and design requirements, out-of-plane skin deformation [37, 49] and/or load-carrying capability [49] in a postbuckling regime need to be considered in the design and optimization of stiffened panels. To evaluate the load-carrying capability, several metrics, such as the critical buckling load, postbuckling stiffness [40], ratio of the postbuckling to prebuckling in-plane stiffness [38, 40], postbuckling strength [34, 42], collapse load [39, 41], postbuckling in-plane deformation [49], and total reaction force for a design loaded by uniform displacements [50], have been used.

Postbuckling analysis of a stiffened panel often cannot be conducted by performing a geometrically nonlinear analysis on a perfect structure, due to the discontinuous response at the point of bifurcation. A geometric imperfection is normally introduced therefore to turn the postbuckling problem into one with a continuous response.

## Simultaneous Sizing, Layout and Topology Optimization for Buckling and Postbuckling of Stiffened Panels

However, postbuckling behaviours of stiffened panels are often strongly influenced by the size and shape of this imperfection, and the analysis results are therefore, usually sensitive to the imperfections added into the original geometry [51]. Many works have investigated the imperfection sensitivity of optimized stiffened panels in terms of the shape, amplitude and direction of the imperfection [34, 42]. However, understanding of how these affect optimization remains limited.

Mode jumping and mode switching can also present challenges for the postbuckling optimization of stiffened panels. As the load is increased a sudden change in buckling shape, known as mode jumping can occur. As a result, a significant change in the displacement configuration and stress distribution of the stiffened panel can occur [52], causing a discontinuous response. Buckling modes can also switch between optimization iterations known as mode switching, which again introduces a discontinuity during optimization. These discontinuities can prevent gradient-based optimization from converging.

### 2.3 Topology Optimization

Topology optimization is one of the structural optimization methods with the greatest degree of design freedom. It can search the largest design space to determine the best possible shape and material distribution of a structure for the prescribed objective. Numerous topology optimization approaches, such as the SIMP method [22-24], the LSM [25-28] and the evolutionary approach [29, 30] have been developed. Generally, in these approaches, the structural topology is described by a black-and-white pixel/voxel image using the SIMP method and the evolutionary approach, or a (zero) level set of a topology description function using the LSM. These approaches have been applied successfully to solve the buckling- and stress-based topology optimization problems for 2- or 3-dimensional continuum structures, as well as the optimization problem for the design of stiffened panels.

#### 2.3.1 Buckling-based Topology Optimization

Topology optimization has been applied to buckling problems [53-56], i.e., the maximization of the critical buckling load with a mass constraint or the minimization of the structural weight with buckling constraints. Among these works, two main issues are always discussed. The first is related to the spurious buckling loads or load factors

being generated by the finite element analysis (FEA), due to low-density regions. To address this issue, different interpolation schemes for the stiffness and geometric stiffness matrices [32, 53, 55] have been explored for both the SIMP and level-set-based methods, and an approach based on the eigenvalue shift and pseudo mode identification [55] has been suggested. The other main challenge identified is related to convergence [57] and is generally caused by inaccurate sensitivity information on the critical buckling loads or load factors, for example due to the influence of the variation of the stress state and the non-differentiability of the multiple eigenvalues being neglected. Switching of the critical buckling mode during optimization can also be a source of convergence problems. First-order sensitivity information is usually used in optimization to predict the variation of buckling loads for the same buckling modes. During optimization however, the buckling mode with the lowest load factor may change. Therefore, the mode shape and gradient information relating to the lowest buckling mode also change, resulting in slow convergence, or even divergence. In Dunning et al. [54], it was demonstrated that including a large number of buckling modes in an optimization can provide comprehensive information on the structure and optimization problem, and improve the convergence. However, this significantly increases the computational cost. In addition, the number of buckling constraints is increased. The constraint-aggregation methods using the  $p$ -norm and Kreisselmeier–Steinhauser (KS) functions have been used to reduce the buckling constraints, in Dienemann et al. [58], Stanford et al. [14], and Ferrari and Sigmund [59]. The aggregation method has also been employed for the problem of the maximization of the critical buckling load. In Ferrari et al. [60], the first few buckling modes are considered in the optimization to address the convergence issue caused by mode switching. The KS function of the inverses of their load factors is used to approximate the inverse of the critical load factor. The objective of the maximization of the critical buckling load is thus transformed into the minimization of the KS function value.

### 2.3.2 Stress-based Topology optimization

For a stress-based topology optimization considering stress either in the objectives or the constraints, Le et al. [61] summarized three main challenges, namely the singularity problem, the local nature of the stress and the highly nonlinear stress behaviour. The singularity problem occurs when the density-based method, i.e., the SIMP method, is used. Elements with low densities can present high stress values, leading to highly

## Simultaneous Sizing, Layout and Topology Optimization for Buckling and Postbuckling of Stiffened Panels

nonlinear stress behaviour. It is difficult to remove such elements using the gradient-based optimization algorithm. To resolve this challenge, stress relaxation is usually applied to ensure the density and stress of an element can decrease simultaneously, especially when the element density approaches zero [62-65]. When the level set method and evolutionary approach are applied, elements with intermediate densities can be avoided, and therefore the singularity problem is naturally solved [29]. The local nature of the stress results in the fact that the stress values must be calculated and controlled at every material point throughout the structure. Therefore, a large number of local stress constraints are required, leading to computationally demanding sensitivity calculation. To address this problem, a global measure, such as the  $p$ -norm or KS function [66-69], can be used to approximate and control the maximum stress value of the structure, however this is at the expense of losing an adequate level of control of local stress behaviour. In stress-constrained problems, adaptive scaling [61, 70, 71] is usually employed to ensure the exact stress limits. The highly nonlinear stress behaviour means that stress values are highly sensitive to changes of the structure, especially in stress concentration regions such as sharp and reentrant corners. To address this problem, a consistent density filtering versus sensitivity filtering has been used for stabilization consideration in the SIMP framework [61]. For the LSM, a least square interpolation approach was developed to provide smoother sensitivities at the boundaries [71]; while for the evolutionary approach, filtered design variables and sensitivities with further stabilization were adopted [72].

### 2.3.3 Topology optimization for stiffened panel design

For stiffened panel design, topology optimization has been used to find the optimal internal topology for each stiffener, or to find the best stiffener layout. Some of the works carried out have considered buckling and stress in either the objectives or the constraints.

For the stiffener internal topology optimization, a panel with a predetermined stiffener layout is assumed, and the internal topology for each stiffener is optimized. As discussed in Section 2.1, in Stanford et al. [31] and Townsend and Kim [32], the optimization of stiffener internal topologies was explored using the SIMP and level set methods respectively, where the maximization of critical buckling load with a volume constraint was performed. For aircraft wingbox applications to optimize the internal

topologies of ribs, numerous optimization problems, such as the compliance minimization (equivalent to the maximization of the overall stiffness of the structure) with a volume constraint [73], the mass minimization with lift, drag and stress constraints [74], the optimization for a flutter and compliance objective under a weight constraint [75], and the mass minimization under buckling and stress constraints [76], have been explored using the SIMP method.

For stiffener layout optimization, the arrangement of the stiffeners, i.e., the orientation, spacing and placement of the stiffeners, are optimized. Three optimization methods have been proposed. The first one is the Ground Structure Approach [77], which places stiffeners everywhere where they can potentially exist, and then decides which stiffeners need to be removed from the structure. For applications relating to the optimal panel placement in an airplane wingbox, the optimization problem including three objectives, i.e., the lift effectiveness maximization, critical buckling load factor maximization and mass minimization under divergence and flutter speeds, buckling factor and stress constraints [78], and the problem for the weight minimization under strength, aeroelasticity, buckling and stiffness constraints [79], have been explored. The second is a group of biologically inspired (gradient-free) methods, such as the Adaptive Growth Method [80, 81]. Inspired by branching systems in nature, the stiffener layout patterns for plate structures are generated by introducing the growing and branching tree model. The minimization of the strain energy with a volume constraint [82] and the maximization of the critical buckling load with a volume constraint [83] have been investigated. The third is the Moving Morphable Component or projection-based approach [84]. A set of structural components are used to represent the stiffeners. The sizes and layout of stiffeners can be optimized by updating the lengths, widths, positions and inclined angles of these components. The minimization of the structural compliance subject to structural volume and buckling load factor constraints is investigated. In the above three methods, the simultaneous optimization of the layout and sizes of stiffeners can be performed; However, the optimization of the internal topology of the stiffeners remains unexplored.

As discussed above, previous works for stiffened panel designs have focused on sizing and layout optimization using gradient-free optimization algorithms. Topology optimization has also been applied to find the optimal internal topology for each stiffener with a pre-assumed stiffener layout, or to find the best stiffener layout with

## Simultaneous Sizing, Layout and Topology Optimization for Buckling and Postbuckling of Stiffened Panels

predetermined stiffener internal topologies. Until now, simultaneous optimization of the thickness distribution and the layout and internal topologies of the stiffeners of a stiffened panel design, has not been investigated. The main challenge here has been that gradient-free optimization approaches are not being expected to solve problems with large numbers of design variables in topology optimization. Meanwhile, there is still no effective structural topology parameterization, enabling the simultaneous sizing, layout and topology optimization for stiffened panel design to be solved using gradient-based optimization algorithms.

The LSM has attracted much attention, particularly in the fields of image processing, interface motion tracking and topology optimization [26, 85, 86]. Its ability to describe variations in topology, increases the design space with the potential to find the global optimum in optimization problems. Compared with other methods describing a structural topology using a black-and-white pixel/voxel image, one advantage of the LSM is that the structural boundaries are well-defined throughout the optimization without a need for postprocessing [87].

- One of the main objectives of this thesis is therefore to develop a level-set-based topology optimization parameterization for stiffened panel design, enabling the simultaneous optimization of the thicknesses of the skin and stiffeners, and the stiffener layout and internal topologies. A panel with straight stiffeners is investigated first. Since buckling and stress are the two most important design criteria in the design and optimization of stiffened panels, the buckling and stress optimization of stiffened panels is explored next.

Postbuckling topology optimization has not yet been investigated, much less the simultaneous sizing, layout and topology optimization for postbuckling of stiffened panels. Understanding of how the optimization objectives, imperfections, mode jumping and mode switching affect optimization and optimization results remains limited.

- Therefore, another of the main objectives of this thesis is to investigate the simultaneous sizing, layout and topology optimization for postbuckling of stiffened panels. Due to the intrinsically nonlinear nature of the problem, the loading level at which the postbuckling buckling behaviour is evaluated also affects optimization results. Two loading levels corresponding to the initial

## Chapter 2: Literature Review

postbuckling and moderately deep postbuckling regimes will therefore be studied in-depth.

Curvilinearly stiffened panels have been shown to have the potential to result in lighter weight designs than straight stiffened panels under particular design loads [2, 14, 88, 89]. In previous work, pre-specified curvilinear functions, e.g., third order uniform rational B-spline, are usually used to construct stiffener curves, leading to a reduced design space.

- The last main objective of this thesis therefore is to develop a level-set-based method to describe and freely manipulate stiffener curves as well as the internal topology optimization of stiffeners. The buckling-based problem is investigated and compared with the optimization for panels stiffened with straight stiffeners.

# 3 SIMULTANEOUS SIZING, LAYOUT AND TOPOLOGY OPTIMIZATION OF PANELS WITH STRAIGHT STIFFENERS UNDER BUCKLING CONSTRAINTS

This chapter presents an investigation of optimum panel designs with straight stiffeners simultaneously optimizing sizing, layout and topology. An effective topology optimization parameterization is performed, enabling the simultaneous optimization of the thicknesses of the skin and stiffeners, and the stiffener layout and internal topologies. Specifically, the stiffened panel is discretized into plate elements. A control mesh is developed to manipulate the stiffener layout, and a free-form mesh deformation method is utilized to adjust the finite element (FE) mesh. The level set method is used to optimize the internal topologies of the stiffeners, where each stiffener is represented by one level set function. The thicknesses of the skin and stiffeners are also optimized simultaneously. The minimum weight problem for stiffened panels subject to buckling constraints is investigated. A gradient-based optimizer is employed to solve the optimization problem. Numerical examples demonstrate the effectiveness of the

proposed approach. The advantages of simultaneous sizing, layout and topology optimization for the design of stiffened panels are also demonstrated. Since stiffness is commonly considered in the topology optimization field, the difference between buckling-driven and stiffness-driven designs is investigated and discussed.

The remainder of this chapter is organized as follows. In Section 3.1, the geometric and FE models of the stiffened panel considered are presented. Section 3.2 describes the mathematical formulation of the problem and the optimization algorithm. Numerical examples to test the proposed method are presented in Section 3.3. Conclusions are given in Section 3.4.

### 3.1 Stiffened Panel Model

In this section, the geometric and FE models for the problem studied are described. A control mesh is developed to manipulate the stiffener layout, and level set functions are used to represent and optimize the internal topologies of the stiffeners. Sizing variables are also included to optimize the thicknesses of the skin and stiffeners. As the stiffener layout changes, a free-form mesh deformation method is used to adjust the FE mesh.

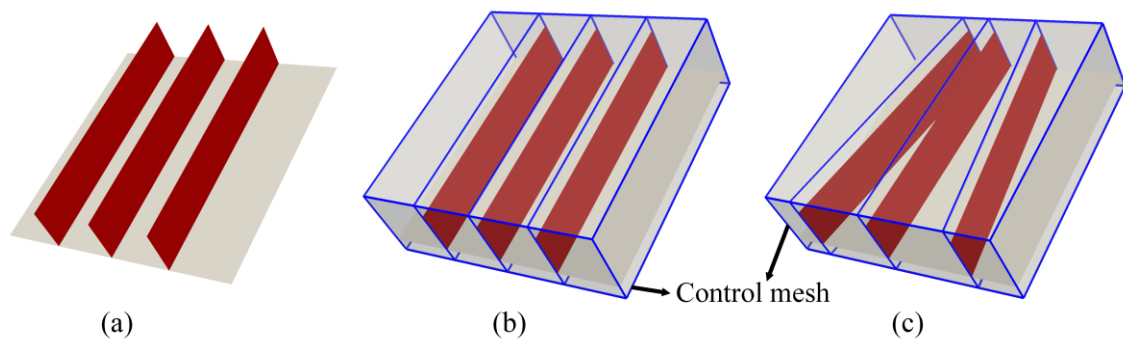


**Figure 3.1 Illustration of updating the stiffener layout using the control mesh: (a) a sample stiffened panel; (b) the initial stiffened panel and control mesh; (c) the updated stiffened panel and control mesh.**

#### 3.1.1 Layout Description

The stiffened panel considered is composed of a skin and stiffeners as shown in Fig. 3.1(a). The positions, rotations and spacing of the stiffeners are all represented by the coordinates of their two ends.

**Simultaneous Sizing, Layout and Topology Optimization  
for Buckling and Postbuckling of Stiffened Panels**

The free-form mesh deformation method with a control mesh is used to adaptively adjust the FE mesh as the stiffener layout changes, avoiding remeshing. The basic idea of the free-form mesh deformation method [90] is to enclose an object within a cube or another hull object, namely the control mesh in this work, and transform the object within the hull as the hull is deformed. In Fig. 3.1(b), the control mesh illustrated by the blue lines is generated. The  $x$  and  $y$  coordinates of nodes on the control mesh are equal to those of the two ends of the stiffeners or the skin vertices. Therefore, as shown in Fig. 3.1(c), the optimal layout of the stiffeners can be obtained by optimizing the coordinates of the nodes on the control mesh.

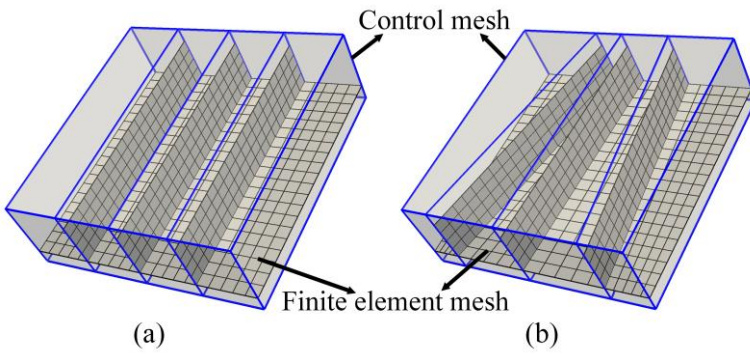


**Figure 3.2 Illustration of updating the FE mesh using free-form mesh deformation with the control mesh: (a) the initial FE and control meshes; (b) the updated FE and control meshes.**

Both the skin and stiffeners are modeled explicitly with four-node mixed interpolation of tensorial components (MITC) plate elements with six degrees of freedom per node, comprising a Mindlin-Reissner plate element [91, 92] combined with a plane stress formulation. Since the FE mesh is enclosed by the control mesh, after every update of the control mesh and stiffener layout, as shown in Fig. 3.2, the FE mesh is adaptively deformed to cater for the updated stiffener layout using the free-form mesh deformation method:

$$\mathbf{x}_{FE} = \mathbf{N} \mathbf{x}_{control} \quad (3-1a)$$

$$\mathbf{x}_{control}^{k+1} = \mathbf{x}_{control}^k + \mathbf{y} \quad (3-1b)$$

$$\mathbf{x}_{FE}^{k+1} = \mathbf{x}_{FE}^k + \mathbf{z} \quad (3-1c)$$

$$\mathbf{z} = \mathbf{N}\mathbf{y} \quad (3-1d)$$

where  $\mathbf{x}_{FE}$  and  $\mathbf{x}_{control}$  are nodal coordinates on the FE and control meshes, respectively.  $\mathbf{N}$  is the shape function.  $\mathbf{y}$  and  $\mathbf{z}$  represent the changes to the coordinates of the control and FE mesh points, respectively.  $\mathbf{y}$  is the design variables in the stiffener layout optimization, and the deformation of the FE mesh can be achieved through Eqs. (3-1c) and (3-1d).

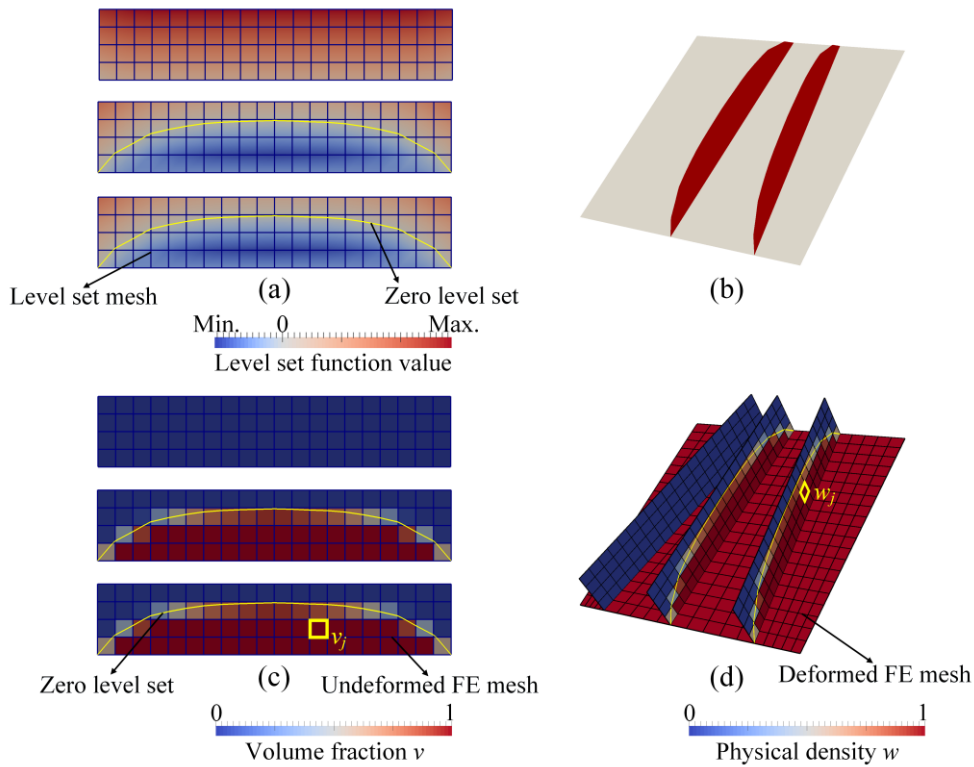


**Figure 3.3 Illustration of the stiffener internal topologies represented by the level set functions: (a) the LSFs corresponding to the three stiffeners respectively, their zero level sets and level set meshes; (b) stiffener layout and topologies; (c) the volume fraction fields, zero level sets and undeformed FE meshes corresponding to the three stiffeners; (d) the deformed FE mesh and corresponding physical density field.**

### 3.1.2 Topology Description

The level set method [25, 26, 28] is used to represent and optimize the internal topologies of the stiffeners. One level set function (LSF) is used to describe the internal topology of each stiffener. The relationship between the level set function values  $\Phi$  and

**Simultaneous Sizing, Layout and Topology Optimization  
for Buckling and Postbuckling of Stiffened Panels**

the resulting structure is shown in Figs. 3.3(a) and 3.3(b). The structural boundary of the  $n$ th stiffener is defined as the zero level set of an implicit function  $\Phi_n(x)$ :

$$\begin{cases} \Phi_n(x) \leq 0 & x \in \Omega_n \\ \Phi_n(x) = 0 & x \in \Gamma_n, \quad n = 1, 2, \dots, N \\ \Phi_n(x) > 0 & x \notin \Omega_n \end{cases} \quad (3-2)$$

where  $\Omega$  is the domain for the structure and  $\Gamma$  is the structural boundary.  $x \in \Omega_{d,n}$ , where  $\Omega_{d,n}$  is the design domain containing the structure,  $\Omega_n \in \Omega_{d,n}$ .  $N$  level set functions are used for the  $N$  stiffeners. Conventionally, the signed distance function is used for the level set function.

To achieve the optimal internal topology of a stiffener, the structural boundary is optimized by iteratively solving the level set equation, Eq. (3-3):

$$\frac{\partial \Phi_n(x, t_f)}{\partial t_f} + \nabla \Phi_n(x) \cdot V(x) = 0 \quad (3-3)$$

where  $t_f$  is a pseudo-time for the level set evolution and  $V$  is the velocity vector.

The level set function at each point is updated by solving the following discretized Hamilton-Jacobi equation using an up-wind differential scheme:

$$\Phi_{n,pt}^{k+1} = \Phi_{n,pt}^k - \Delta t_f \left| \nabla \Phi_{n,pt}^k \right| V_{normal,pt} \quad (3-4)$$

where  $pt$  is a discrete point in the design domain,  $k$  is the iteration number,  $V_{normal}$  is the normal velocity and  $\left| \nabla \Phi_{n,pt}^k \right|$  is computed for each point using the Hamilton-Jacobi Weighted Essentially Non-Oscillatory method (HJ-WENO) [93]. To improve the computational efficiency, the level set update is restricted to points within a narrow band close to the boundary. This results in  $\Phi_{n,pt}$  being given by a signed distance value to the boundary only within this narrow band.  $\Phi_{n,pt}$  is then periodically reinitialized to a signed distance function. For the re-initialization and velocity extension, the fast marching method [85] is used.

It is noted that a level set mesh is the same size as the FE mesh corresponding to one stiffener, and that this is fixed during the optimization. It is easy therefore, to calculate

the volume fraction field of the solid material on the undeformed mesh shown in Fig. 3.3(c). As shown in Fig. 3.4(a), the structural boundary is given by the zero level set, and the LSF is used to perform the subdivision of each element into a subdomain filled with the solid material and a subdomain with the void. For the sake of simplicity, as shown in Fig. 3.4(b), the LSF is approximated by straight lines when searching for the intersection between the element boundary and the zero level set. Then the grey area in each element in Fig. 3.4(c) and the corresponding elemental volume fraction are calculated. The volume fraction fields shown in Fig. 3.3(c) are thus obtained. Due to the one-to-one correspondence between the elements of the undeformed and deformed FE meshes, shown in Figs. 3.3(c) and 3.3(d), a direct mapping can be used and the density distribution  $\mathbf{w}$  for the stiffener is obtained by  $w_j = v_j$ . The density distribution is  $\mathbf{w} = 1$  for all the elements on the skin.

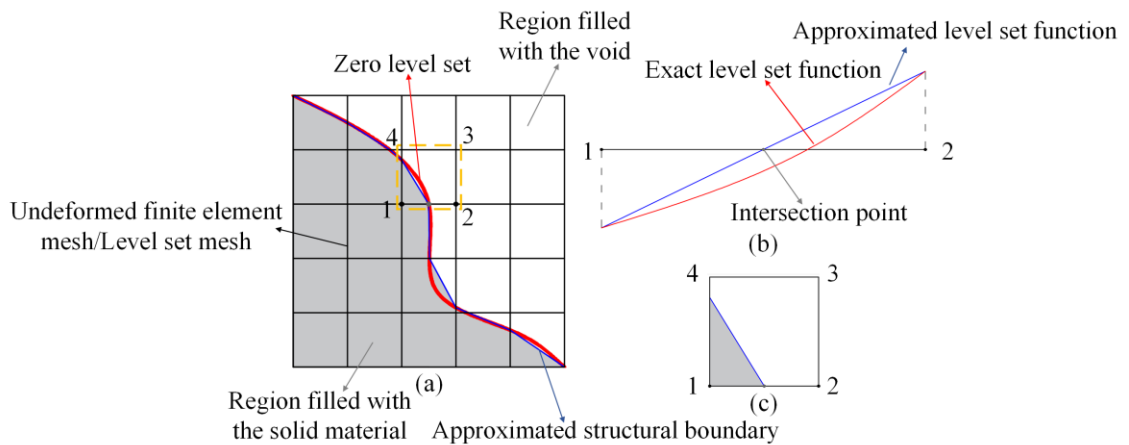


**Figure 3.4 Illustration of the computation of the volume fraction field on an undeformed FE mesh: (a) the structural boundary approximated by straight lines; (b) computation of the intersection between the element boundary and the zero level set; (c) computation of the elemental volume fraction.**

### 3.1.3 Sizing Description

As shown in Fig. 3.5(a), the skin thickness and the thickness of each stiffener are represented by  $t_p$  and  $t_{s,n}$  ( $n=1, 2, \dots, N$ ) and these are optimized as well. A uniform thickness is considered for the skin and for each stiffener. Therefore, as shown in Fig. 3.5(b), the elemental thicknesses of the FE mesh are the same for the whole of the skin or for each stiffener. It is noted that, as shown in Fig. 3.5(c), even when stiffeners are

**Simultaneous Sizing, Layout and Topology Optimization  
for Buckling and Postbuckling of Stiffened Panels**

removed, the design variables corresponding to their thicknesses still remain and need to be optimized.

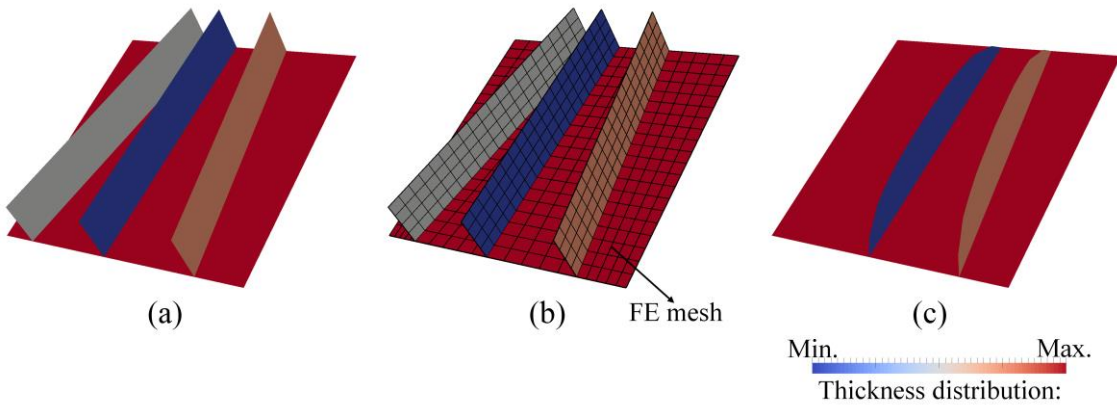


**Figure 3.5 Illustration of the thickness distribution of the stiffened panel: (a) thicknesses for each stiffener and the skin; (b) the elemental thickness distribution on the FE mesh; (c) the geometric model of the stiffened panel, with its thickness distribution, stiffener layout and topologies.**

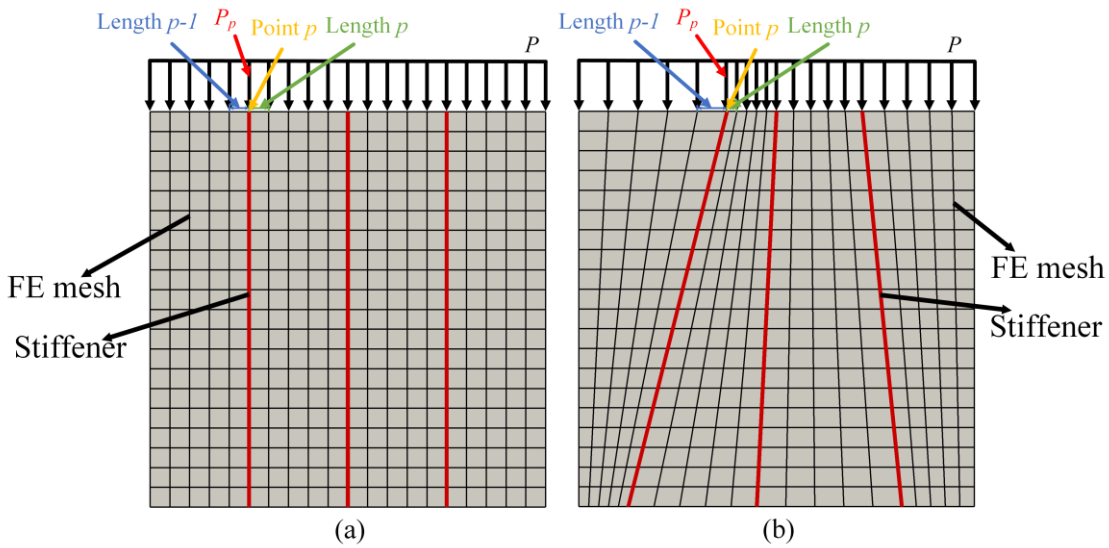


**Figure 3.6 Illustration of the pressure application.**

### 3.1.4 Finite Element Model

Once the stiffener layout is updated and the FE mesh has been deformed, the axial compression and shear loads can no longer be applied by adding uniform forces to the corresponding points. Instead, as shown in Fig. 3.6, the force applied to a point  $pf$  is recalculated as:

**Chapter 3: Simultaneous Sizing, Layout and Topology Optimization of Panels with Straight Stiffeners under Buckling Constraints**

$$P_{pf} = \frac{P(L^{pf-1} + L^{pf})}{2} \quad (3-5)$$

where  $P$  is the pressure value per unit length.  $L^{pf-1}$  and  $L^{pf}$  are the lengths of the elemental boundaries either side of the point  $pf$ .

After updating the nodal coordinates on the FE mesh and obtaining the elemental density and thickness distributions, the stiffness and geometric stiffness matrices for the  $j$ -th finite element can be calculated as [32]:

$$K_j = w_j K_j^s(E_s, \rho_s, \nu, t_j, \mathbf{x}_{FE}) + (1 - w_j) K_j^v(E_v, \rho_v, \nu, t_j, \mathbf{x}_{FE}) \quad (3-6a)$$

$$K_{g,j} = w_j \left( \omega_j K_{g,j}^s(E_s, \rho_s, \nu, t_j, \mathbf{x}_{FE}) + (1 - w_j) K_{g,j}^v(E_v, \rho_v, \nu, t_j, \mathbf{x}_{FE}) \right) \quad (3-6b)$$

where  $K_j^s$  and  $K_j^v$  represent the stiffness matrices of the  $j$ -th finite element solid and void phases, respectively.  $K_{g,j}^s$  and  $K_{g,j}^v$  denote the geometric stiffness matrices of the  $j$ -th finite element solid and void phases, respectively.  $E_s$  and  $E_v$  are the Young's moduli of the  $j$ -th finite element solid and void phases, respectively.  $\rho_s$  and  $\rho_v$  are the densities of the  $j$ -th finite element solid and void phases, respectively.  $t_j$  is the thickness of the  $j$ -th finite element.  $\nu$  is Poisson's ratio.

In order to compute the buckling load factors of the stiffened panel, the stationary equation and the linear buckling equation (Eq. (3-7)) need to be solved.

$$\mathbf{K}\mathbf{u} = \mathbf{f} \quad (3-7a)$$

$$(\mathbf{K} + \lambda \mathbf{K}_g(\mathbf{u}))\mathbf{v} = \mathbf{0} \quad (3-7b)$$

where  $\mathbf{K}$ ,  $\mathbf{u}$  and  $\mathbf{f}$  are the structural stiffness matrix, stationary deflection and applied load, respectively.  $\mathbf{K}_g$  is the geometric stiffness matrix.  $\lambda$  and  $\mathbf{v}$  represent the eigenvalue/eigenvector pair for each buckling mode.

HSL MA57 solver [94] is an open-source code for the direct solution of a sparse symmetric system of linear equations, using the multifrontal method which is based on a sparse variant of Gaussian elimination. ARnoldi PACKage (ARPACK) [95] is a numerical software library for the iterative solution of a large scale eigenvalue problem,

**Simultaneous Sizing, Layout and Topology Optimization  
for Buckling and Postbuckling of Stiffened Panels**

using the Implicitly Restarted Lanczos and Arnoldi Methods for symmetric and nonsymmetric matrices, respectively. Eqs. (3-7a) and (3-7b) are solved using the HSL MA57 solver and ARPACK, respectively.

## 3.2 Problem Formulation and Optimization Method

In this section, the problem considered in this chapter is described. To solve this problem with a gradient-based optimizer, a semi-analytical sensitivity analysis is performed. The optimization algorithm is also presented.

### 3.2.1 Problem Formulation

The minimum weight problem for stiffened panels subject to buckling constraints is formulated as follows.

$$\begin{aligned} \min_{\mathbf{t}, \mathbf{y}, \Phi} \quad & m(\mathbf{t}, \mathbf{y}, \Phi) \\ \text{s.t.} \quad & \lambda_q(\mathbf{t}, \mathbf{y}, \Phi) \geq \lambda_{\min}, \quad q = 1, 2, \dots, N_\lambda \\ & L_l(\mathbf{y}) \geq L_{\min}, \quad l = 1, 2, \dots, N_L \end{aligned} \quad (3-8)$$

where  $\mathbf{t} = [t_p, t_{s,1}, \dots, t_{s,N}]^T$ ,  $\mathbf{y}$  and  $\Phi = [\Phi_1, \dots, \Phi_N]^T$  are the sizing, layout and topology design variables, respectively. The structural weight is evaluated by mass  $m$ . The first  $N_\lambda$  buckling modes are considered in the optimization.  $\lambda_{\min}$  is the lower bound of the critical buckling load factor. Since the free-form mesh deformation with the control mesh is utilized to adaptively adjust the FE mesh, overlap and intersection between adjacent stiffeners are not allowed. To avoid them, spacing constraints are set. The spacing constraints are also used to control the widths of the FE elements, so as to avoid excessive distortion of the FE mesh and ensure the accuracy of the FE model.  $L$  denotes stiffener spacing, and  $L_{\min}$  is its lower bound.  $N_L$  is the total number of spacing constraints.

The mass  $m$  is defined by the mass matrix:

$$m = \mathbf{g}^T \mathbf{M} \mathbf{g} \quad (3-9)$$

where the vector  $\mathbf{g}$  contains ones for deflection degrees of freedom along the gravity direction and zeros elsewhere.

The stiffener spacing  $L$  is defined as the difference between the end coordinates of two adjacent stiffeners:

$$L_l = x_{\text{control}}^{l+1} - x_{\text{control}}^l \quad (3-10)$$

### 3.2.2 Sensitivity Analysis

In this study, the gradient-based optimization algorithm is used to solve the optimization problem described in Eq. (3-8). Therefore, the sensitivities of the mass  $m$ , the buckling load factor  $\lambda_q$  and the stiffener spacing  $L_l$  are needed. A semi-analytical sensitivity analysis with the adjoint method is employed.

#### 3.2.2.1 Sensitivity Analysis for Layout Optimization

To update the stiffener layout, the derivative of  $\lambda_q$  with respect to  $y_i$  is obtained using the adjoint method. First, Eq. (3-7b) and Eq. (3-7a) are pre-multiplied by the eigenvector  $\mathbf{v}_q$  and the adjoint vector  $\mathbf{u}_{ad}$ :

$$\mathbf{v}_q^T (\mathbf{K} + \lambda_q \mathbf{K}_g(\mathbf{u})) \mathbf{v}_q = 0 \quad (3-11a)$$

$$\mathbf{u}_{ad}^T (\mathbf{K}\mathbf{u} - \mathbf{f}) = 0 \quad (3-11b)$$

Substituting Eq. (3-11b) into Eq. (3-11a) yields:

$$\mathbf{v}_q^T (\mathbf{K} + \lambda_q \mathbf{K}_g(\mathbf{u})) \mathbf{v}_q - \mathbf{u}_{ad}^T (\mathbf{K}\mathbf{u} - \mathbf{f}) = 0 \quad (3-12)$$

Then, differentiating Eq. (3-12):

$$\begin{aligned} & 2\mathbf{v}_q^T (\mathbf{K} + \lambda_q \mathbf{K}_g(\mathbf{u})) \frac{\partial \mathbf{v}_q}{\partial y_i} \\ & + \mathbf{v}_q^T \left( \frac{\partial \mathbf{K}}{\partial y_i} + \frac{\partial \lambda_q}{\partial y_i} \mathbf{K}_g(\mathbf{u}) + \lambda_q \frac{\partial \mathbf{K}_g(\mathbf{u})}{\partial y_i} + \lambda_q \frac{\partial \mathbf{K}_g(\mathbf{u})}{\partial \mathbf{u}} \frac{\partial \mathbf{u}}{\partial y_i} \right) \mathbf{v}_q \\ & - \frac{\partial \mathbf{u}_{ad}^T}{\partial y_i} (\mathbf{K}\mathbf{u} - \mathbf{f}) - \mathbf{u}_{ad}^T \left( \frac{\partial \mathbf{K}}{\partial y_i} \mathbf{u} + \mathbf{K} \frac{\partial \mathbf{u}}{\partial y_i} - \frac{d\mathbf{f}}{dy_i} \right) = 0 \end{aligned} \quad (3-13)$$

By collecting the terms with  $\partial \mathbf{u} / \partial y_i$  in Eq. (3-13) and setting them to zero, the derivative of  $\lambda_q$  with respect to  $y_i$  can be calculated as:

**Simultaneous Sizing, Layout and Topology Optimization  
for Buckling and Postbuckling of Stiffened Panels**

$$\frac{\partial \lambda_q}{\partial y_i} = \frac{\mathbf{u}_{ad}^T \left( \frac{\partial \mathbf{K}}{\partial y_i} \mathbf{u} - \frac{\partial \mathbf{f}}{\partial y_i} \right) - \mathbf{v}_q^T \left( \frac{\partial \mathbf{K}}{\partial y_i} + \lambda_q \frac{\partial \mathbf{K}_g(\mathbf{u})}{\partial y_i} \right) \mathbf{v}_q}{\mathbf{v}_q^T \mathbf{K}_g(\mathbf{u}) \mathbf{v}_q} \quad (3-14)$$

where

$$\lambda_q \mathbf{v}_q^T \frac{\partial \mathbf{K}_g(\mathbf{u})}{\partial \mathbf{u}} \mathbf{v}_q = \mathbf{u}_{ad}^T \mathbf{K} \quad (3-15)$$

It is noted that  $\partial \mathbf{f} / \partial y_i \neq \mathbf{0}$  in Eq. (3-14) since the updating of  $\mathbf{y}$  leads to the re-distribution of the force applied on points of the FE mesh via Eq. (3-5) when the load is applied.

Based on Eq. (3-9), the derivative of  $m$  with respect to  $y_i$  can be calculated by:

$$\frac{\partial m}{\partial y_i} = \mathbf{g}^T \frac{\partial \mathbf{M}}{\partial y_i} \mathbf{g} \quad (3-16)$$

The semi-analytical sensitivity analysis method is used to derive sensitivities of  $\lambda_q$  and  $m$  analytically until Eqs. (3-14) and (3-16). For simplification of implementation,  $\partial \mathbf{f} / \partial y$ ,  $\partial \mathbf{K} / \partial y_i$ ,  $\partial \mathbf{K}_g / \partial y_i$  and  $\partial \mathbf{M} / \partial y_i$  are calculated via the central finite difference method as is the derivative  $dL_i / dy_i$  which is related to the spacing constraint in Eq. (3-10). Because  $y_i$  is the change in the nodal coordinates of the control mesh and is used to calculate the nodal coordinates of the finite elements via Eq. (3-1), finite differences are only performed at the element level. Additional FEAs are not needed. This ensures the efficiency of the evaluation. When using the central finite difference method, it is suggested that the smallest possible perturbations are chosen to ensure the accuracy of the calculation can be guaranteed. In this work, the perturbation is chosen as  $0.0001a_0$ , where  $a_0$  is the initial FE element width. The calculated sensitivities  $\partial g / \partial y_i$  in Eqs. (3-14) and (3-16) have been compared with  $(g(y_{i,0} + \Delta y_i) - g(y_{i,0} - \Delta y_i)) / 2\Delta y_i$ , where  $g$  represents an arbitrary equation, i.e.,  $\lambda_q$  and  $m$ , and  $y_{i,0}$  is the value at the current iteration. The error in mass sensitivity is within 0.1%, and the errors in the buckling sensitivities are within 1% when there is no mode switching, which shows the accuracy of the sensitivity calculation.

### 3.2.2.2 Sensitivity Analysis for Topology Optimization

In this thesis, the LSFs are always maintained as signed distance functions during optimization. In order to convert an arbitrary LSF to a signed distance function with the same boundary locations, a combination of the marching squares and fast marching algorithms [86] is applied. In order to ensure the signed distance property  $|\nabla\Phi_n|=1$  after every update of the LSF, the fast velocity extension algorithm [96] is utilized. The relationship between the changes to the LSF values  $\Delta\Phi_{n,b}$  at the boundary and  $\Delta\Phi_n$  in the rest of the design domain is determined as:

$$\Delta\Phi_n = \left[ \frac{\partial\Phi_n}{\partial\Phi_{n,b}} \right] \Delta\Phi_{n,b}, \quad n = 1, 2, \dots, N \quad (3-17)$$

The level set values  $\Phi_{n,b}$  on the boundary points are the design variables in the topology optimization and are updated by the optimizer.

To update the LSFs representing the stiffener internal topologies, derivatives with respect to the level set values of the boundary points  $\Phi_{n,b}$  are computed through the chain rule:

$$\frac{\partial g}{\partial\Phi_{n,b}} = \sum_j \frac{\partial g}{\partial w_j} \frac{\partial w_j}{\partial v_j} \frac{\partial v_j}{\partial\Phi_{n,b}} \quad (3-18)$$

where  $\partial w_j/\partial v_j = 1$  because  $w_j = v_j$ . The function  $g$  represents an arbitrary equation, i.e.,  $m$ ,  $\lambda_q$  and  $L_l$ . In a similar way to the computation of  $\partial\lambda_q/\partial y_i$ , the derivative of  $\lambda_q$  with  $w_j$  is obtained by:

$$\frac{\partial\lambda_q}{\partial w_j} = \frac{\mathbf{u}_{ad}^T \left( \frac{\partial\mathbf{K}}{\partial w_j} \mathbf{u} - \frac{\partial\mathbf{f}}{\partial w_j} \right) - \mathbf{v}_q^T \left( \frac{\partial\mathbf{K}}{\partial w_j} + \lambda_q \frac{\partial\mathbf{K}_g(\mathbf{u})}{\partial w_j} \right) \mathbf{v}_q}{\mathbf{v}_q^T \mathbf{K}_g(\mathbf{u}) \mathbf{v}_q} \quad (3-19)$$

where

$$\lambda_q \mathbf{v}_q^T \frac{\partial\mathbf{K}_g(\mathbf{u})}{\partial u} \mathbf{v}_q = \mathbf{u}_{ad}^T \mathbf{K} \quad (3-20)$$

It is noted that since self-weight loading is ignored in this work,  $\partial\mathbf{f}/\partial w_j=0$  in Eq. (3-19). Therefore, Eq. (3-19) can be simplified as:

**Simultaneous Sizing, Layout and Topology Optimization  
for Buckling and Postbuckling of Stiffened Panels**

$$\frac{\partial \lambda_q}{\partial w_j} = \frac{\mathbf{u}_{ad}^T \frac{\partial \mathbf{K}}{\partial w_j} \mathbf{u} - \mathbf{v}_q^T \left( \frac{\partial \mathbf{K}}{\partial w_j} + \lambda_q \frac{\partial \mathbf{K}_g(\mathbf{u})}{\partial w_j} \right) \mathbf{v}_q}{\mathbf{v}_q^T \mathbf{K}_g(\mathbf{u}) \mathbf{v}_q} \quad (3-21)$$

Based on Eq. (3-9), the derivative of  $m$  with respect to  $w_j$  is calculated by:

$$\frac{\partial m}{\partial w_j} = \mathbf{g}^T \frac{\partial \mathbf{M}}{\partial w_j} \mathbf{g} \quad (3-22)$$

and  $dL_i/dw_j = 0$  due to Eq. (3-10).

Derivatives with respect to the level set values of the boundary points are analytically derived and given by Eq. (3-18) with Eqs. (3-21) and (3-22). In Eq. (3-18), the term  $\partial v_j / \partial \Phi_{n,b}$  can be computed by perturbing the level set boundary implicitly, as shown in Fig. 3.7. For a given boundary point of interest, a small perturbation  $\Delta \Phi_{n,b}$  is assigned to its level set value  $\Phi_{n,b}$ . The change in the LSF  $\Delta \Phi_n$  can be obtained via Eq. (3-17). After implementing the marching squares and fast marching algorithms, as shown in Fig. 3.7(b), the new LSF and the corresponding zero level set are achieved. This results in the new volume fraction  $v_j$ . Then using the central finite difference method, the term  $\partial v_j / \partial \Phi_{n,b}$  can be approximated by:

$$\frac{\partial v_j}{\partial \Phi_{n,b}} = \frac{v_j \Big|_{\Phi_{n,b} = \Phi_{n,b} + \Delta \Phi_{n,b}} - v_j \Big|_{\Phi_{n,b} = \Phi_{n,b} - \Delta \Phi_{n,b}}}{2 \Delta \Phi_{n,b}} \quad (3-23)$$

where the perturbation  $\Delta \Phi_{n,b}$  is chosen as  $0.001 b_{n,0}$ , where  $b_{n,0}$  is the element width of the level set mesh used to describe the stiffener internal topology.

Using the gradient-based optimization method with the sensitivity information in Eq. (3-18),  $\Delta \Phi_{n,b}$  can be obtained. Following this  $\Delta \Phi_n$  can be calculated via Eq. (3-17) such that  $|\nabla(\Phi_n + \Delta \Phi_n)| = 1$ . It is noted that, since the fast velocity extension algorithm is only first order accurate, the LSFs are re-initialized using the fast marching method after each update.

**Chapter 3: Simultaneous Sizing, Layout and Topology Optimization of Panels with Straight Stiffeners under Buckling Constraints**

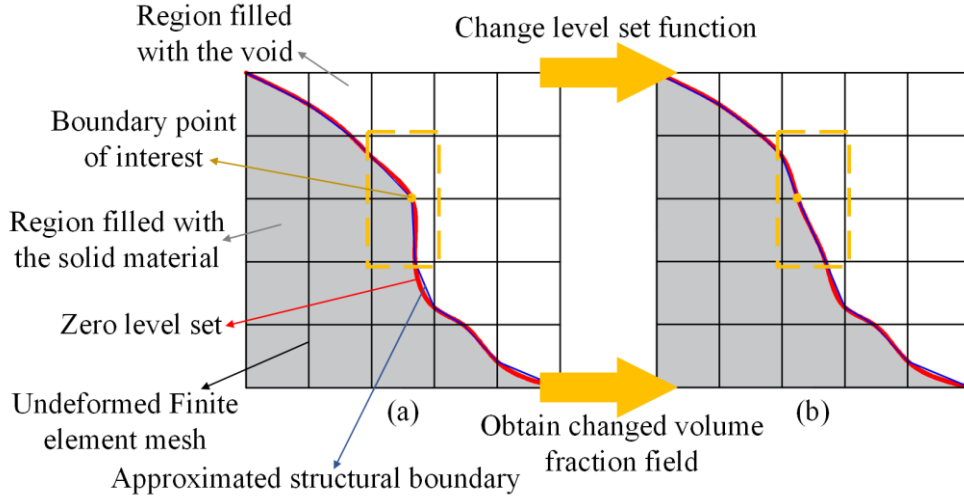


**Figure 3.7 Illustration of the computation of the term  $\partial v_j/\partial \Phi_{n,b}$ : the structural boundary and material distribution (a) before perturbation; (b) after perturbation.**

3.2.2.3 Sensitivity Analysis for sizing Optimization

To implement sizing optimization to determine the optimum thickness distribution of the stiffened panel, derivatives with respect to  $t_p$  and  $t_{s,n}$  are computed using the chain rule:

$$\frac{\partial g}{\partial t_p} = \sum_j \frac{\partial g}{\partial t_j} \frac{\partial t_j}{\partial t_p} \quad (3-24a)$$

$$\frac{\partial g}{\partial t_{s,n}} = \sum_j \frac{\partial g}{\partial t_j} \frac{\partial t_j}{\partial t_{s,n}}, \quad n = 1, 2, \dots, N \quad (3-24b)$$

where

$$\frac{\partial t_j}{\partial t_p} = \begin{cases} 1 & \text{when the } j\text{-th element belongs to the skin} \\ 0 & \text{when the } j\text{-th element does not belong to the skin} \end{cases} \quad (3-25a)$$

$$\frac{\partial t_j}{\partial t_{s,n}} = \begin{cases} 1 & \text{when the } j\text{-th element belongs to the } n\text{-th stiffener} \\ 0 & \text{when the } j\text{-th element does not belong to the } n\text{-th stiffener} \end{cases}, \quad n = 1, 2, \dots, N \quad (3-25b)$$

In a similar way to  $\partial \lambda_q/\partial w_j$  in Eq. (3-21), the derivative of  $\lambda_q$  with respect to  $t_j$  is obtained by:

**Simultaneous Sizing, Layout and Topology Optimization  
for Buckling and Postbuckling of Stiffened Panels**

$$\frac{\partial \lambda_q}{\partial t_j} = \frac{\mathbf{u}_{ad}^T \frac{\partial \mathbf{K}}{\partial t_j} \mathbf{u} - \mathbf{v}_q^T \left( \frac{\partial \mathbf{K}}{\partial t_j} + \lambda_q \frac{\partial \mathbf{K}_g(\mathbf{u})}{\partial t_j} \right) \mathbf{v}_q}{\mathbf{v}_q^T \mathbf{K}_g(\mathbf{u}) \mathbf{v}_q} \quad (3-26)$$

where

$$\lambda_q \mathbf{v}_q^T \frac{\partial \mathbf{K}_g(\mathbf{u})}{\partial u} \mathbf{v}_q = \mathbf{u}_{ad}^T \mathbf{K} \quad (3-27)$$

Based on Eq. (3-9), the derivative of  $m$  with respect to  $t_j$  is calculated by:

$$\frac{\partial m}{\partial t_j} = \mathbf{g}^T \frac{\partial \mathbf{M}}{\partial t_j} \mathbf{g} \quad (3-28)$$

and  $dL_i/dt_j = 0$  due to Eq. (3-10).

Different from layout and topology optimizations, all terms in the derivatives with respect to  $t_p$  and  $t_{s,n}$  in Eq. (3-24) are obtained analytically for sizing optimization.

### 3.2.3 Optimization Algorithm

The Interior Point OPTimizer (IPOPT) [97] is an open-source solver for large scale nonlinear optimization of continuous systems. By implementing an interior point algorithm with a filter line-search, it can be used to find (local) solutions of mathematical optimization problems minimizing an objective function with general nonlinear constraints. Both the objective and constraint functions can be linear or nonlinear, and convex or non-convex, but they should be twice continuously differentiable. Therefore, the second derivative information can be used if it is available. Search directions based on a linearization of the optimality conditions, can be computed in a full-space version by solving a large symmetric linear system. Global convergence of the algorithm is ensured by a line search procedure, based on a filter method. More details and implementation of the algorithm can be found in [97].

Since the optimization problem in Eq. (3-8) is in accordance with the problem being able to be solved by the IPOPT, it is used at each iteration to obtain  $\Delta \mathbf{t}$ ,  $\Delta \mathbf{y}$  and  $\Delta \mathbf{\Phi}_b$  and update the stiffened panels. Linearization of the optimization problem using Taylor's expansion yields the following.

**Chapter 3: Simultaneous Sizing, Layout and Topology Optimization of Panels with Straight Stiffeners under Buckling Constraints**

$$\begin{aligned}
 & \min_{\Delta \mathbf{t}, \Delta \mathbf{y}, \Delta \Phi_b} \left( m_0 + \left[ \frac{\partial m}{\partial t} \right]^T \Delta \mathbf{t} + \left[ \frac{\partial m}{\partial y} \right]^T \Delta \mathbf{y} + \left[ \frac{\partial m}{\partial \Phi_b} \right]^T \Delta \Phi_b \right) \\
 & s.t. \quad \lambda_{q,0} + \left[ \frac{\partial \lambda_q}{\partial t} \right]^T \Delta \mathbf{t} + \left[ \frac{\partial \lambda_q}{\partial y} \right]^T \Delta \mathbf{y} + \left[ \frac{\partial \lambda_q}{\partial \Phi_b} \right]^T \Delta \Phi_b \geq \lambda_{\min}, \quad q = 1, 2, \dots, N_\lambda \\
 & \quad L_{l,0} + \left[ \frac{dL_l}{dy} \right]^T \Delta \mathbf{y} \geq L_{\min}, \quad l = 1, 2, \dots, N_L \\
 & \quad -\gamma_1 \leq \Delta \mathbf{t} \leq \gamma_1 \\
 & \quad -\gamma_2 \leq \Delta \mathbf{y} \leq \gamma_2 \\
 & \quad -\gamma_3 \leq \Delta \Phi_b \leq \gamma_3
 \end{aligned} \tag{3-29}$$

where  $m_0$ ,  $\lambda_{q,0}$  and  $L_{l,0}$  are the values at the current iteration and  $\gamma_1$ ,  $\gamma_2$  and  $\gamma_3$  are the move limits for  $\Delta \mathbf{t}$ ,  $\Delta \mathbf{y}$  and  $\Delta \Phi_b$ , respectively.

It is noted in Eq. (3-29) that the buckling constraints are approximated as:

$$\begin{aligned}
 \left[ \lambda_q^k \right]_{\text{approximation}} &= \lambda_q^{k-1} + \left[ \frac{\partial \lambda_q}{\partial t} \right]_{k-1}^T \Delta \mathbf{t}_{k-1} + \left[ \frac{\partial \lambda_q}{\partial y} \right]_{k-1}^T \Delta \mathbf{y}_{k-1} + \left[ \frac{\partial \lambda_q}{\partial \Phi_b} \right]_{k-1}^T \Delta \Phi_{b,k-1} \geq \lambda_{\min}, \\
 & \quad q = 1, 2, \dots, N_\lambda
 \end{aligned} \tag{3-30}$$

Using the IPOPT, the constraints in Eq. (3-30) are satisfied at each iteration of the optimization. However, since only first-order sensitivity information is used and higher-order sensitivity information is ignored, the prediction of buckling load factors  $\left[ \lambda_q^k \right]_{\text{approximation}}$  from Eq. (3-30) is not sufficiently accurate leading to the potential for them to be slightly larger than the real ones  $\lambda_q^k$ . This may lead to the violation of the actual buckling constraint  $\lambda_1 \geq \lambda_{\min}$ . Therefore, an additional adaptive scaling constraint scheme is introduced and the buckling constraints in Eq. (3-29) are re-written as:

$$\alpha \left( \lambda_{q,0} + \left[ \frac{\partial \lambda_q}{\partial t} \right]^T \Delta \mathbf{t} + \left[ \frac{\partial \lambda_q}{\partial y} \right]^T \Delta \mathbf{y} + \left[ \frac{\partial \lambda_q}{\partial \Phi_b} \right]^T \Delta \Phi_b \right) \geq \lambda_{\min} \tag{3-31}$$

where  $\alpha^k = \frac{\lambda_1^k}{\left[ \lambda_1^k \right]_{\text{approximation}}}$ .

## Simultaneous Sizing, Layout and Topology Optimization for Buckling and Postbuckling of Stiffened Panels

The proposed method and optimization process are illustrated in Fig. 3.8.

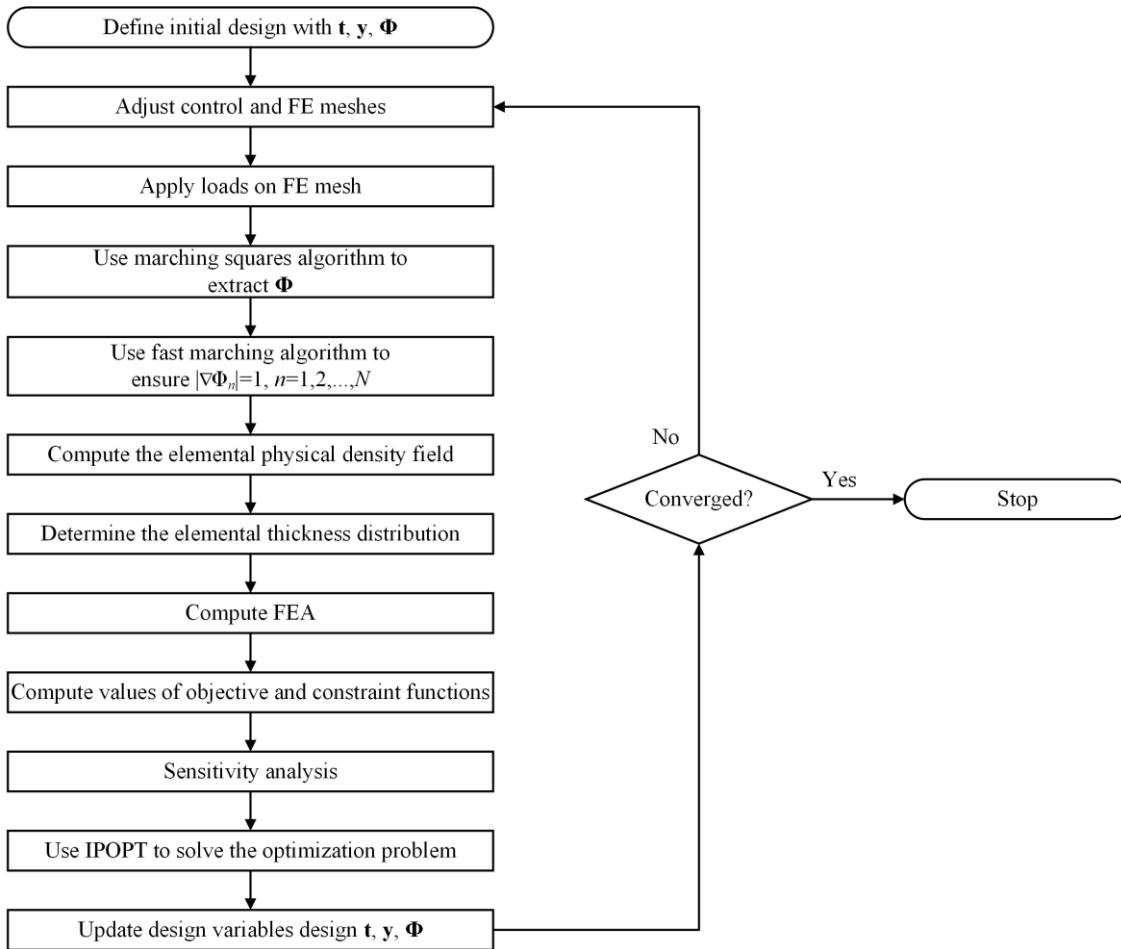


**Figure 3.8** Flowchart of the proposed method.

### 3.3 Numerical Examples

In this section, three numerical examples are presented to study simultaneous sizing, layout and topology optimization of stiffened panels. In these examples, the Young's moduli of the solid material and void phases are  $E_s = 73$  GPa and  $E_v = 10^{-6} \times 73$  GPa, respectively. The densities are  $\rho_s = 2795$  kg/m<sup>3</sup> and  $\rho_v = 0$  for the solid material and void phase, respectively. The Poisson's ratio is  $\nu = 0.33$ .

#### 3.3.1 Stiffened Panel under Shear Loading

The stiffened panel with the loading and boundary conditions shown in Fig. 3.9 is considered for optimization. A shear load  $P = 300$  kN/m is applied to the top edge. The skin is discretized with  $80 \times 80$  plate elements. The lower and upper bounds of the thicknesses of both the skin and the stiffeners are 0.001 m and 0.003 m, respectively.

**Chapter 3: Simultaneous Sizing, Layout and Topology Optimization of Panels with Straight Stiffeners under Buckling Constraints**

The lower bound of the critical buckling load factor  $\lambda_{\min} = 1$ . The lower bound of the stiffener spacing  $L_{\min} = 15$  mm.

The initial design which comprises a skin and 7 vertical stiffeners, each with a height of 0.03 m, is given in Fig. 3.10. The initial thicknesses are set to 0.002 m for both the skin and the stiffeners. The stiffeners are discretized with 8 elements along their height. To represent the 7 stiffeners, 7 level set functions are used. The first 50 buckling modes are considered in the optimization.

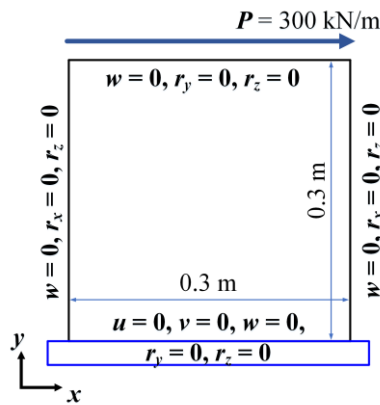


**Figure 3.9 Loading and boundary conditions for the design of a stiffened panel under shear loading.**

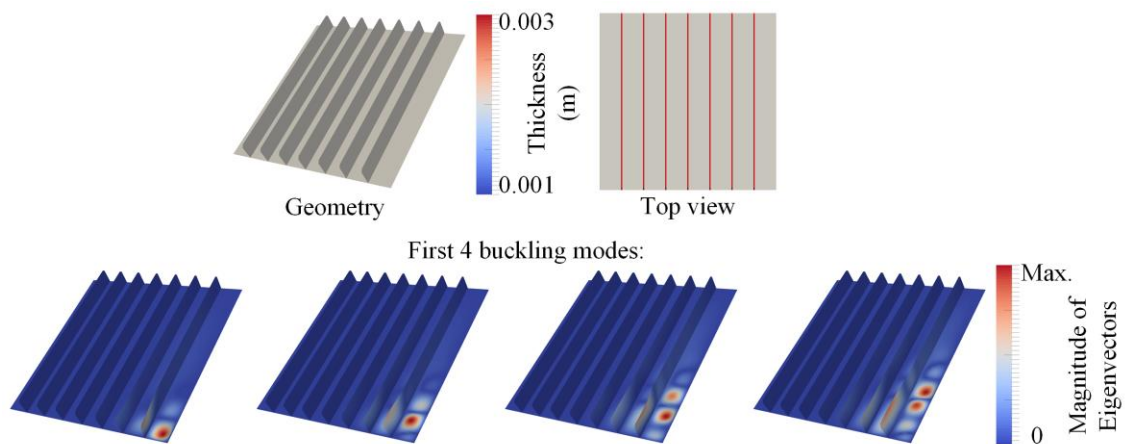


**Figure 3.10 Initial design with 7 vertical stiffeners,  $m = 0.855$  kg, and its first 4 buckling modes under shear loading,  $\lambda_1 = 1.141$ ,  $\lambda_2 = 1.459$ ,  $\lambda_3 = 1.702$ ,  $\lambda_4 = 1.903$ .**

**Simultaneous Sizing, Layout and Topology Optimization  
for Buckling and Postbuckling of Stiffened Panels**

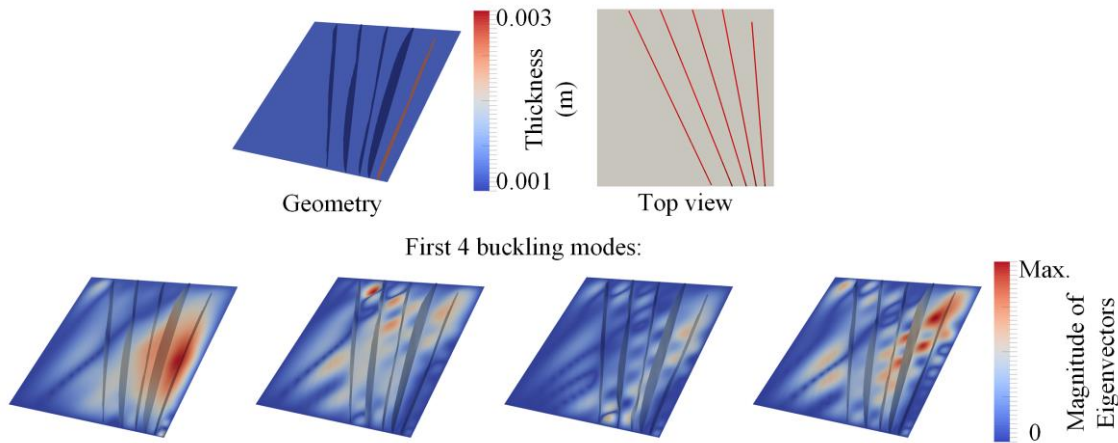


**Figure 3.11 Optimized design,  $m = 0.356$  kg, and its first 4 buckling modes under shear loading,  $\lambda_1 = 1.010$ ,  $\lambda_2 = 1.017$ ,  $\lambda_3 = 1.021$ ,  $\lambda_4 = 1.024$ .**

From the initial design and corresponding first 4 buckling modes in Fig. 3.10, it can be seen that there is a tendency for the bottom right-hand side of the panel to buckle under the given load case with the structure buckling between the stiffeners, i.e., local buckling. This shows that the stiffeners are stiff enough to force the plate to buckle locally. The optimized design is shown in Fig. 3.11. The furthest left stiffener is redundant and is removed, and the remaining stiffeners are moved to the right-hand side of the structure to increase the stiffness and reduce the buckling in the bottom right-hand region of the panel. For similar reasons, the thickness of the furthest right stiffener is much greater than that of the other stiffeners. Meanwhile, the topology and thickness of each remaining stiffener and the skin thickness are optimized, and redundant material is removed. For the first buckling mode of the optimized design, buckles cross the stiffeners, and hence a global mode is observed with local modes seen for its second to fourth buckling modes. The differences between the first 4 buckling load factors are within 1.39% which is 97.9% lower than that of the initial design. This agrees with the observation in [3] that the optimum stiffened panel design is found when global and local buckling loads coincide.

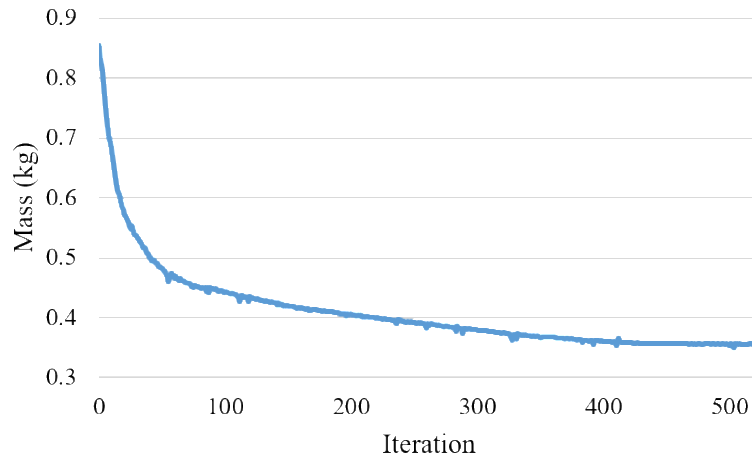


**Figure 3.12** Convergence curve of the mass for the design of the stiffened panel under shear loading.

The convergence curves for the mass and buckling load factors during the optimization are given in Figs. 3.12 and 3.13, respectively. Many small oscillations are found in the convergence curves. To understand why these occur, the first buckling mode from the 201st to the 210th iteration and the first 50 buckling modes in the 201st and 202nd iterations are examined in Figs. 3.14 and 3.15, respectively. In Fig. 3.14, it can be seen that mode-switching occurs with the first buckling mode changing between adjacent iterations. In Fig. 3.15, it can be observed that the first buckling mode in the 202nd iteration cannot even be found in the first 50 buckling modes in the 201st iteration, indicating that the sensitivity information for this first buckling mode in the 202nd iteration cannot be obtained based on the buckling modes in the 201st iteration. Both of these effects cause the oscillations seen in the convergence history. Fig. 3.15 also shows that, in both the 201st and 202nd iterations the higher buckling modes are local modes which occur between the stiffeners, while global ones which cross the stiffeners usually appear in the lower modes. As mentioned above, in the 202nd iteration the new first buckling mode, not be found in the higher modes in the 201st iteration, appears. Therefore, including lots of buckling modes in the optimization, i.e., 50 buckling modes, would still not give the sensitivity for the newly introduced first buckling mode. Considering this, an appropriate number of buckling modes needs to be chosen to ensure convergence and computational efficiency.

**Simultaneous Sizing, Layout and Topology Optimization  
for Buckling and Postbuckling of Stiffened Panels**

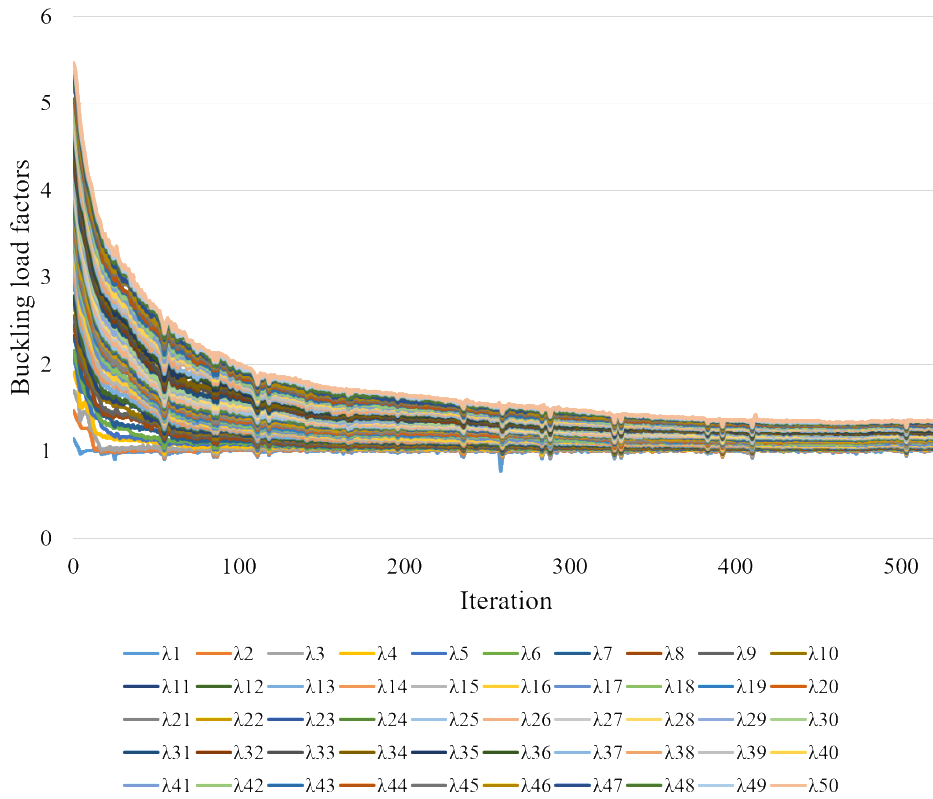


**Figure 3.13** Convergence curves of the buckling load factors for the design of the stiffened panel under shear loading.

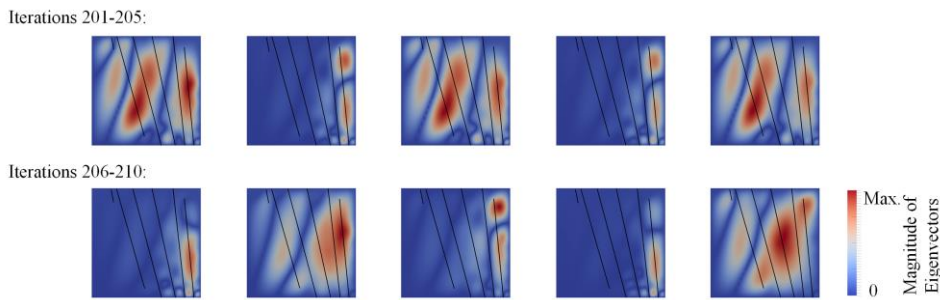


**Figure 3.14** First buckling modes from the 201st to the 210th iterations for the design of the stiffened panel under shear loading.

### Chapter 3: Simultaneous Sizing, Layout and Topology Optimization of Panels with Straight Stiffeners under Buckling Constraints

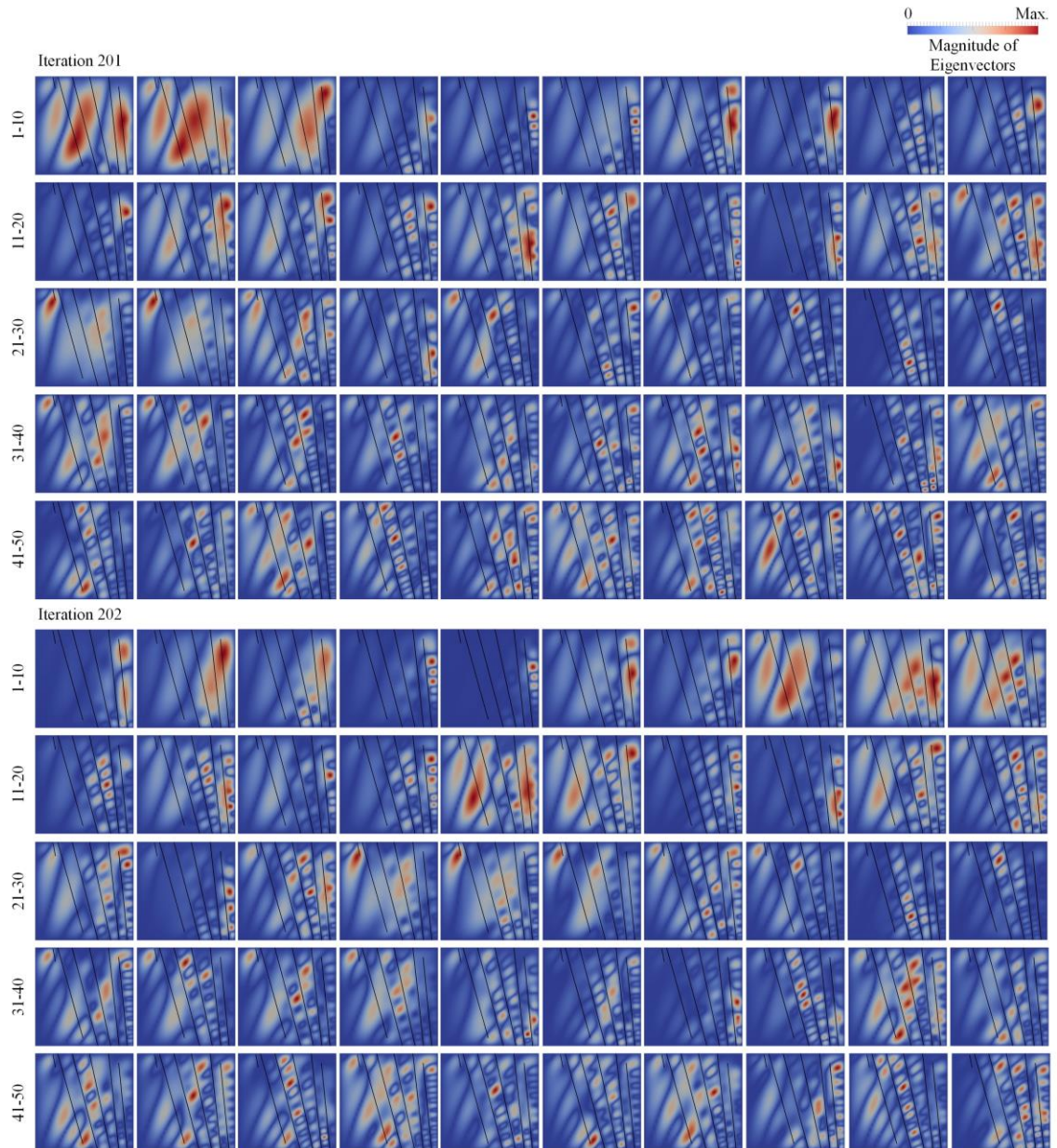


**Figure 3.15 First 50 buckling modes in 201st and 202nd iterations for the design of the stiffened panel under shear loading.**

In order to investigate how many buckling modes need to be considered in the optimization, the optimization problem is solved using the first 1, 4, 7, 10, 15, 25, 50 and 100 buckling modes. The resulting structures are presented in Fig. 3.16. Comparisons of the solution times and the optimization results are shown in Table 3.1 (the problems are solved on a 2.9 GHz 6-Core Intel Core i9 Processor with 16 GB 2400 MHz DDR4 Memory). Similar feasible solutions are obtained using 4 or more buckling modes, and the difference between their masses (the objective function) is within 0.85%. When only the first buckling mode is used in the optimization, the optimization

### Simultaneous Sizing, Layout and Topology Optimization for Buckling and Postbuckling of Stiffened Panels

fails to converge in 800 iterations. It is also noted that, although the mass of the optimized design using the first 4 buckling modes is less than that obtained using more than 4 buckling modes, it takes more than 200 additional iterations to converge and the total optimization time is 51.4% more than that using the first 10 buckling modes.

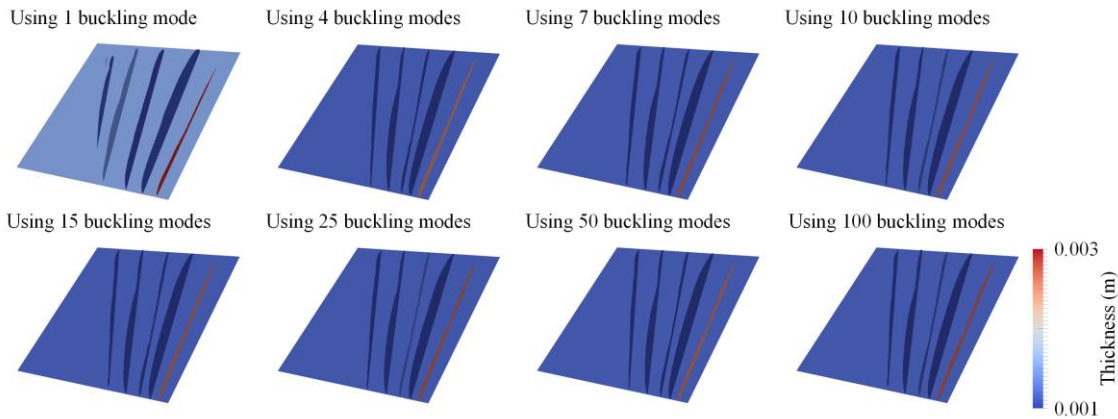


**Figure 3.16 Geometries of the optimized designs under shear loading, using different numbers of buckling modes.**

The optimization problem is next solved considering different initial designs. The first 10 buckling modes are used in the optimization. The initial and optimized designs are given in Figs. 3.17-3.20. These are compared in Table 3.2. For the initial designs in Figs. 3.19(b) and 3.20(b), the height of the stiffeners is only 0.00375 m. The structures behave more like plates, and their first buckling modes are different from the one shown in Fig. 3.10, which, consequently, indicates different optimization paths. From the optimized designs in Figs. 3.19(d) and 3.20(d), it can be seen that material is added to the stiffeners, and the layout of the stiffeners and thicknesses of the stiffened panel are optimized simultaneously. Their geometries are almost the same as that in Fig. 3.11. The differences between the masses of all the optimized designs in Figs. 3.17-3.20 are within 8.3%, while the differences excluding the two in Figs. 3.18(d) and 3.20(c) are within 2.5%. The optimized designs in Figs. 3.18(d) and 3.20(c) are local optima. They have one less stiffener than the other results but greater masses. This is because, in the initial designs in Figs. 3.18(a) and 3.20(a), more material is distributed in the left-hand side of the panel, which is thought redundant and removed by the optimizer at the beginning of the optimization. Nevertheless, it can be observed that all the optimized designs follow the same trend. The thickness of the furthest right stiffener is the greatest, and the remaining stiffeners are moved to the right-hand side of the panel to

provide additional support to the bottom right-hand region of the panel. In Figs. 3.18(d) and 3.20(c), even though another stiffener is removed or in other words, the design space is reduced, the optimizer still finds reasonable designs within the limited design space.

**Table 3.1 Solution times and optimization results for the design of a stiffened panel under shear loading, using different numbers of buckling modes.**

No. modes	Average time for each optimization iteration (s)							Mass (kg)	$\lambda_1$	Iteration needed	Total time (s)
	Compute <b>K</b>	Solve Eq. (3-7a)	Compute <b>K<sub>g</sub></b>	Solve Eq. (3-7b)	Sensitivity analysis	Solve Eq. (3-29)	Total time				
1	2.59	0.01	1.31	6.87	27.98	0.25	39.0	0.449	1.01	Max. iter. (800)	
4	2.49	0.01	1.28	6.48	28.25	0.36	38.88	0.354	1.00	733	28496
7	2.48	0.01	1.27	4.76	29.32	0.43	38.27	0.356	1.00	509	19478
10	2.49	0.01	1.28	4.57	30.51	0.51	39.38	0.356	1.01	478	18822
15	2.55	0.01	1.29	4.57	32.76	0.61	41.79	0.356	1.00	478	19977
25	2.64	0.01	1.33	5.70	37.36	0.90	47.93	0.356	1.00	472	22626
50	2.60	0.01	1.31	9.78	45.92	1.80	61.41	0.356	1.01	523	32125
100	2.54	0.01	1.28	22.17	62.68	3.76	92.43	0.357	1.01	495	45761

### Simultaneous Sizing, Layout and Topology Optimization for Buckling and Postbuckling of Stiffened Panels

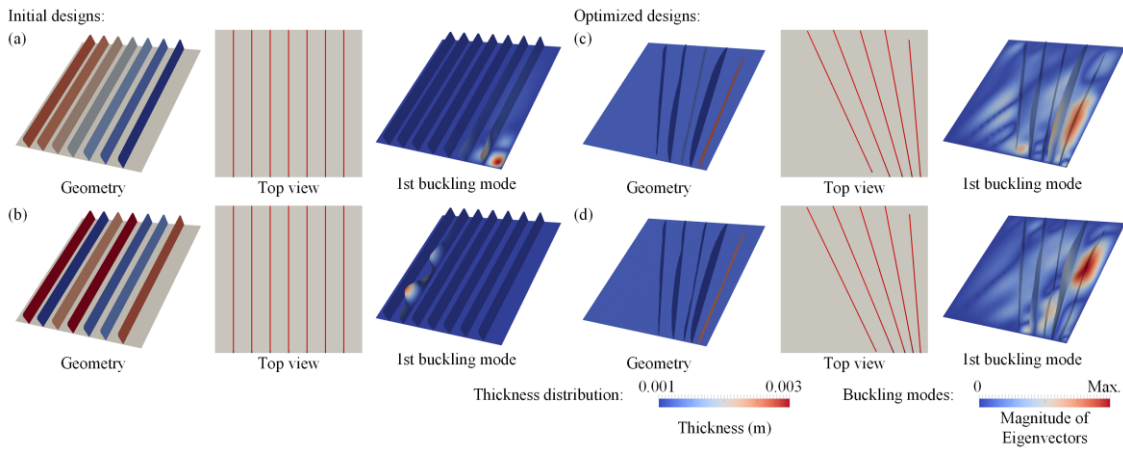


**Figure 3.17** Optimized designs under shear loading, employing initial designs with different thickness distributions.

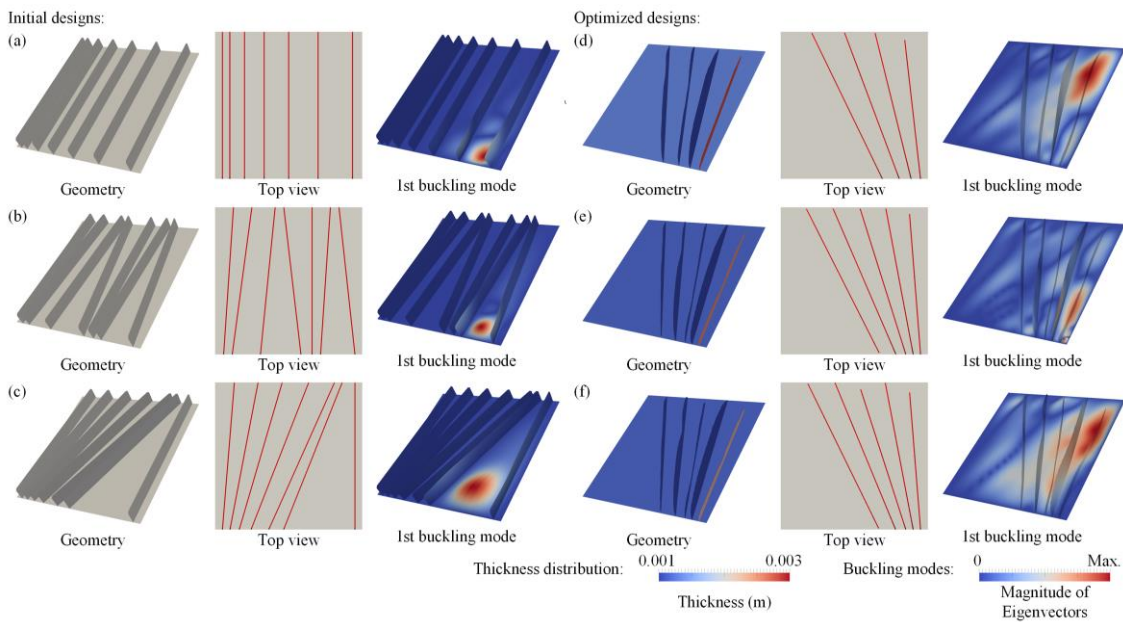


**Figure 3.18** Optimized designs under shear loading, employing initial designs with different stiffener layouts.

### Chapter 3: Simultaneous Sizing, Layout and Topology Optimization of Panels with Straight Stiffeners under Buckling Constraints

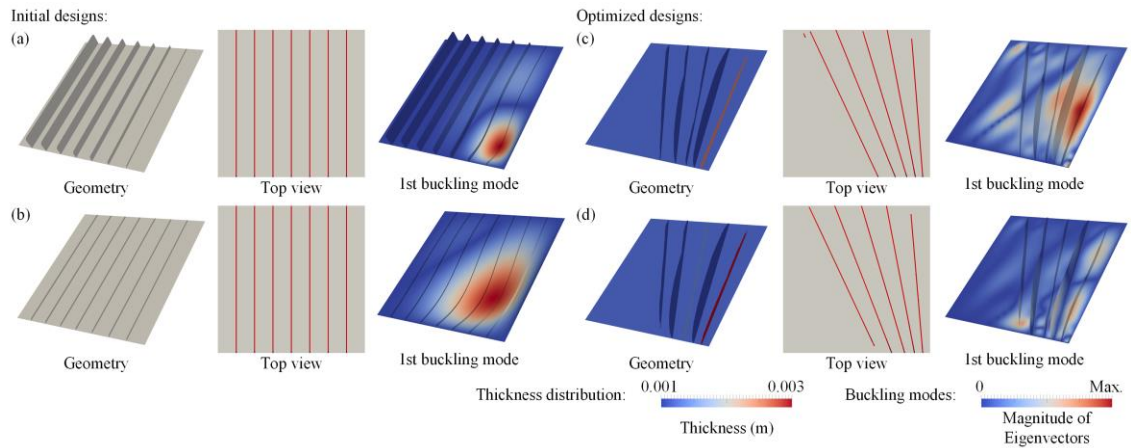


**Figure 3.19** Optimized designs under shear loading, employing initial designs with different stiffener topologies.

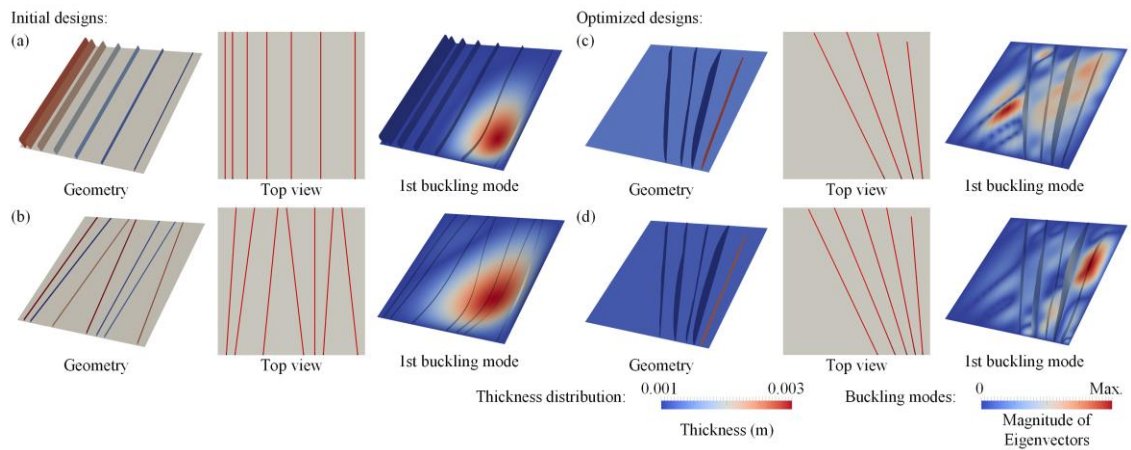


**Figure 3.20** Optimized designs under shear loading, employing initial designs with different thickness distributions, stiffener layouts and topologies.

The stiffened panel is further optimized by (a) sizing optimization, (b) sizing and layout optimization, (c) topology optimization, (d) sizing and topology optimization, and (e) layout and topology optimization. The first 10 buckling modes are considered for all of the optimizations. The optimized results are presented in Fig. 3.21 and compared in Table 3.3. Compared with the optimized design obtained from (f) simultaneous sizing, layout and topology optimization, their masses are 88.2%, 32.6%, 66.6%, 57.0% and 57.0% greater. This shows the simultaneous sizing, layout and topology optimization can obtain an optimized design with a significantly lighter weight for same structural performance.

**Simultaneous Sizing, Layout and Topology Optimization  
for Buckling and Postbuckling of Stiffened Panels**

**Table 3.2 Comparison of the optimized results under shear loading, employing different initial designs.**

Optimization with different initial designs	Initial design			Optimized design		
	Figure	Mass (kg)	$\lambda_1$	Figure	Mass (kg)	$\lambda_1$
Different thickness distributions	3.17(a)	0.835	1.066	5.17(c)	0.360	1.008
	3.17(b)	0.872	1.147	5.17(d)	0.354	1.002
Different stiffener layouts	3.18(a)	0.855	0.705	5.18(d)	0.384	1.001
	3.18(b)	0.856	0.798	5.18(e)	0.353	1.002
	3.18(c)	0.870	0.312	5.18(f)	0.355	1.007
Different stiffener topologies	3.19(a)	0.701	0.390	5.19(c)	0.355	1.011
	3.19(b)	0.547	0.151	5.19(d)	0.362	1.007
Different thickness distributions, and stiffener layouts and topologies	3.20(a)	0.719	0.261	5.20(c)	0.385	1.008
	3.20(b)	0.549	0.155	5.20(d)	0.356	1.006

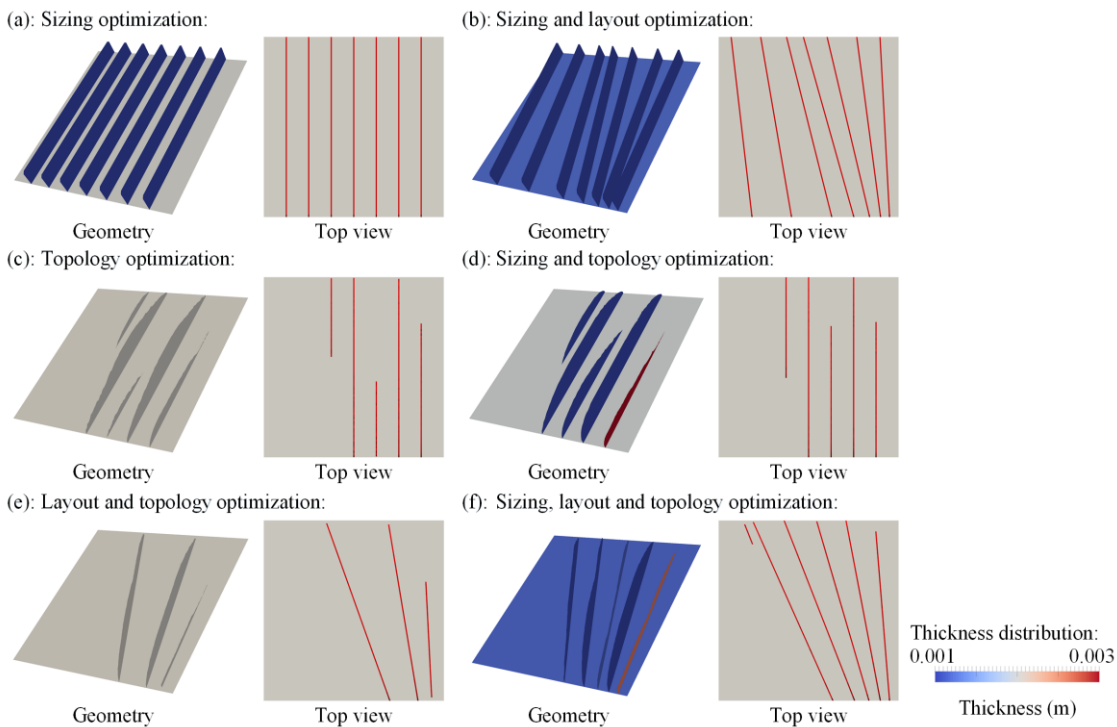


**Figure 3.21 Optimized designs under shear loading, using different kinds of optimization.**

**Table 3.3 Comparison of the optimized results under shear loading, using different kinds of optimization.**

Optimization	Mass (kg)	$\lambda_1$
(a) Sizing optimization	0.670	1.000
(b) Sizing and layout optimization	0.472	1.001
(c) Topology optimization	0.593	1.003
(d) Sizing and topology optimization	0.559	1.006
(e) Layout and topology optimization	0.559	1.007
(f) Sizing, layout and topology optimization	0.356	1.007

### 3.3.2 Stiffened Panel under Combined Shear and Compression

The stiffened panel with the loading and boundary conditions shown in Fig. 3.22 is considered for optimization next. The axial loads  $N_{xx} = 20$  kN/m and  $N_{yy} = 100$  kN/m are applied, with an in-plane shear load  $N_{xy} = 100$  kN/m. The skin is discretized with  $160 \times 80$  plate elements. The lower and upper bounds of the thicknesses of both the skin and the stiffeners are 0.002 m and 0.005 m, respectively. The initial thicknesses are set to 0.003 m for both the skin and the stiffeners. The lower bound of the critical buckling load factor  $\lambda_{\min} = 1$ . The first 10 buckling modes are considered in the optimization. The lower bound of the stiffener spacing  $L_{\min} = 25$  mm.

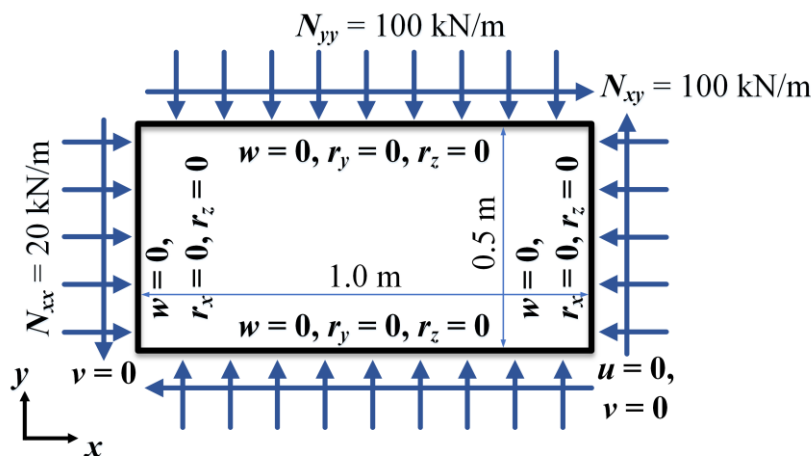


**Figure 3.22 Loading and boundary conditions for the design of a stiffened panel under combined shear and compression.**

### Simultaneous Sizing, Layout and Topology Optimization for Buckling and Postbuckling of Stiffened Panels

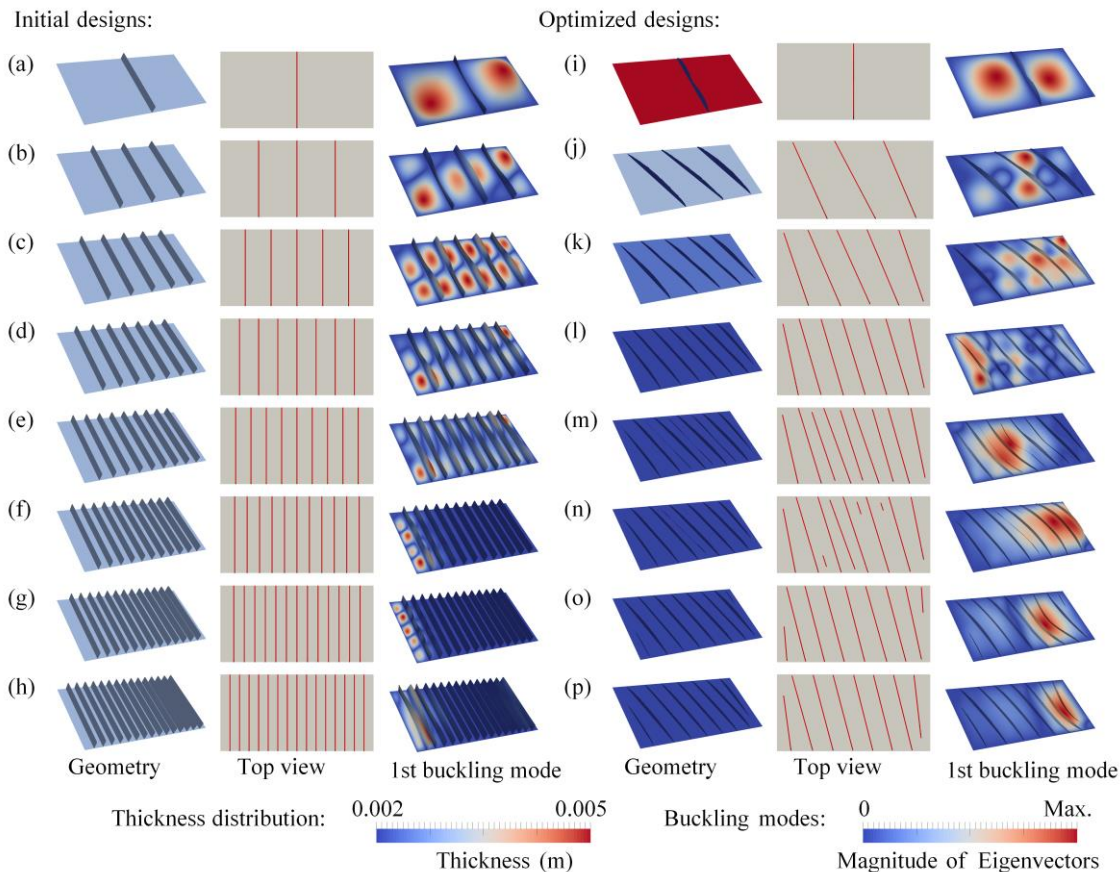


**Figure 3.23 Initial and optimized designs under combined shear and compression, employing initial designs with different numbers of stiffeners.**

The optimization problem is solved considering initial designs with different numbers of stiffeners. The initial configurations and their corresponding optimized designs are given in Fig. 3.23 and compared in Table 3.4. The stiffeners, with heights of 0.0625 m, are discretized with 10 elements along their height for all the initial designs. The number of stiffeners in the initial design determines the maximum allowable number of stiffeners in the corresponding optimized design. The more stiffeners in the initial configuration, the larger the design space to be searched. As the number of stiffeners in the initial design increases from 1 to 3, 5 and 7, more promising stiffener configurations are found to resist the buckling and the thickness of the skin is therefore reduced. Correspondingly, the masses of the optimized designs are reduced by 35.8%, 48.7% and 55.1%, respectively. When enough stiffeners (7 or more) are applied in the initial configuration, the differences between the masses of the optimized designs converge to within 0.378% even though their stiffener layouts and buckling modes are different. This indicates that multiple local optima exist in this problem. To further investigate

**Chapter 3: Simultaneous Sizing, Layout and Topology Optimization of Panels with Straight Stiffeners under Buckling Constraints**

this, another set of optimization problems are solved considering initial designs with the same numbers (11) of stiffeners but different stiffener spacing, as shown in Fig. 3.24 and Table 3.5. The initial thicknesses are set to 0.002 m for both the skin and the stiffeners. The differences in the buckling modes in the initial designs indicate different optimization paths. Optimized designs with different stiffener layouts and higher buckling modes are obtained, but the difference between their masses is only 0.252%. Therefore, it can be concluded that several local optimal designs exist in this problem and that the optimizer is able to explore the design space effectively and achieve equally good design solutions. With different initial designs, i.e., ones with different numbers or spacing of stiffeners, the proposed optimization method can offer multiple design options to engineers.

**Table 3.4 Comparison of the optimized results under combined shear and compression, employing initial designs with different numbers of stiffeners.**

Number of stiffeners in the initial design	Initial design			Optimized design		
	Figure	Mass (kg)	$\lambda_1$	Figure	Mass (kg)	$\lambda_1$
1	3.23(a)	4.454	0.228	3.23(i)	7.055	1.003
3	3.23(b)	4.978	0.862	3.23(j)	4.529	1.003
5	3.23(c)	5.501	1.900	3.23(k)	3.622	1.001
7	3.23(d)	6.024	3.389	3.23(l)	3.165	1.009
9	3.23(e)	6.548	5.290	3.23(m)	3.177	1.004
11	3.23(f)	7.071	6.474	3.23(n)	3.166	1.001
13	3.23(g)	7.595	7.537	3.23(o)	3.176	1.006
15	3.23(h)	8.118	12.65	3.23(p)	3.175	1.007

### 3.3.3 Stiffened Panel under a Concentrated Load

The stiffened panel with the loading and boundary conditions shown in Fig. 3.25 is also considered for optimization. A concentrated load  $F = 100$  kN is applied at the center of its upper edge. The skin is discretized with  $160 \times 80$  plate elements. The lower and upper bounds of the thicknesses of both the skin and the stiffeners are 0.002 m and 0.005 m, respectively. The initial thicknesses are set to 0.003 m for both the skin and

**Simultaneous Sizing, Layout and Topology Optimization  
for Buckling and Postbuckling of Stiffened Panels**

the stiffeners. The lower bound of the stiffener spacing  $L_{\min} = 12.5$  mm. The first 10 buckling modes are considered in the optimization.

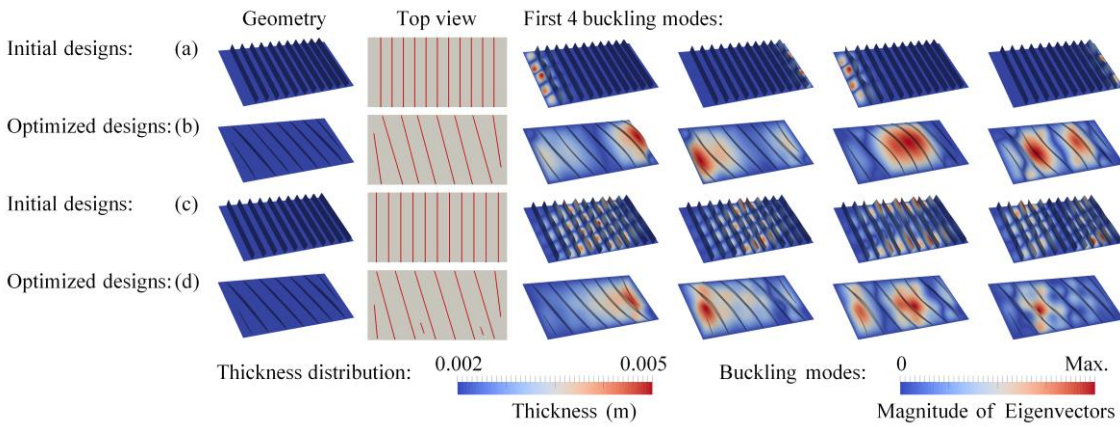


**Figure 3.24 Initial and optimized designs under combined shear and compression, employing initial designs with 11 stiffeners but different stiffener spacing.**

**Table 3.5 Comparison of the optimized results under combined shear and compression, employing initial designs with 11 stiffeners but different stiffener spacing.**

Initial design						Optimized design					
Figure	Mass (kg)	$\lambda_1$	$\lambda_2$	$\lambda_3$	$\lambda_4$	Figure	Mass (kg)	$\lambda_1$	$\lambda_2$	$\lambda_3$	$\lambda_4$
3.24(a)	4.714	1.941	1.941	1.952	1.953	3.24(b)	3.173	1.001	1.004	1.027	1.047
3.24(c)	4.714	2.305	2.306	2.335	2.361	3.24(d)	3.165	1.003	1.009	1.015	1.024

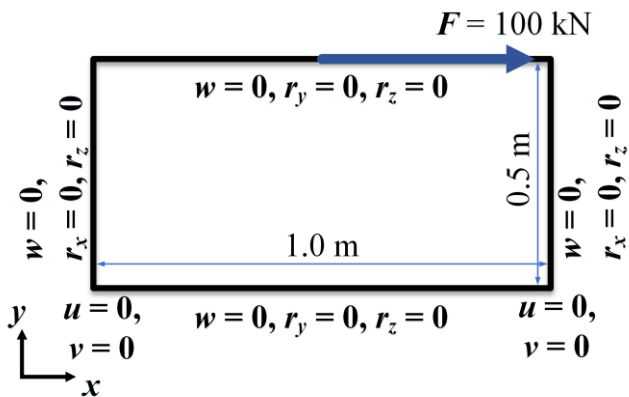


**Figure 3.25 Loading and boundary conditions for the design of a stiffened panel under a concentrated load.**

### Chapter 3: Simultaneous Sizing, Layout and Topology Optimization of Panels with Straight Stiffeners under Buckling Constraints

Stiffness-based topology optimization based on compliance has been well-developed and used in the automotive [98], aerospace [1, 99] and civil engineering industries [100]. In this example, the buckling-based formulations in Eq. (3-30) are studied to compare with the stiffness-based optimization. The first one in Eq. (3-30a) is mass minimization with buckling constraints. For the second and third formulations in Eqs. (3-30b) and (3-30c), compliance is considered in either the constraints or the objective.

$$\begin{aligned}
 & \min_{\mathbf{t}, \mathbf{y}, \Phi} m(\mathbf{t}, \mathbf{y}, \Phi) \\
 & s.t. \quad \lambda_q(\mathbf{t}, \mathbf{y}, \Phi) \geq \lambda_{\min}, \quad q = 1, 2, \dots, N_\lambda \\
 & \quad \quad L_l(\mathbf{y}) \geq L_{\min}, \quad l = 1, 2, \dots, N_L
 \end{aligned} \tag{3-30a}$$

$$\begin{aligned}
 & \min_{\mathbf{t}, \mathbf{y}, \Phi} m(\mathbf{t}, \mathbf{y}, \Phi) \\
 & s.t. \quad \lambda_q(\mathbf{t}, \mathbf{y}, \Phi) \geq \lambda_{\min}, \quad q = 1, 2, \dots, N_\lambda \\
 & \quad \quad c(\mathbf{t}, \mathbf{y}, \Phi) \leq c_{\max} \\
 & \quad \quad L_l(\mathbf{y}) \geq L_{\min}, \quad l = 1, 2, \dots, N_L
 \end{aligned} \tag{3-30b}$$

$$\begin{aligned}
 & \min_{\mathbf{t}, \mathbf{y}, \Phi} c(\mathbf{t}, \mathbf{y}, \Phi) \\
 & s.t. \quad \lambda_q(\mathbf{t}, \mathbf{y}, \Phi) \geq \lambda_{\min}, \quad q = 1, 2, \dots, N_\lambda \\
 & \quad \quad m(\mathbf{t}, \mathbf{y}, \Phi) \leq m_{\max} \\
 & \quad \quad L_l(\mathbf{y}) \geq L_{\min}, \quad l = 1, 2, \dots, N_L
 \end{aligned} \tag{3-30c}$$

where  $c$  is the compliance,  $c_{\max}$  is its upper bound and  $m_{\max}$  is the upper bound of the mass. To understand how the thicknesses of the skin and stiffeners are optimized, optimizations with and without skin thickness optimization are conducted. In the case without the skin thickness optimization, the skin thickness,  $t_p = 0.0024$  m, is fixed during the optimization.

The initial designs are shown in Fig. 3.26, where 3 and 15 stiffeners with heights of 0.0625 m are considered. The stiffeners are discretized with 10 elements along their height. The structural data are given in Table 3.6. The lower bound of the critical buckling load factor  $\lambda_{\min} = 1$  for all three optimization problems. For the second optimization problem, the mass minimization problem with buckling and compliance constraints, the upper bound of the compliance  $c_{\max} = 425$ . For the third optimization problem, the compliance minimization with buckling and mass constraints, the upper

**Simultaneous Sizing, Layout and Topology Optimization  
for Buckling and Postbuckling of Stiffened Panels**

bound of the mass  $m_{\max} = 4.061$ . The optimization results corresponding to the three problem formulations in Eq. (3-30) are given in Figs. 3.26 and compared in Table 3.7.

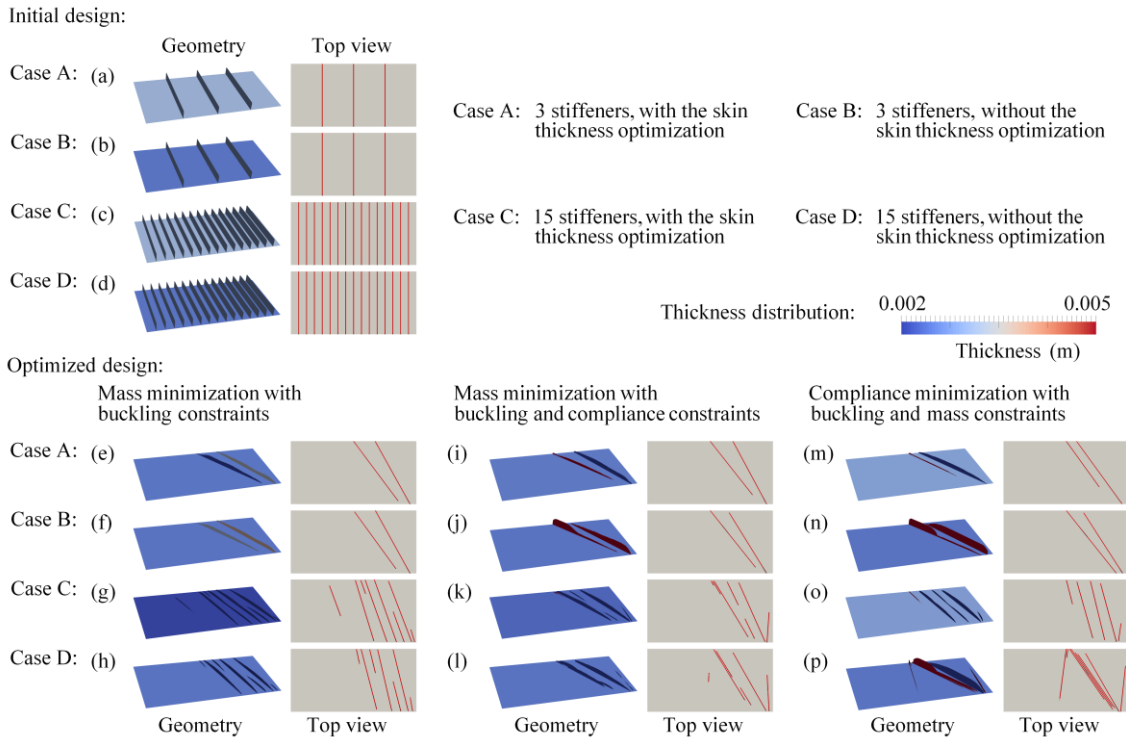


**Figure 3.26 Initial and optimized designs under a concentrated load, considering different optimization problems with or without skin thickness optimization and employing initial designs with different numbers of stiffeners.**

**Table 3.6 Initial designs under a concentrated load, considering different optimization problems with or without skin thickness optimization and employing initial designs with different numbers of stiffeners.**

Number of stiffeners in the initial design	Including the skin thickness optimization	Figure	Mass (kg)	$\lambda_1$	Compliance	Skin thickness (mm)
3	Yes	3.26(a)	4.978	0.502	371.3	3.000
3	No	3.26(b)	4.139	0.261	464.1	2.400
15	Yes	3.26(c)	8.118	1.872	369.7	3.000
15	No	3.26(d)	7.280	0.996	460.4	2.400

From the optimized designs in Figs. 3.26(e)-3.26(h) with the first problem formulation in Eq. (3-30a), it can be seen that optimization is conducted successfully without the

**Chapter 3: Simultaneous Sizing, Layout and Topology Optimization of Panels with Straight Stiffeners under Buckling Constraints**

compliance in the problem formulation. Comparing the optimized designs in Fig. 3.26, it can be observed that different stiffener layouts and shapes are obtained when compliance is considered, especially for the designs considering the 15-stiffener initial design. The stiffeners to the right-hand side of the panel are moved closer to the right-hand edge to limit the deformation. Comparing the optimized designs in Figs. 3.26(g), 3.26(k) and 3.26(o), it can be seen that considering compliance leads to thicker skins. The masses of the optimized designs in Figs. 3.26(k) and 3.26(o) are 11.0% and 33.5% greater than that of the optimized design based on mass minimization with only a buckling constraint in Fig. 3.26(g), respectively.

**Table 3.7 Comparison of optimized designs under a concentrated load, considering different optimization problems with or without skin thickness optimization and employing initial designs with different numbers of stiffeners.**

Optimization	Number of stiffeners in the initial design	Including the skin thickness optimization	Figure	Mass (kg)	$\lambda_1$	Compliance	Skin thickness (mm)
Mass minimization with buckling constraints in Eq. (3-30a)	3	Yes	3.26(e)	3.578	1.002	451.4	2.411
	3	No	3.26(f)	3.603	1.006	467.7	2.400
	15	Yes	3.26(g)	3.043	1.002	542.2	2.000
	15	No	3.26(h)	3.572	1.010	469.1	2.400
Mass minimization with buckling and compliance constraints in Eq. (3-30b)	3	Yes	3.26(i)	3.642	1.005	425.0	2.454
	3	No	3.26(j)	3.871	1.007	425.0	2.400
	15	Yes	3.26(k)	3.378	1.002	425.0	2.291
	15	No	3.26(l)	3.536	1.003	424.0	2.400
Compliance minimization with buckling and mass constraints in Eq. (3-30c)	3	Yes	3.26(m)	4.061	1.001	376.2	2.805
	3	No	3.26(n)	4.061	1.001	424.4	2.400
	15	Yes	3.26(o)	4.061	1.010	375.9	2.773
	15	No	3.26(p)	4.061	1.000	398.1	2.400

The initial designs with 15 stiffeners offer a larger design space than the ones with 3 stiffeners. When the first and second optimization formulations of the mass minimization in Eqs. (3-30a) and (3-30b) are implemented, it can be seen in Figs.

## Simultaneous Sizing, Layout and Topology Optimization for Buckling and Postbuckling of Stiffened Panels

3.26(e) - 3.26(l) that for the initial designs with 15 stiffeners, the better stiffener configurations are found to control the structural buckling and deformation, and thus the thicknesses of the skins can be further reduced. The masses of the optimized designs are 0.86% - 15.0% lower than those considering initial designs with 3 stiffeners. When the third optimization formulation in Eq. (3-30c) is applied, for similar reasons, the compliances of the optimized designs considering initial designs with 15 stiffeners in Figs. 3.26(o) and 3.26(p) are 0.080% and 6.20% lower than those considering initial designs with 3 stiffeners shown in Figs. 3.26(m) and 3.26(n), respectively.

With the first and second optimization formulations for mass minimization in Eqs. (3-30a) and (3-30b), it can be found from Figs. 3.26(e) - 3.26(l) and Table 3.7 that the masses of the optimized designs including skin thickness optimization are 0.694% - 14.8% less than those with fixed skin thicknesses. When the 3-stiffener initial design is considered, the skin thicknesses of the optimized designs including skin thickness optimization are greater than those without skin thickness optimization; while the skin thicknesses are thinner when the 15-stiffener initial design is considered. This is because, when more stiffeners are considered in the initial design, a wider range of stiffener configurations can be generated to make up for the loss of stiffness due to the reduced skin thickness. With the third optimization formulation for compliance minimization in Eq. (3-30c), when skin thickness optimization is considered, more material is distributed to the skin to increase the stiffness of the whole structure, with less material available for the stiffeners due to the mass constraint. The compliances of the optimized designs in Figs. 3.26(m) and 3.26(o) are 11.4% and 5.58% lower than those without the skin thickness optimization in Figs. 3.26(n) and 3.26(p), respectively.

### 3.4 Conclusions

This chapter investigates the weight minimization of stiffened panels simultaneously optimizing sizing, layout and topology under buckling constraints. An effective level-set based topology optimization formulation is presented. The construction and updating of geometric and FE models of stiffened panels are described in detail. To solve the optimization problem, a semi-analytical sensitivity analysis is presented. The optimization algorithm is also outlined.

### **Chapter 3: Simultaneous Sizing, Layout and Topology Optimization of Panels with Straight Stiffeners under Buckling Constraints**

The numerical results show the effectiveness of the proposed method. The effect of the buckling modes used is explored. Increasing the number of buckling modes usually helps with improving the convergence of the optimization by resolving mode switching. However, in a stiffened panel the higher buckling modes are local modes corresponding to the stiffener layout. As the stiffened panel, particularly the stiffener layout, is optimized, additional first buckling modes, not be found in the higher modes in the previous optimization iteration begin to appear. Considering this, an appropriate number of buckling modes needs to be chosen to ensure convergence and computational efficiency. The numerical examples presented also show that whilst this optimization problem is initial-design-dependent and has several local optimal solutions with similar structural performances, the proposed method can reliably find useful design candidates within the given design space.

The benefit of simultaneously conducting sizing, layout and topology optimization for the design of stiffened panels is demonstrated. The difference between buckling-driven and stiffness-driven designs is investigated. When structural stiffness is considered, more material is prone to be distributed on the skin, along with corresponding changes to stiffener configurations. This can lead to a heavier design.

It is noted that in this work, the free-form mesh deformation method is used to adaptively adjust the FE mesh to cater for the optimized stiffener layout. This causes inconsistency of mesh densities on different skin bays and stiffeners. The effect of the deformation of the FE mesh on the critical buckling load and mass, has been accounted for in sensitivity information for optimization. So far, no issues on FE analysis and optimization of stiffened panels, caused by the mesh inconsistency, have been found.

# 4 SIMULTANEOUS SIZING, LAYOUT AND TOPOLOGY OPTIMIZATION OF PANELS WITH STRAIGHT STIFFENERS UNDER STRESS AND BUCKLING CONSTRAINTS

In Chapter 3, the feasibility of applying the level set topology optimization method to simultaneously optimize the size, layout and topology of stiffened panels against buckling, was demonstrated. This was achieved by employing plate elements to model the stiffeners which were parametrized by multiple implicit level set functions (LSFs) thus optimizing the internal topology and size of each stiffener at the same time as the placement, orientation and number of stiffeners and the skin thickness. By using 2D plate elements, the mesh density could be several orders of magnitude less than for an equivalent mesh of 3D continuum elements.

So far, only optimization against linear buckling has been studied. In this chapter the same method is extended to both of the critical failure criteria, stress and buckling, enabling the weight minimization of stiffened panels simultaneously optimizing size, layout and topology. The stiffened panel is again discretized with plate elements. The

layout of the stiffeners is optimized, and the free-form mesh deformation approach is improved to adjust the finite element mesh for the changing stiffener layout. The level set method is utilized to optimize the topologies of the stiffeners, as well as the thicknesses of the skin and stiffeners. Bending, shear and membrane stresses are evaluated at the bottom, middle and top surfaces of the elements. The local stress constraints are aggregated into a global constraint using a  $p$ -norm function. A gradient-based optimizer is employed to solve the optimization problem. Numerical examples demonstrate the effectiveness of the proposed approach.

The remainder of this chapter is organized as follows. In Section 4.1, the geometric and finite element (FE) models of the stiffened panel are presented. Section 4.2 describes the mathematical formulation and the optimization methodology. Numerical examples and investigations of the optimum stiffened panels are presented in Section 4.3, followed by conclusions in Section 4.4.

## 4.1 Stiffened Panel Model

In this section, the geometric and FE models are described. The coordinates of the stiffener ends are used to manipulate the stiffener layout, and LSFs are used to represent and optimize the internal topologies of the stiffeners. Sizing variables are also included to optimize the thicknesses of the skin and stiffeners. As the stiffener layout changes, an modified free-form mesh deformation method is used to adjust the FE mesh.

### 4.1.1 Geometric Model

Figure 4.1 illustrates how the geometric model of the panel with straight stiffeners is constructed and updated. The same method, as described in Sections 3.1.1 - 3.1.3, is adopted. As shown in Figs. 4.1(i) and 4.1(j), the stiffened panel is described in terms of the stiffener layout, the internal topologies of the stiffeners and the thicknesses of the skin and stiffeners, and updated by optimizing them. As shown in Figs. 4.1(a) and 4.1(b), the positions, rotations and spacing of the stiffeners are represented and manipulated by their two ends' coordinates. The level set topology optimization methodology is used to optimize the internal topologies of the stiffeners. One LSF is used for the description of the internal topology of each stiffener. The relationship between the LSF values  $\Phi$  and the resulting structure is shown in Figs. 4.1(c) and 4.1(e), and Figs. 4.1(d) and 4.1(f). The skin and each of the stiffeners are considered to

## Simultaneous Sizing, Layout and Topology Optimization for Buckling and Postbuckling of Stiffened Panels

have the same thickness throughout. As shown in Figs. 4.1(g) and 4.1(h), the skin thickness and the thickness of each stiffener are denoted by  $t_p$  and  $t_{s,n}$  ( $n=1, 2, \dots, N$ , where  $N$  is number of stiffeners) and optimized as well.

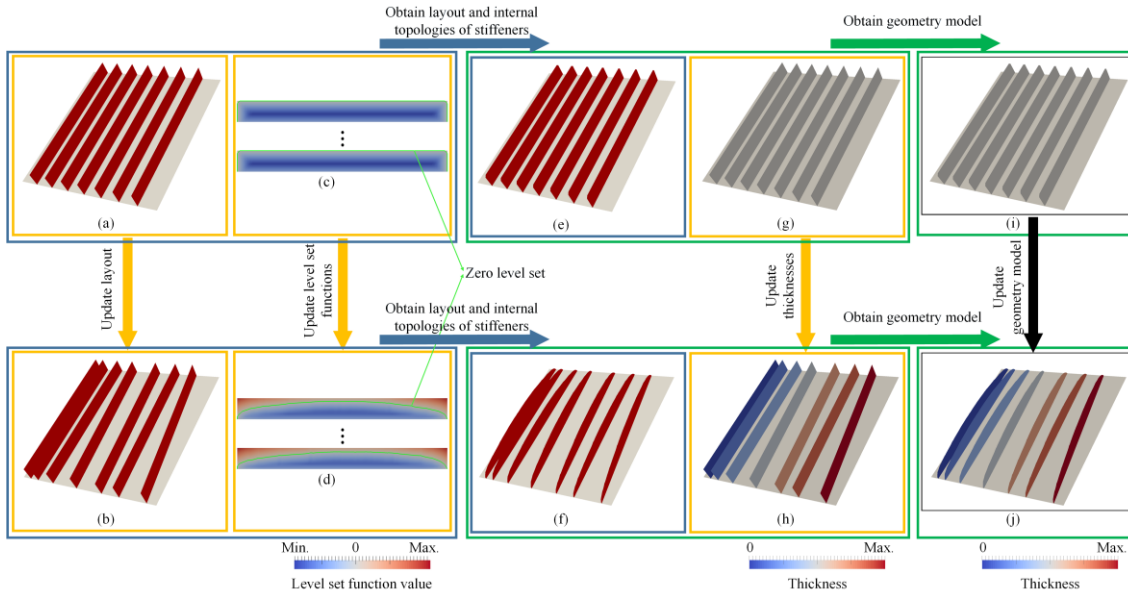


**Figure 4.1** Illustration of how to construct and update the geometric model of a sample stiffened panel: (a) the initial stiffened layout; (b) the updated stiffened layout; (c) the initial LSFs and their zero level set for the internal topologies of the stiffeners; (d) the updated LSFs and their zero level set for the internal topologies of the stiffeners; (e) the initial layout and internal topologies of the stiffeners; (f) the updated layout and internal topologies of the stiffeners; (g) the initial thickness distribution; (h) the updated thickness distribution; (i) the initial geometric model; (j) the updated geometric model.

### 4.1.2 Finite Element Model

#### 4.1.2.1 Modified Free-Form Mesh Deformation Method

In this study, both the skin and stiffeners are modeled explicitly using four-node mixed interpolation of tensorial components (MITC) plate elements with six degrees of freedom per node, comprising a Mindlin-Reissner plate element [91, 92] combined with a plane stress formulation. In the works in Chapter 3, the free-form mesh deformation method [90] was used to deform the FE mesh to account for the updated stiffener layout. As shown in Fig. 4.2, a control mesh is established. The  $x$  and  $y$  coordinates of nodes on the control mesh are equal to those of the two ends of the stiffeners or the

**Chapter 4: Simultaneous Sizing, Layout and Topology Optimization of Panels with Straight Stiffeners under Stress and Buckling Constraints**

panel vertices. As shown in Figs. 4.2(c) and 4.2(d), the optimal layout of the stiffeners can be obtained by optimizing the coordinates of the nodes on the control mesh. The FE mesh is deformed to cater for the updated stiffener layout:

$$\mathbf{x}_{FE} = \mathbf{N}\mathbf{x}_{control} \quad (4-1a)$$

$$\mathbf{x}_{control}^{k+1} = \mathbf{x}_{control}^k + \mathbf{y} \quad (4-1b)$$

$$\mathbf{x}_{FE}^{k+1} = \mathbf{x}_{FE}^k + \mathbf{z} \quad (4-1c)$$

$$\mathbf{z} = \mathbf{N}\mathbf{y} \quad (4-1d)$$

where  $\mathbf{x}_{FE}$  and  $\mathbf{x}_{control}$  are nodal coordinates on the FE and control meshes, respectively.  $\mathbf{z}$  and  $\mathbf{y}$  represent their changes.  $\mathbf{N}$  is the shape function.

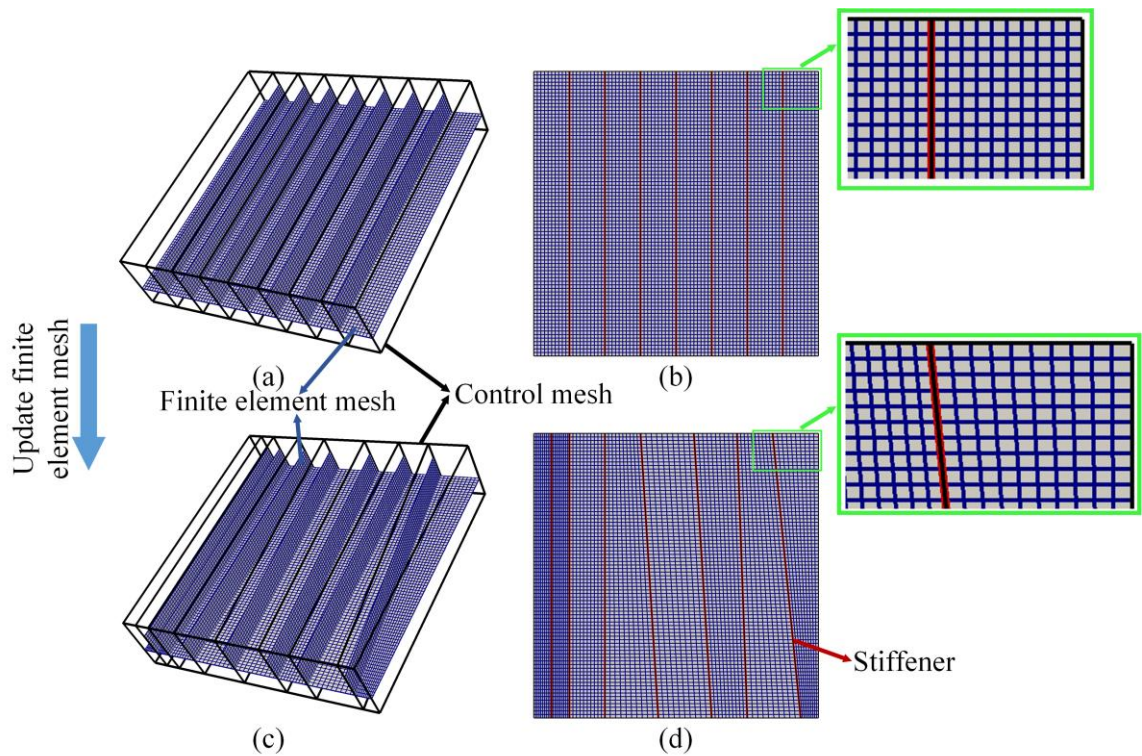


**Figure 4.2 Illustration of updating the finite element mesh using the free-form mesh deformation method with control mesh: (a) the initial finite element and control meshes; (b) top view of the initial finite element and control meshes; (c) the updated finite element and control meshes; (d) top view of the updated finite element and control meshes.**

**Simultaneous Sizing, Layout and Topology Optimization  
for Buckling and Postbuckling of Stiffened Panels**

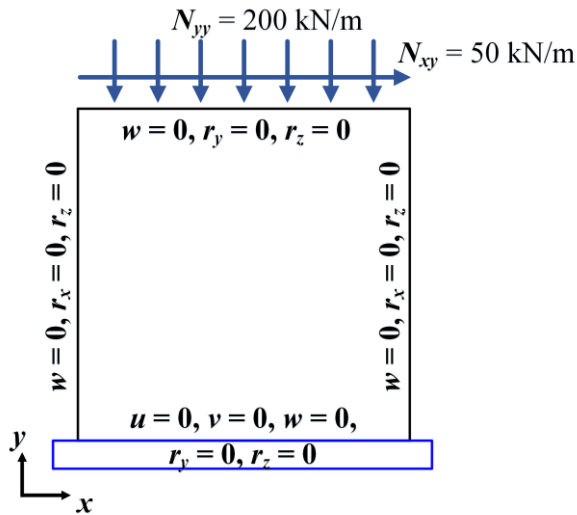


**Figure 4.3 Loading and boundary conditions for the design of a stiffened panel under combined compression and shear.**

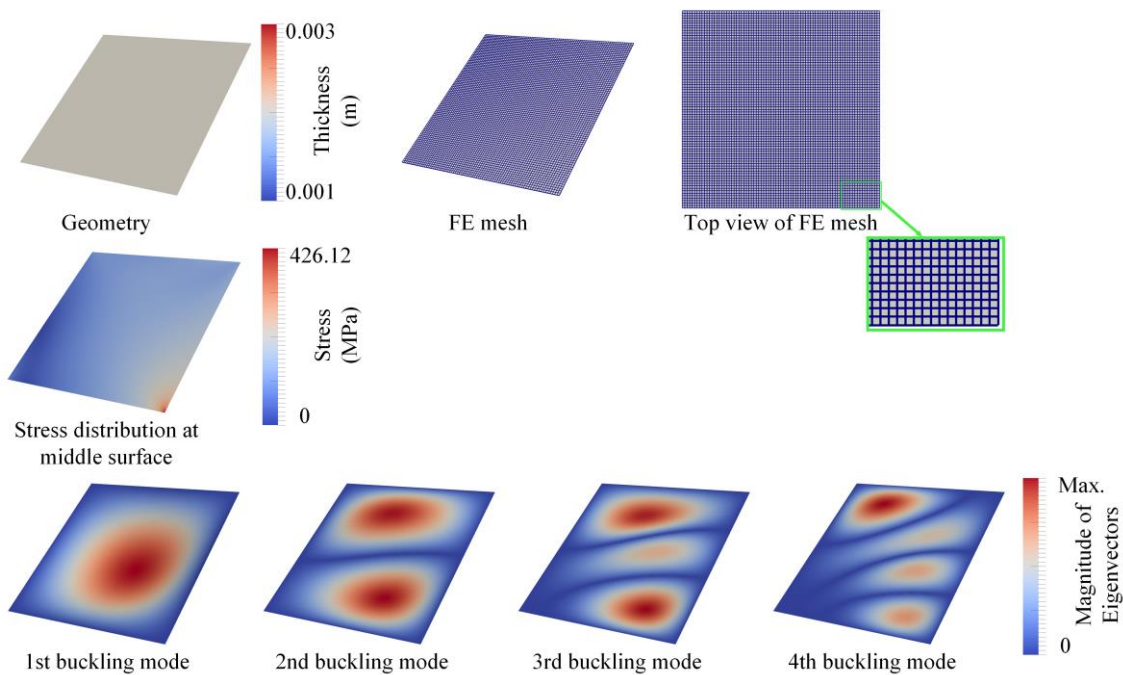


**Figure 4.4 Panel with the undeformed FE mesh, and its stress distribution at the middle surface and first four buckling modes under combined compression and shear,  $\sigma_{vm,m,max} = 426.12$  MPa,  $\lambda_1 = 0.1154$ ,  $\lambda_2 = 0.1717$ ,  $\lambda_3 = 0.2828$ ,  $\lambda_4 = 0.4191$ .**

Using the existing free-form mesh deformation method however can cause inaccuracies in the stress. This is demonstrated in the example shown in Fig. 4.3, where a stiffened panel of  $0.3 \text{ m} \times 0.3 \text{ m}$  is considered. The Young's modulus of the material is  $E = 73.085 \text{ GPa}$ . The Poisson's ratio is  $\nu = 0.33$ . As shown in Fig. 4.4, the panel is

#### Chapter 4: Simultaneous Sizing, Layout and Topology Optimization of Panels with Straight Stiffeners under Stress and Buckling Constraints

discretized uniformly with  $80 \times 80$  plate elements and its stress distribution at the middle surface and first four buckling modes are given.  $\sigma_{vm,m,max}$  is the maximum von Mises stress at the middle surface, which occurs at the bottom right-hand corner of the panel.  $\lambda_1 - \lambda_4$  are the first four buckling load factors. Figure 4.5 shows that the free-form mesh deformation method decreases  $\sigma_{vm,m,max}$  by 5.9%. This is because, the FE mesh is deformed to make the widths of the elements around the bottom right-hand corner of the panel larger. The distances between the central and Gauss points of these elements and the bottom right-hand vertex of the panel is thus increased.

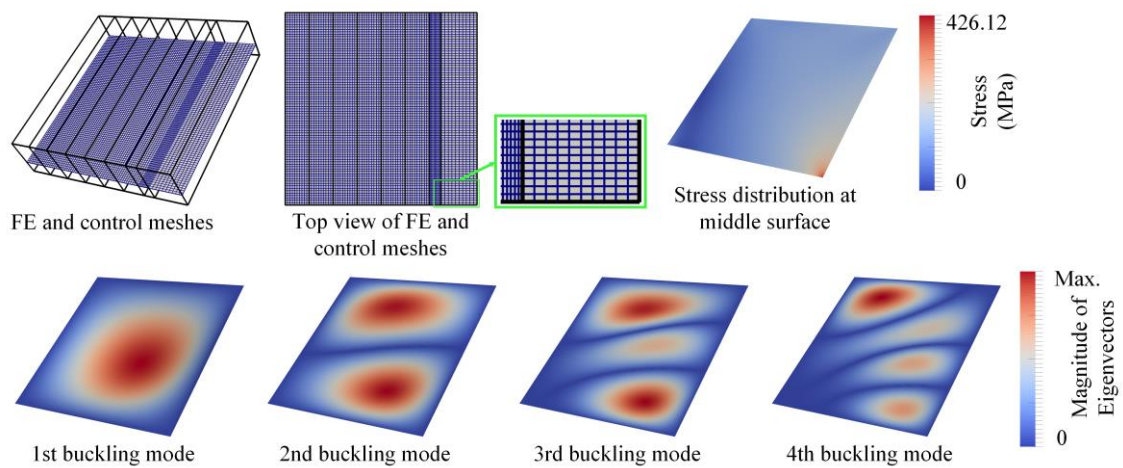


**Figure 4.5 Panel with the FE mesh using the free-form mesh deformation method with control mesh, and its stress distribution at the middle surface and first four buckling modes under combined compression and shear,  $\sigma_{vm,m,max} = 400.91$  MPa,  $\lambda_1 = 0.1154$ ,  $\lambda_2 = 0.1717$ ,  $\lambda_3 = 0.2828$ ,  $\lambda_4 = 0.4191$ .**

Due to this discrepancy, the optimizer attempts to decrease the maximum stress primarily by deforming the FE mesh and moving the stiffeners. Specifically, when the central and Gauss points move closer to the maximum stress location via moving the stiffeners, the stresses evaluated on these central and Gauss points can be increased and may then exceed the upper bound of the stress due to the effect of the mesh deformation on the stress computation instead of the structural stiffness variation caused by the stiffener movement. To ensure stresses remain below the upper limit, the optimizer needs to control the distances between the central and Gauss points and the maximum stress location, by keeping the stiffeners from approaching the maximum stress location, or even moving the stiffeners farther away. The maximum stress usually occurs around the stiffeners and panel edges. In order to minimize the effect of the mesh

**Simultaneous Sizing, Layout and Topology Optimization  
for Buckling and Postbuckling of Stiffened Panels**

deformation on the stress computation, the mesh deformation method is modified to maintain the size of the FEs in these regions to be unchanged during the optimization. Figure 4.6 shows the modified free-form mesh deformation method developed to achieve this. The element boundaries of the control mesh are placed on  $d$  FEs ( $d = 1$  in Fig. 4.6) away from the stiffeners or panel edges. As shown in Figs. 4.6(c) and 4.6(d), the movement of the element boundary of the control mesh is then the same as that of the nearest stiffeners or panel edges:

$$\mathbf{y} = \mathbf{A}\mathbf{y}_{\text{stiffener}} \quad (4-2)$$

where  $\mathbf{y}_{\text{stiffener}}$  represents the changes in the coordinates of the stiffener ends.  $\mathbf{A}$  is the mapping matrix.  $\mathbf{y}_{\text{stiffener}}$  is the design variables in the stiffener layout optimization, and the deformation of the FE mesh can be achieved through Eqs. (4-1c), (4-1d) and (4-2). Unlike in the case in Fig. 4.2, the widths of the FEs within  $d$  elements away from the stiffeners or panel edges now remain unchanged as the stiffener layout is updated.

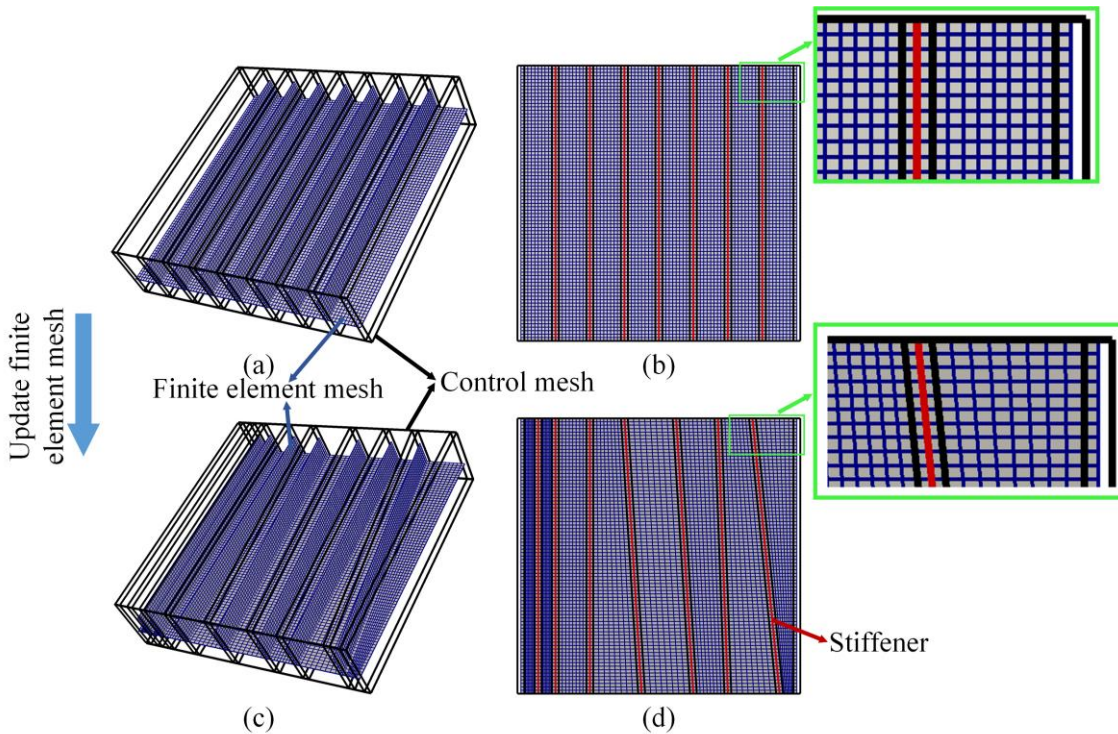


**Figure 4.6** Illustration of updating the finite element mesh using the modified free-form mesh deformation method with control mesh: (a) the initial finite element and control meshes; (b) top view of the initial finite element and control meshes; (c) the updated finite element and control meshes; (d) top view of the updated finite element and control meshes.

**Chapter 4: Simultaneous Sizing, Layout and Topology Optimization of Panels with Straight Stiffeners under Stress and Buckling Constraints**

For the panel shown in Fig. 4.3, the FE mesh in Fig. 4.4 is deformed (shown in Fig. 4.7) using the modified free-form mesh deformation method, with the same movements of “pseudo stiffeners” in Fig. 4.5. The discrepancy between the values of  $\sigma_{vm,m,max}$  for the two FE meshes in Figs. 4.4 and 4.7 is 0.36%. Compared with the result using the previous free-form mesh deformation method in Fig. 4.4, the discrepancy is reduced by 94%. This shows the effectiveness of the modified free-form mesh deformation method for stress computations. It is noted that, for both the original and modified free-form mesh deformation methods, the differences between  $\lambda_1 - \lambda_4$  are within 0.024%. To test the modified free-form mesh deformation method, different mesh sizes and values of the parameter  $d$  ( $d \geq 1$ ) have been used. It has been found that, for the same mesh size, the maximum difference between  $\sigma_{vm,m,max}$  for different values of  $d$  is 0.24% and the maximum difference between  $\lambda_1 - \lambda_4$  is 0.035%. Therefore, for the numerical examples in following sections,  $d = 1$  is used.

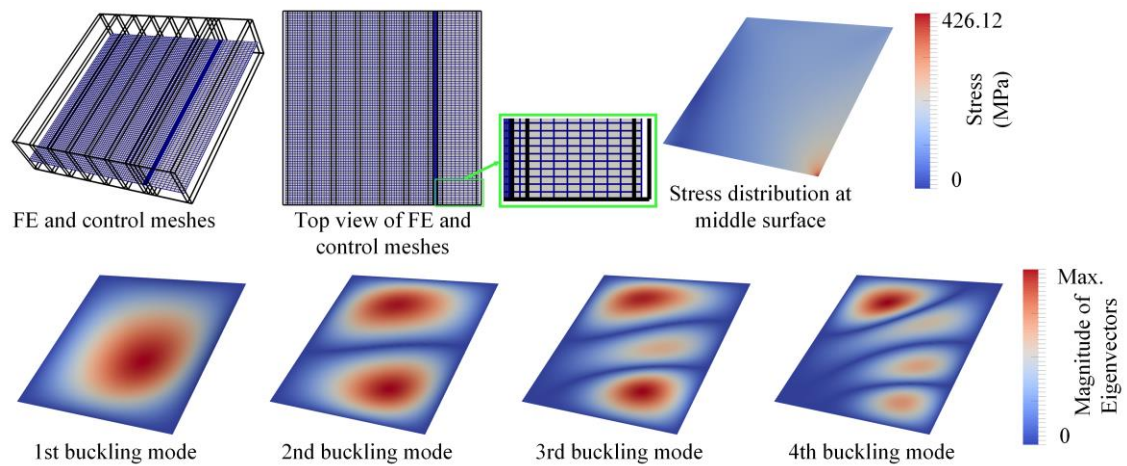


**Figure 4.7 Panel with the FE mesh using the modified free-form mesh deformation method with control mesh, and its stress distribution at the middle surface and first four buckling modes under combined compression and shear,  $\sigma_{vm,m,max} = 424.60$  MPa,  $\lambda_1 = 0.1154$ ,  $\lambda_2 = 0.1717$ ,  $\lambda_3 = 0.2828$ ,  $\lambda_4 = 0.4192$ .**

**Simultaneous Sizing, Layout and Topology Optimization  
for Buckling and Postbuckling of Stiffened Panels**

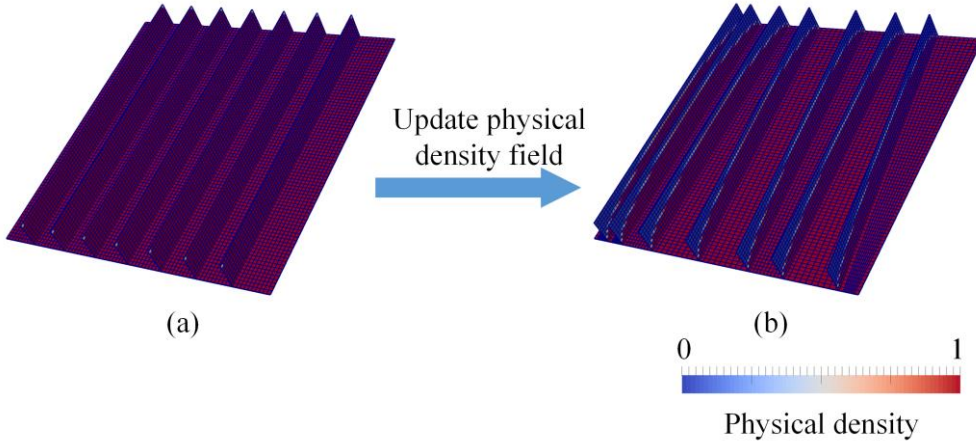


**Figure 4.8 Physical density field: (a) initial; (b) updated.**

As described in Section 3.1.2 and shown in Figs. 4.1(c) and 4.1(d), based on the undeformed mesh, it is straight forward to calculate the elemental density values  $\mathbf{w}^u$  for each stiffener. Due to the one-to-one correspondence between the elements of the undeformed and deformed FE meshes, shown in Figs. 4.8(a) and 4.8(b), a direct mapping can be used and the density distribution  $\mathbf{w}$  for the stiffener is obtained by  $w_j = v_j$ . The density distribution is  $\mathbf{w} = 1$  for all the elements on the skin.

After updating the nodal coordinates on the FE mesh and obtaining the elemental density and thickness distributions, the stiffness and geometric stiffness matrices for the  $j$ -th finite element can be calculated, as in Chapter 3:

$$K_j = w_j K_j^s(E_s, \rho_s, \nu, t_j, \mathbf{x}_{FE}) + (1 - w_j) K_j^v(E_v, \rho_v, \nu, t_j, \mathbf{x}_{FE}) \quad (4-3a)$$

$$K_{g,j} = w_j \left( \omega_j K_{g,j}^s(E_s, \rho_s, \nu, t_j, \mathbf{x}_{FE}) + (1 - \omega_j) K_{g,j}^v(E_v, \rho_v, \nu, t_j, \mathbf{x}_{FE}) \right) \quad (4-3b)$$

where  $K_j^s$  and  $K_j^v$  represent the stiffness matrices of the  $j$ -th finite element with solid and void phases, respectively.  $K_{g,j}^s$  and  $K_{g,j}^v$  denote the geometric stiffness matrices of the  $j$ -th finite element with solid and void phases, respectively.  $E_s$  and  $E_v$  are the Young's moduli of the  $j$ -th finite element with solid and void phases, respectively.  $\rho_s$  and  $\rho_v$  are the densities of the  $j$ -th finite element with solid and void phases, respectively.  $t_j$  is the thickness of the  $j$ -th finite element.  $\nu$  is Poisson's ratio.

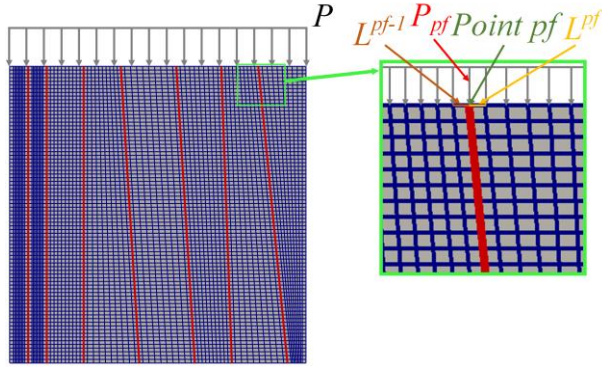


Figure 4.9 Illustration of the application of pressure.

When pressure is applied, the forces applied on the FE mesh are redistributed as the stiffener layout is updated. As shown in Fig. 4.9, the force applied to a point  $pf$  is calculated as:

$$P_{pf} = \frac{P(L^{pf-1} + L^{pf})}{2} \quad (4-4)$$

where  $P$  is the pressure value per unit length.  $L^{pf-1}$  and  $L^{pf}$  are the lengths of the elemental boundaries with the point  $pf$ .

To compute the displacement and buckling load factors of the stiffened panel, the linear elasticity and eigen-buckling equations in Eq. (4-5) are solved using the HSL MA57 solver [94] and ARPACK [95], respectively:

$$\mathbf{K}\mathbf{u} = \mathbf{f} \quad (4-5a)$$

$$(\mathbf{K} + \lambda\mathbf{K}_g(\mathbf{u}))\mathbf{v} = \mathbf{0} \quad (4-5b)$$

where  $\mathbf{K}$ ,  $\mathbf{u}$  and  $\mathbf{f}$  are the structural stiffness matrix, static deflection and applied load, respectively.  $\mathbf{K}_g$  is the geometric stiffness matrix.  $\lambda$  and  $\mathbf{v}$  represent the eigenvalue/eigenvector pair for buckling.

The von Mises stress of the element is calculated by:

$$\sigma_{vm} = \left( w_j \mathbf{u}_j^T \mathbf{Q}_{vm,j} \mathbf{u}_j \right)^{\frac{1}{2}} \quad (4-6)$$

where

**Simultaneous Sizing, Layout and Topology Optimization  
for Buckling and Postbuckling of Stiffened Panels**

$$\mathbf{Q}_{vm} = \int_A \mathbf{B}_b^T \mathbf{D}_b^T \mathbf{V} \mathbf{D}_b \mathbf{B}_b dA + \int_A \mathbf{B}_s^T \mathbf{C}_s^T \mathbf{V} \mathbf{C}_s \mathbf{B}_s dA + \int_A \mathbf{B}_m^T \mathbf{C}_m^T \mathbf{V} \mathbf{C}_m \mathbf{B}_m dA \quad (4-7a)$$

$$\mathbf{D}_b = z \mathbf{C}_b \quad (4-7b)$$

The notations  $\mathbf{C}_b$ ,  $\mathbf{C}_s$  and  $\mathbf{C}_m$  are the constitutive matrices for the bending, shear and membrane stresses, respectively.  $\mathbf{B}_b$ ,  $\mathbf{B}_s$  and  $\mathbf{B}_m$  are the relative strain–displacement matrices.  $A$  is the area of the element.  $\mathbf{V}$  is the Voigt matrix.  $z$  is the distance from the middle surface,  $-t/2 \leq z \leq t/2$ . The von Mises stresses  $\sigma_{vm,b}$ ,  $\sigma_{vm,m}$  and  $\sigma_{vm,t}$  of the element at the bottom, middle and top surfaces can be represented as:

$$\sigma_{vm,b} = \sigma_{vm} \Big|_{z=-h/2} \quad (4-8a)$$

$$\sigma_{vm,m} = \sigma_{vm} \Big|_{z=0} \quad (4-8b)$$

$$\sigma_{vm,t} = \sigma_{vm} \Big|_{z=h/2} \quad (4-8c)$$

## 4.2 Problem Formulation and Optimization Method

In this section, the problem considered in this work is described. To solve this problem with a gradient-based optimizer, a semi-analytical sensitivity analysis is performed. The optimization algorithm is also presented.

### 4.2.1 Problem Formulation

The minimum weight problem for stiffened panels subject to stress and buckling constraints can be written as:

$$\begin{aligned} & \min_{\mathbf{t}, \mathbf{y}_{\text{stiffener}}, \Phi} m(\mathbf{t}, \mathbf{y}_{\text{stiffener}}, \Phi) \\ \text{s.t. } & \sigma_{vm,b,j}(\mathbf{t}, \mathbf{y}_{\text{stiffener}}, \Phi) \leq \sigma_{\text{upper\_bound}}, \quad j = 1, 2, \dots, N_e \\ & \sigma_{vm,m,j}(\mathbf{t}, \mathbf{y}_{\text{stiffener}}, \Phi) \leq \sigma_{\text{upper\_bound}}, \quad j = 1, 2, \dots, N_e \\ & \sigma_{vm,t,j}(\mathbf{t}, \mathbf{y}_{\text{stiffener}}, \Phi) \leq \sigma_{\text{upper\_bound}}, \quad j = 1, 2, \dots, N_e \\ & \lambda_q(\mathbf{t}, \mathbf{y}_{\text{stiffener}}, \Phi) \geq \lambda_{\text{lower\_bound}}, \quad q = 1, 2, \dots, N_\lambda \\ & L_l(\mathbf{y}_{\text{stiffener}}) \geq L_{\text{lower\_bound}}, \quad l = 1, 2, \dots, N_L \end{aligned} \quad (4-9)$$

where  $\mathbf{t} = [t_p, t_{s,1}, \dots, t_{s,N}]^T$ ,  $\mathbf{y}_{\text{stiffener}}$  and  $\Phi = [\Phi_1, \dots, \Phi_N]^T$  are the sizing, layout and topology design variables, respectively.  $\sigma_{\text{upper\_bound}}$  is the upper bound of the von Mises

#### Chapter 4: Simultaneous Sizing, Layout and Topology Optimization of Panels with Straight Stiffeners under Stress and Buckling Constraints

stress.  $N_e$  is the number of the finite elements. The first  $N_\lambda$  buckling modes are considered and  $\lambda_{\text{lower\_bound}}$  is the lower bound of the critical buckling load factor. Since the modified free-form mesh deformation method is utilized to adaptively adjust the FE mesh, overlap and intersection between the adjacent stiffeners are prevented by setting the spacing constraints.  $L$  denotes stiffener spacing, and  $L_{\text{lower\_bound}}$  is its lower bound.  $N_L$  is the total number of spacing constraints. These have the effect of controlling the widths of the finite elements, which naturally avoids excessive element distortion.

The stiffener spacing  $L$  is controlled via the difference between the coordinates of the adjacent nodes on the control mesh:

$$L_l = x_{\text{control}}^{l+1} - x_{\text{control}}^l \quad (4-10)$$

As in Eq. (3-9), the mass  $m$  is defined by the mass matrix:

$$m = \mathbf{g}^T \mathbf{M} \mathbf{g} \quad (4-11)$$

where the vector  $\mathbf{g}$  contains ones for deflection degrees of freedom along the gravity direction and zeros elsewhere.

In Eq. (4-9), the von Mises stresses  $\sigma_{vm,b}$ ,  $\sigma_{vm,m}$  and  $\sigma_{vm,t}$  of each element at the bottom, middle and top surfaces are considered. In this work, the  $p$ -norm function is used as a stress aggregation to approximate the maximum stress:

$$\sigma_{pn} = \left( \sum_{j=1}^{N_e} \left( \sigma_{vm,b,j}^p + \sigma_{vm,m,j}^p + \sigma_{vm,t,j}^p \right) \right)^{1/p} \quad (4-12)$$

where  $p$  is a  $p$ -norm parameter. Since the  $p$ -norm is always greater than the maximum with finite  $p$ , the adaptive scaling constraint [61] is employed to enforce a constraint on the actual maximum stress:

$$\alpha \sigma_{pn} \leq \sigma_{\text{upper\_bound}} \quad (4-13)$$

where  $\alpha$  is computed at the  $k$ -th iteration:

$$\alpha^k = \frac{\max \left( \sigma_{vm,b,j}^{k-1}, \sigma_{vm,m,j}^{k-1}, \sigma_{vm,t,j}^{k-1} \right)}{\sigma_{pn}^{k-1}} \quad (4-14)$$

## Simultaneous Sizing, Layout and Topology Optimization for Buckling and Postbuckling of Stiffened Panels

Therefore, the optimization problem in Eq. (4-9) becomes:

$$\begin{aligned}
 & \min_{\mathbf{t}, \mathbf{y}_{\text{stiffener}}, \Phi} m(\mathbf{t}, \mathbf{y}_{\text{stiffener}}, \Phi) \\
 & s.t. \quad \alpha \sigma_{pn}(\mathbf{t}, \mathbf{y}_{\text{stiffener}}, \Phi) \leq \sigma_{\text{upper\_bound}} \\
 & \quad \lambda_q(\mathbf{t}, \mathbf{y}_{\text{stiffener}}, \Phi) \geq \lambda_{\text{lower\_bound}}, \quad q = 1, 2, \dots, N_\lambda \\
 & \quad L_l(\mathbf{y}_{\text{stiffener}}) \geq L_{\text{lower\_bound}}, \quad l = 1, 2, \dots, N_L
 \end{aligned} \tag{4-15}$$

### 4.2.2 Sensitivity Analysis

The gradient-based optimizer, IPOPT [97], is again used to solve the optimization problem described in Eq. (4-15). Therefore, the sensitivities of the mass  $m$ , the  $p$ -norm function of the von Mises stress  $\sigma_{pn}$ , the buckling load factor  $\lambda_q$  and the stiffener spacing  $L_l$  are required. A semi-analytical sensitivity analysis with the adjoint method is employed.

#### 4.2.2.1 Sensitivity Analysis for Layout Optimization

The derivative of  $m$  with respect to  $y_i$  can be calculated by:

$$\frac{\partial m}{\partial y_i} = \mathbf{g}^T \frac{\partial \mathbf{M}}{\partial y_i} \mathbf{g} \tag{4-16}$$

To calculate the sensitivity of  $\sigma_{pn}$ , the augmented Lagrangian functional for  $\sigma_{pn}$  is given by:

$$\Psi = \sigma_{pn} + \mathbf{u}_{ad,s}^T (\mathbf{K}\mathbf{u} - \mathbf{f}) \tag{4-17}$$

where  $\mathbf{u}_{ad,s}$  is the adjoint vector.

Differentiating Eq. (4-17):

**Chapter 4: Simultaneous Sizing, Layout and Topology Optimization of Panels with Straight Stiffeners under Stress and Buckling Constraints**

$$\begin{aligned}
\frac{\partial \Psi}{\partial y_i} = & \frac{1}{p} \sigma_{pn}^{1-p} \left( \sum_{j=1}^{N_e} \left( \frac{p}{2} \sigma_{vm,b,j}^{p-2} (2w_j \frac{\partial \mathbf{u}_j^T}{\partial y_i} \mathbf{Q}_{vm,b,j} \mathbf{u}_j + w_j \mathbf{u}_j^T \frac{\partial \mathbf{Q}_{vm,b,j}}{\partial y_i} \mathbf{u}_j) \right. \right. \\
& + \frac{p}{2} \sigma_{vm,m,j}^{p-2} (2w_j \frac{\partial \mathbf{u}_j^T}{\partial y_i} \mathbf{Q}_{vm,m,j} \mathbf{u}_j + w_j \mathbf{u}_j^T \frac{\partial \mathbf{Q}_{vm,m,j}}{\partial y_i} \mathbf{u}_j) \\
& + \left. \left. \frac{p}{2} \sigma_{vm,t,j}^{p-2} (2w_j \frac{\partial \mathbf{u}_j^T}{\partial y_i} \mathbf{Q}_{vm,t,j} \mathbf{u}_j + w_j \mathbf{u}_j^T \frac{\partial \mathbf{Q}_{vm,t,j}}{\partial y_i} \mathbf{u}_j) \right) \right) \\
& + \frac{\partial \mathbf{u}_{ad,s}^T}{\partial y_i} (\mathbf{K} \mathbf{u} - \mathbf{f}) + \mathbf{u}_{ad,s}^T \left( \frac{\partial \mathbf{K}}{\partial y_i} \mathbf{u} + \mathbf{K} \frac{\partial \mathbf{u}}{\partial y_i} - \frac{d\mathbf{f}}{dy_i} \right)
\end{aligned} \tag{4-18}$$

By collecting the terms with  $\partial \mathbf{u} / \partial y_i$  in Eq. (4-18) and setting them to zero, the derivative of the augmented Lagrangian functional for  $\sigma_{pn}$  with respect to  $y_i$  can be calculated by:

$$\begin{aligned}
\frac{\partial \Psi}{\partial y_i} = & \frac{1}{p} \sigma_{pn}^{1-p} \left( \sum_{j=1}^{N_e} \left( \frac{p}{2} \sigma_{vm,b,j}^{p-2} (w_j \mathbf{u}_j^T \frac{\partial \mathbf{Q}_{vm,b,j}}{\partial y_i} \mathbf{u}_j) + \frac{p}{2} \sigma_{vm,m,j}^{p-2} (w_j \mathbf{u}_j^T \frac{\partial \mathbf{Q}_{vm,m,j}}{\partial y_i} \mathbf{u}_j) \right. \right. \\
& + \left. \left. \frac{p}{2} \sigma_{vm,t,j}^{p-2} (w_j \mathbf{u}_j^T \frac{\partial \mathbf{Q}_{vm,t,j}}{\partial y_i} \mathbf{u}_j) \right) \right) + \mathbf{u}_{ad,s}^T \left( \frac{\partial \mathbf{K}}{\partial y_i} \mathbf{u} - \frac{d\mathbf{f}}{dy_i} \right)
\end{aligned} \tag{4-19}$$

where

$$\begin{aligned}
& \frac{1}{p} \sigma_{pn}^{1-p} \left( \sum_{j=1}^{N_e} \left( \frac{p}{2} \sigma_{vm,b,j}^{p-2} (2w_j \mathbf{Q}_{vm,b,j} \mathbf{u}_j) + \frac{p}{2} \sigma_{vm,m,j}^{p-2} (2w_j \mathbf{Q}_{vm,m,j} \mathbf{u}_j) \right. \right. \\
& + \left. \left. \frac{p}{2} \sigma_{vm,t,j}^{p-2} (2w_j \mathbf{Q}_{vm,t,j} \mathbf{u}_j) \right) \right) + \mathbf{K} \mathbf{u}_{ad,s} = 0
\end{aligned} \tag{4-20}$$

The derivative  $\partial \sigma_{pn} / \partial y_i$  is equivalent to  $\partial \Psi / \partial y_i$  in Eq. (4-19) due to the adjoint method.

As shown in Eq. (3-14), the sensitivity of  $\lambda_q$  is calculated as:

$$\frac{\partial \lambda_q}{\partial y_i} = \frac{\mathbf{u}_{ad,b}^T \left( \frac{\partial \mathbf{K}}{\partial y_i} \mathbf{u} - \frac{d\mathbf{f}}{dy_i} \right) - \mathbf{v}_q^T \left( \frac{\partial \mathbf{K}}{\partial y_i} + \lambda_q \frac{\partial \mathbf{K}_g(\mathbf{u})}{\partial y_i} \right) \mathbf{v}_q}{\mathbf{v}_q^T \mathbf{K}_g(\mathbf{u}) \mathbf{v}_q} \tag{4-21}$$

where  $\mathbf{u}_{ad,b}$  is the adjoint vector and

$$\lambda_q \mathbf{v}_q^T \frac{\partial \mathbf{K}_g(\mathbf{u})}{\partial \mathbf{u}} \mathbf{v}_q - \mathbf{u}_{ad,b}^T \mathbf{K} = 0 \tag{4-22}$$

It is noted that  $d\mathbf{f}/dy_i \neq 0$  in Eqs. (4-19) and (4-21). This is because, when the pressure is applied, the forces applied on points of the FE mesh are changed based on Eq. (4-4) as  $\mathbf{y}$

**Simultaneous Sizing, Layout and Topology Optimization  
for Buckling and Postbuckling of Stiffened Panels**

is updated. The sensitivities of  $m$ ,  $\sigma_{pn}$  and  $\lambda_q$  are analytically derived and given in Eqs. (4-16), (4-19) and (4-21). For simplicity,  $\partial\mathbf{M}/\partial y_i$ ,  $\mathbf{df}/dy_i$ ,  $\partial\mathbf{K}/\partial y_i$ , and  $\partial\mathbf{K}_g/\partial y_i$  are calculated via the finite difference method as is the derivative  $dL_l/dy_i$  for the spacing constraint.

#### 4.2.2.2 Sensitivity Analysis for Topology Optimization

As described in Eq. (3-18), to update the LSFs representing the stiffener internal topologies, derivatives with respect to the level set value of the boundary points  $\Phi_{n,b}$  are computed by:

$$\frac{\partial g}{\partial \Phi_{n,b}} = \sum_j \frac{\partial g}{\partial w_j} \frac{\partial w_j}{\partial v_j} \frac{\partial v_j}{\partial \Phi_{n,b}} \quad (4-23)$$

where  $\partial w_j/\partial v_j = 1$  because  $w_j = v_j$ . The function  $g$  represents an equation, i.e.  $m$ ,  $\sigma_{pn}$ ,  $\lambda_q$  and  $L_l$ .  $dL_l/dw_j = 0$ .

The derivative of  $m$  with respect to  $w_j$  is calculated by:

$$\frac{\partial m}{\partial w_j} = \mathbf{g}^T \frac{\partial \mathbf{M}}{\partial w_j} \mathbf{g} \quad (4-24)$$

In a similar way to the computation of  $\partial\sigma_{pn}/\partial y_i$ , the derivative of  $\sigma_{pn}$  with respect to  $w_j$  is obtained by:

$$\begin{aligned} \frac{\partial \sigma_{pn}}{\partial w_j} = & \frac{1}{p} \sigma_{pn}^{1-p} \left( \left( \frac{p}{2} \sigma_{vm,b,j}^{p-2} (\mathbf{u}_j^T \mathbf{Q}_{vm,b,j} \mathbf{u}_j) + \frac{p}{2} \sigma_{vm,m,j}^{p-2} (\mathbf{u}_j^T \mathbf{Q}_{vm,m,j} \mathbf{u}_j) \right. \right. \\ & \left. \left. + \frac{p}{2} \sigma_{vm,t,j}^{p-2} (\mathbf{u}_j^T \mathbf{Q}_{vm,t,j} \mathbf{u}_j) \right) \right) + \mathbf{u}_{ad,s}^T \frac{\partial \mathbf{K}}{\partial w_j} \mathbf{u} \end{aligned} \quad (4-25)$$

In a similar way to the computation of  $\partial\lambda_q/\partial y_i$ , the derivative of  $\lambda_q$  with  $w_j$  is obtained by:

$$\frac{\partial \lambda_q}{\partial w_j} = \frac{\mathbf{u}_{ad,b}^T \frac{\partial \mathbf{K}}{\partial w_j} \mathbf{u} - \mathbf{v}_q^T \left( \frac{\partial \mathbf{K}}{\partial w_j} + \lambda_q \frac{\partial \mathbf{K}_g(\mathbf{u})}{\partial w_j} \right) \mathbf{v}_q}{\mathbf{v}_q^T \mathbf{K}_g(\mathbf{u}) \mathbf{v}_q} \quad (4-26)$$

As described in Section 3.2.2.2, in this work, the LSFs are always maintained as signed distance functions by a combination of the marching squares and fast marching

**Chapter 4: Simultaneous Sizing, Layout and Topology Optimization of Panels with Straight Stiffeners under Stress and Buckling Constraints**

algorithms [86]. In order to ensure the signed distance property  $|\nabla\Phi|=1$  after every update of the LSF, the fast velocity extension algorithm [96] is utilized. The relationship between the changes to the LSF values  $\Delta\Phi_{n,b}$  at the boundary and  $\Delta\Phi_n$  in the rest of the design domain is determined as:

$$\Delta\Phi_n = \left[ \frac{\partial\Phi_n}{\partial\Phi_{n,b}} \right] \Delta\Phi_{n,b}, \quad n = 1, 2, \dots, N \quad (4-27)$$

Then the term  $\partial v_j / \partial \Phi_{n,b}$  can be computed via the implicit perturbation of the level set boundary. Specifically, a small perturbation  $\Delta\Phi_{n,b}$  is assigned to the level set value  $\Phi_{n,b}$  of the given boundary point of interest. Then the changes in the LSF  $\Delta\Phi_n$  in the rest of the design domain can be obtained using Eq. (4-27). After implementing the marching squares and fast marching algorithms, the new LSF and corresponding zero level set are obtained. This results in the new volume fraction  $v_j$ . Then the term  $\partial v_j / \partial \Phi_{n,b}$  can be approximated by the finite difference method.

#### 4.2.2.3 Sensitivity Analysis for sizing Optimization

To implement the sizing optimization and update the thickness distribution of the stiffened panel, derivatives with respect to  $\mathbf{t}$  are computed through the chain rule:

$$\frac{\partial g}{\partial t_p} = \sum_j \frac{\partial g}{\partial t_j} \frac{\partial t_j}{\partial t_p} \quad (4-28a)$$

$$\frac{\partial g}{\partial t_{s,n}} = \sum_j \frac{\partial g}{\partial t_j} \frac{\partial t_j}{\partial t_{s,n}}, \quad n = 1, 2, \dots, N \quad (4-28b)$$

where

$$\frac{\partial t_j}{\partial t_p} = \begin{cases} 1 & \text{when the } j\text{-th element belongs to the panel} \\ 0 & \text{when the } j\text{-th element does not belong to the panel} \end{cases} \quad (4-29a)$$

$$\frac{\partial t_j}{\partial t_{s,n}} = \begin{cases} 1 & \text{when the } j\text{-th element belongs to the } n\text{-th stiffener} \\ 0 & \text{when the } j\text{-th element does not belong to the } n\text{-th stiffener} \end{cases}, \quad n = 1, 2, \dots, N \quad (4-29b)$$

Similarly,

**Simultaneous Sizing, Layout and Topology Optimization  
for Buckling and Postbuckling of Stiffened Panels**

$$\frac{\partial m}{\partial t_j} = \mathbf{g}^T \frac{\partial \mathbf{M}}{\partial t_j} \mathbf{g} \quad (4-30a)$$

$$\begin{aligned} \frac{\partial \sigma_{pn}}{\partial t_j} = & \frac{1}{p} \sigma_{pn}^{1-p} \left( \left( \frac{p}{2} \sigma_{vm,b,j}^{p-2} (w_j \mathbf{u}_j^T \frac{\partial \mathbf{Q}_{vm,b,j}}{\partial t_j} \mathbf{u}_j) + \frac{p}{2} \sigma_{vm,m,j}^{p-2} (w_j \mathbf{u}_j^T \frac{\partial \mathbf{Q}_{vm,m,j}}{\partial t_j} \mathbf{u}_j) \right. \right. \\ & \left. \left. + \frac{p}{2} \sigma_{vm,t,j}^{p-2} (w_j \mathbf{u}_j^T \frac{\partial \mathbf{Q}_{vm,t,j}}{\partial t_j} \mathbf{u}_j) \right) \right) + \mathbf{u}_{ad,s}^T \frac{\partial \mathbf{K}}{\partial w_j} \mathbf{u} \end{aligned} \quad (4-30b)$$

$$\frac{\partial \lambda_q}{\partial t_j} = \frac{\mathbf{u}_{ad,b}^T \frac{\partial \mathbf{K}}{\partial t_j} \mathbf{u} - \mathbf{v}_q^T \left( \frac{\partial \mathbf{K}}{\partial t_j} + \lambda_q \frac{\partial \mathbf{K}_g(\mathbf{u})}{\partial t_j} \right) \mathbf{v}_q}{\mathbf{v}_q^T \mathbf{K}_g(\mathbf{u}) \mathbf{v}_q} \quad (4-30c)$$

$$\frac{\partial L_l}{\partial t_j} = 0 \quad (4-30d)$$

### 4.2.3 Optimization Algorithm

Linearization of the optimization problem in Eq. (4-15) using Taylor's expansion yields:

$$\begin{aligned} \min_{\Delta \mathbf{t}, \Delta \mathbf{y}_{\text{stiffener}}, \Delta \Phi_b} & \left( m_0 + \left[ \frac{\partial m}{\partial \mathbf{t}} \right]^T \Delta \mathbf{t} + \left[ \frac{\partial m}{\partial \mathbf{y}_{\text{stiffener}}} \right]^T \Delta \mathbf{y}_{\text{stiffener}} + \left[ \frac{\partial m}{\partial \Phi_b} \right]^T \Delta \Phi_b \right) \\ \text{s.t.} & \left( \sigma_{pn,0} + \left[ \frac{\partial \sigma_{pn}}{\partial \mathbf{t}} \right]^T \Delta \mathbf{t} + \left[ \frac{\partial \sigma_{pn}}{\partial \mathbf{y}_{\text{stiffener}}} \right]^T \Delta \mathbf{y}_{\text{stiffener}} + \left[ \frac{\partial \sigma_{pn}}{\partial \Phi_b} \right]^T \Delta \Phi_b \right) \geq \sigma_{\text{upper\_bound}} \\ & \lambda_{q,0} + \left[ \frac{\partial \lambda_q}{\partial \mathbf{t}} \right]^T \Delta \mathbf{t} + \left[ \frac{\partial \lambda_q}{\partial \mathbf{y}_{\text{stiffener}}} \right]^T \Delta \mathbf{y}_{\text{stiffener}} + \left[ \frac{\partial \lambda_q}{\partial \Phi_b} \right]^T \Delta \Phi_b \geq \lambda_{\text{lower\_bound}}, \quad q = 1, 2, \dots, N_\lambda \\ & L_{l,0} + \left[ \frac{dL_l}{d\mathbf{y}_{\text{stiffener}}} \right]^T \Delta \mathbf{y}_{\text{stiffener}} \geq L_{\text{lower\_bound}}, \quad l = 1, 2, \dots, N_L \\ & -\gamma_1 \leq \Delta \mathbf{t} \leq \gamma_1 \\ & -\gamma_2 \leq \Delta \mathbf{y}_{\text{stiffener}} \leq \gamma_2 \\ & -\gamma_3 \leq \Delta \Phi_b \leq \gamma_3 \end{aligned} \quad (4-31)$$

where  $m_0$ ,  $\sigma_{pn,0}$ ,  $\lambda_{q,0}$  and  $L_{l,0}$  are the values at the current iteration.  $\gamma_1$ ,  $\gamma_2$  and  $\gamma_3$  are the move limits for  $\Delta \mathbf{t}$ ,  $\Delta \mathbf{y}_{\text{stiffener}}$  and  $\Delta \Phi_b$ , respectively. IPOPT [97] is used to solve the

**Chapter 4: Simultaneous Sizing, Layout and Topology Optimization of Panels with Straight Stiffeners under Stress and Buckling Constraints**

optimization problem in Eq. (4-31) at each iteration to obtain  $\Delta \mathbf{t}$ ,  $\Delta \mathbf{y}_{\text{stiffener}}$  and  $\Delta \Phi_b$  to update the stiffened panels.

The optimization methodology is illustrated in Fig. 4.10.  $\mathbf{t}$ ,  $\mathbf{y}_{\text{stiffener}}$  and  $\Phi$  are optimized simultaneously.

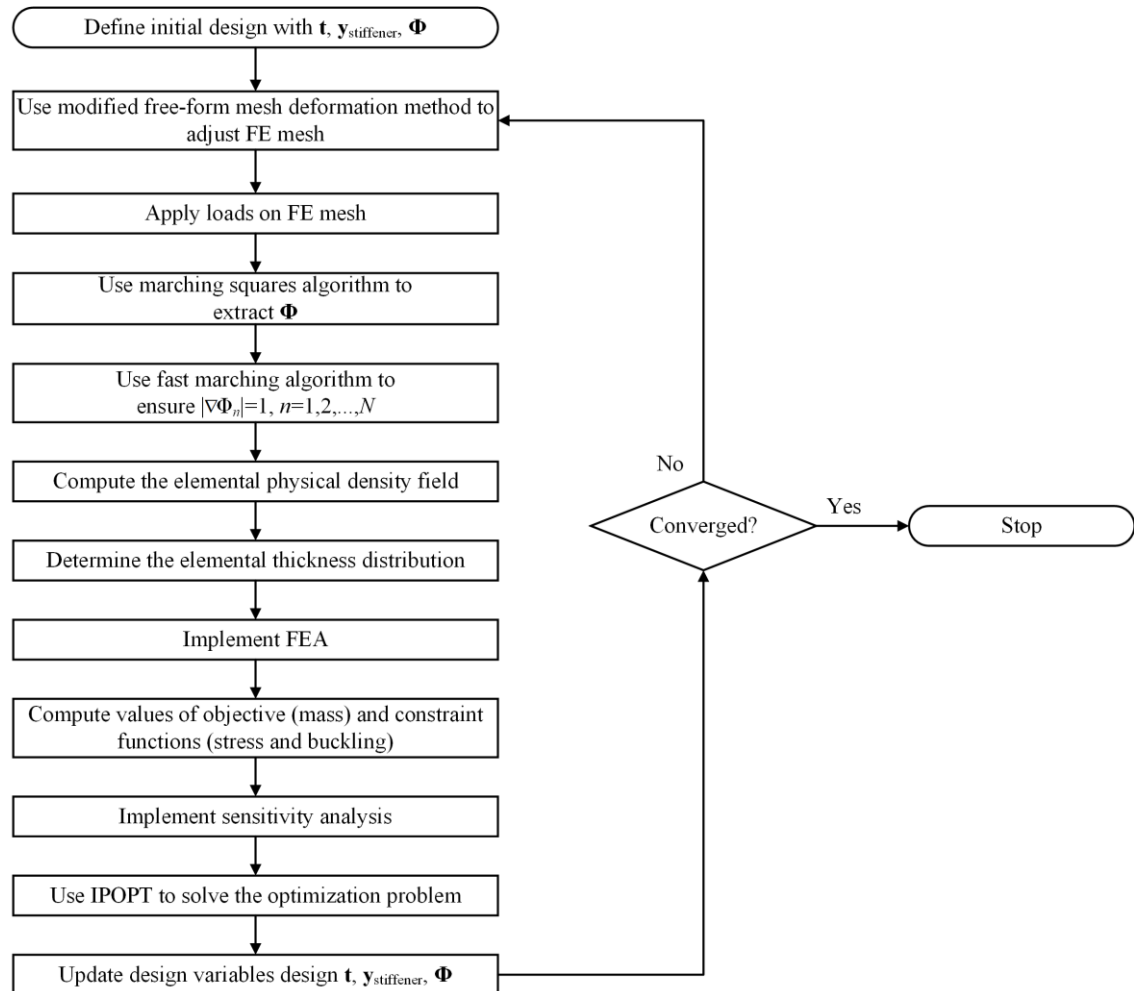


**Figure 4.10 Flowchart of the level set based stiffened panel optimization method.**

### 4.3 Numerical Examples

Two numerical examples are presented to demonstrate and validate the optimization method. In these examples, the aluminum alloy, Al 2139, is used. Young’s moduli of the solid material and void phases are  $E_s = 73.085$  GPa and  $E_v = 10^{-6} \times 73.085$  GPa, respectively. The densities are  $\rho_s = 2700$  kg/m<sup>3</sup> and  $\rho_v = 0$  for the solid material and void phase, respectively. Poisson’s ratio is  $\nu = 0.33$ .

### 4.3.1 Stiffened Panel under Compression and Shear

A stiffened panel of  $0.3 \text{ m} \times 0.3 \text{ m}$  with the loading and boundary conditions shown in Fig. 4.3 is considered for optimization. The lower and upper bounds of the thicknesses of both the skin and the stiffeners are  $0.001 \text{ m}$  and  $0.003 \text{ m}$ , respectively. The upper bound of the von Mises stress  $\sigma_{\text{upper\_bound}} = 427.5 \text{ MPa}$  [9]. The lower bound of the critical buckling load factor is  $\lambda_{\text{lower\_bound}} = 1$ . The lower bound of the stiffener spacing  $L_{\text{min}} = 7.5 \text{ mm}$ .

The initial design with seven vertical stiffeners, each with a height of  $0.03 \text{ m}$ , is given in Fig. 4.11. The initial thicknesses are set to  $0.002 \text{ m}$  for both the skin and the stiffeners. The skin is discretized with  $80 \times 80$  plate elements, with 8 elements along the height of the stiffeners. Seven level set functions are used to represent the seven stiffeners.  $\sigma_{\text{vm,b,max}}$ ,  $\sigma_{\text{vm,m,max}}$  and  $\sigma_{\text{vm,t,max}}$  are the maximum von Mises stresses of elements at the bottom, middle and top surfaces, respectively.  $p = 12$  is used for Eq. (4-12). Based on the work in Chapter 3, the first 10 buckling modes are considered as constraints.

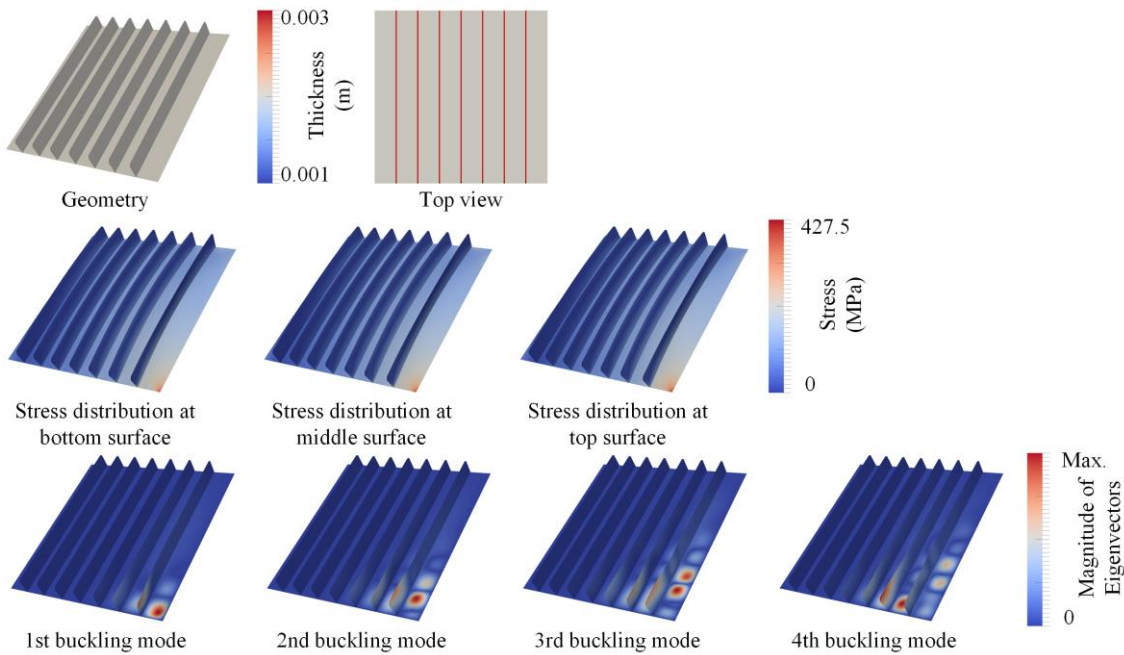


**Figure 4.11 Initial design with seven vertical stiffeners,  $m = 0.826 \text{ kg}$ , and its stress distributions and first four buckling modes under combined compression and shear,  $\sigma_{\text{vm,b,max}} = 375.5 \text{ MPa}$ ,  $\sigma_{\text{vm,m,max}} = 387.1 \text{ MPa}$ ,  $\sigma_{\text{vm,t,max}} = 401.9 \text{ MPa}$ ,  $\lambda_1 = 3.822$ ,  $\lambda_2 = 4.767$ ,  $\lambda_3 = 5.395$ ,  $\lambda_4 = 5.700$ .**

**Chapter 4: Simultaneous Sizing, Layout and Topology Optimization of Panels with Straight Stiffeners under Stress and Buckling Constraints**

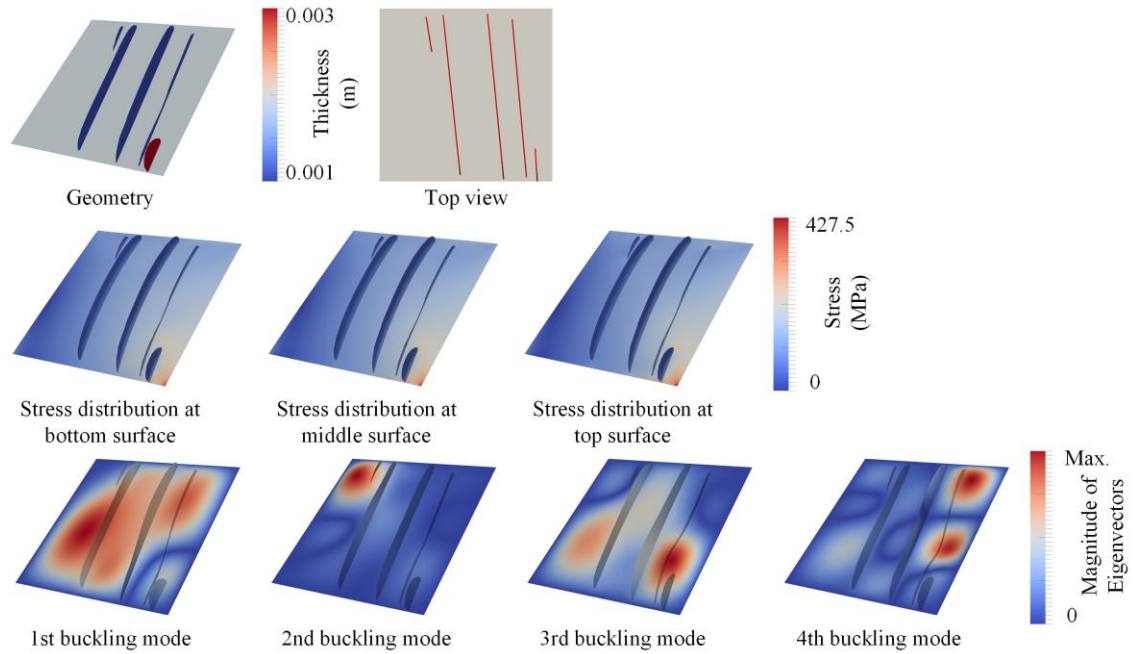


**Figure 4.12 Optimized design ( $\sigma_{\text{upper\_bound}} = 427.5$  MPa and  $\lambda_{\text{lower\_bound}} = 1$ ),  $m = 0.507$  kg, and its stress distributions and first four buckling modes under combined compression and shear,  $\sigma_{\text{vm,b,max}} = 398.9$  MPa,  $\sigma_{\text{vm,m,max}} = 411.2$  MPa,  $\sigma_{\text{vm,t,max}} = 427.3$  MPa,  $\lambda_1 = 1.001$ ,  $\lambda_2 = 1.013$ ,  $\lambda_3 = 1.038$ ,  $\lambda_4 = 1.119$ .**

From the initial design and its buckling modes in Fig. 4.11, it can be seen that buckling occurs towards the bottom right-hand corner of the panel. The optimized design is given in Fig. 4.12, with the convergence curves in Fig. 4.13. In Fig. 4.12, it can be seen that the number of stiffeners is optimized to three diagonal stiffeners with two short stiffeners. The layout optimization places the stiffeners to the right-hand side of the structure to increase the stiffness in this region. Meanwhile, with the topology and sizing optimization, the internal topology, height and width of the remaining stiffeners are optimized as well as their thicknesses. As a result, the buckling modes are less localized than those of the initial design while the mass of the optimized design is decreased by 38.6%. Both the stress and buckling constraints are satisfied.

### Simultaneous Sizing, Layout and Topology Optimization for Buckling and Postbuckling of Stiffened Panels

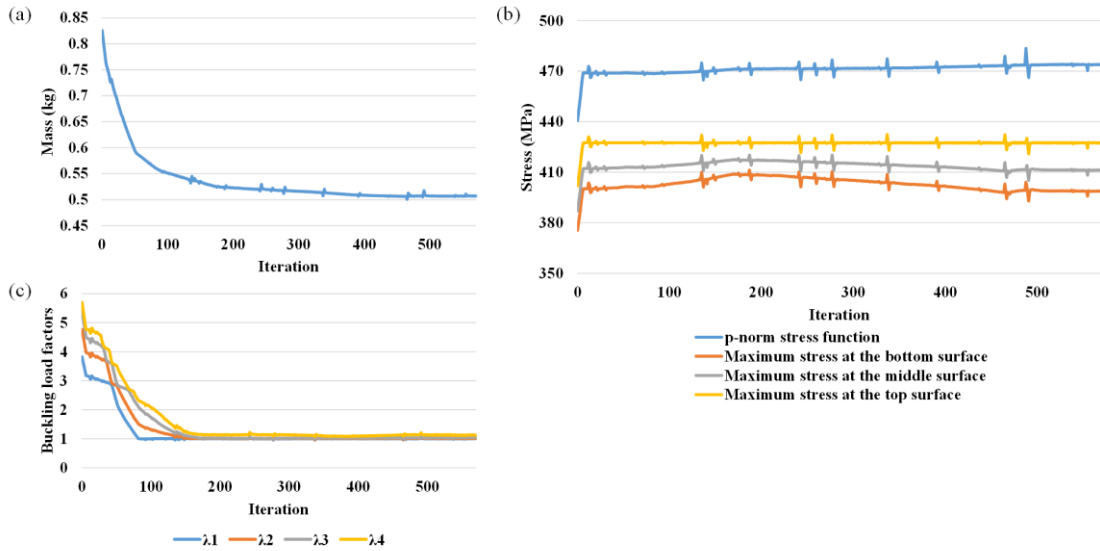


**Figure 4.13 Convergence curves: (a) mass; (b)  $p$ -norm stress function and maximum stresses at the bottom, middle and top surfaces; (c) buckling load factors.**

To investigate the effect of the stress constraint on the optimized design, the optimization problem is solved again with different upper bounds and without a stress constraint. The buckling constraints are still set with  $\lambda_{\text{lower\_bound}} = 1$ . The optimized designs are given in Figs. 4.14-4.16. The comparison is given in Table 4.1. For all the optimized designs, the stress and buckling constraints are satisfied. The stress is concentrated at the bottom right-hand corner of the panel. As  $\sigma_{\text{upper\_bound}}$  increases, the thickness and the stiffness of the skin are decreased. Correspondingly, more stiffeners are needed to resist the buckling and ensure the buckling constraint is satisfied.

**Chapter 4: Simultaneous Sizing, Layout and Topology Optimization of Panels with Straight Stiffeners under Stress and Buckling Constraints**

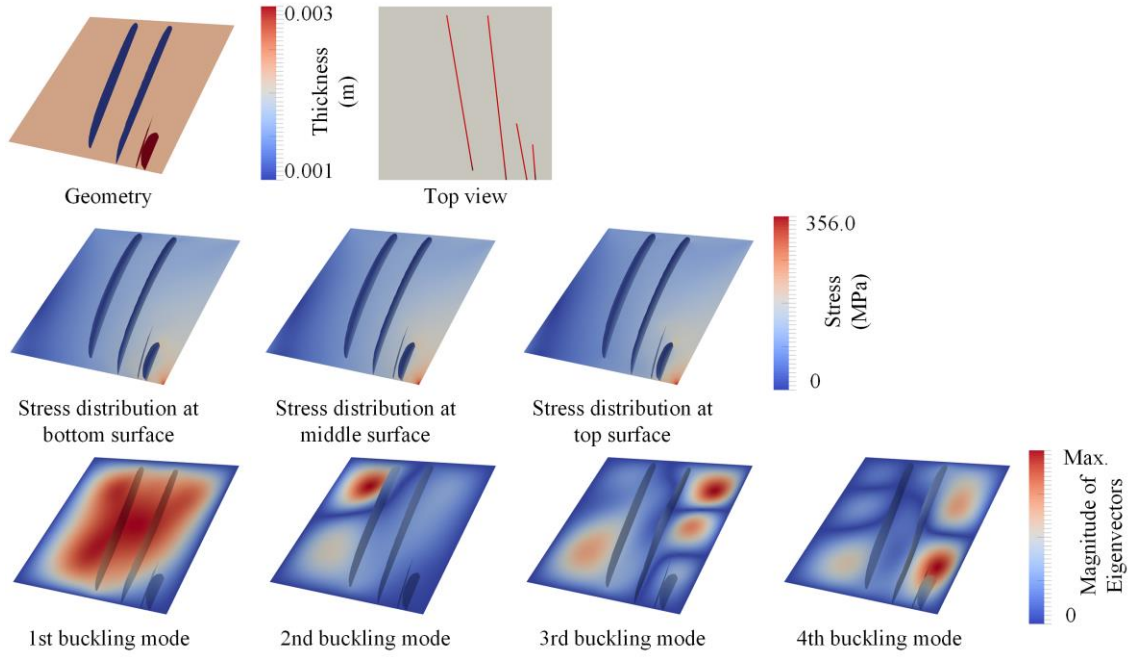


**Figure 4.14 Optimized design ( $\sigma_{upper\_bound} = 356 \text{ MPa}$  and  $\lambda_{lower\_bound} = 1$ ),  $m = 0.594 \text{ kg}$ , and its stress distributions and first four buckling modes under combined compression and shear,  $\sigma_{vm,b,max} = 330.7 \text{ MPa}$ ,  $\sigma_{vm,m,max} = 341.6 \text{ MPa}$ ,  $\sigma_{vm,t,max} = 356.0 \text{ MPa}$ ,  $\lambda_1 = 1.007$ ,  $\lambda_2 = 1.152$ ,  $\lambda_3 = 1.304$ ,  $\lambda_4 = 1.399$ .**

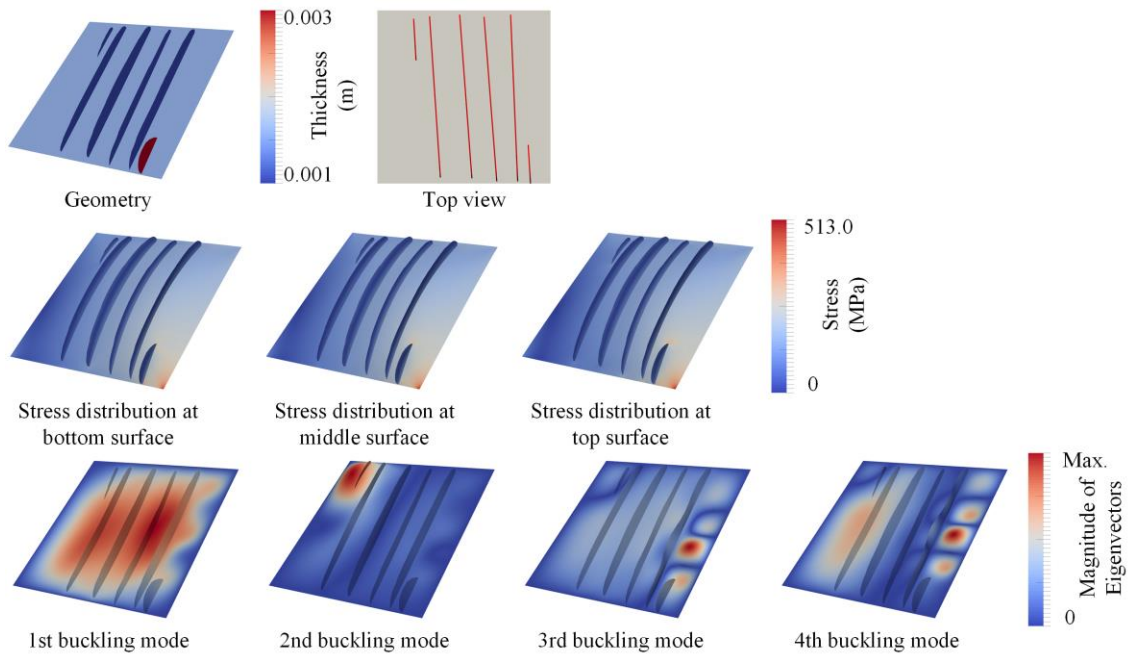


**Figure 4.15 Optimized design ( $\sigma_{upper\_bound} = 513 \text{ MPa}$  and  $\lambda_{lower\_bound} = 1$ ),  $m = 0.443 \text{ kg}$ , and its stress distributions and first four buckling modes under combined compression and shear,  $\sigma_{vm,b,max} = 481.4 \text{ MPa}$ ,  $\sigma_{vm,m,max} = 495.3 \text{ MPa}$ ,  $\sigma_{vm,t,max} = 512.9 \text{ MPa}$ ,  $\lambda_1 = 1.004$ ,  $\lambda_2 = 1.007$ ,  $\lambda_3 = 1.013$ ,  $\lambda_4 = 1.052$ .**

**Simultaneous Sizing, Layout and Topology Optimization  
for Buckling and Postbuckling of Stiffened Panels**

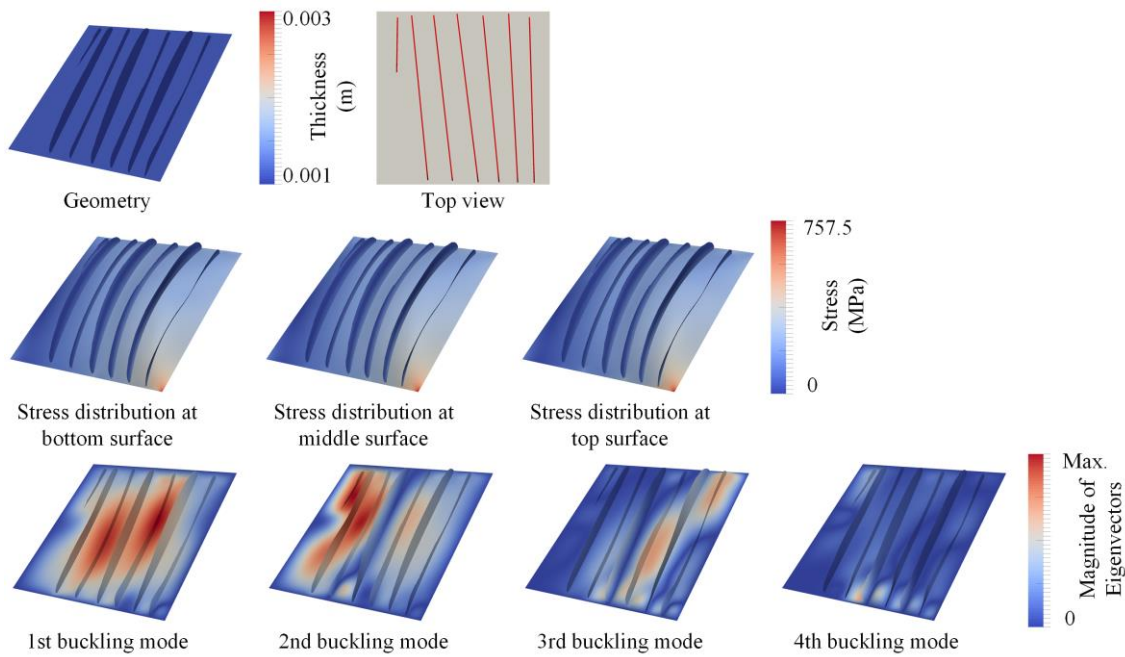


**Figure 4.16** Optimized design (without stress constraint and  $\lambda_{\text{lower\_bound}} = 1$ ),  $m = 0.341$  kg, and its stress distributions and first four buckling modes under combined compression and shear,  $\sigma_{\text{vm,b,max}} = 696.1$  MPa,  $\sigma_{\text{vm,m,max}} = 722.1$  MPa,  $\sigma_{\text{vm,t,max}} = 757.5$  MPa,  $\lambda_1 = 1.001$ ,  $\lambda_2 = 1.006$ ,  $\lambda_3 = 1.018$ ,  $\lambda_4 = 1.024$ .

**Table 4.1** Comparison of the optimized results with different stress constraints and without a stress constraint.

$\sigma_{\text{upper\_bound}}$ (MPa)	$\lambda_{\text{lower\_bound}}$	$m$ (kg)	$\sigma_{\text{vm,b,max}}$ (MPa)	$\sigma_{\text{vm,m,max}}$ (MPa)	$\sigma_{\text{vm,t,max}}$ (MPa)	$\lambda_1$	$\lambda_2$	$\lambda_3$	$\lambda_4$
356	1	0.594	330.7	341.6	356.0	1.007	1.152	1.304	1.399
427.5	1	0.507	398.8	411.2	427.3	1.001	1.013	1.038	1.119
513	1	0.443	481.4	495.3	512.9	1.004	1.007	1.013	1.052
No stress constraint	1	0.341	696.1	722.1	757.5	1.001	1.006	1.018	1.024

To investigate the effect of the buckling constraints on the optimized design, the problem is also solved with buckling constraints with different lower bounds. The stress constraint is set with  $\sigma_{\text{upper\_bound}} = 427.5$  MPa. The optimized designs are given in Figs. 4.17 and 4.18. The comparison is given in Table 4.2. For the optimized designs with  $\lambda_{\text{lower\_bound}} = 1, 2$  and  $3$  in Figs. 4.12, 4.17 and 4.18, their skin thicknesses are  $1.886 \times 10^{-3}$  m,  $1.874 \times 10^{-3}$  m and  $1.865 \times 10^{-3}$  m, respectively. The difference is within 1.1%.

#### Chapter 4: Simultaneous Sizing, Layout and Topology Optimization of Panels with Straight Stiffeners under Stress and Buckling Constraints

As  $\lambda_{\text{lower\_bound}}$  increases, more stiffeners remain in the optimized design. This shows that, the impact of the buckling constraints on the stiffeners is greater than that on the skin.

Further optimization problems including (a) sizing optimization only, (b) sizing and layout optimization, (c) topology optimization only, (d) sizing and topology optimization and (e) layout and topology optimization, are also solved for the design of the stiffened panel. In each case the stress and buckling constraints are set with  $\sigma_{\text{upper\_bound}} = 427.5$  MPa and  $\lambda_{\text{lower\_bound}} = 1$ , respectively. Figure 4.19 shows the optimized designs. All of their stress and buckling constraints are satisfied. From Table 4.3, however, it can be seen that their masses are all greater than that in Fig. 4.12.

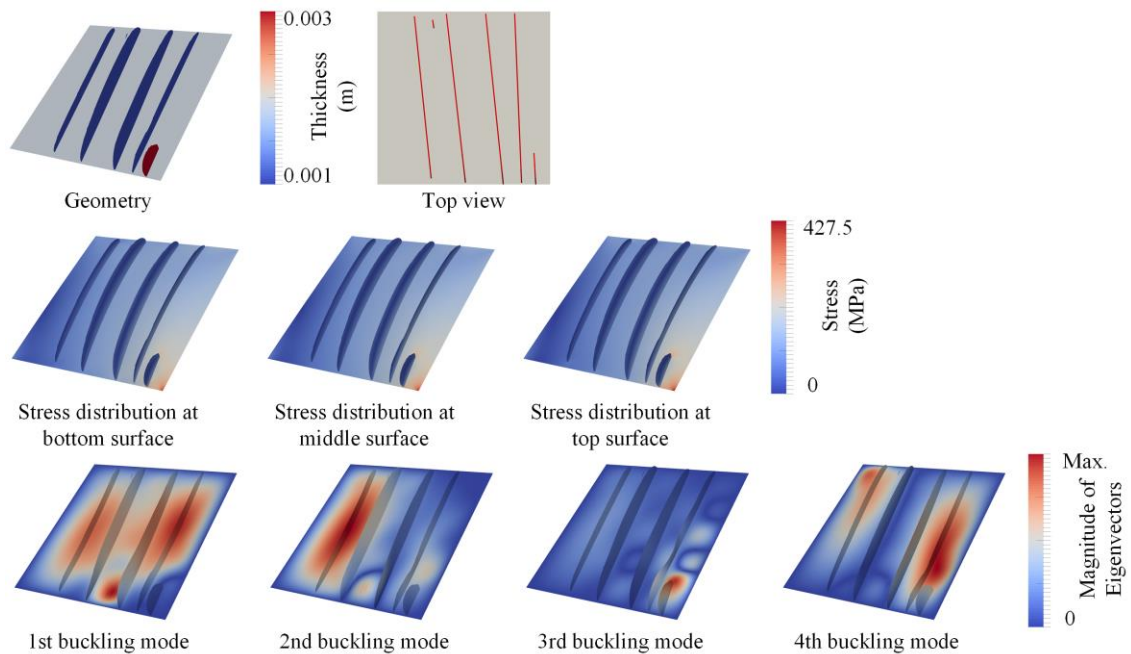


**Figure 4.17 Optimized design ( $\sigma_{\text{upper\_bound}} = 427.5$  MPa and  $\lambda_{\text{lower\_bound}} = 2$ ),  $m = 0.528$  kg, and its stress distributions and first four buckling modes under combined compression and shear,  $\sigma_{\text{vm,b,max}} = 395.7$  MPa,  $\sigma_{\text{vm,m,max}} = 409.3$  MPa,  $\sigma_{\text{vm,t,max}} = 427.4$  MPa,  $\lambda_1 = 2.006$ ,  $\lambda_2 = 2.017$ ,  $\lambda_3 = 2.029$ ,  $\lambda_4 = 2.035$ .**

**Simultaneous Sizing, Layout and Topology Optimization  
for Buckling and Postbuckling of Stiffened Panels**

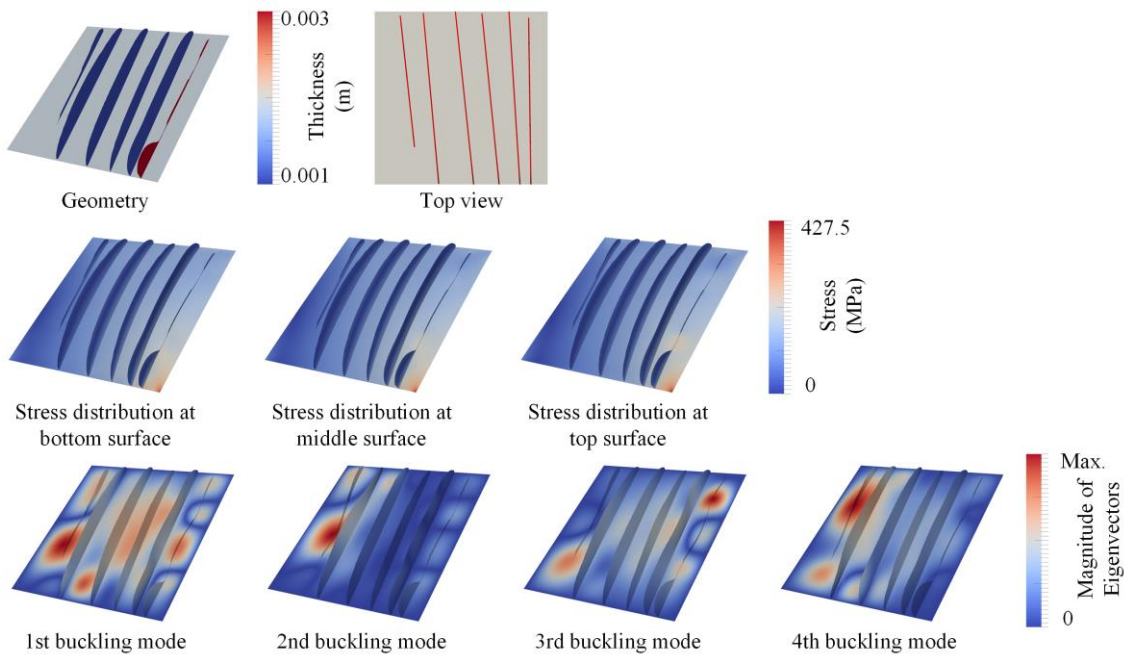


**Figure 4.18 Optimized design ( $\sigma_{upper\_bound} = 427.5$  MPa and  $\lambda_{lower\_bound} = 3$ ),  $m = 0.552$  kg, and its stress distributions and first four buckling modes under combined compression and shear,  $\sigma_{vm,b,max} = 398.3$  MPa,  $\sigma_{vm,m,max} = 411.0$  MPa,  $\sigma_{vm,t,max} = 427.4$  MPa,  $\lambda_1 = 3.018$ ,  $\lambda_2 = 3.032$ ,  $\lambda_3 = 3.046$ ,  $\lambda_4 = 3.056$ .**

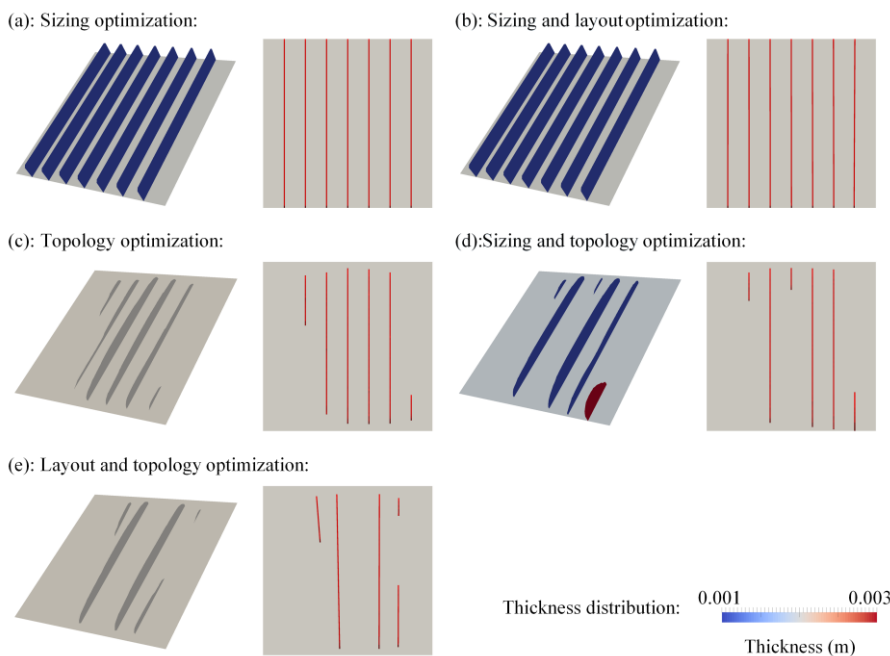


**Figure 4.19 Optimized design using different kinds of optimization with  $\sigma_{upper\_bound} = 427.5$  MPa and  $\lambda_{lower\_bound} = 1$ : (a) sizing optimization; (b) sizing and layout optimization; (c) topology optimization; (d) sizing and topology optimization; (e) layout and topology optimization.**

**Table 4.2 Comparison of the optimized results with different buckling constraints.**

$\sigma_{\text{upper\_bound}}$ (MPa)	$\lambda_{\text{lower\_bound}}$	$m$ (kg)	$\sigma_{\text{vm,b,max}}$ (MPa)	$\sigma_{\text{vm,m,max}}$ (MPa)	$\sigma_{\text{vm,t,max}}$ (MPa)	$\lambda_1$	$\lambda_2$	$\lambda_3$	$\lambda_4$
427.5	1	0.507	398.8	411.2	427.3	1.001	1.013	1.038	1.119
427.5	2	0.528	395.7	409.3	427.4	2.006	2.017	2.029	2.035
427.5	3	0.552	398.3	411.0	427.4	3.018	3.032	3.046	3.056

**Table 4.3 Comparison of the optimized results using different kinds of optimization with  $\sigma_{\text{upper\_bound}} = 427.5$  MPa and  $\lambda_{\text{lower\_bound}} = 1$ .**

Optimization	$m$ (kg)	Percentage greater than (f) for the mass	$\sigma_{\text{vm,b,max}}$ (MPa)	$\sigma_{\text{vm,m,max}}$ (MPa)	$\sigma_{\text{vm,t,max}}$ (MPa)	$\lambda_1$	$\lambda_2$	$\lambda_3$	$\lambda_4$
(a) Sizing	0.646	27.4%	401.6	413.1	427.5	3.247	3.943	4.325	4.415
(b) Sizing and layout	0.645	27.2%	402.3	413.5	427.5	3.126	3.859	4.297	4.489
(c) Topology	0.564	11.2%	397.6	407.8	420.2	1.007	1.011	1.044	1.099
(d) Sizing and topology	0.514	1.38%	406.0	415.7	427.5	1.002	1.004	1.028	1.101
(e) Layout and topology	0.545	7.50%	401.7	411.1	422.3	1.002	1.011	1.034	1.081
(f) Sizing, layout and topology	0.507	0%	398.8	411.2	427.3	1.001	1.013	1.038	1.119

### 4.3.2 Stiffened Panel under Compression, Shear and Bending

The stiffened panel with the loading and boundary conditions shown in Fig. 4.20 is considered for optimization. The size of the panel is 0.3 m  $\times$  0.3 m. The lower and upper bounds of the thicknesses of both the skin and the stiffeners are 0.001 m and 0.003 m, respectively. The upper bound of the von Mises stress  $\sigma_{\text{upper\_bound}} = 427.5$  MPa. The lower bound of the critical buckling load factor is  $\lambda_{\text{lower\_bound}} = 1$ . The lower bound of the stiffener spacing  $L_{\text{min}} = 7.5$  mm.

**Simultaneous Sizing, Layout and Topology Optimization  
for Buckling and Postbuckling of Stiffened Panels**

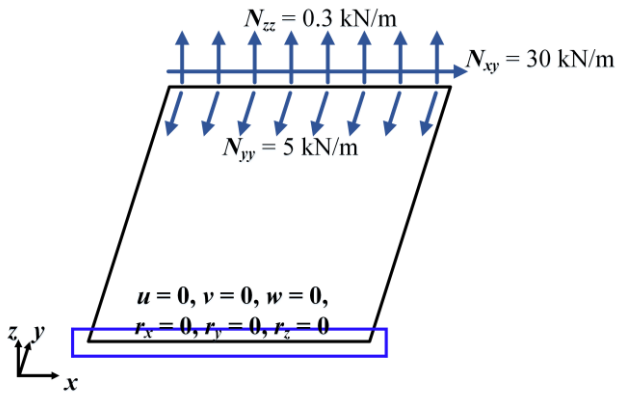


**Figure 4.20 Loading and boundary conditions for the design of a stiffened panel under combined compression, shear and bending.**

The same initial design as shown in Fig. 4.11 is used. Its stress distributions and buckling modes are shown in Fig. 4.21. The first 10 buckling modes are considered in the optimization.

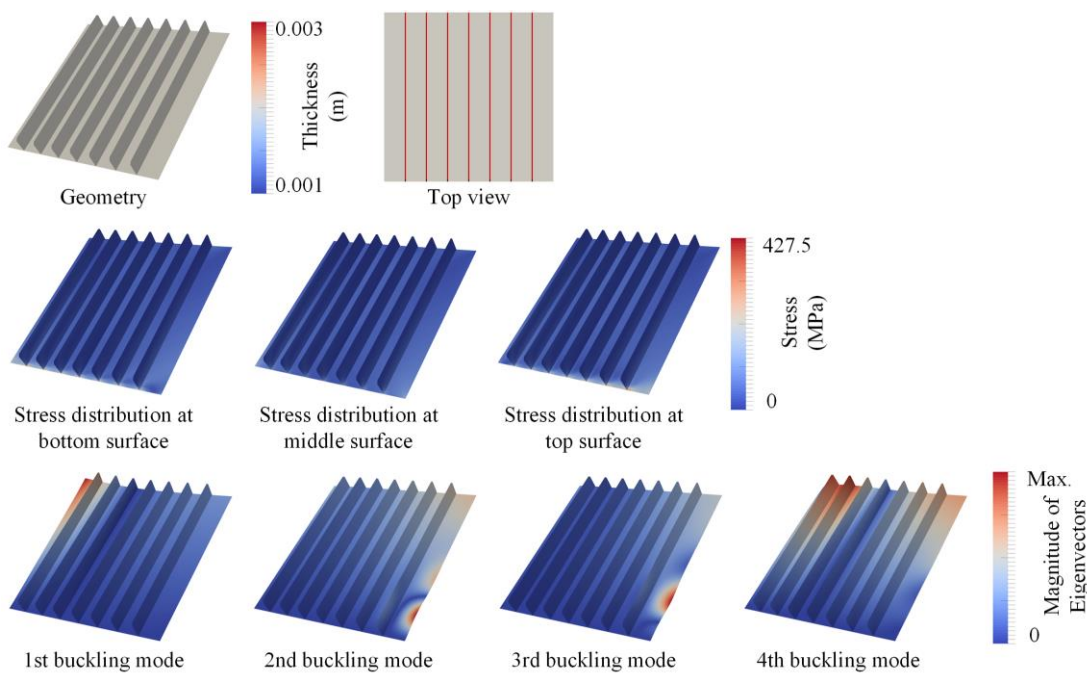


**Figure 4.21 Initial design with seven vertical stiffeners,  $m = 0.826$  kg, and its stress distributions and first four buckling modes under combined compression, shear and bending,  $\sigma_{b,max} = 268.7$  MPa,  $\sigma_{m,max} = 182.6$  MPa,  $\sigma_{t,max} = 323.4$  MPa,  $\lambda_1 = 1.485$ ,  $\lambda_2 = 3.449$ ,  $\lambda_3 = 3.866$ ,  $\lambda_4 = 4.618$ .**

**Chapter 4: Simultaneous Sizing, Layout and Topology Optimization of Panels with Straight Stiffeners under Stress and Buckling Constraints**

To investigate the effect of  $p$  in the  $p$ -norm stress function in Eq. (4-12) on the optimized design, the problem is solved with a range of  $p$  values. The optimized designs are given in Figs. 4.22-4.27. They are compared in Table 4.4.

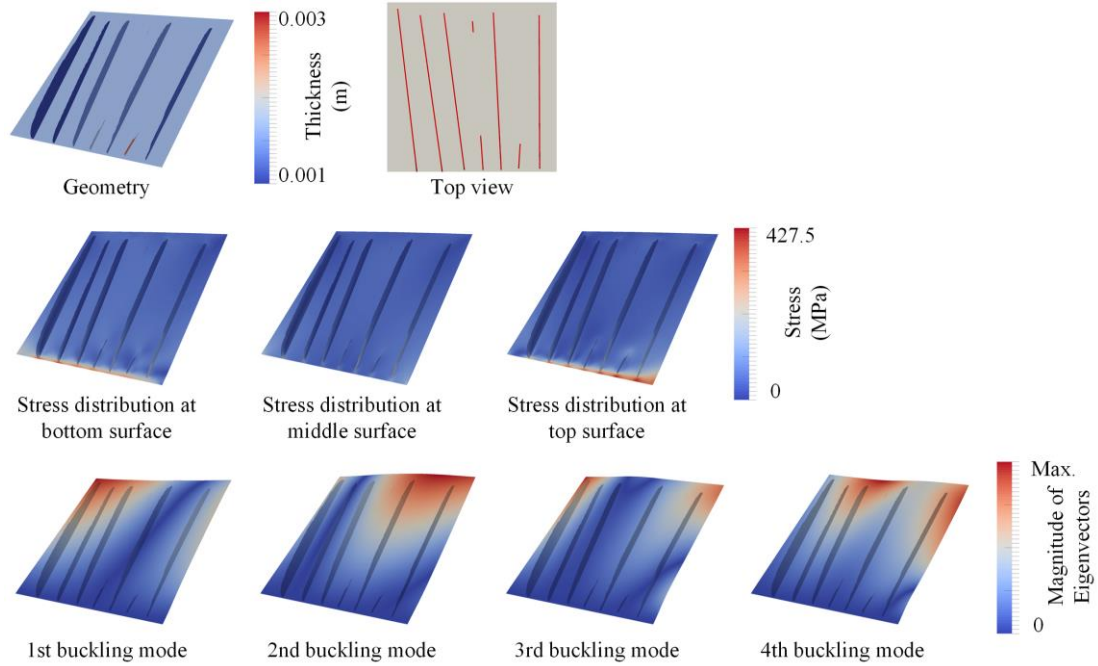


**Figure 4.22** Optimized design with  $p = 6$ ,  $m = 0.458$  kg, and its stress distributions and first four buckling modes under combined compression, shear and bending.

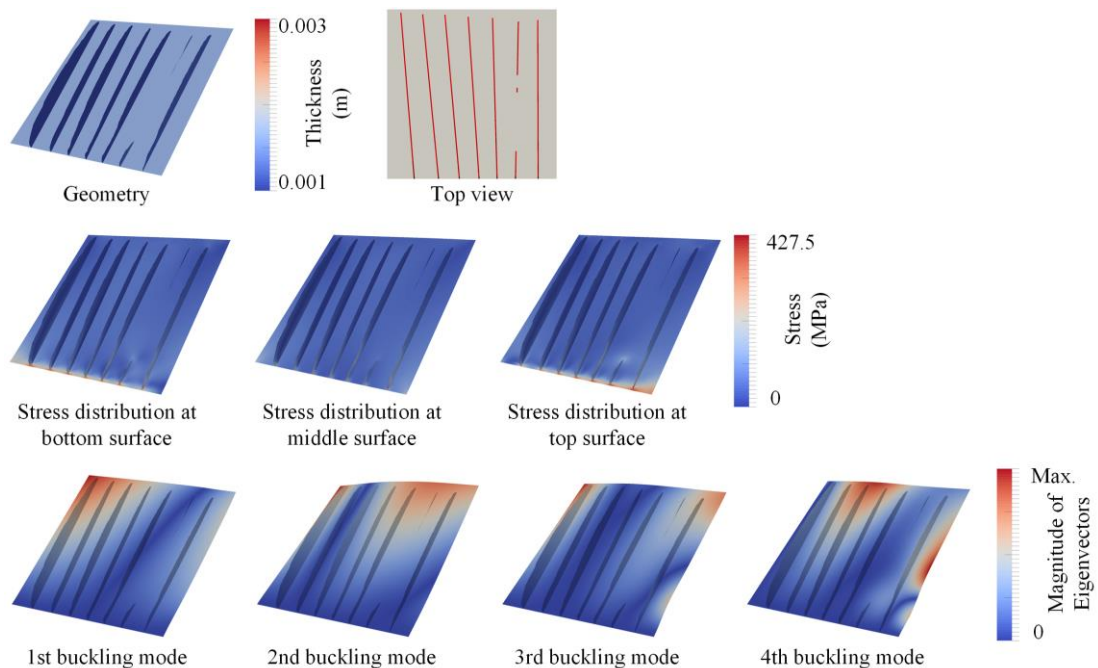


**Figure 4.23** Optimized design with  $p = 8$ ,  $m = 0.454$  kg, and its stress distributions and first four buckling modes under combined compression, shear and bending.

**Simultaneous Sizing, Layout and Topology Optimization  
for Buckling and Postbuckling of Stiffened Panels**

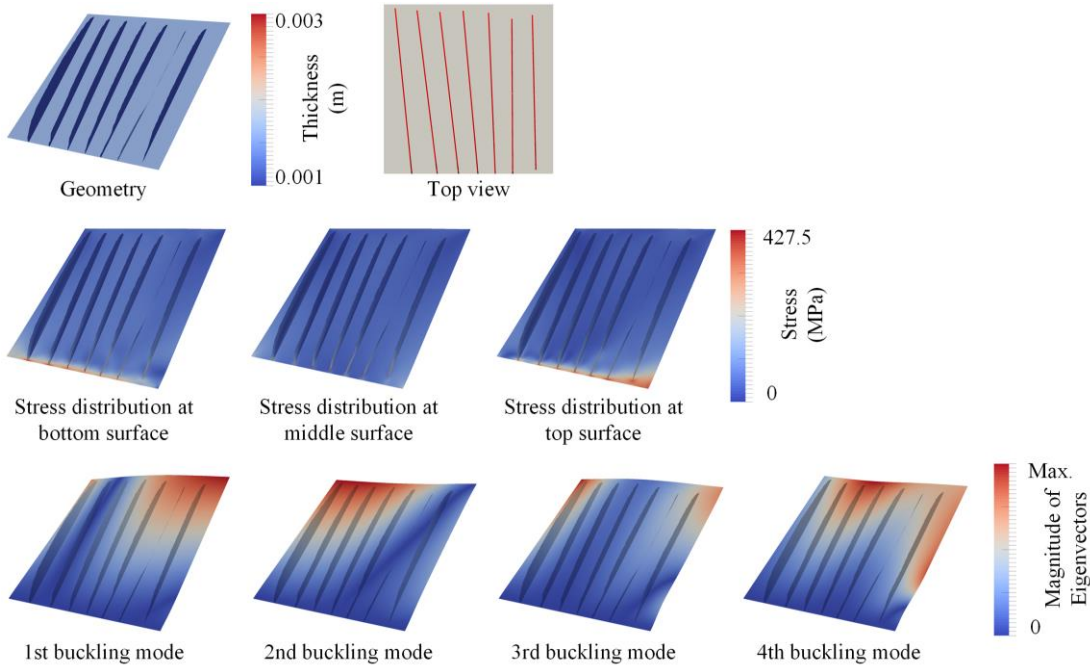


**Figure 4.24 Optimized design with  $p = 10$ ,  $m = 0.453$  kg, and its stress distributions and first four buckling modes under combined compression, shear and bending.**

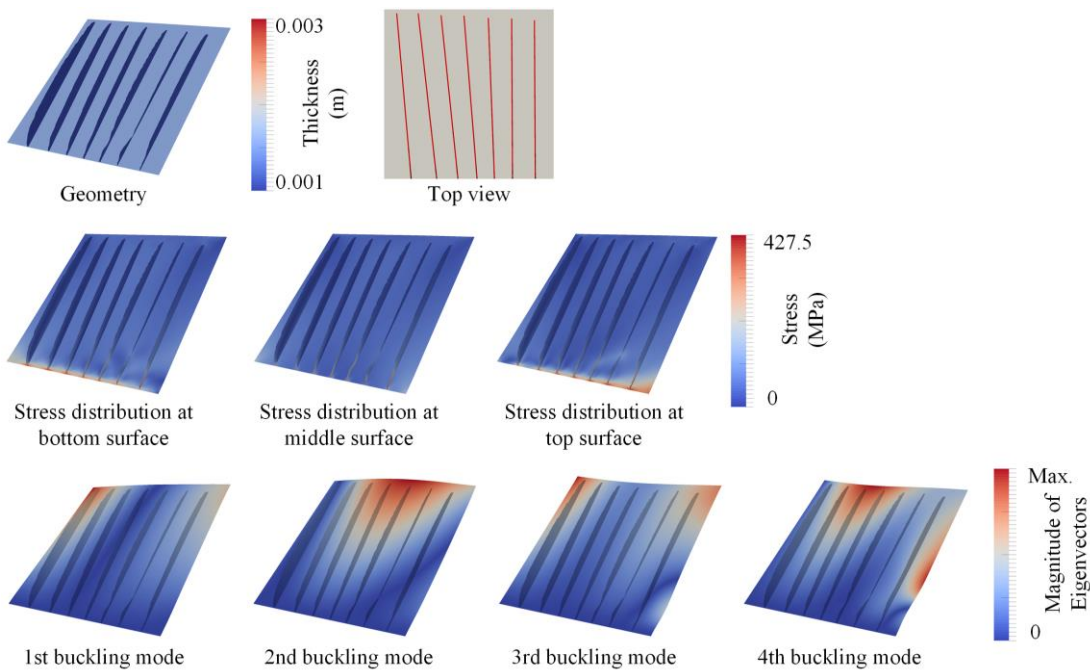


**Figure 4.25 Optimized design with  $p = 12$ ,  $m = 0.448$  kg, and its stress distributions and first four buckling modes under combined compression, shear and bending.**

**Chapter 4: Simultaneous Sizing, Layout and Topology Optimization of Panels with Straight Stiffeners under Stress and Buckling Constraints**

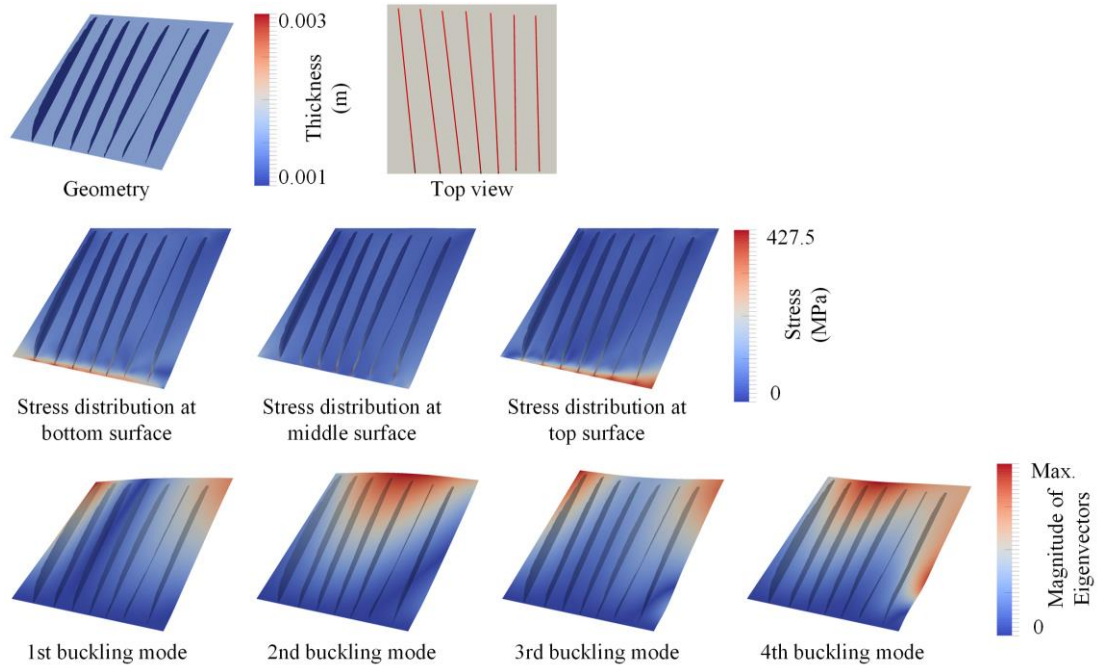


**Figure 4.26 Optimized design with  $p = 18$ ,  $m = 0.443$  kg, and its stress distributions and first four buckling modes under combined compression, shear and bending.**

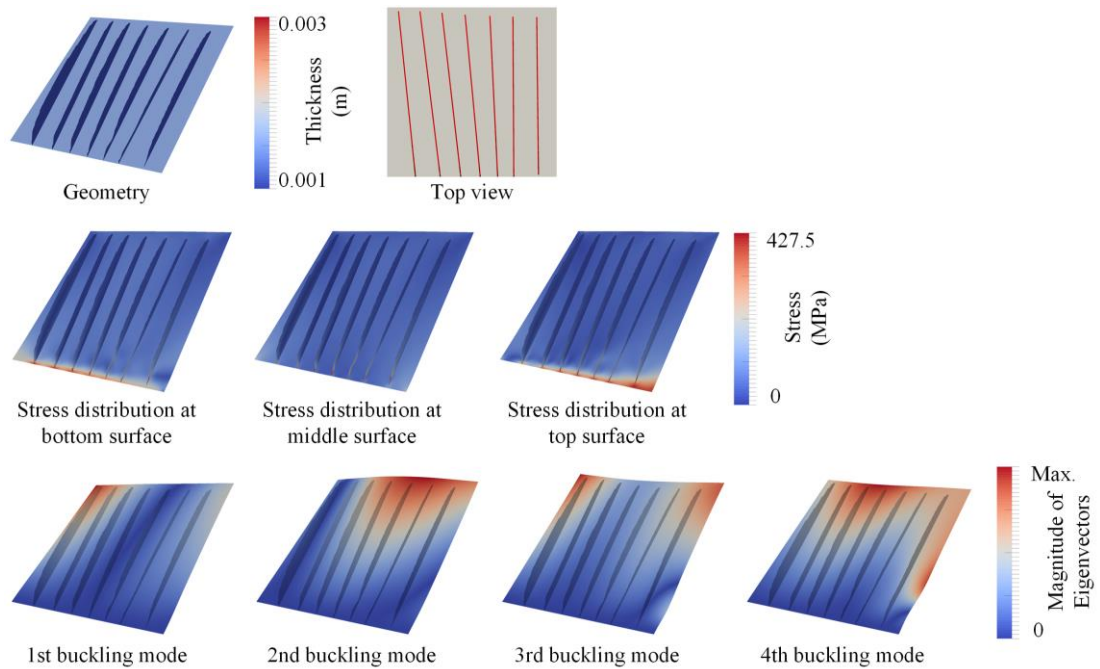


**Figure 4.27 Optimized design with  $p = 24$ ,  $m = 0.444$  kg, and its stress distributions and first four buckling modes under combined compression, shear and bending.**

**Simultaneous Sizing, Layout and Topology Optimization  
for Buckling and Postbuckling of Stiffened Panels**

For this example, it can be seen from Figs. 4.21-4.27 that the stress concentrations occur around the ends of the stiffeners. Compared with the previous loading condition in Fig. 4.3, the stress distribution and locations of the stress concentrations are more dependent on the configuration of the stiffeners. The optimized designs in Fig. 4.22-4.27 all satisfy the stress and buckling constraints. However, when  $p$  increases from 6 to 10, there are obvious changes in the internal topologies of the stiffeners. The 4th and 6th stiffeners get longer and higher. When  $p$  is 12 or greater, the thickness distributions, layouts and internal topologies of the stiffeners stay almost the same. From Table 4.4, it can be observed that, when  $p$  increases from 6 to 18, the masses of the optimized designs are gradually decreased. When  $p$  increases from 18 to 24, the masses of the optimized designs remain roughly the same. The difference is only 0.11%. This shows that, when  $p$  is low, the optimization may converge to a local optimum. Nevertheless, the difference between the masses of the optimized designs in Figs. 4.22-4.27 are within 3.3%. The optimized results are reasonably insensitive to the selection of the value of  $p$ . Therefore, when the value of  $p$  is selected in the range from 6 to 24, acceptable optimized designs can be obtained.

**Table 4.4 Comparison of the optimized results with different  $p$  in the  $p$ -norm stress function.**

$p$	$m$ (kg)	$\sigma_{vm,b,max}$ (MPa)	$\sigma_{vm,m,max}$ (MPa)	$\sigma_{vm,t,max}$ (MPa)	$\lambda_1$	$\lambda_2$	$\lambda_3$	$\lambda_4$
6	0.458	420.5	374.7	425.8	1.002	1.013	1.534	1.845
8	0.454	406.6	355.1	427.0	1.006	1.012	1.489	1.781
10	0.453	421.6	366.2	424.0	1.001	1.004	1.455	1.819
12	0.448	422.2	362.7	420.6	1.005	1.019	1.465	1.695
18	0.443	414.4	396.2	426.9	1.002	1.014	1.424	1.714
24	0.444	423.4	404.5	425.1	1.004	1.009	1.446	1.666

## 4.4 Conclusions

This chapter presents a computational scheme for stiffened panel design simultaneously optimizing size, layout and topology under stress and buckling constraints. An effective level-set based topology optimization formulation is presented. The geometric and FE model updating procedure is described in detail and, a semi-analytical sensitivity

#### **Chapter 4: Simultaneous Sizing, Layout and Topology Optimization of Panels with Straight Stiffeners under Stress and Buckling Constraints**

analysis is presented. The optimization algorithm is also outlined. The numerical investigations show the presented method is able to effectively solve stiffened panel design problems. The stiffener layout is optimized, the stiffener number is reduced, and the material in the skin and remaining stiffeners is redistributed to produce minimum weight designs while satisfying stress and buckling constraints. The influences of the stress constraint, buckling constraints and  $p$  in the  $p$ -norm stress function on the optimized solutions are demonstrated. The presented method offers a practical design tool to design and optimize a stiffened panel configuration with the greatest design freedom.

# 5 SIMULTANEOUS SIZING, LAYOUT AND TOPOLOGY OPTIMIZATION FOR POSTBUCKLING OF PANELS WITH STRAIGHT STIFFENERS

In Chapters 3 and 4, a level-set-based topology optimization method is developed to simultaneously optimize the size, layout and topology of stiffened panels. The weight minimization with buckling and stress constraints has been investigated, but only linear buckling has been considered. If stiffened panels are allowed to continuously operate into the nonlinear postbuckling regime, further weight saving can be achieved.

In this chapter, the level-set-based topology optimization method is extended for postbuckling optimization. It is noted that snap-through and snap-back may occur in the postbuckling regime. For fully tracing these behaviours, an arc-length scheme is required. However, for a geometrically nonlinear optimization, information about the full trajectory is not needed and a Newton-Raphson scheme with load/displacement control is sufficient [101], where the selection of load control or displacement control depends on the type of applied loading [102, 103]. In this chapter, panels under force/displacement loading are considered. The Newton-Raphson scheme with load/displacement control is used for the finite element (FE) analysis, where a small

imperfection in the form of the first linear buckling mode is imposed on the FE model. Five optimization formulations based on different loading and postbuckling metrics are studied. A semi-analytical sensitivity analysis is performed, and a gradient-based optimizer is used to solve the optimization problem. Numerical examples are used to demonstrate the application of the proposed method. Due to the intrinsic nonlinear nature of the problem, the loading level at which the postbuckling buckling behaviour is evaluated affects the optimization result. Two loading levels corresponding to the initial postbuckling and moderately deep postbuckling regimes are therefore studied. The effect of imperfections introduced into the FE model on the optimization is also investigated as are the phenomena of mode jumping and mode switching during the optimization.

The remainder of this chapter is organized as follows. In Section 5.1, the construction and updating of the geometric and FE models of the stiffened panel are reviewed, and the postbuckling analysis is described. Section 5.2 presents the mathematical formulations of the optimization problems, and Section 5.3 describes the optimization algorithm and sensitivity analysis. Numerical examples to test the proposed method are presented in Section 5.4. Conclusions are given in Section 5.5.

## 5.1 Stiffened Panel Model and Postbuckling Analysis

In this section, the construction and updating of the geometric and FE models of a stiffened panel in the optimization process are described. The level-set-based topology optimization parameterization, developed in Section 3.1 of Chapter 3 and illustrated in Fig. 5.1, is employed, enabling the simultaneous sizing, layout and topology optimization of stiffened panels with a path following method used for the postbuckling analysis.

## Simultaneous Sizing, Layout and Topology Optimization for Buckling and Postbuckling of Stiffened Panels

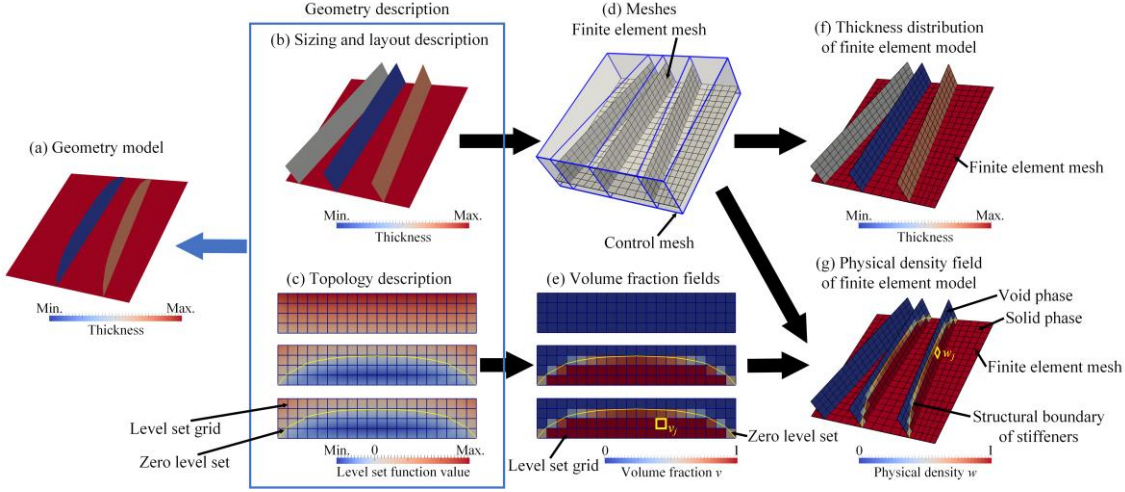


**Figure 5.1** Illustration of the geometric and FE models of a sample stiffened panel.

### 5.1.1 Geometric Model

As shown in Fig. 5.1(a), the stiffened panel is composed of a skin and stiffeners. In Fig. 5.1(b), the skin thickness and the thickness of each of the stiffeners are represented by  $t_p$  and  $t_{s,n}$  ( $n=1, 2, \dots, N$ ). The layout of the stiffeners, i.e., positions, rotations and spacing, is represented by the coordinates of their two ends. Both the thicknesses of the skin and stiffeners and the end coordinates of the stiffeners can be optimized.

The level set method [25, 26, 28] is used to represent and optimize the internal topologies of the stiffeners. As shown in Fig. 5.1(c), the internal topology of each stiffener is described by a separate level set function (LSF). The structural boundary of the  $n$ -th stiffener is defined as the zero level set of an implicit function  $\Phi_n(x)$ , as shown in Fig. 5.1(c):

$$\begin{cases} \Phi_n(x) \leq 0 & x \in \Omega_n \\ \Phi_n(x) = 0 & x \in \Gamma_n, \\ \Phi_n(x) > 0 & x \notin \Omega_n \end{cases} \quad n = 1, 2, 3, \dots, N \quad (5-1)$$

where  $x$  is a coordinate in a level set grid.  $\Omega$  is the domain for the structure, contained in the design domain.  $\Gamma$  is the structural boundary.  $N$  level set functions are used for the  $N$  stiffeners. Each level set function is updated by solving a discretized Hamilton-Jacobi equation using an up-wind differential scheme [26]. To improve the computational efficiency, the level set update is restricted to points within a narrow band close to the boundary. This results in  $\Phi_n$  being given only within this narrow band. In this work, the

LSFs are always maintained as signed distance functions. To ensure the signed distance property  $|\nabla\Phi_n|=1$  in the whole design domain after every update of the LSF, the fast velocity extension algorithm [96] is utilized.

### 5.1.2 Finite Element Model

In this work, the well-known von Kármán large deflection plate theory [104] is employed for postbuckling analysis. Both the skin and stiffeners are modeled explicitly with four-node mixed interpolation of tensorial components (MITC) plate elements with six degrees of freedom per node [91].

The free-form mesh deformation method [90] is used so that the FE mesh can be deformed to cater for different stiffener layouts and re-meshing after every update of the stiffener layout can be avoided. Specifically, as shown in Fig. 5.1(d), a control mesh is generated. Its nodal coordinates are equal to those of the two ends of the stiffeners or the skin vertices. The relationship between the FE and control meshes is given by:

$$\mathbf{x}_{\text{FE}} = \mathbf{N}\mathbf{x}_{\text{control}} \quad (5-2)$$

where  $\mathbf{x}_{\text{FE}}$  and  $\mathbf{x}_{\text{control}}$  are the nodal coordinates of the FE and control meshes, respectively.  $\mathbf{N}$  is the shape function. When the stiffener layout is optimized, the nodal coordinates of the control mesh are updated accordingly:

$$\mathbf{y}_{\text{control}}^k = \mathbf{y}^k \quad (5-3a)$$

$$\mathbf{x}_{\text{control}}^{k+1} = \mathbf{x}_{\text{control}}^k + \mathbf{y}_{\text{control}}^k \quad (5-3b)$$

where  $\mathbf{y}_{\text{control}}$  and  $\mathbf{y}$  are changes to the coordinates of the control mesh nodes and stiffener ends, respectively.  $k$  is the optimization iteration. The FE mesh is then deformed by:

$$\mathbf{z}^k = \mathbf{N}\mathbf{y}_{\text{control}}^k \quad (5-4a)$$

$$\mathbf{x}_{\text{FE}}^{k+1} = \mathbf{x}_{\text{FE}}^k + \mathbf{z}^k \quad (5-4b)$$

where  $\mathbf{z}$  represents the changes to the nodal coordinates of the FE mesh.

**Simultaneous Sizing, Layout and Topology Optimization  
for Buckling and Postbuckling of Stiffened Panels**

As shown in Fig. 5.1(f), the thickness of each element is decided by the skin or stiffener thicknesses,  $t_p$  and  $t_{s,n}$  ( $n=1, 2, \dots, N$ ). As shown in Fig. 5.1(e), it is straightforward to calculate the volume fraction field  $\mathbf{v}$  of the solid phase in the level set grid based on the corresponding level set function values  $\Phi_n$ . The same element numbers are used for the level set grid and the FE mesh for each stiffener in this work. Due to the one-to-one correspondence between the elements of the two meshes, a direct mapping can be used and the physical density for the  $j$ -th element in the FE mesh is obtained by  $w_j = v_j$ , as shown in Fig. 5.1(g). The density distribution  $\mathbf{w} = 1$  for all the elements in the skin.

To avoid excessive mesh distortion in the region with the void phase, which can cause divergence of the nonlinear finite element analysis, a linear analysis is conducted for elements with the void phase [105, 106]; while a nonlinear analysis is performed for elements with the solid phase. For the  $j$ -th finite element, the secant and tangent stiffness matrices,  $\mathbf{K}_{S,j}$  and  $\mathbf{K}_{T,j}$ , are calculated by:

$$\mathbf{K}_{S,j} = \mathbf{K}_{\text{linear},j}^{\text{void}} + w_j \left( \mathbf{K}_{S,j}^{\text{solid}} - \mathbf{K}_{\text{linear},j}^{\text{void}} \right) \quad (5-5a)$$

$$\mathbf{K}_{T,j} = \mathbf{K}_{\text{linear},j}^{\text{void}} + w_j \left( \mathbf{K}_{T,j}^{\text{solid}} - \mathbf{K}_{\text{linear},j}^{\text{void}} \right) \quad (5-5b)$$

where  $\mathbf{K}_{S,j}^{\text{solid}}$  and  $\mathbf{K}_{T,j}^{\text{solid}}$  are the  $j$ -th element secant and tangent stiffness matrices [107, 108] with the solid phase, and  $\mathbf{K}_{\text{linear},j}^{\text{void}}$  is the  $j$ -th element linear stiffness matrix with the void phase.

For a FE model with a deformed mesh, it is easy to add displacements to the corresponding nodes when displacement loading is applied; however as discussed in Section 3.1.4, pressure loading, i.e., the axial compression and shear loads, cannot be applied directly by adding uniform forces to the corresponding nodes. Instead, as shown in Fig. 5.2, the force applied to a node  $pf$  is calculated as:

$$P_{pf} = \frac{P \left( L^{pf-1} + L^{pf} \right)}{2} \quad (5-6)$$

where  $P$  is the pressure value per unit length.  $L^{pf-1}$  and  $L^{pf}$  are the lengths of the elemental boundaries with the node  $pf$ .

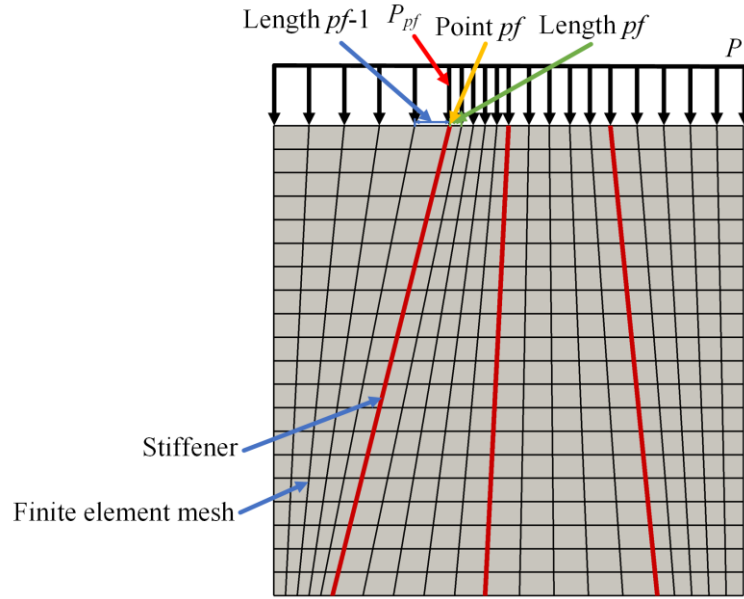


Figure 5.2 Illustration of applying a pressure loading.

### 5.1.3 Postbuckling Analysis

For a nonlinear system, the equilibrium equation is:

$$\mathbf{R} = \mathbf{F}_{\text{int}} - \mathbf{F}_{\text{ext}} = \mathbf{K}_S \mathbf{u} - \mathbf{F}_{\text{ext}} = \mathbf{0} \quad (5-7)$$

where  $\mathbf{R}$  is the residual vector.  $\mathbf{F}_{\text{int}}$  and  $\mathbf{F}_{\text{ext}}$  are internal and external force vectors.  $\mathbf{K}_S$  is the system secant stiffness matrix.  $\mathbf{u}$  is the displacement vector.

In this work, Eq. (5-7) is solved using the Newton-Raphson method. Since bifurcation-type buckling causes discontinuous responses in the postbuckling analysis of a stiffened panel, in this work an imperfection in the form of the first linear buckling mode is introduced.

The postbuckling analysis of a stiffened panel consists of the following steps:

- 1) An eigen-buckling analysis is performed on the perfect structure to obtain the first buckling mode:

$$\mathbf{K}_{\text{linear}} \mathbf{u}_{\text{linear}} = \mathbf{F}_{\text{ext}} \quad (5-8a)$$

$$\left( \mathbf{K}_{\text{linear}} + \lambda \mathbf{K}_g(\mathbf{u}_{\text{linear}}) \right) \phi = \mathbf{0} \quad (5-8b)$$

**Simultaneous Sizing, Layout and Topology Optimization  
for Buckling and Postbuckling of Stiffened Panels**

where  $\mathbf{K}_{\text{linear}}$  and  $\mathbf{u}_{\text{linear}}$  are the linear stiffness matrix and static deflection vector, respectively.  $\mathbf{K}_g$  is the geometric stiffness matrix.  $\lambda$  and  $\phi$  represent the eigenvalue/eigenvector pair for linear buckling. The linear elasticity and eigen-buckling equations in Eq. (5-8) are solved using the HSL MA57 solver [94] and ARPACK [95], respectively.

2) An imperfection in the form of the first linear buckling mode is introduced to the perfect geometry:

$$\hat{\mathbf{x}}_{\text{FE}} = \mathbf{x}_{\text{FE}} + \mathbf{z}_{im} \quad (5-9a)$$

$$\mathbf{z}_{im} = \alpha_{im} \frac{\phi}{\max(|\phi|)} \quad (5-9b)$$

where  $\hat{\mathbf{x}}_{\text{FE}}$  is the vector of nodal coordinates of the FE mesh after the imperfection  $\mathbf{z}_{im}$  is introduced.  $\phi_1$  is the eigenvector of the first linear buckling mode. For the solution of Eq. (5-8b),  $\phi_1$  can be taken as positive or negative, giving different results when solving Eq. (5-7b). To ensure the consistency of optimization results and that the same imperfection can always be introduced for a stiffened panel, the  $\phi_1$  having the maximum positive amplitude is taken as the positive imperfection. Unless otherwise stated, the positive imperfection is always employed in this work.  $\alpha_{im}$  is an adjusting parameter to ensure that  $\mathbf{z}_{im}$  is a positive imperfection, and to adjust the maximum imperfection amplitude. The maximum amplitude of the imperfection normally takes 0.1% to 10% of the skin thickness [37, 109-112].

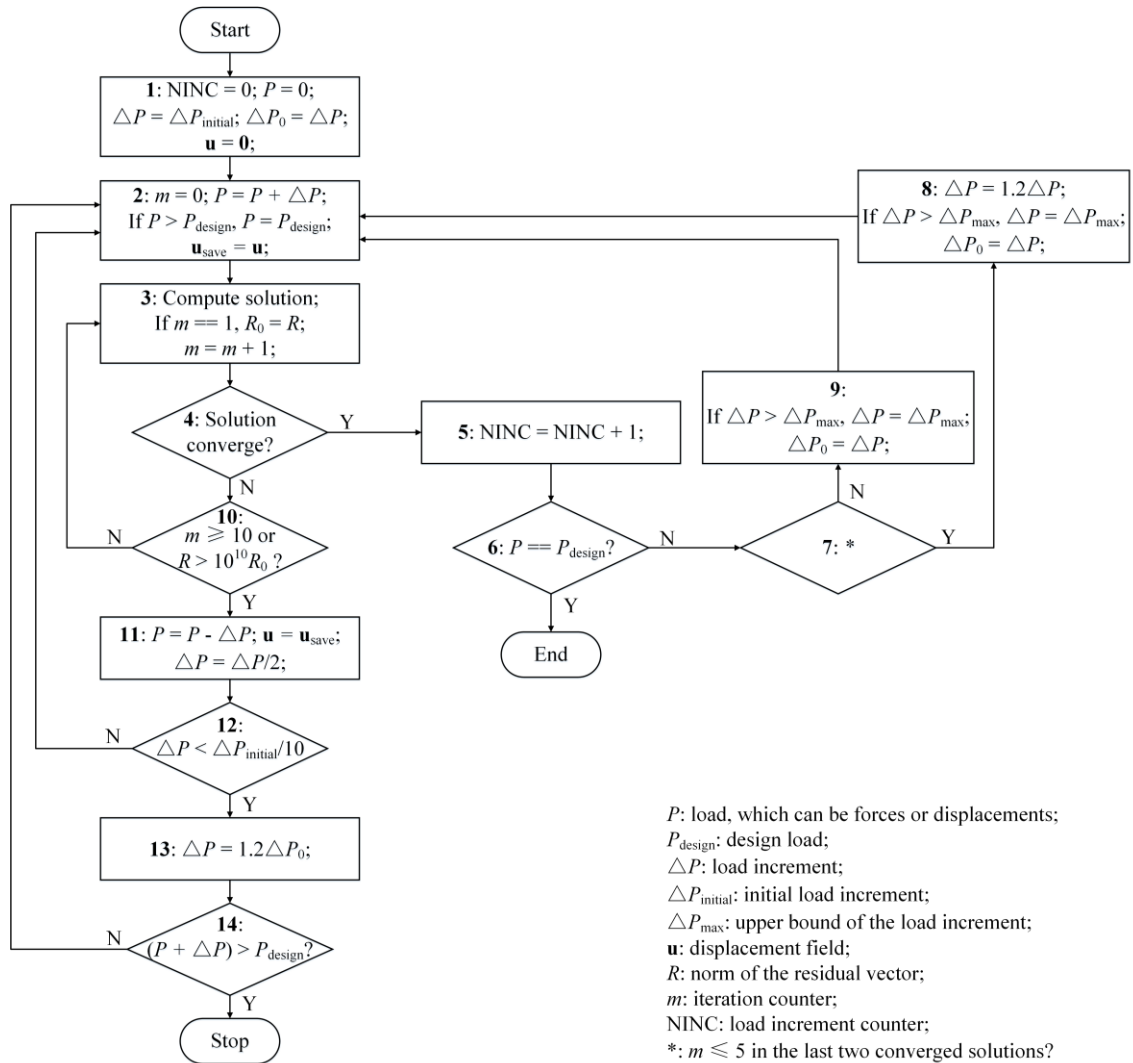


Figure 5.3 Procedure for the geometrically nonlinear analysis, employing a modified automatic load incrementation scheme.

3) The geometrically nonlinear analysis in Eq. (5-7) is performed for the structure containing the imperfection, using the Newton-Raphson method under load control for stiffened panels loaded by forces or under displacement control for those loaded by displacements. A modified automatic load (force/displacement) incrementation scheme based on the one used in [113] is developed. The procedure for the geometrically nonlinear analysis is illustrated in Fig. 5.3 and described as follows:

**Step 1:** Initialise the whole analysis. Start counting the load increment times; set the initial load and load increment values; record the current load increment value  $\Delta P_0$ ; initialize the displacement field; go to Step 2.

**Simultaneous Sizing, Layout and Topology Optimization  
for Buckling and Postbuckling of Stiffened Panels**

Step 2: Initialise the analysis for a new load step. Start counting the iteration times in the current load step; increase the load; if the load is larger than the design load, re-set the load to the design load; record the current displacement field; go to Step 3.

Step 3: Solve Eq. (5-10a) and update the displacement vector in Eq. (5-10b). If this is the first iteration at the current load step, record the norm of the residual vector  $R_0$ ; increase the iteration counter; go to Step 4.

$$\mathbf{R}_{\text{NINC}+1}^m + \mathbf{K}_T d\mathbf{u}_{\text{NINC}+1}^m = \mathbf{0} \quad (5-10a)$$

$$\mathbf{u}_{\text{NINC}+1}^{m+1} = \mathbf{u}_{\text{NINC}+1}^m + d\mathbf{u}_{\text{NINC}+1}^m \quad (5-10b)$$

where  $m$  denotes the iteration number and NINC denotes the load step number.  $\mathbf{K}_T$  is the system tangent matrix and  $d\mathbf{u}$  is the increment in the displacement vector.  $\mathbf{R}$  is the residual vector calculated by:

$$\mathbf{R}_{\text{NINC}+1}^m = \mathbf{K}_{S,\text{NINC}+1}^m \mathbf{u}_{\text{NINC}+1}^m - \mathbf{F}_{\text{ext},\text{NINC}+1} \quad (5-11)$$

Step 4: Check the convergence criterion at the current load step – if the norm of the residual vector is less than the tolerance level ( $10^{-3}$  in this work), go to Step 5; otherwise, go to Step 10.

Step 5: Update the number of the load increments; go to Step 6.

Step 6: Check the convergence criterion of the whole analysis – if the current load is equal to the design load, the whole analysis is **finished** and Eq. (5-7) is solved successfully; otherwise, go to Step 7.

Step 7: Check the load increment increase criterion – if the last two converged solutions are both obtained within a certain number of iterations (5 iterations in this work), go to Step 8; otherwise, go to Step 9.

Step 8: Increase the load increment, by 20% in this work; if the load increment is larger than its upper bound, the load increment is re-set to the value of its upper bound; record the current load increment value  $\Delta P_0$ ; go to Step 2.

Step 9: If the load increment is larger than its upper bound, re-set the load increment to the value of its upper bound; record the current load increment value  $\Delta P_0$ ; go to Step 2.

## Chapter 5: Simultaneous Sizing, Layout and Topology Optimization for Postbuckling of Panels with Straight Stiffeners

Step **10**: Check the load increment reduction criterion – if the solution cannot converge within a certain number of iterations (10 iterations in this work) or the solution diverges (In this work, when the norm of the residual vector is larger than  $10^{10}$  times the value of  $R_0$  recorded in Step **3**, the solution is regarded as diverging), go to Step **11**; otherwise, go to Step **3**.

Step **11**: Go back to the previous load step. Reduce the load by the current load increment; re-set the displacement field to the saved value; reduce the load increment, by 50% in this work; go to Step **12**.

Step **12**: Check the load increment re-setting criterion – if the load increment is smaller than one-tenth of the initial value, go to Step **13**; otherwise, go to Step **2**.

Step **13**: Re-set the load increment, to 1.2 times  $\Delta P_0$  in this work; go to Step **14**.

Step **14**: Check the analysis aborting criterion – if the load plus the load increment is larger than the design load, the analysis is **stopped** and the solution to Eq. (5-7) fails; otherwise, go to Step **2**.

Compared with the automatic load incrementation scheme used in [113], the following key modifications are made for the postbuckling analysis of stiffened panels.

- 1) In [113], the analysis starts with the load increment set to the design load. However, a large load increment can lead to an incorrect solution for the postbuckling analysis. Usually, a convergence study for the load increment is needed to ensure the accuracy of the solution. However, to avoid conducting a convergence study for the load increment at each optimization iteration, the initial value and upper bound of the load increment are taken as small values, one-hundredth and one-fiftieth of the design load in this work.
- 2) When mode jumping occurs, reducing the load increment in Step **11** may not help the solution converge. Instead, in this work the larger load increment in Step **13** can be used to enable the solution to ‘jump over’ the point where mode jumping occurs.
- 3) Although a large load increment can be used to handle the convergence issue caused by mode jumping, it is still possible that the solution is aborted when the point where mode jumping occurs is near the design load. When this happens, the solution at the last converged load step is used for optimization.

## 5.2 Optimization Formulations

In this section, the optimization formulations investigated in this work are described. As discussed in the introduction, the maximum out-of-plane displacement of the skin and the load-carrying capability are considered for the postbuckling optimization of stiffened panels under displacement/force loading. In this work, the total reaction force at a given displacement and the applied displacement at a design load are used to evaluate the load-carrying capability of stiffened panels loaded by displacements; while the maximum in-plane displacement of the skin at a given load is considered for those loaded by forces.

**Table 5.1 Objective and constraints for different postbuckling optimizations.**

Postbuckling optimization for stiffened panels under displacement loading			
Objective	Minimization of the $p$ -norm function of the out-of-plane skin displacements at a given displacement	Maximization of the total reaction force at a given displacement	Minimization of the applied displacement at a design load
Constraints	Total reaction force; Mass; Stiffener spacing	Mass; Stiffener spacing	Mass; Stiffener spacing
Formulation	Eq. (5-12a)	Eq. (5-12b)	Eq. (5-12c)
Postbuckling optimization for stiffened panels under force loading			
Objective	Minimization of the $p$ -norm function of the out-of-plane skin displacements at a given load	Minimization of the $p$ -norm function of the in-plane skin displacements at a given load	
Constraints	Mass; Stiffener spacing	Mass; Stiffener spacing	
Formulation	Eq. (5-13a)	Eq. (5-13b)	

The five optimization formulations in Table 5.1 are investigated in this work to improve the postbuckling behaviours of stiffened panels under a mass constraint, as given below in Eqs. (5-12) and (5-13). In the formulations based on the maximum out-of-plane and in-plane skin displacements, the  $p$ -norm function is used to approximate the maximum values. However, when minimizing the  $p$ -norm function of the out-of-plane skin displacements of stiffened panels loaded by displacements, there is an undesirable

outcome in which the out-of-plane skin displacements are decreased by reducing the reaction force. To avoid this solution which would result in having too small a reaction force resulting in a significant drop in load-carrying capability, a total reaction force constraint is added. In addition, since the free-form mesh deformation method is utilized to adaptively adjust the FE mesh, constraints on stiffener spacing, defined as the difference between the end coordinates of the two adjacent stiffeners, are applied for all five optimization formulations to prevent overlap and intersection between adjacent stiffeners.

### 5.2.1 Optimization Formulations for Stiffened Panels under Displacement Loading

1) Minimization of the  $p$ -norm function of the out-of-plane skin displacements at a given displacement, under total reaction force, mass and stiffener spacing constraints:

$$\begin{aligned} \min_{\mathbf{t}, \mathbf{y}, \Phi} P_{w, \text{skin}} &= \left( \sum_{i=1}^{N_{\text{DOF}}} (I_{w, \text{skin}, i} (\hat{u}_i))^p \right)^{\frac{1}{p}} \\ \text{s.t. } F_{r, \text{total}} &\geq F_{r, \text{total}, \text{min}} \\ m &\leq m_{\text{max}} \\ L_l &\geq L_{\text{min}}, \quad l = 1, 2, \dots, N_L \end{aligned} \quad (5-12a)$$

where  $\mathbf{t} = [t_p, t_{s,1}, t_{s,2}, \dots, t_{s,N}]$ .  $P_{w, \text{skin}}$  is the  $p$ -norm function of the out-of-plane displacements of the skin, and  $p$  is a  $p$ -norm parameter. The  $N_{\text{DOF}}$  (number of degrees of freedom)  $\times 1$  vector  $\mathbf{I}_{w, \text{skin}}$  contains ones for the degrees of freedom for the out-of-plane displacements of the skin, and zeros elsewhere. In this work, the geometrical imperfection is taken as the initial displacement. Therefore, the displacement  $\hat{\mathbf{u}}$  is the sum of the  $\mathbf{u}$  obtained from the geometrically nonlinear analysis in Eq. (5-7) for the imperfect structure and the introduced imperfection  $\mathbf{z}_{im}$  in Eq. (5-9b), namely  $\hat{\mathbf{u}} = \mathbf{u} + \mathbf{z}_{im}$ .  $F_{r, \text{total}}$  is the total reaction force, given in Eq. (5-12b), and  $F_{r, \text{total}, \text{min}}$  is its lower bound.  $m$  and  $m_{\text{max}}$  are the structural mass and its upper bound, respectively.  $L$  and  $L_{\text{min}}$  denote the stiffener spacing and its lower bound, respectively.  $N_L$  is the total number of spacing constraints.

**Simultaneous Sizing, Layout and Topology Optimization  
for Buckling and Postbuckling of Stiffened Panels**

2) Maximization of the total reaction force at a given displacement, under mass and stiffener spacing constraints:

$$\begin{aligned} \max_{\mathbf{t}, \mathbf{y}, \Phi} F_{r, \text{total}} &= \mathbf{I}_r^T \mathbf{K}_S \mathbf{u} \\ \text{s.t. } m &\leq m_{\max} \\ L_l &\geq L_{\min}, \quad l = 1, 2, \dots, N_L \end{aligned} \quad (5-12b)$$

where the  $N_{\text{DOF}} \times 1$  vector  $\mathbf{I}_r$  contains ones for the degrees of freedom where displacement loading is applied, and zeros elsewhere.

3) Minimization of the applied displacement at a design load, under mass and stiffener spacing constraints:

$$\begin{aligned} \min_{\mathbf{t}, \mathbf{y}, \Phi} u_a &\text{ at a design load } F_d \\ \text{s.t. } m &\leq m_{\max} \\ L_l &\geq L_{\min}, \quad l = 1, 2, \dots, N_L \end{aligned} \quad (5-12c)$$

where  $u_a$  is the applied displacement and  $F_d$  is the design load.

### 5.2.2 Optimization Formulations for Stiffened Panels under Force Loading

1) Minimization of the  $p$ -norm function of the out-of-plane skin displacements at a given load, under mass and stiffener spacing constraints:

$$\begin{aligned} \min_{\mathbf{t}, \mathbf{y}, \Phi} P_{w, \text{skin}} &= \left( \sum_{i=1}^{N_{\text{DOF}}} (I_{w, \text{skin}, i} (\hat{u}_i))^p \right)^{\frac{1}{p}} \\ \text{s.t. } m &\leq m_{\max} \\ L_l &\geq L_{\min}, \quad l = 1, 2, \dots, N_L \end{aligned} \quad (5-13a)$$

2) Minimization of the  $p$ -norm function of the in-plane skin displacements at a given load, under mass and stiffener spacing constraints:

$$\begin{aligned} \min_{\mathbf{t}, \mathbf{y}, \Phi} P_{in, \text{skin}} &= \left( \sum_{i=1}^{N_{\text{node}}} \left( I_{in, \text{skin}, i} \hat{u}_{in, x, i}^2 + I_{in, \text{skin}, i} \hat{u}_{in, y, i}^2 \right)^{\frac{p}{2}} \right)^{\frac{1}{p}} \\ \text{s.t. } m &\leq m_{\max} \\ L_l &\geq L_{\min}, \quad l = 1, 2, \dots, N_L \end{aligned} \quad (5-13b)$$

where  $P_{in,skin}$  is the  $p$ -norm function of the in-plane skin displacements. The  $N_{node}$  (number of FE mesh nodes)  $\times 1$  vector  $\mathbf{I}_{in,skin}$  contains ones for the nodes on the skin, and zeros elsewhere.  $\hat{u}_{in,x,i}$  and  $\hat{u}_{in,y,i}$  are the in-plane skin displacements of the  $i$ -th node.

### 5.3 Optimization Algorithm and Sensitivity Analysis

In this section, the optimization algorithm is described. To solve the problems in Eqs. (5-12) and (5-13) with a gradient-based optimizer, a semi-analytical sensitivity analysis is performed.

The optimization algorithm developed in Chapter 3 is employed in this work. The gradient-based optimizer, IPOPT [97], is used. For the sizing and layout optimization,  $\mathbf{t}$  and  $\mathbf{y}$  are the design variables being updated by the optimizer. For the topology optimization, the LSFs are always maintained as signed distance functions. In order to ensure the signed distance property  $|\nabla\Phi_n|=1$  after every update of the LSF, the fast velocity extension algorithm presented in [96] is utilized. The relationship between the changes to the LSF values  $\Delta\Phi_{n,b}$  at the boundary and  $\Delta\Phi_n$  in the rest of the design domain is determined, as:

$$\Delta\Phi_n = \left[ \frac{\partial\Phi_n}{\partial\Phi_{n,b}} \right] \Delta\Phi_{n,b}, \quad n = 1, 2, \dots, N \quad (5-14)$$

The level set values  $\Phi_{n,b}$  on the boundary points are the design variables in the topology optimization and are updated by the optimizer.

At each optimization iteration, IPOPT is used to solve the optimization problem to obtain  $\Delta\mathbf{t}$ ,  $\Delta\mathbf{y}$  and  $\Delta\Phi_b$  to update the stiffened panels. Linearization of an arbitrary optimization problem using Taylor's expansion yields the following:

**Simultaneous Sizing, Layout and Topology Optimization  
for Buckling and Postbuckling of Stiffened Panels**

$$\begin{aligned}
& \min_{\Delta \mathbf{t}, \Delta \mathbf{y}, \Delta \Phi_b} \left( f_0 + \left[ \frac{\partial f}{\partial \mathbf{t}} \right]^T \Delta \mathbf{t} + \left[ \frac{\partial f}{\partial \mathbf{y}} \right]^T \Delta \mathbf{y} + \left[ \frac{\partial f}{\partial \Phi_b} \right]^T \Delta \Phi_b \right) \\
& s.t. \quad g_{q,0} + \left[ \frac{\partial g_q}{\partial \mathbf{t}} \right]^T \Delta \mathbf{t} + \left[ \frac{\partial g_q}{\partial \mathbf{y}} \right]^T \Delta \mathbf{y} + \left[ \frac{\partial g_q}{\partial \Phi_b} \right]^T \Delta \Phi_b \geq g_{q,\min}, \quad q = 1, 2, \dots, N_{g1} \\
& \quad \quad g_{q,0} + \left[ \frac{\partial g_q}{\partial \mathbf{t}} \right]^T \Delta \mathbf{t} + \left[ \frac{\partial g_q}{\partial \mathbf{y}} \right]^T \Delta \mathbf{y} + \left[ \frac{\partial g_q}{\partial \Phi_b} \right]^T \Delta \Phi_b \leq g_{q,\max}, \quad q = N_{g1} + 1, 2, \dots, N_{g1} + N_{g2} \\
& \quad \quad -\gamma_1 \leq \Delta \mathbf{t} \leq \gamma_1 \\
& \quad \quad -\gamma_2 \leq \Delta \mathbf{y}_{\text{stiffener}} \leq \gamma_2 \\
& \quad \quad -\gamma_3 \leq \Delta \Phi_b \leq \gamma_3
\end{aligned} \tag{5-15}$$

where  $f_0$  and  $g_{q,0}$  are the objective and constraint function values at the current iteration.  $N_{g1}$  and  $N_{g2}$  are the numbers of inequality constraints.  $g_{q,\min}$  and  $g_{q,\max}$  are the lower and upper bounds of the constraint function values, respectively.  $\gamma_1$ ,  $\gamma_2$  and  $\gamma_3$  are the move limits for  $\Delta \mathbf{t}$ ,  $\Delta \mathbf{y}$  and  $\Delta \Phi_b$ , respectively. To solve the problem of maximizing  $F_{r,\text{total}}$  in Eq. (5-12b), the objective is transformed into minimizing  $-F_{r,\text{total}}$ , namely  $f = -F_{r,\text{total}}$  in Eq. (5-15).

To solve Eq. (5-15), the sensitivities of the objective and constraint functions, which depend only on the final equilibrium at the design loading and disregard the solution equilibrium path are required. However, as mentioned in Section 5.1, if the solution is aborted at the design loading, the solution at the last converged load step is used for calculating the sensitivities. A semi-analytical sensitivity analysis with the adjoint method is used for sensitivity calculation.

### 5.3.1 Sensitivity Analysis for the Optimization of Stiffened Panels under Displacement Loading

#### 1) Sensitivity of the $p$ -norm function of the out-of-plane skin displacements

To calculate the sensitivity of  $P_{w,\text{skin}}$ , the augmented Lagrangian functional for  $P_{w,\text{skin}}$  is given by:

$$\Psi_A = P_{w,\text{skin}} + \lambda_A^T (\mathbf{F}_{\text{int}} - \mathbf{F}_{\text{ext}}) \tag{5-16}$$

where  $\lambda_A$  is the adjoint vector.

Differentiating Eq. (5-16):

$$\begin{aligned} \frac{\partial \Psi_A}{\partial a} = & \frac{1}{p} P_{w,skin}^{1-p} \left( \sum_{i=1}^{N_{DOF}} \left( p \left( I_{w,skin,i}(\hat{u}_i) \right)^{p-1} I_{w,skin,i} \left( \frac{\partial u_i}{\partial a} + \frac{\partial z_{im,i}}{\partial a} \right) \right) \right) \\ & + \lambda_A^T \left( \frac{\partial \mathbf{K}_S}{\partial a} \mathbf{u} - \frac{\partial \mathbf{F}_{ext}}{\partial a} \right) + \lambda_A^T \left( \mathbf{K}_T \frac{\partial \mathbf{u}}{\partial a} - \frac{\partial \mathbf{F}_{ext}}{\partial \mathbf{u}} \frac{\partial \mathbf{u}}{\partial a} \right) \end{aligned} \quad (5-17)$$

where  $a$  is an arbitrary design variable.

By collecting the terms with  $\partial \mathbf{u} / \partial a$  and  $\partial \mathbf{F}_{ext} / \partial a$  in Eq. (5-17) and setting them to zero, respectively, the derivative of the augmented Lagrangian functional for  $P_{w,skin}$  with respect to  $a$  can be calculated by:

$$\frac{\partial \Psi_A}{\partial a} = \frac{1}{p} P_{w,skin}^{1-p} \left( \sum_{i=1}^{N_{DOF}} \left( p \left( I_{w,skin,i}(\hat{u}_i) \right)^{p-1} I_{w,skin,i} \frac{\partial z_{im,i}}{\partial a} \right) \right) + \lambda_A^T \frac{\partial \mathbf{K}_S}{\partial a} \mathbf{u} \quad (5-18)$$

where  $\lambda_A$  needs to satisfy the following equations:

$$\frac{1}{p} P_{w,skin}^{1-p} \left( \sum_{i=1}^{N_{DOF}} \left( p \left( I_{w,skin,i}(\hat{u}_i) \right)^{p-1} I_{w,skin,i} \frac{\partial u_i}{\partial a} \right) \right) + \lambda_A^T \left( \mathbf{K}_T \frac{\partial \mathbf{u}}{\partial a} - \frac{\partial \mathbf{F}_{ext}}{\partial \mathbf{u}} \frac{\partial \mathbf{u}}{\partial a} \right) = 0 \quad (5-19a)$$

$$\lambda_A^T \frac{\partial \mathbf{F}_{ext}}{\partial a} = 0 \quad (5-19b)$$

Based on Eqs. (5-19a) and (5-19b), it can be obtained that  $\lambda_A = \mathbf{0}$  for the prescribed degrees of freedom where the displacements are known. For the non-prescribed degrees of freedom,  $\lambda_A$  can be solved by:

$$\frac{1}{p} P_{w,skin}^{1-p} \left( \sum_{i=1}^{N_{DOF}} \left( p \left( I_{w,skin,i}(\hat{u}_i) \right)^{p-1} I_{w,skin,i} \frac{\partial u_i}{\partial a} \right) \right) + \lambda_A^T \mathbf{K}_T \frac{\partial \mathbf{u}}{\partial a} = 0 \quad (5-20)$$

## 2) Sensitivity of the total reaction force

To calculate the sensitivity of  $F_{r,total}$ , the augmented Lagrangian functional for  $F_{r,total}$  is given by:

$$\Psi_B = F_{r,total} + \lambda_B^T (\mathbf{F}_{int} - \mathbf{F}_{ext}) \quad (5-21)$$

where  $\lambda_B$  is the adjoint vector.

**Simultaneous Sizing, Layout and Topology Optimization  
for Buckling and Postbuckling of Stiffened Panels**

Differentiating Eq. (5-21):

$$\frac{\partial \Psi_B}{\partial a} = \mathbf{I}_r^T \mathbf{K}_T \frac{\partial \mathbf{u}}{\partial a} + \mathbf{I}_r^T \frac{\partial \mathbf{K}_S}{\partial a} \mathbf{u} + \lambda_B^T \left( \frac{\partial \mathbf{K}_S}{\partial a} \mathbf{u} - \frac{\partial \mathbf{F}_{\text{ext}}}{\partial a} \right) + \lambda_B^T \left( \mathbf{K}_T \frac{\partial \mathbf{u}}{\partial a} - \frac{\partial \mathbf{F}_{\text{ext}}}{\partial \mathbf{u}} \frac{\partial \mathbf{u}}{\partial a} \right) \quad (5-22)$$

By collecting the terms with  $\partial \mathbf{u} / \partial a$  and  $\partial \mathbf{F}_{\text{ext}} / \partial a$  in Eq. (5-22) and setting them to zero, respectively, the derivative of the augmented Lagrangian functional for  $F_{r,\text{total}}$  with respect to  $a$  can be calculated by:

$$\frac{\partial \Psi_B}{\partial a} = \mathbf{I}_r^T \frac{\partial \mathbf{K}_S}{\partial a} \mathbf{u} + \lambda_B^T \frac{\partial \mathbf{K}_S}{\partial a} \mathbf{u} \quad (5-23)$$

where  $\lambda_B$  needs to satisfy the following equations:

$$\mathbf{I}_r^T \mathbf{K}_T \frac{\partial \mathbf{u}}{\partial a} + \lambda_B^T \left( \mathbf{K}_T \frac{\partial \mathbf{u}}{\partial a} - \frac{\partial \mathbf{F}_{\text{ext}}}{\partial \mathbf{u}} \frac{\partial \mathbf{u}}{\partial a} \right) = 0 \quad (5-24a)$$

$$\lambda_B^T \frac{\partial \mathbf{F}_{\text{ext}}}{\partial a} = 0 \quad (5-24b)$$

Based on Eqs. (5-24a) and (5-24b), it can be obtained that  $\lambda_B = \mathbf{0}$  for the prescribed degrees of freedom. For the non-prescribed degrees of freedom,  $\lambda_B$  can be solved by:

$$\mathbf{I}_{r,p}^T \mathbf{K}_{T,pf} \frac{\partial \mathbf{u}_f}{\partial a} + \lambda_{B,f}^T \mathbf{K}_{T,ff} \frac{\partial \mathbf{u}_f}{\partial a} = 0 \quad (5-25)$$

where the subscripts  $p$  and  $f$  denote the prescribed and non-prescribed degrees of freedom, respectively.

The optimization problem of minimizing  $u_a$  at a given design load in Eq. (5-12c) can be solved by transforming it into the optimization problem maximizing  $F_{r,\text{total}}$  in Eq. (5-12b) at each optimization iteration using a bisection method. Further details are given in Section 5.4.1.2). Therefore, the sensitivity of  $u_a$  at the design load is not calculated.

### 5.3.2 Sensitivity Analysis for the Optimization of Stiffened Panels under Force Loading

1) Sensitivity of the  $p$ -norm function of the out-of-plane skin displacements

In a similar way to deriving the sensitivity of  $P_{w,skin}$  in Eq. (5-18) for stiffened panels under displacement loading, the derivative of the augmented Lagrangian functional for  $P_{w,skin}$  for panels under force loading is given by:

$$\frac{\partial \Psi_c}{\partial a} = \frac{1}{p} P_{w,skin}^{1-p} \left( \sum_{i=1}^{N_{DOF}} \left( p (I_{w,skin,i} (\hat{u}_i))^{p-1} I_{w,skin,i} \frac{\partial z_{im,i}}{\partial a} \right) \right) + \lambda_c^T \frac{\partial \mathbf{K}_s}{\partial a} \mathbf{u} - \lambda_c^T \frac{\partial \mathbf{F}_{ext}}{\partial a} \quad (5-26)$$

where  $\lambda_c$  is the adjoint vector which can be solved by:

$$\frac{1}{p} P_{w,skin}^{1-p} \left( \sum_{i=1}^{N_{DOF}} \left( p (I_{w,skin,i} (\hat{u}_i))^{p-1} I_{w,skin,i} \frac{\partial u_i}{\partial a} \right) \right) + \lambda_c^T \mathbf{K}_T \frac{\partial \mathbf{u}}{\partial a} = 0 \quad (5-27)$$

It is noted that unlike the sensitivity in Eq. (5-18), the term with  $\partial \mathbf{F}_{ext} / \partial a$  in Eq. (5-26) needs to be calculated. For the layout optimization,  $\partial \mathbf{F}_{ext} / \partial \mathbf{y} \neq \mathbf{0}$  since according to Eq. (5-6), the forces applied on points of the FE mesh are changed as the stiffener layout is updated. For simplicity, this is calculated via the finite difference method. For the sizing and topology optimization  $\partial \mathbf{F}_{ext} / \partial a$  is equal to  $\mathbf{0}$ .

2) Sensitivity of the  $p$ -norm function of the in-plane skin displacements

In a similar way to calculating the sensitivity in Eq. (5-26), the derivative of the augmented Lagrangian functional for  $P_{in,skin}$  is given by:

$$\begin{aligned} \frac{\partial \Psi_D}{\partial a} = & \frac{1}{p} P_{in,skin}^{1-p} \left( \sum_{i=1}^{N_{node}} \left( \frac{p}{2} (I_{in,skin,i} \hat{u}_{in,x,i}^2 + I_{in,skin,i} \hat{u}_{in,y,i}^2)^{\frac{p-2}{2}} \left( 2I_{in,skin,i} \hat{u}_{in,x,i} \frac{\partial z_{im,in,x,i}}{\partial a} + 2I_{in,skin,i} \hat{u}_{in,y,i} \frac{\partial z_{im,in,y,i}}{\partial a} \right) \right) \right) \\ & + \lambda_D^T \frac{\partial \mathbf{K}_s}{\partial a} \mathbf{u} - \lambda_D^T \frac{\partial \mathbf{F}_{ext}}{\partial a} \end{aligned} \quad (5-28)$$

where  $\lambda_D$  is the adjoint vector which can be solved by:

**Simultaneous Sizing, Layout and Topology Optimization  
for Buckling and Postbuckling of Stiffened Panels**

$$\frac{1}{p} P_{in,skin}^{1-p} \left( \sum_{i=1}^{N_{node}} \left( \frac{P}{2} \left( I_{in,skin,i} \hat{u}_{in,x,i}^2 + I_{in,skin,i} \hat{u}_{in,y,i}^2 \right) \right)^{\frac{p-2}{2}} \left( 2I_{in,skin,i} \hat{u}_{in,x,i} \frac{\partial u_{in,x,i}}{\partial a} + 2I_{in,skin,i} \hat{u}_{in,y,i} \frac{\partial u_{in,y,i}}{\partial a} \right) \right) + \lambda_{in,skin}^T \mathbf{K}_T \frac{\partial \mathbf{u}}{\partial a} = 0 \quad (5-29)$$

Since the adjoint method is used for the sensitivity calculation, the sensitivity of a function  $f$ , i.e.,  $P_{w,skin}$ ,  $F_{r,total}$  and  $P_{in,skin}$ , is equivalent to the derivative of its augmented Lagrangian functional, i.e.,  $\partial P_{w,skin}/\partial a$  in Eq. (5-18) and  $\partial F_{r,total}/\partial a$  in Eq. (5-23) for the design under displacement loading and  $\partial P_{w,skin}/\partial a$  in Eq. (5-26) and  $\partial P_{in,skin}/\partial a$  in Eq. (5-28) for the design under force loading.

For the sizing optimization, derivatives with respect to  $t_p$  and  $t_{s,n}$  are computed using the chain rule:

$$\frac{\partial f}{\partial t_p} = \sum_{j=1}^{N_{ele}} \frac{\partial f}{\partial t_j} \frac{\partial t_j}{\partial t_p} \quad (5-30a)$$

$$\frac{\partial f}{\partial t_{s,n}} = \sum_{j=1}^{N_{ele}} \frac{\partial f}{\partial t_j} \frac{\partial t_j}{\partial t_{s,n}}, \quad n = 1, 2, \dots, N \quad (5-30b)$$

where  $N_{ele}$  is the total number of finite elements in the structure. Values of  $\partial f/\partial t_j$  are calculated based on Eqs. (5-18), (5-23), (5-26) and (5-28), and

$$\frac{\partial t_j}{\partial t_p} = \begin{cases} 1 & \text{when the } j\text{-th element belongs to the skin} \\ 0 & \text{when the } j\text{-th element does not belong to the skin} \end{cases} \quad (5-31a)$$

$$\frac{\partial t_j}{\partial t_{s,n}} = \begin{cases} 1 & \text{when the } j\text{-th element belongs to the } n\text{-th stiffener} \\ 0 & \text{when the } j\text{-th element does not belong to the } n\text{-th stiffener} \end{cases}, \quad n = 1, 2, \dots, N \quad (5-31b)$$

For the layout optimization, the calculation of derivatives with respect to  $\mathbf{y}$  is based on Eqs. (5-18), (5-23), (5-26) and (5-28), where  $\partial \mathbf{K}_s/\partial y_i$  and  $\partial \mathbf{F}_{ext}/\partial y_i$  are calculated via the central finite difference method.

For the topology optimization, derivatives with respect to the level set values of the boundary points  $\Phi_{n,b}$  are computed through the chain rule:

$$\frac{\partial f}{\partial \Phi_{n,b}} = \sum_{j=1}^{N_{ele}} \frac{\partial f}{\partial w_j} \frac{\partial w_j}{\partial v_j} \frac{\partial v_j}{\partial \Phi_{n,b}} \quad (5-32)$$

where the values of  $\partial f/\partial w_j$  are calculated based on Eqs. (5-18), (5-23), (5-26) and (5-28), and  $\partial w_j/\partial v_j = 1$ .  $\partial v_j/\partial \Phi_{n,b}$  can be computed via the implicit perturbation of the level set boundary, as described in Section 3.2.2.

The calculation of sensitivities of other functions, i.e.,  $m$  and  $L$ , can be found in Section 3.2.2 as well as more details on the implementation of the sensitivity calculation.

## 5.4 Numerical Examples

Three numerical examples are presented to demonstrate and validate the optimization method. In these examples, the aluminum alloy, Al 2139, is used. The Young's moduli of the solid material and void phases are 73.085 and  $73.085 \times 10^{-6}$  GPa, respectively. The densities of the solid material and void phases are 2700 and 0 kg/m<sup>3</sup>, respectively. Poisson's ratio is 0.33.

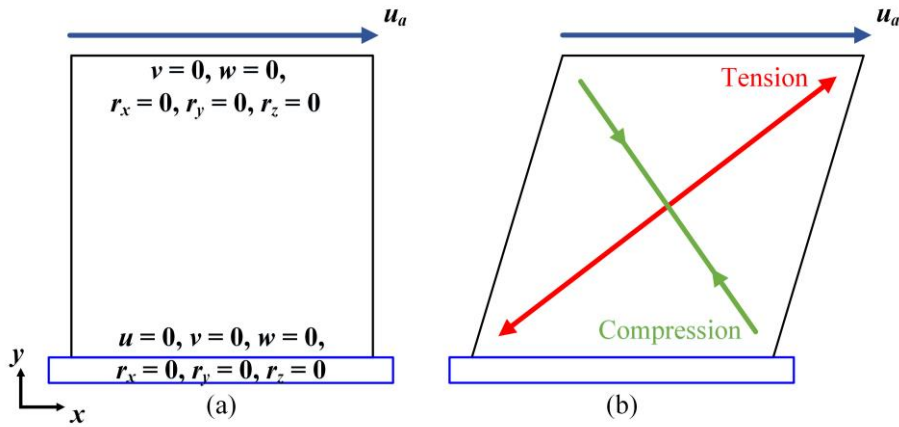


**Figure 5.4 Design of a stiffened panel loaded by shear displacement: (a) loading and boundary conditions; (b) force diagram.**

### 5.4.1 Stiffened panel loaded by Shear Displacement

A stiffened panel of 300 mm  $\times$  300 mm with the loading and boundary conditions shown in Fig. 5.4(a) is considered for optimization. A shear displacement is applied on the top edge. Three optimizations, the minimization of  $P_{w,skin}$  and maximization of  $F_{r,total}$  at a particular design displacement in Eqs. (5-12a) and (5-12b), and the minimization of

**Simultaneous Sizing, Layout and Topology Optimization  
for Buckling and Postbuckling of Stiffened Panels**

$u_a$  at a design load in Eq. (5-12c), are investigated. For all three optimizations, the upper bound of the structural mass  $m_{\max} = 0.56$  kg. The lower bound of the stiffener spacing  $L_{\min} = 7.5$  mm. The lower and upper bounds of the thicknesses of both the skin and the stiffeners are 1 and 3 mm, respectively.

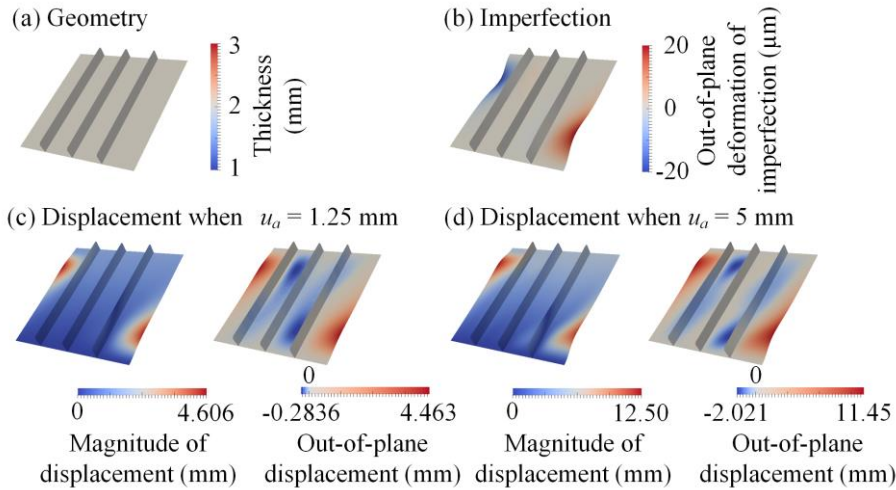


**Figure 5.5 Initial design of the stiffened panel loaded by shear displacement.**

1) Optimization at a design displacement

Two optimizations, i.e., the minimization of  $P_{w,skin}$  in Eq. (5-12a) and the maximization of  $F_{r,total}$  in Eq. (5-12b) are investigated, and two design displacement levels  $u_a = 1.25$  and 5 mm are explored. For the minimization of  $P_{w,skin}$  in Eq. (5-12a),  $p = 6$  is used in the  $p$ -norm function. The initial design with three vertical stiffeners, each with a height of 30 mm, is given in Fig. 5.5(a). The initial thicknesses are set to 2 mm for both the skin and the stiffeners. The skin is discretized with  $80 \times 80$  plate elements, and 8 elements along the height of the stiffeners. The imperfection introduced for postbuckling analysis is shown in Fig. 5.5(b). Its maximum amplitude is set to 1% of the skin thickness of the initial design i.e. 20  $\mu\text{m}$ . For the displacement configurations in Figs. 5.5(c) and 5.5(d), the magnitude of the displacement is the total displacement including both in-plane and out-of-plane displacements, which is then compared to the out-of-plane displacement on its own. In Figs. 5.5(c) and 5.5(d), it can be observed that for the initial design, the largest out-of-plane displacements occur at the two free side edges of the skin at both the loading levels  $u_a = 1.25$  and 5 mm. The structure also buckles between the stiffeners. The ratio of the maximum magnitudes of the out-of-plane displacements between the stiffeners and at the two free edges is 0.063 at  $u_a =$

1.25 mm. As the applied displacement is increased, this ratio increases to 0.177 at  $u_a = 5$  mm. For the optimization minimizing  $P_{w,skin}$  in Eq. (5-12a), the lower bound of the total reaction force takes the value of the initial design.

Design displacement level  $u_a = 1.25$  mm:

The optimized designs under the design shear displacement  $u_a = 1.25$  mm are shown in Fig. 5.6. The equilibrium paths are given in Fig. 5.7. A comparison between the initial and optimized designs is given in Table 5.2. From Fig. 5.6, it can be seen that the skin and stiffener thicknesses, stiffener layout and stiffener internal topologies are all optimized. In both Fig. 5.6(a) optimizing  $P_{w,skin}$  using Eq. (5-12a) and Fig. 5.6(f) optimizing  $F_{r,total}$  using Eq. (5-12b), the two outermost stiffeners move closer to the side edges of the skin to decrease the out-of-plane displacements along these edges. For the design in Fig. 5.6(a) optimizing  $P_{w,skin}$ , the three stiffeners remain parallel to each other to reduce the width of the unsupported regions of the skin between them and hence limit out-of-plane displacements. The out-of-plane skin displacements are also decreased via the optimization of the stiffener internal topologies. For example, for the middle stiffener, the height in the middle is larger than that at the two ends, in order to suppress the out-of-plane displacement in the center of the skin where it would otherwise be largest. Compared with the optimized design in Fig. 5.6(f) maximizing  $F_{r,total}$ , the stiffeners in Fig. 5.6(a) are taller increasing the second moment of area and providing better suppression of out-of-plane displacements. The optimized design in Fig. 5.6(f) maximizing  $F_{r,total}$  on the other hand has a thicker skin to improve its load-carrying capability particularly along the tension diagonal, as shown in Fig. 5.4(b). For the same reason, its stiffeners lean more to the left, aligning with the direction of maximum compression.

In Fig. 5.7, it can be observed that the initial design starts to buckle at around  $u_a = 0.5368$  mm, with the out-of-plane displacement dominating when  $u_a$  is increased to 1.25 mm as shown in figure 5.5(c). A significant improvement in this buckling behaviour is seen for both optimized designs as shown in Fig. 5.6. When  $u_a = 1.25$  mm, the structures are only just beginning to buckle with the in-plane displacements dominating, especially for the optimized design in Fig. 5.6(a) minimizing  $P_{w,skin}$ . As shown in Table 5.2, compared with the initial design,  $P_{w,skin}$  is decreased by 88.8% for the optimized design in Fig. 5.6(a) minimizing  $P_{w,skin}$  with its  $F_{r,total}$  also being improved by 13.9%,

## Simultaneous Sizing, Layout and Topology Optimization for Buckling and Postbuckling of Stiffened Panels

and therefore satisfying the total reaction force constraint. Compared with the initial design,  $F_{r,\text{total}}$  is increased by 18.6% for the optimized design in Fig. 5.6(h) maximizing  $F_{r,\text{total}}$ .

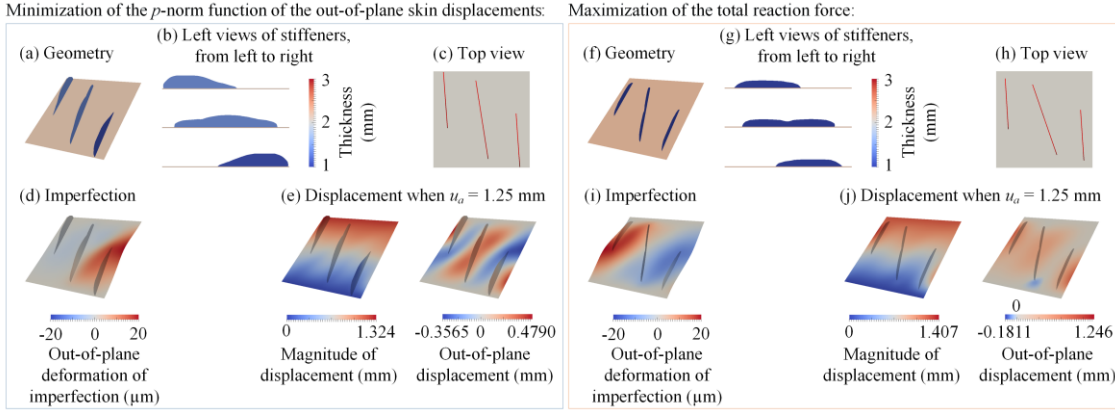


**Figure 5.6** Optimized designs of the stiffened panel under the design shear displacement  $u_a = 1.25$  mm.

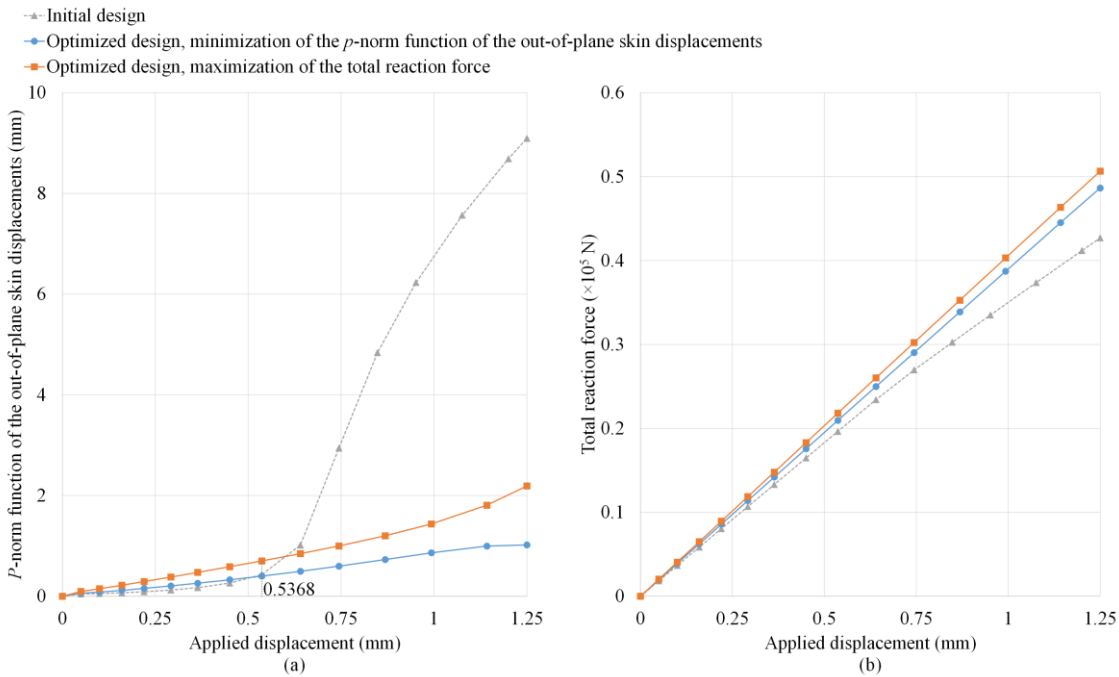


**Figure 5.7** Equilibrium paths for the initial and optimized designs of the stiffened panel under the design shear displacement  $u_a = 1.25$  mm.

**Table 5.2 Comparison of the initial and optimized designs of the stiffened panel under the design shear displacement  $u_a = 1.25$  mm.**

	$P_{w,skin}$	Percentage of improvement for $P_{w,skin}$ , compared to the initial design	$F_{r,total}$	Percentage of improvement for $F_{r,total}$ , compared to the initial design
Initial design	9.093	-	0.4270	-
Optimized design in Fig. 5.6(a) minimizing $P_{w,skin}$ using Eq. (5-12a)	1.020	88.8%	0.4864	13.9%
Optimized design in Fig. 5.6(f) maximizing $F_{r,total}$ using Eq. (5-12b)	2.191	75.9%	0.5064	18.6%

It is well known that the postbuckling analyses of stiffened panels can be sensitive to the imperfection introduced into the FE model. The optimized design in Fig. 5.6(a) optimizing  $P_{w,skin}$  is re-analyzed employing imperfections with different directions and maximum amplitudes. The analysis results are shown in Fig. 5.8. For a positive imperfection, the largest out-of-plane deformation occurs at the top of the right-hand side free edge, where the direction of the imperfection is opposite to that of the out-of-plane displacement of the panel. Therefore, when a positive imperfection is introduced, the magnitude of the out-of-plane displacements at the top of the right-hand-side free edge decreases as the maximum imperfection amplitude is increased. For the negative imperfection on the other hand, since directions of the out-of-plane displacement and negative imperfection deformation at the top right-hand-side free edge are the same, the magnitude of the out-of-plane displacements there increases. As shown in Fig. 5.9, employing imperfections with different directions having a maximum amplitude equal to  $20 \mu\text{m}$  in the postbuckling analysis, leads to a difference in the  $P_{w,skin}$  value of 112.5%. When the maximum imperfection amplitude is decreased to  $0.2 \mu\text{m}$  however, the difference is reduced to 0.81%. This shows that employing small imperfections can help to decrease the influence of the imperfection direction on the value of  $P_{w,skin}$ . This is in line with the general practice of using the imperfection with the smallest amplitude necessary to create a continuous path at the bifurcation point so that it has minimal effect on the structural overall behaviour. From Fig. 5.9(b), it can be found that  $F_{r,total}$  is less sensitive to the imperfection, compared with  $P_{w,skin}$ . For the optimized design in Fig. 5.6(a) optimizing  $P_{w,skin}$  employing imperfections with different directions and

**Simultaneous Sizing, Layout and Topology Optimization  
for Buckling and Postbuckling of Stiffened Panels**

maximum amplitudes from 0.2  $\mu\text{m}$  to 20  $\mu\text{m}$  for postbuckling analysis, the difference in  $F_{r,\text{total}}$  is within 0.21%.

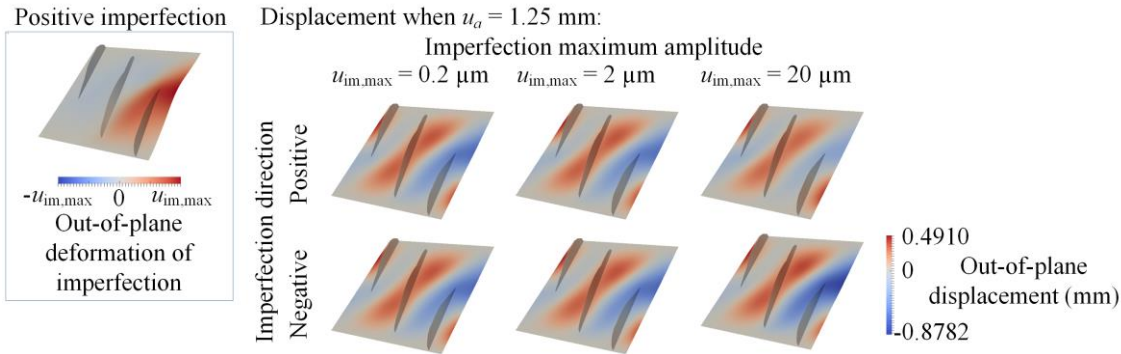


**Figure 5.8 Displacement configurations of the optimized design minimizing  $P_{w,\text{skin}}$ , employing different imperfections in the analysis, for the stiffened panel under the design shear displacement  $u_a = 1.25$  mm.**

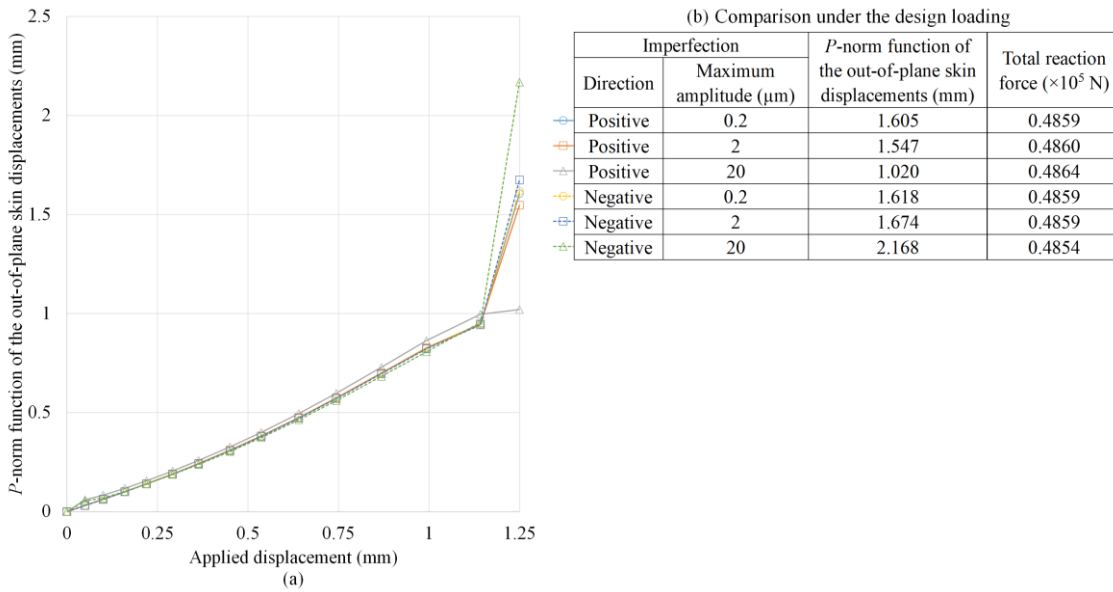


**Figure 5.9 Equilibrium paths and comparison of the optimized design minimizing  $P_{w,\text{skin}}$ , employing different imperfections in the analysis, for the stiffened panel under the design shear displacement  $u_a = 1.25$  mm.**

Understanding of how the imperfection introduced affects postbuckling optimization is still limited. To further investigate this, the optimization minimizing  $P_{w,\text{skin}}$  is repeated employing imperfections with different directions and maximum amplitudes. The results are shown in Fig. 5.10 and compared in Table 5.3. The imperfection direction and maximum amplitude listed in the first column is considered for all finite element

## Chapter 5: Simultaneous Sizing, Layout and Topology Optimization for Postbuckling of Panels with Straight Stiffeners

analyses in the optimization. The corresponding final optimized structure is given in the second to fourth columns. For the final optimized design, the imperfection introduced is shown in the fifth column. The final optimized design is then re-analyzed using this imperfection with different directions and maximum amplitudes. The analysis results are shown in the sixth to ninth columns. It can be observed from Fig. 5.10 that similar geometries and stiffener layouts can be obtained for optimizations minimizing  $P_{w,skin}$  employing imperfections with different directions and maximum amplitudes. As discussed for Figs. 5.8 and 5.9 however, the out-of-plane displacement configurations of the optimized designs are imperfection-sensitive. As shown in Table 5.3, their  $P_{w,skin}$  values vary greatly. For analyses employing the same imperfection directions and maximum amplitudes,  $P_{w,skin}$  achieves the lowest value when the same imperfection directions and maximum amplitudes are also employed in the optimization. However, a worse local optimum might be found. For the optimized design obtained from the optimization employing a negative imperfection with its maximum amplitude equal to  $0.2 \mu\text{m}$ , its  $P_{w,skin}$  value is larger than those obtained from the optimizations employing a positive imperfection, when the negative imperfection with the same maximum amplitude of  $0.2 \mu\text{m}$  is used. For all the designs employing imperfections with different directions and maximum amplitudes in analysis, the difference in their  $F_{r,total}$  values is within 0.8%, indicating these configurations are equally able to carry a similar load.

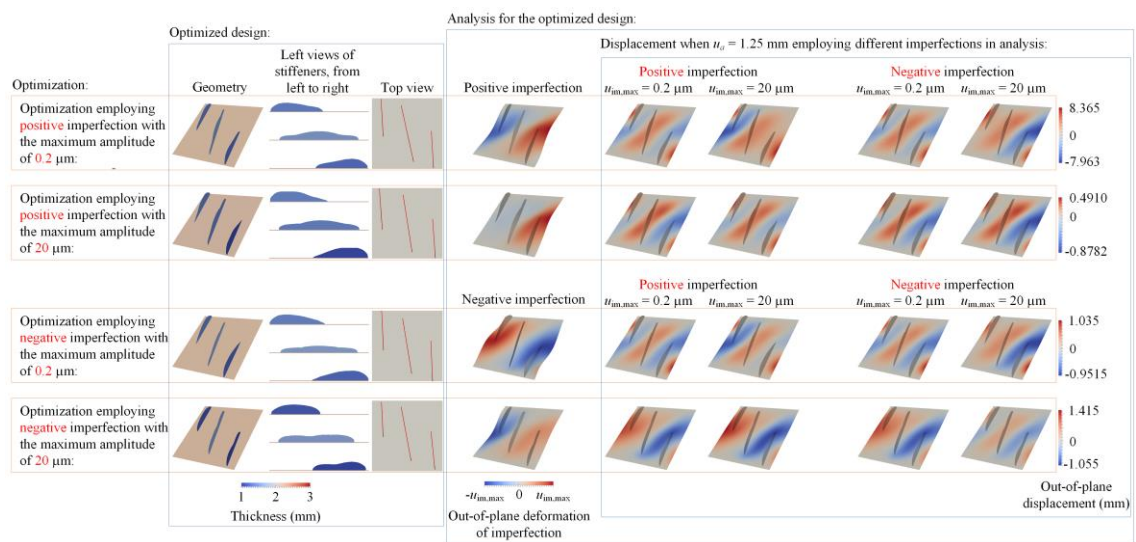


**Figure 5.10 Optimization results of minimizing  $P_{w,skin}$  employing different imperfections, for the stiffened panel under the design shear displacement  $u_a = 1.25 \text{ mm}$ .**

**Table 5.3 Comparison of the optimization results of minimizing  $P_{w,skin}$  employing different imperfections, for the stiffened panel under the design shear displacement  $u_a = 1.25$  mm.**

		Imperfection in analysis		Direction of imperfection in optimization			
				Positive		Negative	
		Direction	Maximum amplitude ( $\mu\text{m}$ )	$P_{w,skin}$ (mm)	$F_{r,total}$ ( $\times 10^5$ N)	$P_{w,skin}$ (mm)	$F_{r,total}$ ( $\times 10^5$ N)
Maximum amplitude of imperfection in optimization ( $\mu\text{m}$ )	0.2	Positive	0.2	1.560	0.4878	1.962	0.4849
			20	1.976	0.4876	2.255	0.4850
		Negative	0.2	1.561	0.4878	1.968	0.4849
			20	2.027	0.4876	2.533	0.4846
	20	Positive	0.2	1.605	0.4859	3.138	0.4870
			20	1.020	0.4864	3.684	0.4862
		Negative	0.2	1.618	0.4859	3.124	0.4870
			20	2.168	0.4854	1.591	0.4883

To study the convergence of the proposed algorithm, convergence history curves of the optimization minimizing  $P_{w,skin}$  employing positive imperfections with a maximum amplitude of 20  $\mu\text{m}$  (the optimized design given in Fig. 5.6(a)) are shown in Fig. 5.11. The total reaction force constraint is inactive during the whole optimization. At the beginning of the optimization, though the structural mass is decreased due to the mass constraint, both  $P_{w,skin}$  and  $F_{r,total}$  are improved due to the layout update and material redistribution. From the 47th iteration this behaviour changes and as the mass continues to be reduced,  $F_{r,total}$  starts to decrease. This changes again when the 88th iteration is reached, where the mass constraint is satisfied, and  $F_{r,total}$  begins to increase again. During the optimization, oscillations are seen in the curve of the objective function  $P_{w,skin}$ . To investigate the reason for this, the structure's geometry and response at the 66th-73rd iterations, is investigated (Figs. 5.12 and 5.13). In Fig. 5.12, it can be observed that for the 66th and 67th iterations, whilst the imperfections employed in the analysis are the same, mode switching occurs. The buckling modes have the same shape but different amplitudes. It is noted that for the structures at the 66th and 67th iterations,

the amplitudes of their first linear buckling modes at the bottom left-hand-side free edge are larger than those at the top right-hand-side free edge. Therefore, according to the definition of the positive imperfection, the deformations of the imperfections employed in the analysis are upward at the bottom left-hand-side free edge, and downward at the top right-hand-side free edge. As the structure is optimized, the first linear buckling mode gradually changes. At the 68th iteration, the amplitude of the first linear buckling mode at the top right-hand-side free edge becomes larger than that at the bottom left-hand-side free edge. Therefore, the deformation direction of the imperfection is changed, and it is opposite to those at the 66th and 67th iterations. The opposite direction of the out-of-plane displacements is also observed. This shows the direction of the out-of-plane displacements depends on the deformation direction of the employed imperfection. From the 68th iteration to the 72nd iteration, two imperfections with different amplitudes switch with each other, as well as two buckling modes with different maximum magnitudes of out-of-plane displacements. From the 72nd iteration to the 73rd iteration, the deformation direction of the imperfection is changed again, and mode switching occurs – a buckling mode with a different shape is introduced. In Fig. 5.13, it can be observed that for the 66th-73rd iterations, the differences in the  $P_{w,skin}$  values start to become larger from  $u_a = 0.744$  mm, but the values are still close for those with the same buckling modes. Though there are differences in the  $P_{w,skin}$  values at  $u_a = 1.25$  mm of up to 79.2%, the corresponding differences in  $F_{r,total}$  are within 1.5%. It is noted that for a design, a smaller  $P_{w,skin}$  value does not necessarily mean a larger  $F_{r,total}$ , e.g., for the 66th and 73rd iterations.

**Simultaneous Sizing, Layout and Topology Optimization  
for Buckling and Postbuckling of Stiffened Panels**

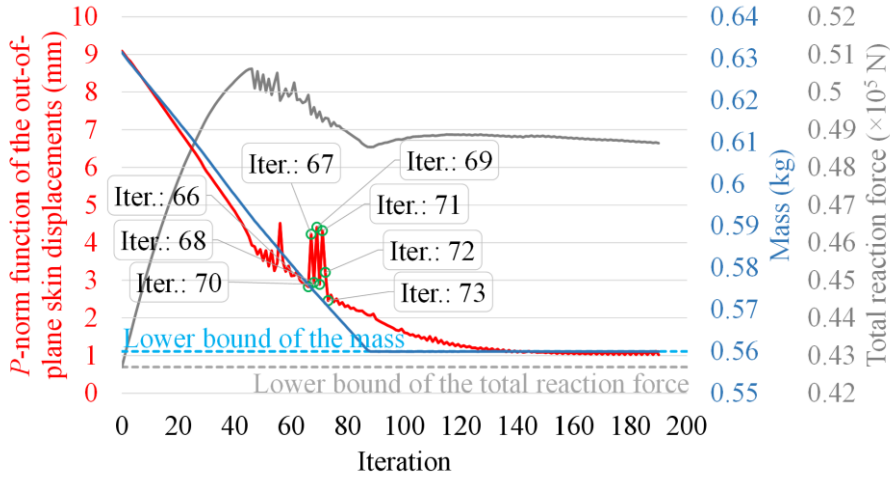


**Figure 5.11** Convergence history curves of the optimization minimizing  $P_{w,skin}$  employing positive imperfections with an amplitude of  $20\ \mu\text{m}$ , for the stiffened panel under the design shear displacement  $u_a = 1.25\ \text{mm}$ .

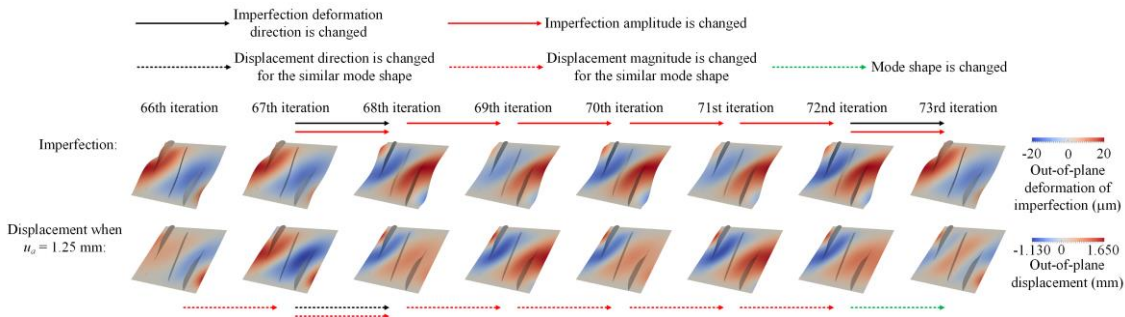


**Figure 5.12** Employed imperfection and displacement configurations of the optimized designs at the 66th-73rd iterations of minimizing  $P_{w,skin}$  employing positive imperfections with an amplitude of  $20\ \mu\text{m}$ , for the stiffened panel under the design shear displacement  $u_a = 1.25\ \text{mm}$ .

**Chapter 5: Simultaneous Sizing, Layout and Topology Optimization for Postbuckling of Panels with Straight Stiffeners**

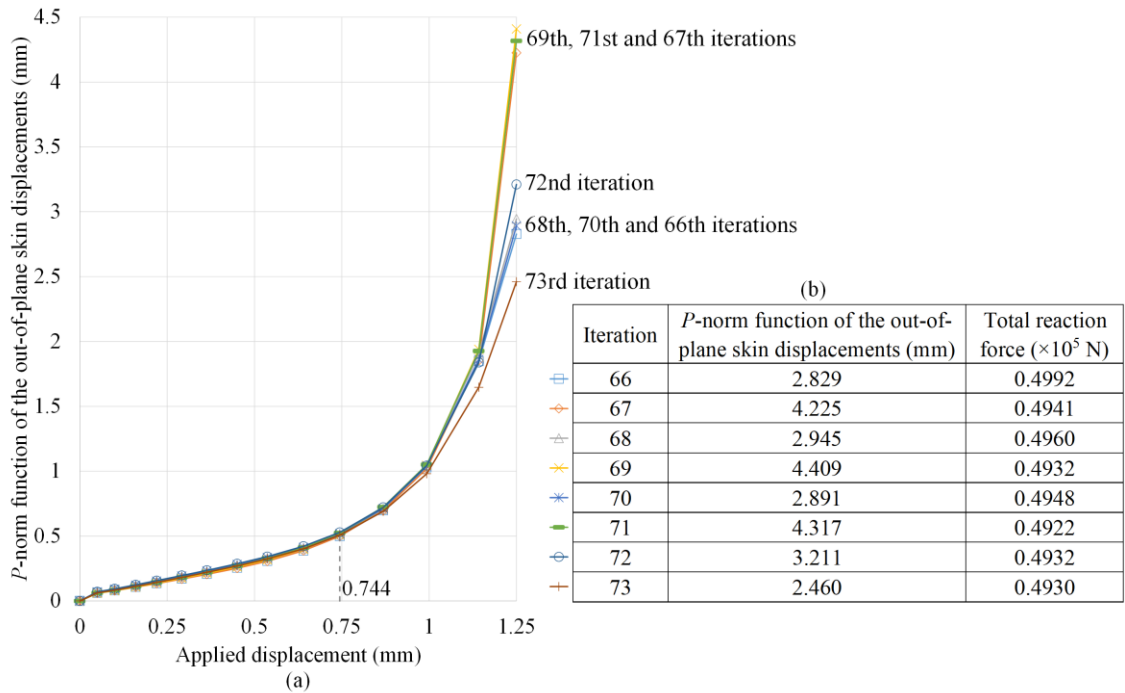


**Figure 5.13** Equilibrium paths of the optimized designs at the 66th-73rd iterations of minimizing  $P_{w,skin}$  employing positive imperfections with an amplitude of  $20 \mu\text{m}$ , for the stiffened panel under the design shear displacement  $u_a = 1.25 \text{ mm}$ .

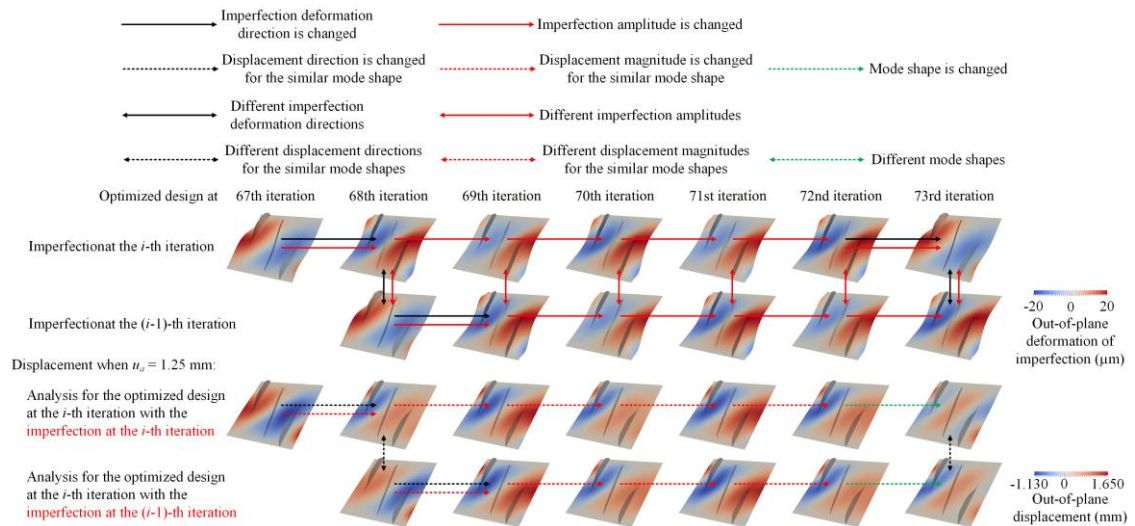


**Figure 5.14** Comparison of displacement configurations of the structures at the  $i$ -th iterations, employing the imperfections at the  $i$ -th and  $(i-1)$ -th iterations in analysis, for the optimized designs at the 68th-73rd iterations of minimizing  $P_{w,skin}$  under the design shear displacement  $u_a = 1.25 \text{ mm}$ .

**Simultaneous Sizing, Layout and Topology Optimization  
for Buckling and Postbuckling of Stiffened Panels**

**Table 5.4 Comparison of the  $P_{w,skin}$  value of the structures at the  $i$ -th iterations, employing the imperfections at the  $i$ -th and  $(i-1)$ -th iterations in the analysis, for the optimized designs at the 68th-73rd iterations of minimizing  $P_{w,skin}$  under the design shear displacement  $u_a = 1.25$  mm.**

Iteration	$P_{w,skin}$ (mm)	
	Employing the imperfection at the $i$ -th iteration	Employing the imperfection at the $(i-1)$ -th iteration
67	4.225	-
68	2.945	3.151
69	4.409	4.410
70	2.891	3.186
71	4.317	4.330
72	3.211	3.028
73	2.460	2.731

As shown in Figs. 5.12 and 5.13, mode switching is the main reason for the increase in the objective function value from the 66th to 67th iteration, but the oscillations from the 67th to 73rd iterations, could be caused by either/both mode switching and changes of imperfections. To investigate the underlying cause, the designs at the 68th-73rd iterations are re-analyzed with the imperfections at the previous iterations. The results are shown in Fig. 5.14 and compared in Table 5.4. For the structure at the 68th iteration, two imperfections at the 67th and 68th iterations with different deformation directions are employed for analysis, respectively. As discussed above, the direction of the out-of-plane displacement depends on the deformation direction of the imperfection employed in the analysis. When the structure is analyzed employing the imperfection at the 67th iteration, both the buckling mode and the imperfection have the upward deformation at the bottom left-hand-side free edge, and downward deformation at the top right-hand-side free edge. When the imperfection at the 68th iteration is employed in the analysis, the out-of-plane displacements become downward at the bottom left-hand-side free edge and upward at the top right-hand-side free edge, in accordance with the deformation direction of the employed imperfection and opposite to the one at the 67th iteration. However, the difference between their  $P_{w,skin}$  values at  $u_a = 1.25$  mm is 7.0%, much less than this (43.5%, the calculation is based on the  $P_{w,skin}$  value (2.945) for the

## Chapter 5: Simultaneous Sizing, Layout and Topology Optimization for Postbuckling of Panels with Straight Stiffeners

structure at the 68th iteration employing the imperfection at the 68th iteration) between the designs at 67th and 68th iterations employing the imperfections at the corresponding iterations. While when the imperfection at the 67th iteration is employed in the analyses for both the structures at 67th and 68th iterations, the difference in their  $P_{w,skin}$  values at  $u_a = 1.25$  mm is 25.4%, close to this (30.3%, the calculation is based on the  $P_{w,skin}$  value (4.225) for the structure at the 67th iteration employing the imperfection at the 67th iteration) between the designs at 67th and 68th iterations employing the imperfections at the corresponding iterations. This shows that mode switching is the main reason for the oscillation.

For the design at the 69th iteration, the imperfections at the 68th and 69th iterations are respectively employed in the analysis. Though the two imperfections have different ratios between their positive and negative amplitudes, the same buckling modes are obtained. The difference between the  $P_{w,skin}$  values at  $u_a = 1.25$  mm is only 0.023%. The same phenomenon is found for the designs at the 70th-72nd iterations.

As shown in Fig. 5.12, it is obvious that mode switching occurs between the designs at the 72nd and 73rd iterations. In Fig. 5.14 however, it can be observed that for the buckling modes of the design at the 73rd iteration respectively employing the imperfections at the 72nd and 73rd iterations, though the change of deformation direction of the imperfection causes different negative amplitudes, their shapes are still similar. The results therefore show that although the imperfections have an influence on the results of the analysis, the underlying cause of the change in buckling modes and oscillations of the objective function value during the optimization is mode switching. This conclusion is also applied to other oscillations shown in Fig. 5.11 which have been investigated, but not shown.

The convergence of the optimization maximizing  $F_{r,total}$  in Eq. (5-12b) has also been investigated. Only small oscillations of the objective function value are found during the optimization, and mode switching is also found to be the underlying reason.

Design displacement level  $u_a = 5$  mm:

The optimized designs under the design shear displacement  $u_a = 5$  mm are shown in Fig. 5.15. Their equilibrium paths are given in Fig. 5.16. A comparison between the initial and optimized designs is given in Table 5.5. In the same way as for the optimized

**Simultaneous Sizing, Layout and Topology Optimization  
for Buckling and Postbuckling of Stiffened Panels**

design in Fig. 5.6(a) optimizing  $P_{w,skin}$  at  $u_a = 1.25$  mm, for the optimized design in Fig. 5.15(a) optimizing  $P_{w,skin}$  at  $u_a = 5$  mm, the outermost stiffeners, move closer to the side edges of the skin, with its three stiffeners remaining parallel to each other, to decrease the out-of-plane skin displacements. In this case however its stiffeners are longer since buckling occurs over the whole panel.

Compared with the optimized design in Fig. 5.15(a) minimizing  $P_{w,skin}$ , the optimized design in Fig. 5.15(h) maximizing  $F_{r,total}$  has a thicker skin, and its stiffeners lean more to the left, aligning with the direction of maximum compression. Compared with the design in Fig. 5.6(f) maximizing  $F_{r,total}$  at  $u_a = 1.25$  mm, the design in Fig. 5.15(h) maximizing  $F_{r,total}$  at  $u_a = 5$  mm also has longer stiffeners.

As shown in Figs. 5.15 and 5.16, mode jumping is found at around  $u_a = 1.972$  mm for the optimized design in Fig. 5.15(a) minimizing  $P_{w,skin}$ , but not for the one in Fig. 5.15(h) maximizing  $F_{r,total}$ . Table 5.5 highlights a decrease in the  $P_{w,skin}$  of 62.0% for the optimized design in Fig. 5.15(a) minimizing  $P_{w,skin}$  compared with initial configuration whilst  $F_{r,total}$  is improved by 1.00%, satisfying the total reaction force constraint. When maximizing  $F_{r,total}$ , its value is increased by 24.9% for the optimized design in Fig. 5.15(h), compared with the initial design.

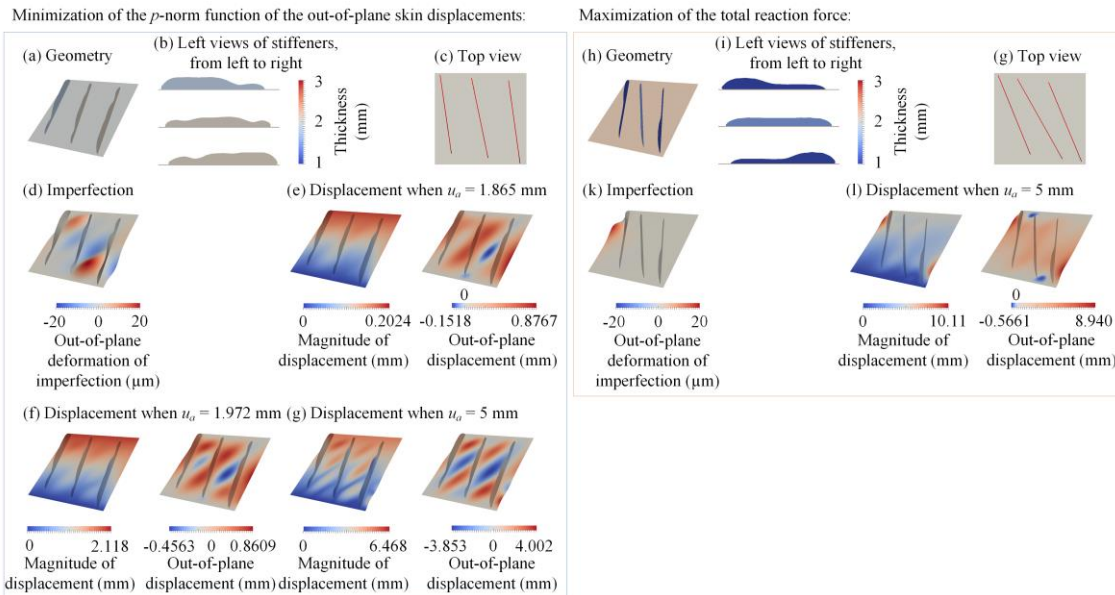


**Figure 5.15 Optimized designs of the stiffened panel under the design shear displacement  $u_a = 5$  mm.**

## Chapter 5: Simultaneous Sizing, Layout and Topology Optimization for Postbuckling of Panels with Straight Stiffeners

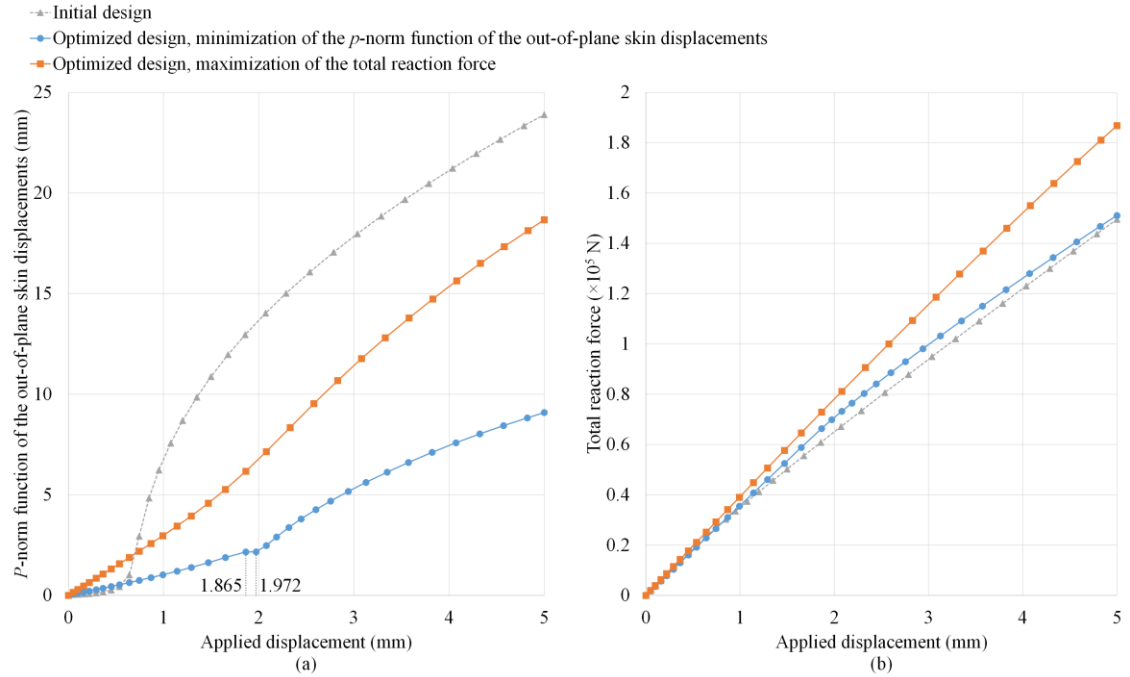


**Figure 5.16** Equilibrium paths for the initial and optimized designs of the stiffened panel under the design shear displacement  $u_a = 5$  mm.

**Table 5.5** Comparison of the initial and optimized designs of the stiffened panel under the design shear displacement  $u_a = 5$  mm.

	$P_{w,skin}$	Percentage of improvement for $P_{w,skin}$ , compared to the initial design	$F_{r,total}$	Percentage of improvement for $F_{r,total}$ , compared to the initial design
Initial design	23.90	-	1.496	-
Optimized design in Fig. 5.15(a) minimizing $P_{w,skin}$ in Eq. (5-12a)	9.090	62.0%	1.511	1.00%
Optimized design in Fig. 5.15(h) maximizing $F_{r,total}$ in Eq. (5-12b)	18.67	21.9%	1.868	24.9%

To again examine the effect of imperfections, the optimized design in Fig. 5.15(a) optimizing  $P_{w,skin}$  is re-analyzed, employing imperfections with different directions and maximum amplitudes. The results are shown in Figs. 5.17 and 5.18 and compared in Table 5.6. From Fig. 5.17 and 5.18, it can be seen that when  $u_a = 1.865$  mm, the structure is in the initial postbuckling regime. As discussed for Figs. 5.8 and 5.9, the  $P_{w,skin}$  value is sensitive to the employed imperfection. The maximum value of the downward out-of-plane displacements between the stiffeners at the right-hand side is

**Simultaneous Sizing, Layout and Topology Optimization  
for Buckling and Postbuckling of Stiffened Panels**

dependent on the direction and amplitude of the imperfection. As  $u_a$  is increased, mode jumping occurs in all cases. For both the cases employing positive and negative imperfections with maximum amplitudes equal to  $0.2 \mu\text{m}$  and  $2 \mu\text{m}$ , the buckling modes observed are the same. The differences in their  $P_{w,skin}$  values are within 0.1%. For the case employing the negative imperfection with the maximum amplitude equal to  $20 \mu\text{m}$ , the buckling mode is the same as that found in the other cases until  $u_a = 4.947$  mm. However, another mode jumping occurs after that, leading to a change in the buckling mode. Compared with the other cases, its  $P_{w,skin}$  value at  $u_a = 5$  mm is increased by 32%. For  $F_{r,total}$ , it is less sensitive to the employed imperfection. Compared with the other cases,  $F_{r,total}$  for the case employing the negative imperfection with the maximum amplitude equal to  $20 \mu\text{m}$  is decreased by 1.0% at  $u_a = 5$  mm.

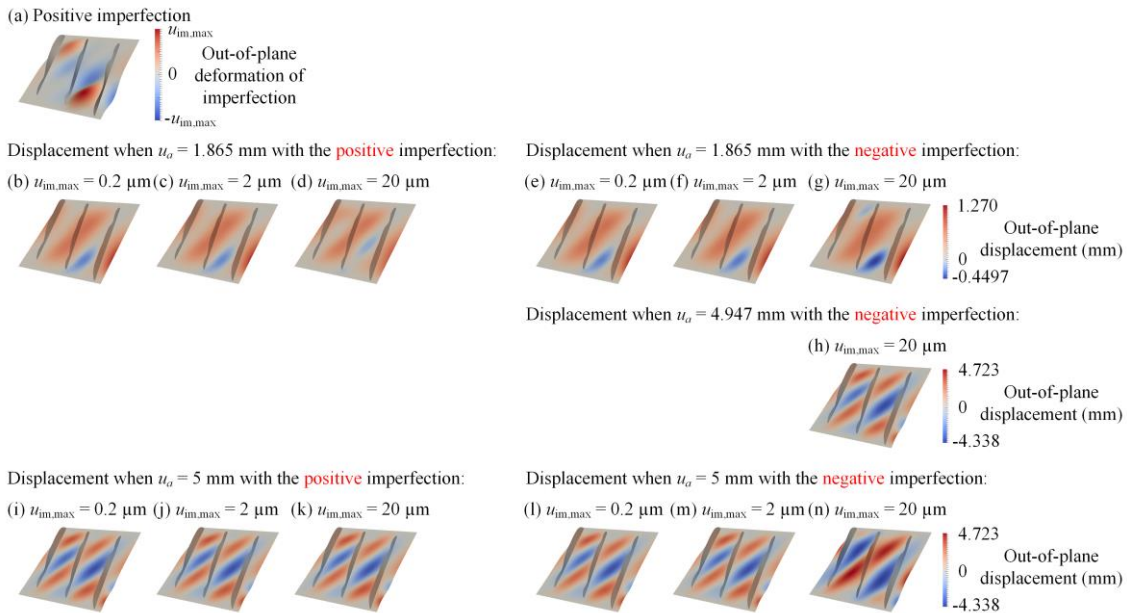


**Figure 5.17 Displacement configurations of the optimized design of minimizing  $P_{w,skin}$ , employing imperfections with different directions and amplitudes in the analysis, for the stiffened panel under the design shear displacement  $u_a = 5$  mm.**

## Chapter 5: Simultaneous Sizing, Layout and Topology Optimization for Postbuckling of Panels with Straight Stiffeners

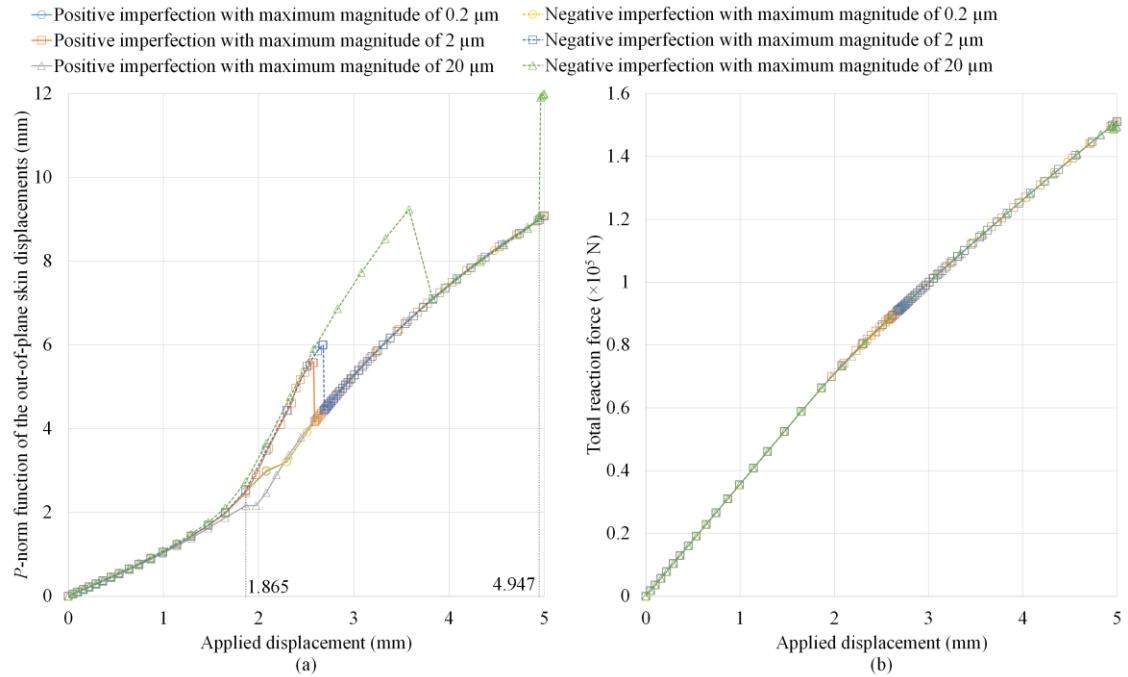


**Figure 5.18** Equilibrium paths for the optimized design of minimizing  $P_{w,skin}$ , employing imperfections with different directions and amplitudes in the analysis, for the stiffened panel under the design shear displacement  $u_a = 5$  mm.

**Table 5.6** Comparison of analysis results of the optimized design of minimizing  $P_{w,skin}$ , employing imperfections with different directions and amplitudes in the analysis, for the stiffened panel under the design shear displacement  $u_a = 5$  mm.

Imperfection		$P_{w,skin}$ (mm)	$F_{r,total}$ ( $\times 10^5$ N)
Direction	Amplitude ( $\mu\text{m}$ )		
Positive	0.2	9.083	1.511
Positive	2	9.081	1.511
Positive	20	9.090	1.511
Negative	0.2	9.083	1.511
Negative	2	9.087	1.511
Negative	20	11.99	1.496

To study the convergence of the proposed algorithm for design in the moderately deep postbuckling regime, convergence history curves of the optimization minimizing  $P_{w,skin}$  (the optimized design given in Fig. 5.15(a)) are shown in Fig. 5.19. To investigate the reasons for the oscillations, some of the iterations with oscillations are investigated.

**Simultaneous Sizing, Layout and Topology Optimization  
for Buckling and Postbuckling of Stiffened Panels**

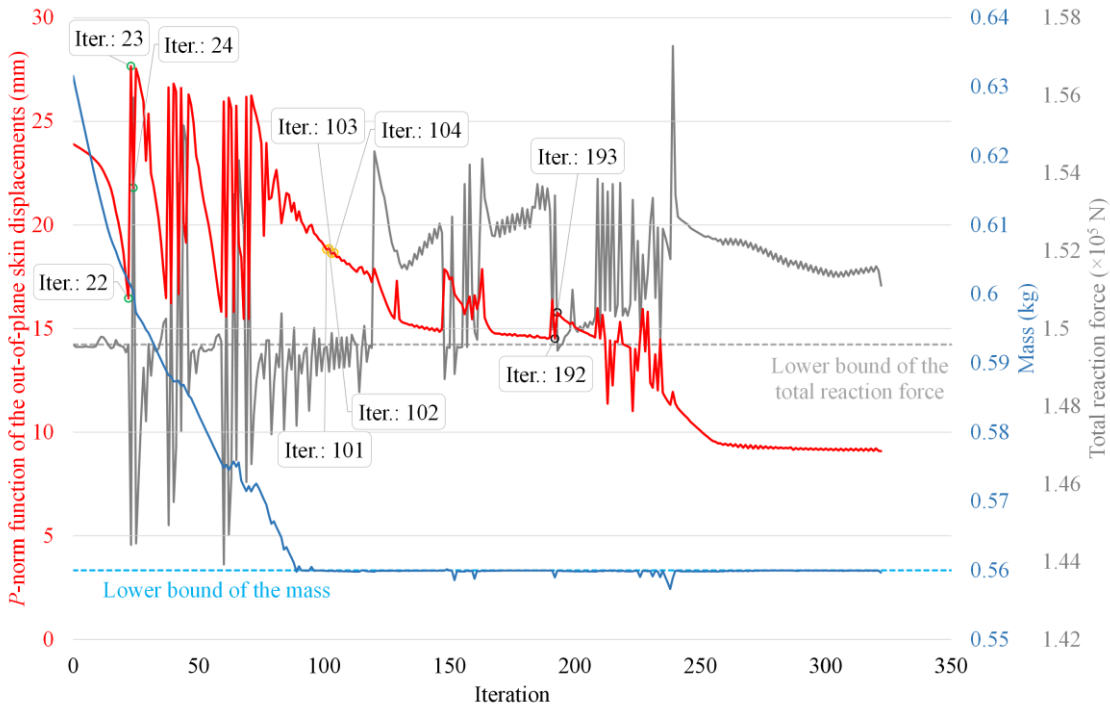


**Figure 5.19** Convergence history curves of the optimization minimizing  $P_{w,skin}$ , for the stiffened panel under the design shear displacement  $u_a = 5$  mm.

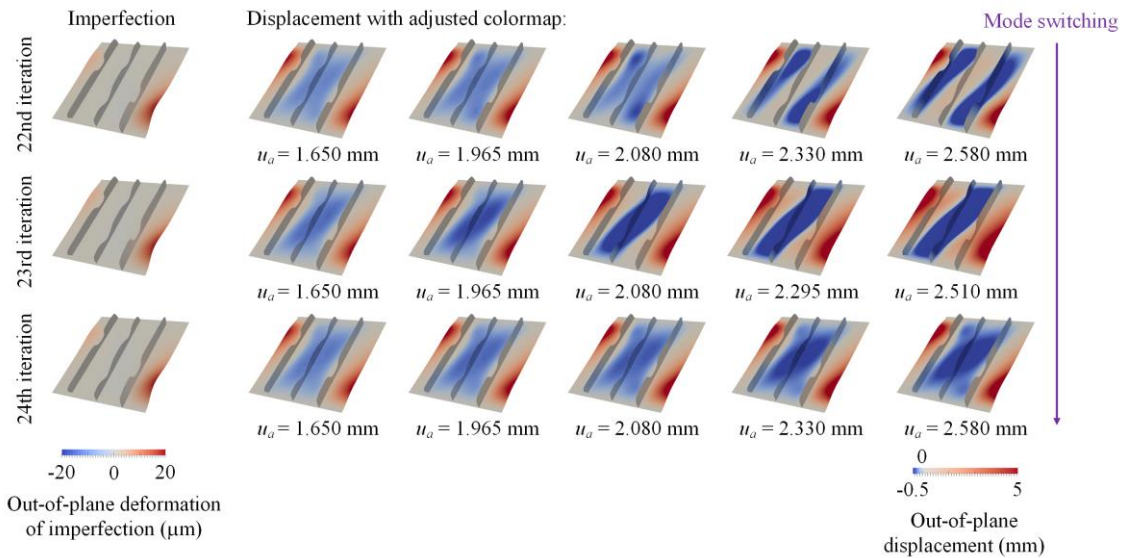


**Figure 5.20** Employed imperfections and displacement configurations of the optimized designs at the 22nd-24th iterations of minimizing  $P_{w,skin}$ , for the stiffened panel under the design shear displacement  $u_a = 5$  mm.

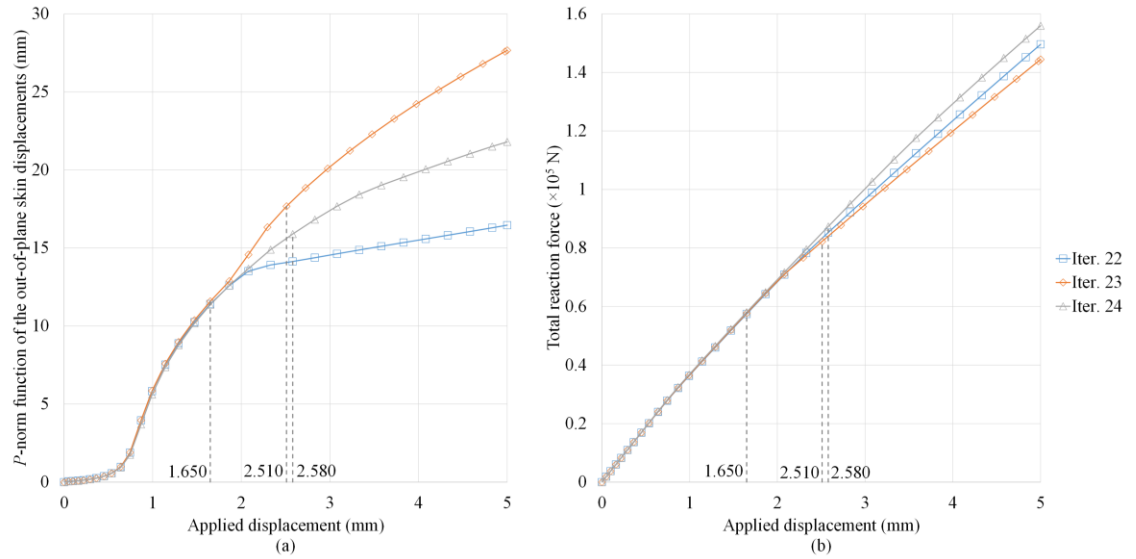


**Figure 5.21** Equilibrium paths for the optimized designs at the 22nd-24th iterations of minimizing  $P_{w,skin}$ , for the stiffened panel under the design shear displacement  $u_a = 5$  mm.

**Table 5.7** Comparison of the optimized designs at the 22nd-24th iterations of minimizing  $P_{w,skin}$ , for the stiffened panel under the design shear displacement  $u_a = 5$  mm.

Iteration	$P_{w,skin}$ (mm)	$F_{r,total}$ ( $\times 10^5$ N)
22	16.46	1.496
23	27.66	1.444
24	21.80	1.559

The optimized structures and corresponding structural responses from the 22nd-24th iterations are shown in Figs. 5.20 and 5.21. Noted that the colormap of the out-of-plane displacement is adjusted to allow all the figures to share the same colormap for comparison and still be readable. Displacements over the upper and lower bounds of the colormap have the same colors as those at the upper and lower bounds. From Fig. 5.19, it can be observed that until the 22nd iteration, though the mass is reduced due to the mass constraint, the value of  $P_{w,skin}$  decreases due to the layout optimization and material redistribution. At the 23rd iteration however, it becomes larger. This is because of mode switching – a buckling mode, different from the one at the 22nd iteration, occurs. It can be seen in Fig. 5.20 that at the 22nd iteration, the structure buckles at the

### Simultaneous Sizing, Layout and Topology Optimization for Buckling and Postbuckling of Stiffened Panels

two free edges with upward deformations, and between the stiffeners with downward deformations when  $u_a = 1.650$  mm. As  $u_a$  is increased, the downward deformations between the stiffeners become larger. When  $u_a = 2.330$  mm, buckles crossing the two side stiffeners are observed. For the design at the 23rd iteration, when  $u_a = 1.650$  mm, the downward out-of-plane displacements crossing the middle stiffener are larger than those at the 22nd iteration. As  $u_a$  is increased, the buckling shape progresses. The deformations at the two free edges and crossing the middle stiffener increase. It is noted that at the 23rd iteration, mode switching not only causes the  $P_{w,skin}$  to increase, it also stops the total reaction force constraint from being satisfied. At the 24th iteration, mode switching also occurs. A buckling mode, different from those at the previous two iterations, is found. Though the  $P_{w,skin}$  value of the design at the 24th iteration is still larger than that at the 22nd iteration, it is decreased compared with the design at the 23rd iteration. Meanwhile,  $F_{r,total}$  is increased and the total reaction force constraint is satisfied again.

The optimized structures and corresponding structural responses at the 101st-104th iterations are shown in Figs. 5.22 and 5.23 and compared in Table 5.8. For all the analyses at the 101st-104th iterations, the same imperfections are employed. Similar buckling modes are found for all the designs at  $u_a = 2.330$  mm, but when  $u_a$  is increased to 2.580 mm, the buckling shapes are progressed and different buckling shapes are observed. This shows that mode switching occurs among these iterations. For the designs at the 101st and 103rd iterations, the buckling has upward deformation dominating the second bay (defined as the region between the panel edge and the side stiffener, or between the adjacent stiffeners, counted from left to right) and downward deformation crossing the third stiffener (counted from left to right). While for the 102nd and 104th iterations, the buckling has the upward deformation dominating on the third bay and downward deformation crossing the first stiffener. However, since the buckling mode has the largest deformations at the two free edges for all four designs and their magnitudes are close, the differences in the  $P_{w,skin}$  values of the four designs are within 1.4% at  $u_a = 2.580$  mm. When  $u_a$  is increased to 2.830 mm, the mode shapes continue to progress for the designs at the 101st and 103rd iterations, while mode jumping occurs for the designs at the 102nd and 104th iterations. The downward deformation of the buckling becomes to cross the middle stiffener. It can be seen from Fig. 5.23(a) that when  $u_a = 2.830$  mm, the differences in the  $P_{w,skin}$  values of the four designs increases to

## Chapter 5: Simultaneous Sizing, Layout and Topology Optimization for Postbuckling of Panels with Straight Stiffeners

6.0%. Mode jumping occurs at  $u_a = 3.580$  mm for the design at the 101st iteration, and at  $u_a = 3.592$  mm for the design at the 103rd iteration. An additional buckle occurs at the third bay and the buckle with the downward deformation crosses the middle stiffener. From Fig. 5.23(a), it can be found that the  $P_{w,skin}$  values of the four designs become close again after  $u_a = 3.592$  mm. The same phenomenon is found for the total reaction forces, as shown in Fig. 5.23(b). This is because, as shown in Fig. 5.22, after mode jumping occurs for all the four designs, the buckling shapes between adjacent iterations are basically symmetrical along the diagonal from the bottom left to the top right of the panel, resulting in similar postbuckling behaviours under the shear loading and boundary conditions in this example. It can be seen in Table 5.8 that for the four optimized structures at the 101st-104th iterations, the differences in their  $P_{w,skin}$  values and their  $F_{r,total}$  are within 1.3% and 0.7% at  $u_a = 5$  mm, respectively.

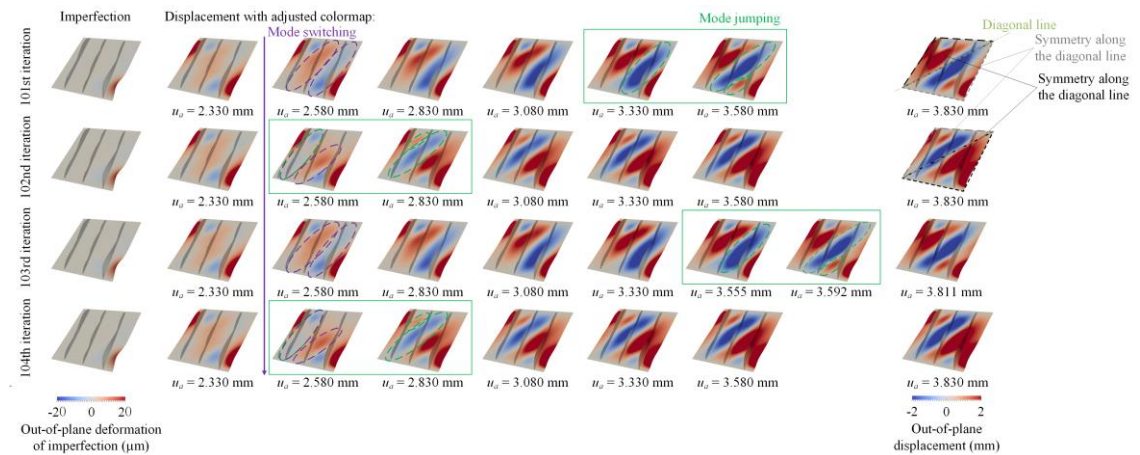


**Figure 5.22** Employed imperfections and displacement configurations of the optimized designs at the 101st-104th iterations of minimizing  $P_{w,skin}$ , for the stiffened panel under the design shear displacement  $u_a = 5$  mm.

**Simultaneous Sizing, Layout and Topology Optimization  
for Buckling and Postbuckling of Stiffened Panels**

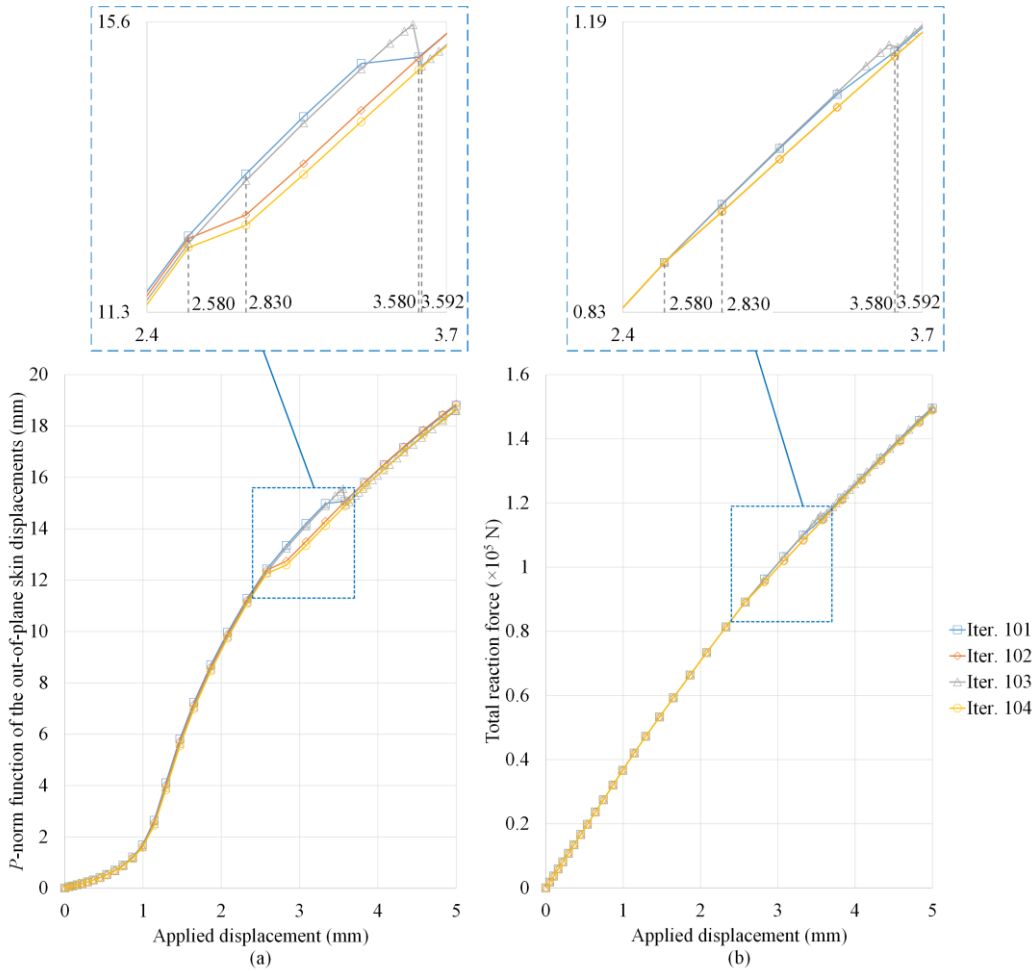


**Figure 5.23** Equilibrium paths for the optimized designs at the 101st-104th iterations of minimizing  $P_{w,skin}$ , for the stiffened panel under the design shear displacement  $u_a = 5$  mm.

**Table 5.8** Comparison of the optimized designs at the 101st-104th iterations of minimizing  $P_{w,skin}$ , for the stiffened panel under the design shear displacement  $u_a = 5$  mm.

Iteration	$P_{w,skin}$ (mm)	$F_{r,total}$ ( $\times 10^5$ N)
101	18.81	1.495
102	18.86	1.489
103	18.62	1.499
104	18.66	1.490

The optimized structures and corresponding structural responses at the 192nd-193rd iterations are shown in Figs. 5.24 and 5.25, and compared in Table 5.9. Mode switching and mode jumping both contribute to the  $P_{w,skin}$  value increasing at the 193rd iteration. In Fig. 5.24, different buckling modes are found at  $u_a = 3.580$  mm for the two iterations, indicating that mode switching occurs. For the 192nd iteration, when  $u_a$  is 4.330 mm, the buckling regions with downward deformations in the third and fourth bays start to be connected and cross the right-hand side stiffener. As shown in Fig. 5.25, the  $P_{w,skin}$  value decreases after that. As  $u_a$  continues to increase, the buckling shape progresses and the  $P_{w,skin}$  value increases again. For the 193rd iteration, mode jumping is observed when  $u_a = 3.805$  mm, leading to sudden decreases in both the  $P_{w,skin}$  and  $F_{r,total}$  values which become smaller than those at the 192nd iteration. However, as  $u_a$  is increased with the progressed buckling shape, the  $P_{w,skin}$  value increases rapidly. When  $u_a = 5$  mm, its value is 8.75% larger than that at the 192nd iteration.

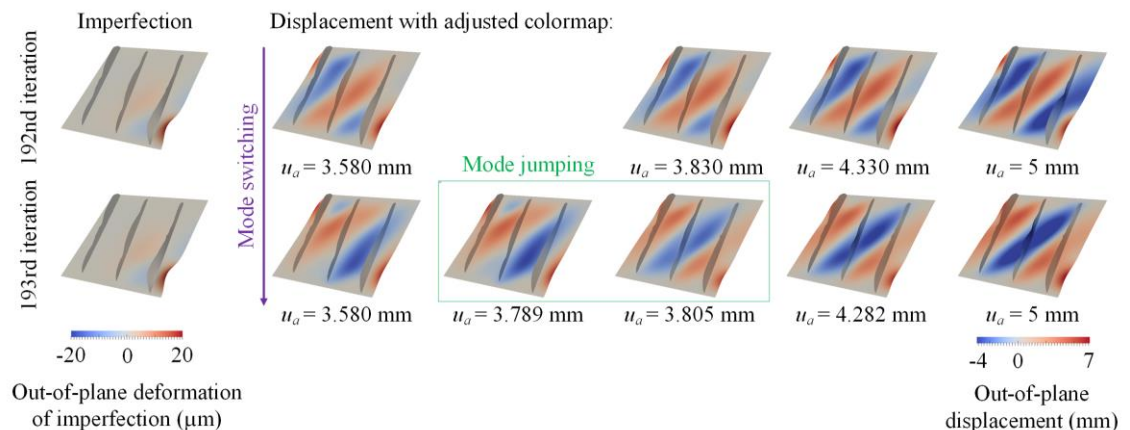


**Figure 5.24** Employed imperfections and displacement configurations of the optimized designs at the 192nd-193rd iterations of minimizing  $P_{w,skin}$ , for the stiffened panel under the design shear displacement  $u_a = 5$  mm.

### Simultaneous Sizing, Layout and Topology Optimization for Buckling and Postbuckling of Stiffened Panels

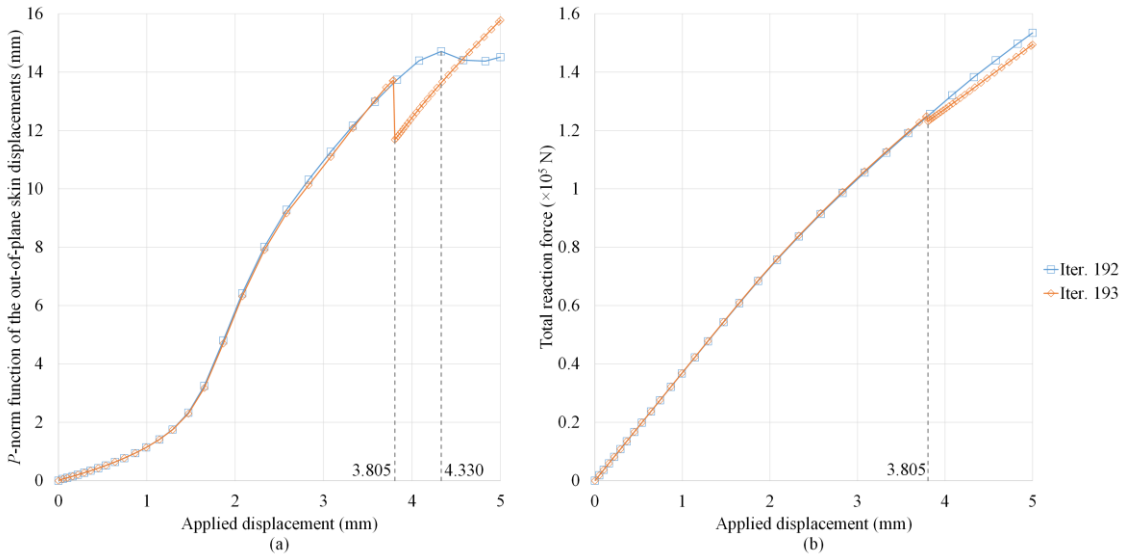


**Figure 5.25** Equilibrium paths for the optimized designs at the 192nd-193rd iterations of minimizing  $P_{w,skin}$ , for the stiffened panel under the design shear displacement  $u_a = 5$  mm.

**Table 5.9** Comparison of the optimized designs at the 192nd-193rd iterations of minimizing  $P_{w,skin}$ , for the stiffened panel under the design shear displacement  $u_a = 5$  mm.

Iteration	$P_{w,skin}$ (mm)	$F_{r,total}$ ( $\times 10^5$ N)
192	14.51	1.534
193	15.78	1.494

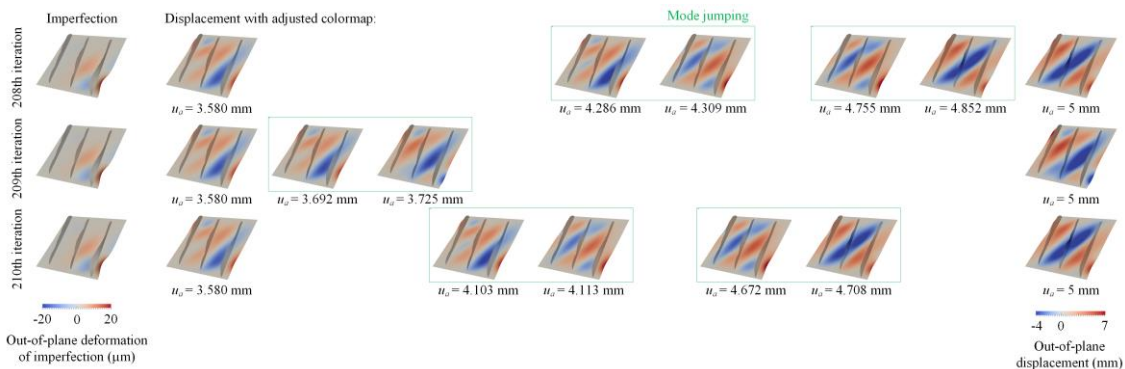


**Figure 5.26** Employed imperfections and displacement configurations of the optimized designs at the 208th-210th iterations of minimizing  $P_{w,skin}$ , for the stiffened panel under the design shear displacement  $u_a = 5$  mm.

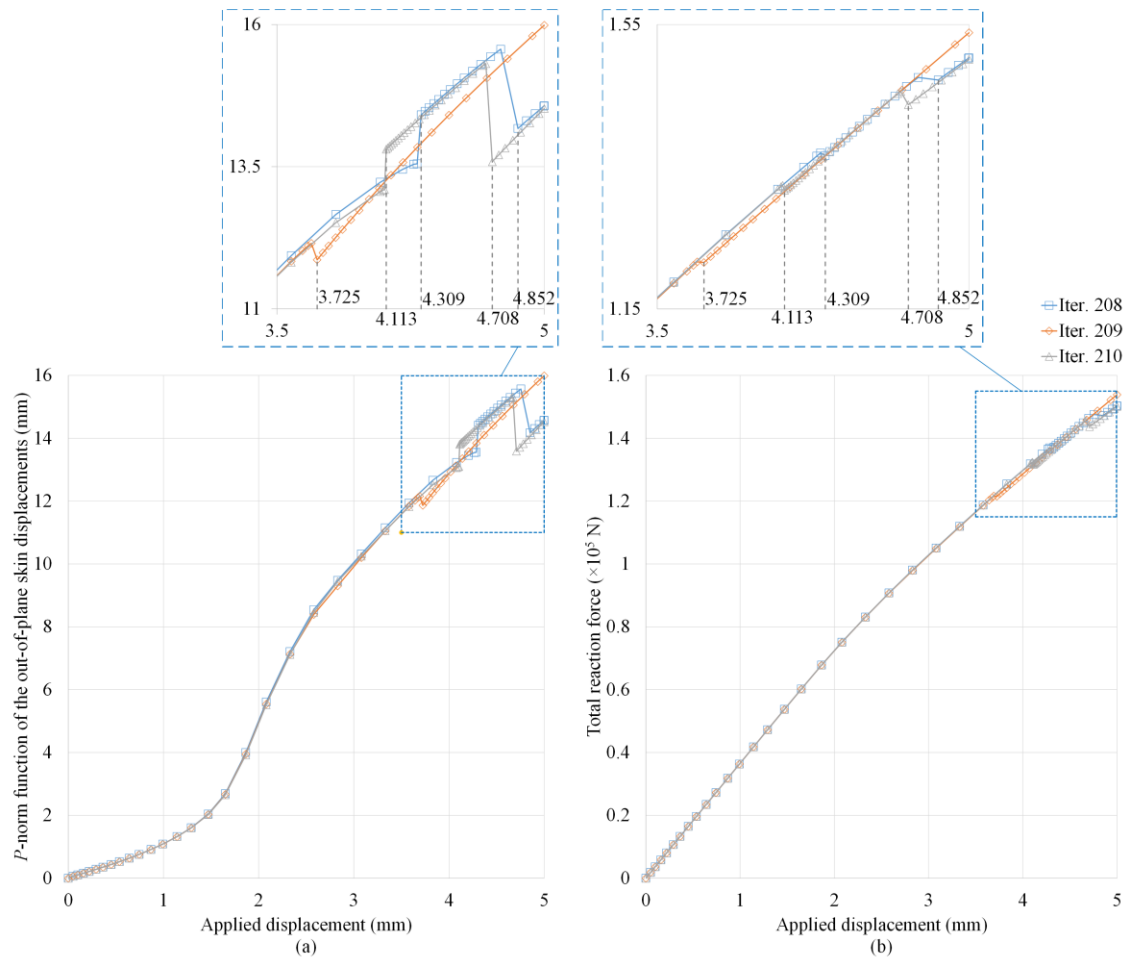


Figure 5.27 Equilibrium paths for the optimized designs at the 208th-210th iterations of minimizing  $P_{w,skin}$ , for the stiffened panel under the design shear displacement  $u_a = 5$  mm.

Table 5.10 Comparison of the optimized designs at the 208th-210th iterations of minimizing  $P_{w,skin}$ , for the stiffened panel under the design shear displacement  $u_a = 5$  mm.

Iteration	$P_{w,skin}$ (mm)	$F_{r,total}$ ( $\times 10^5$ N)
208	14.57	1.503
209	15.99	1.539
210	14.52	1.501

In this case, in the optimization minimizing  $P_{w,skin}$ , more complex postbuckling behaviours are observed. For a particular design, mode jumping sometimes occurs more than once, resulting in multiple significant changes in the  $P_{w,skin}$  value. During

### Simultaneous Sizing, Layout and Topology Optimization for Buckling and Postbuckling of Stiffened Panels

optimization, mode jumping can occur different times at different iterations and different buckling modes can be found at the design loading. This causes discontinuities in the optimization and oscillations in the objective function value. For example, the optimized structures and corresponding structural responses at the 208th-210th iterations are shown in Figs. 5.26 and 5.27 and compared in Table 5.10. At  $u_a = 3.580$  mm, the same buckling modes are found for all three iterations, showing that no mode switching occurs. During the 208th iteration however, mode jumping occurs twice at  $u_a = 4.309$  mm and 4.852 mm as is the case at  $u_a = 4.113$  mm and 4.708 mm during the 210th iteration. During the 209th iteration this reduces to one mode jump at  $u_a = 3.725$  mm with a different buckling mode from those at the 208th and 210th iterations, observed at the design displacement  $u_a = 5$  mm. Compared with the 208th iteration, the  $P_{w,skin}$  value at  $u_a = 5$  mm is increased by 9.75% at the 209th iteration. The same buckling modes are found at the 208th and 210th iterations. Compared with the 208th iteration, the value at the 210th iteration is improved by 0.343%. The same phenomenon is observed for  $F_{r,total}$ . Compared with the 208th iteration,  $F_{r,total}$  at  $u_a = 5$  mm is reduced by 2.40% at the 209th iteration and improved by 0.133% at the 210th iteration.

Though Fig. 5.17 shows that a change in imperfection direction can introduce mode jumping and lead to a different analysis result for the optimized design, it has not caused any oscillation in this example. To further investigate the influence of the imperfection direction on the optimization result, the optimization is repeated with negative imperfections. The optimized result and its comparison with the optimized design in Fig. 5.15(a) employing positive imperfections in the optimization are shown in Figs. 5.28 and 5.29. From Fig. 5.28, it can be seen that almost the same optimized designs are obtained, despite different imperfection directions being employed in the two optimizations. In Fig. 5.29 it can be seen that at first, different  $P_{w,skin}$  values are found for the two optimized designs. This is because, as discussed for Figs. 5.8 and 5.9,  $P_{w,skin}$  is sensitive to the employed imperfection during the initial postbuckling regime. As  $u_a$  increases, mode jumping occurs for the optimized design employing the negative imperfection. After that, the influence of the employed imperfection on the analysis is reduced and the two equilibrium paths for  $P_{w,skin}$  almost coincide. The difference between the  $P_{w,skin}$  values at  $u_a = 5$  mm is within 0.08%. For these two optimized designs, the curves of the equilibrium paths for  $F_{r,total}$  are very similar. The difference in  $F_{r,total}$  at  $u_a = 5$  mm is within 0.27%.

## Chapter 5: Simultaneous Sizing, Layout and Topology Optimization for Postbuckling of Panels with Straight Stiffeners

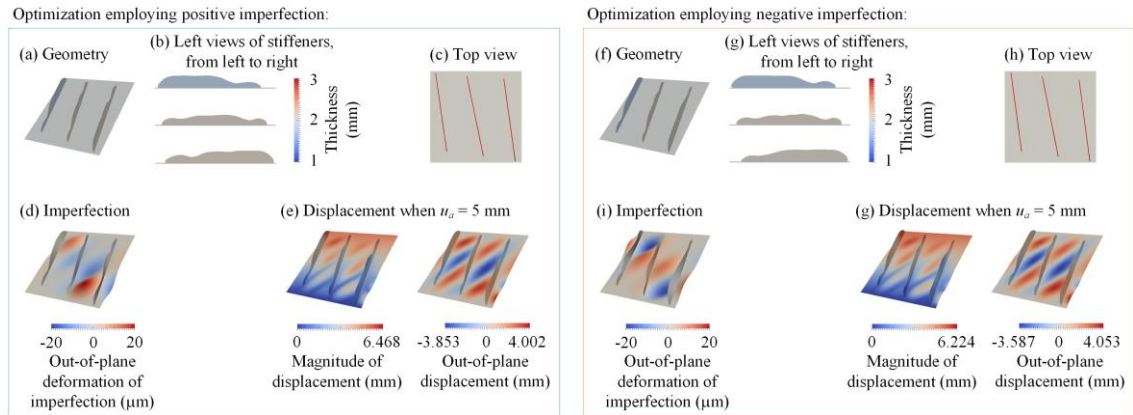


**Figure 5.28 Comparison of the optimized designs of minimizing  $P_{w,skin}$  employing positive and negative imperfections, for the stiffened panel under the design shear displacement  $u_a = 5$  mm.**

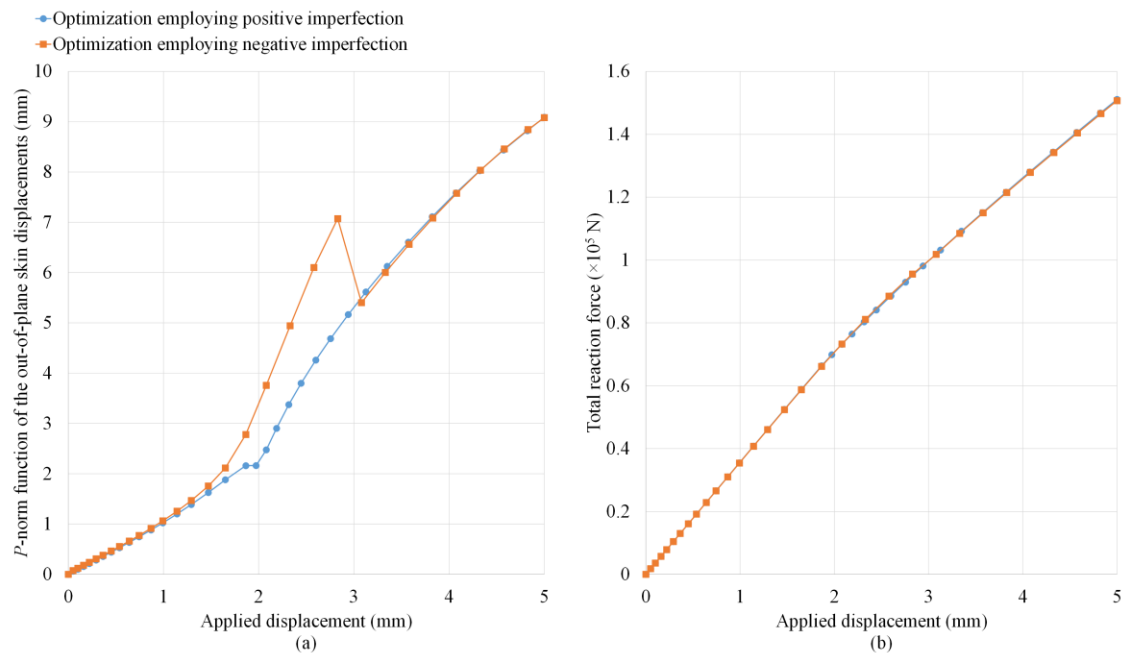


**Figure 5.29 Equilibrium paths for the optimized designs of minimizing  $P_{w,skin}$  employing positive and negative imperfections, for the stiffened panel under the design shear displacement  $u_a = 5$  mm.**

The convergence history curves for maximizing  $F_{r,total}$  (the optimized design given in Fig. 5.15(h)) are shown in Fig. 5.30. Though many oscillations are observed, an overall rise in  $F_{r,total}$  can be found after the mass constraint is satisfied. To investigate the reasons for these oscillations and their effect on the optimization, some of the iterations with oscillations are also investigated. The optimized structures and

**Simultaneous Sizing, Layout and Topology Optimization  
for Buckling and Postbuckling of Stiffened Panels**

corresponding structural responses at the 16th-19th iterations are shown in Figs. 5.31 and 5.32. When  $u_a = 4.580$  mm, the same buckling modes are found for these four optimized designs. For the 16th iteration, no mode jumping is found as  $u_a$  is increased to 5 mm. Whilst the buckling amplitude is increased, the mode shape stays the same. For the 17th iteration, mode jumping occurs at  $u_a = 4.830$  mm. This causes a decrease in  $F_{r,\text{total}}$ . For the 18th iteration, the same mode occurs but at a larger value of  $u_a = 4.979$  mm. Compared with the 17th iteration,  $F_{r,\text{total}}$  at  $u_a = 5$  mm is improved, though it is still lower than that at the 16th iteration. For the 19th iteration, mode jumping does not occur and the same buckling shape as the one at the 16th iteration is observed at  $u_a = 5$  mm. Compared with the 16th iteration,  $F_{r,\text{total}}$  at  $u_a = 5$  mm is improved by 0.968%. These iterations therefore indicate that without a mode jump the value of  $F_{r,\text{total}}$  achieved is higher.

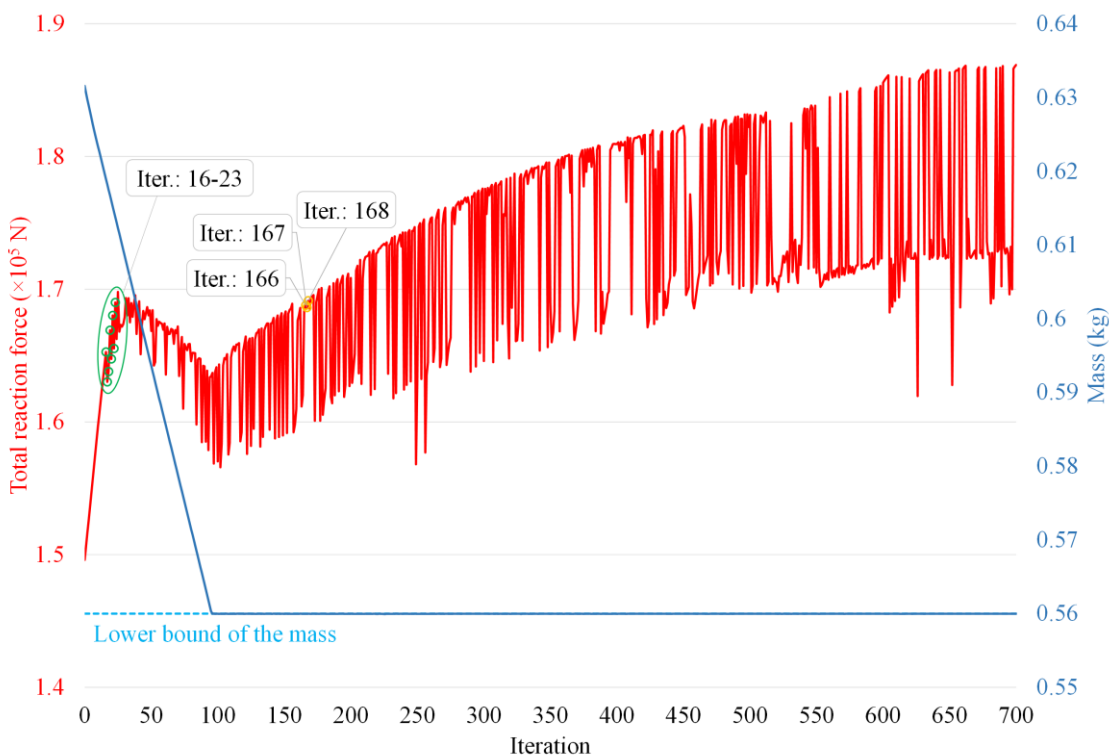


**Figure 5.30 Convergence history curves of the optimization maximizing  $F_{r,\text{total}}$ , for the stiffened panel under the design shear displacement  $u_a = 5$  mm.**

**Chapter 5: Simultaneous Sizing, Layout and Topology Optimization for Postbuckling of Panels with Straight Stiffeners**

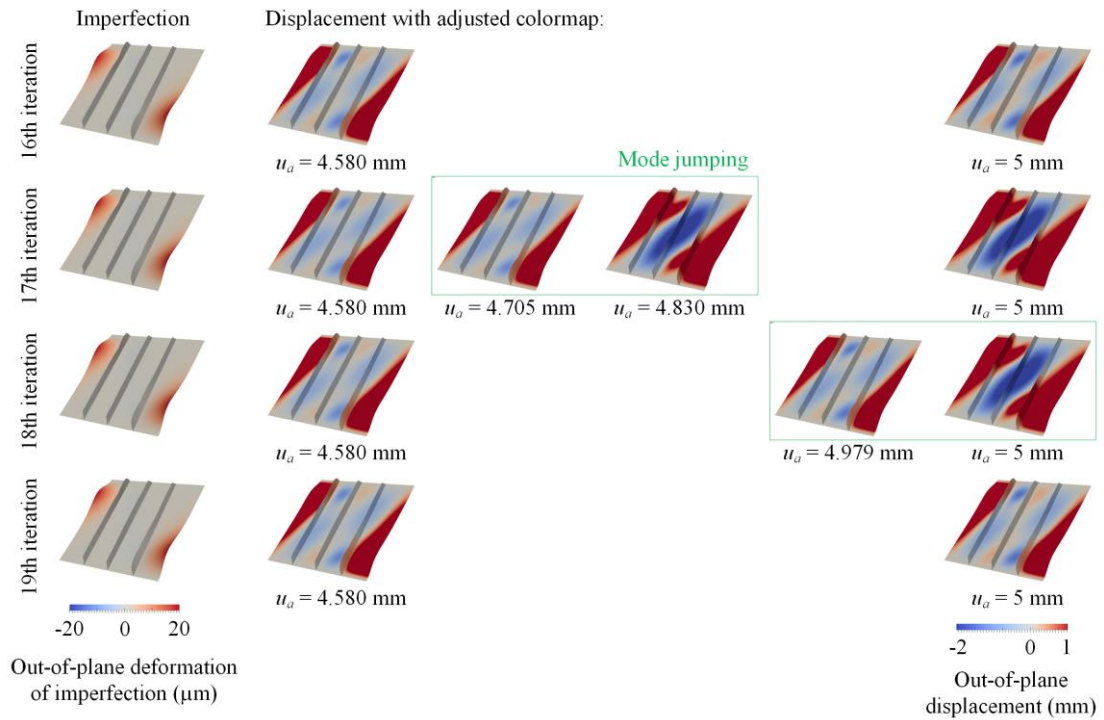


**Figure 5.31** Employed imperfections and displacement configurations of the optimized designs at the 16th-19th iterations of maximizing  $F_{r,total}$ , for the stiffened panel under the design shear displacement  $u_a = 5$  mm.

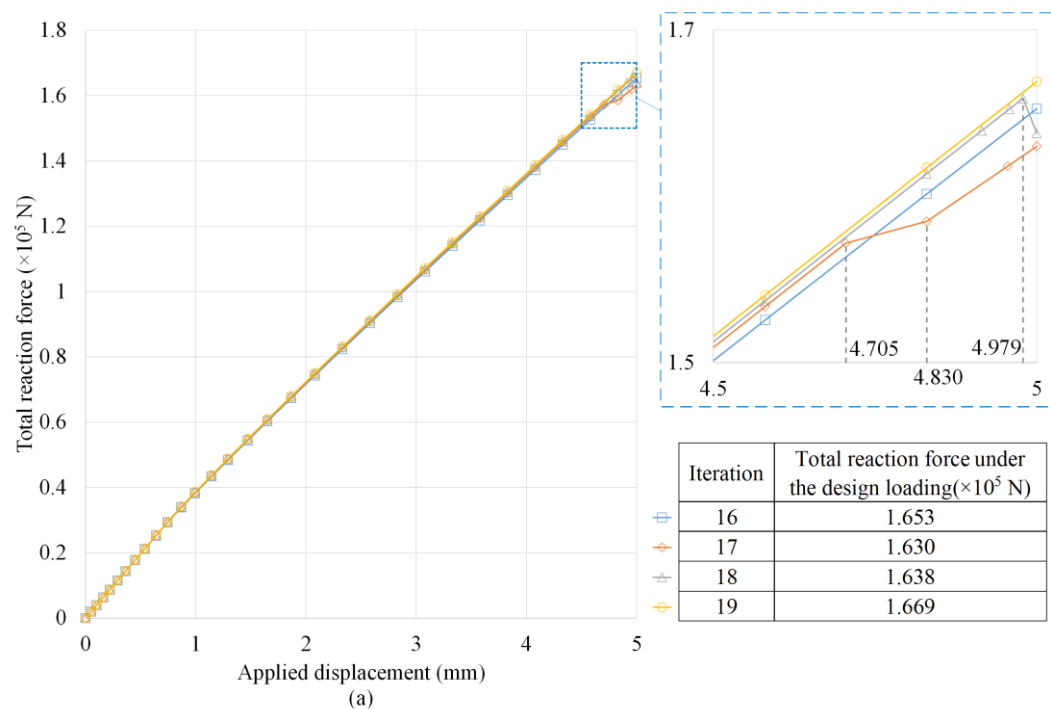


**Figure 5.32** Equilibrium paths and comparison of the optimized designs at the 16th-19th iterations of maximizing  $F_{r,total}$ , for the stiffened panel under the design shear displacement  $u_a = 5$  mm.

**Simultaneous Sizing, Layout and Topology Optimization  
for Buckling and Postbuckling of Stiffened Panels**

The optimized structures and corresponding structural responses at the following (19th-23rd) iterations are shown in Fig. 5.33, as well as their partial geometry parameters.  $y_1$ - $y_6$  are changes to the coordinates of the stiffeners' endpoints from left to right, top to bottom.  $t_1$ - $t_3$  are the thicknesses of the stiffeners from left to right.  $t_p$  is the skin thickness. It can be seen in Fig. 5.33(a) that two buckling shapes are repeatedly switched at  $u_a = 0.005$  m, causing the oscillations in the objective value shown in Fig. 5.33(b). Nevertheless, as shown in Fig. 5.33(c), the structures are continuously optimized. The outer two stiffeners move closer to the edges of the skin, and the middle stiffener leans more to the left. In order to increase  $F_{r,total}$ , the skin thickness is increased. To compensate for this and to continue to satisfy the mass constraint, the amount of material in the stiffeners is reduced. The optimization progresses well and  $F_{r,total}$  is continuously improved for the iterations having the same buckling shapes, i.e., 19th, 21st and 23rd iterations, and 20th and 22nd iterations.

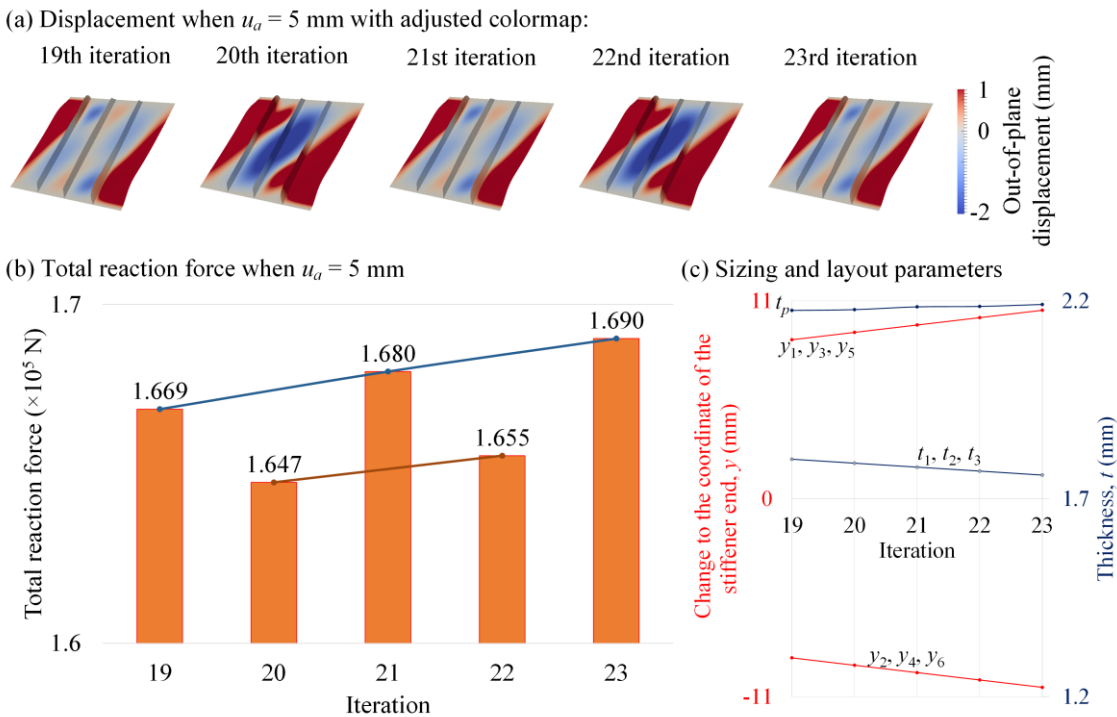


**Figure 5.33 Convergence study for the optimized designs at the 19th-23rd iterations of maximizing  $F_{r,total}$ , for the stiffened panel under the design shear displacement  $u_a = 5$  mm.**

In this example, the stiffened panel is under symmetric loading and boundary conditions along a diagonal line from bottom left to top right, and therefore the optimized designs are expected to be symmetric. However, the introduction of unsymmetric imperfections

results in an unsymmetrical displacement field and sensitivity distribution. Therefore, the obtained designs are not symmetric. Meanwhile, it is observed in Figs. 5.12 and 5.22 that for the optimization minimizing  $P_{w,skin}$ , the buckling shapes in adjacent iterations are symmetric along the diagonal and frequently switched. Small oscillations are found at the corresponding iterations. The same phenomenon is also found in the optimization maximizing  $F_{r,total}$ , i.e., the 166th-168th iterations in Fig. 5.30. This indicates that the optimizer might focus on updating one side of the structure at one iteration, and the other side at the next iteration, resulting in slow convergence. Symmetry control, illustrated in Fig. 5.34, is developed to address this issue. The design variables for half the design domain (in this example, either above or below the diagonal) are updated by the optimizer. Based on the mapping relationship given in Fig. 5.34, the geometric parameters for the other half of the design domain are also updated. In the optimization, the sensitivities information is given as:

$$\frac{\partial f}{\partial \mathbf{T}_i} = \sum_{n=1}^N \frac{\partial f}{\partial t_{s,n}} \frac{t_{s,n}}{\partial \mathbf{T}_i}, \quad i = 1, 2, \dots, (N+1)/2 \quad (\text{or } n = 1, 2, \dots, N/2) \quad (5-33a)$$

$$\frac{\partial f}{\partial \mathbf{Y}_i} = \sum_{j=1}^{2N} \frac{\partial f}{\partial y_j} \frac{y_j}{\partial \mathbf{Y}_i}, \quad i = 1, 2, \dots, N \quad (5-33b)$$

$$\frac{\partial f}{\partial \mathbf{H}_{n,b}} = \sum_{jj=1}^{N_{ele}/2} \sum_{j=1}^{N_{ele}} \frac{\partial f}{\partial w_j} \frac{\partial w_j}{\partial v_j} \frac{\partial v_j}{\partial \mathbf{V}_{jj}} \frac{\partial \mathbf{V}_{jj}}{\partial \mathbf{H}_{n,b}}, \quad n = 1, 2, \dots, (N+1)/2 \quad (\text{or } n = 1, 2, \dots, N/2) \quad (5-33c)$$

where T, Y and H are the design variables in the sizing, layout and topology optimizations using symmetry control, respectively.

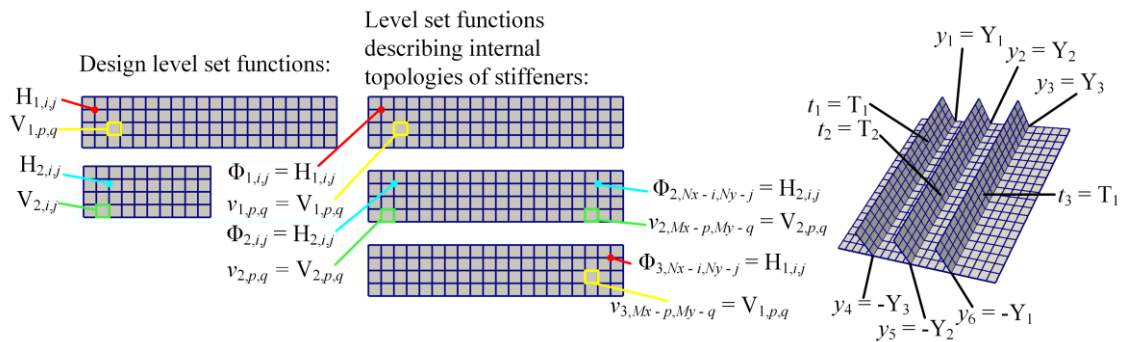
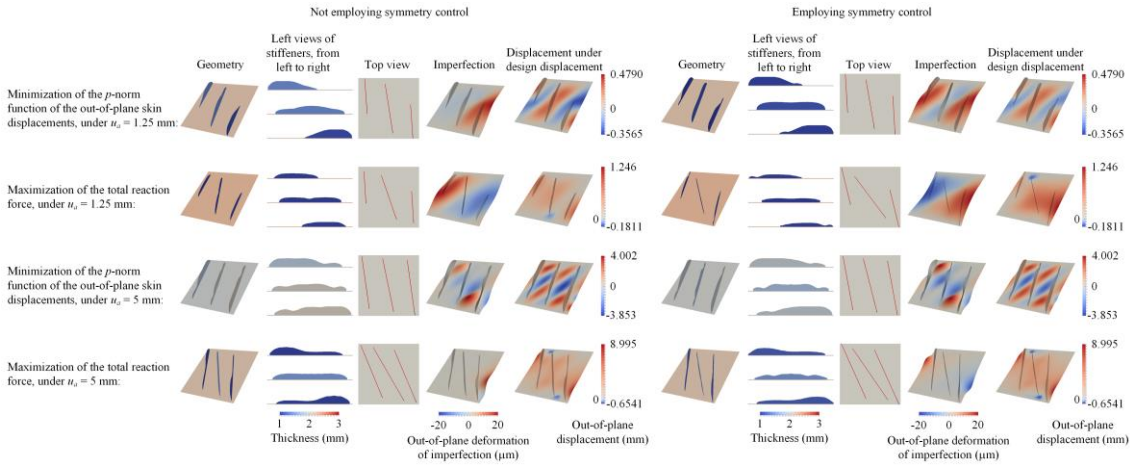


Figure 5.34 Illustration of symmetry control.

## Simultaneous Sizing, Layout and Topology Optimization for Buckling and Postbuckling of Stiffened Panels



**Figure 5.35 Comparison of the optimized results with and without the use of symmetry control, for the stiffened panel under the design shear displacement  $u_a = 5$  mm.**

**Table 5.11 Comparison of the optimized results with and without the use of symmetry control, for the stiffened panel under the design shear displacement  $u_a = 5$  mm.**

Optimization	Design shear displacement (mm)	Not using symmetry control		Using symmetry control	
		$P_{w,skin}$ (mm)	$F_{r,total}$ ( $\times 10^5$ N)	$P_{w,skin}$ (mm)	$F_{r,total}$ ( $\times 10^5$ N)
Minimizing $P_{w,skin}$ in Eq. (5-12a)	1.25	1.020	0.4864	0.8938	0.4858
Maximizing $F_{r,total}$ in Eq. (5-12b)	1.25	2.191	0.5064	3.194	0.5145
Minimizing $P_{w,skin}$ in Eq. (5-12a)	5	9.090	1.511	8.550	1.562
Maximizing $F_{r,total}$ in Eq. (5-12b)	5	18.67	1.868	18.95	1.900

Both optimizations, the minimization of  $P_{w,skin}$  in Eq. (5-12a) and the maximization of  $F_{r,total}$  in Eq. (5-12b) under the design displacement levels  $u_a = 1.25$  and 5 mm are repeated with symmetry control. The optimized results and a comparison of the optimized designs obtained with and without symmetry control are given in Fig. 5.35 and Table 5.11. For the optimization minimizing  $P_{w,skin}$ , though the structures obtained and the buckling shapes under the design loading are almost the same, the  $P_{w,skin}$  values are improved by 12.4% and 5.94% under the design displacement levels  $u_a = 1.25$  and 5 mm respectively when using symmetry control. For the optimization maximizing  $F_{r,total}$

in Eq. (5-12b), it can be seen that using symmetry control results in the middle stiffeners leaning more to the left, aligning more with the direction of maximum compression and  $F_{r,total}$  being improved by 1.60% and 1.71% for the optimizations under the design displacement levels  $u_a = 1.25$  and 5 mm, respectively.

2) Optimization at a design load

To solve the optimization problem of the minimization of  $u_a$  at a design load under displacement loading (Eq. (5-12c)), the problem is transformed into the maximization of  $F_{r,total}$  at each optimization iteration as shown in Fig. 5.36.

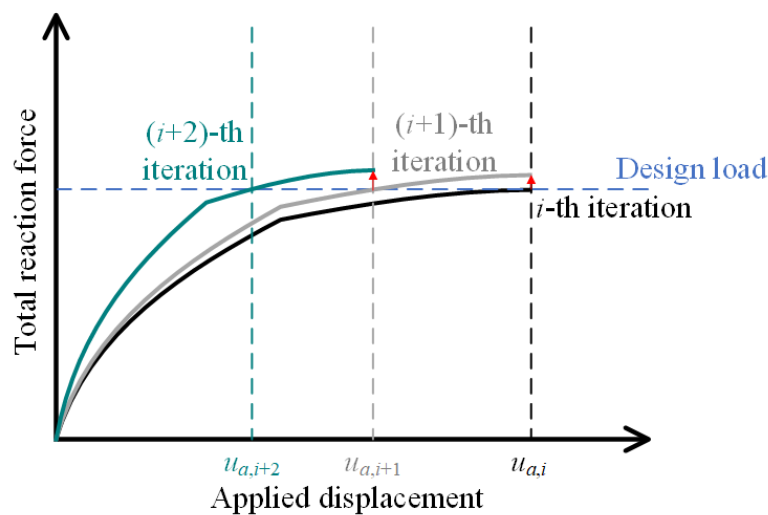


**Figure 5.36 Illustration of the algorithm for minimizing the applied displacement at a design load under displacement loading.**

The geometrically nonlinear analysis algorithm in Fig. 5.3 is combined with the bisection method to find the applied displacement where  $F_{r,total}$  is equal to the design load, each time the design is updated. The algorithm developed is shown in Fig. 5.37. The steps which are different from the algorithm in Fig. 5.3 are marked in red and described as follows:

## Simultaneous Sizing, Layout and Topology Optimization for Buckling and Postbuckling of Stiffened Panels

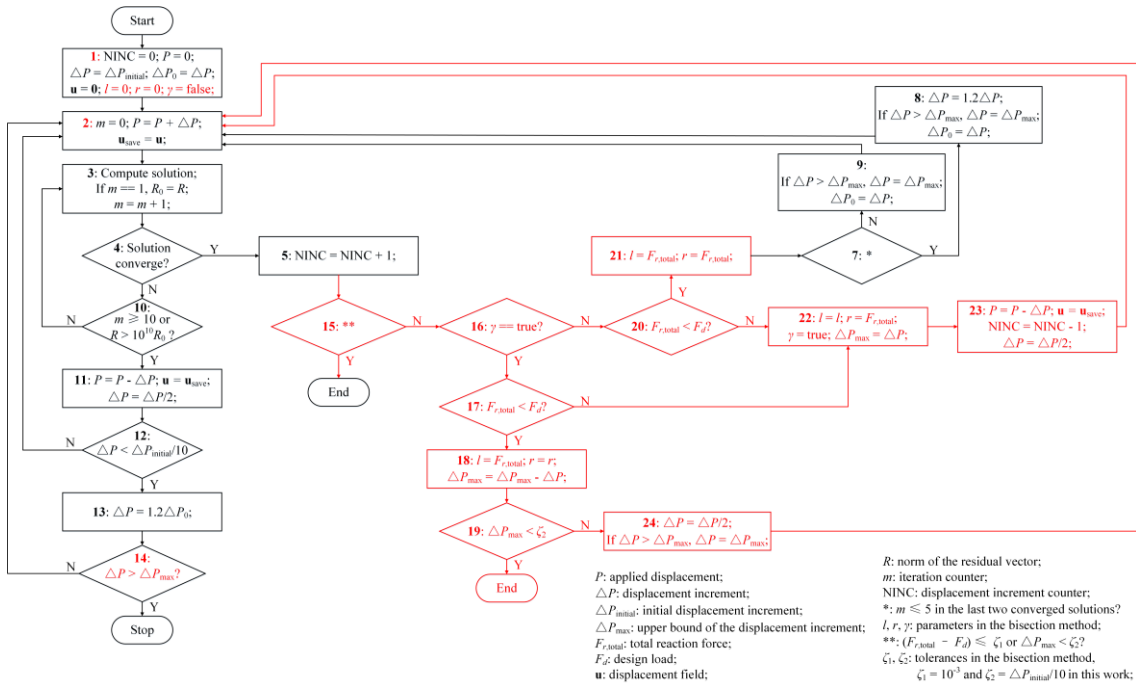


**Figure 5.37 Procedure for the geometrically nonlinear analysis, combined with the bisection method.**

Step 1: Initialise the whole analysis. Start counting the load increment times; set the initial load and load increment values; record the current load increment value  $\Delta P_0$ ; initialise the displacement field; initialise the parameters in the bisection method; go to Step 2.

Step 2: Initialise the analysis for a new load step. Start counting the iteration times in the current load step; increase the load; record the current displacement field; go to Step 3.

...

Step 5: Update the number of the load increments; go to Step 15.

...

Step 14: Check the analysis aborting criterion – if the load increment is larger than its upper bound, the analysis is **stopped** and the solution to Eq. (5-7) fails; otherwise, go to Step 2.

Step 15: Check the convergence criterion for the whole analysis – if  $F_{r,\text{total}}$  is close enough to the design load or the upper bound of the displacement increment becomes

## Chapter 5: Simultaneous Sizing, Layout and Topology Optimization for Postbuckling of Panels with Straight Stiffeners

very small, the whole analysis is **finished** and the applied displacement where  $F_{r,\text{total}}$  is equal to the design load is found; otherwise, go to Step **16**.

Step **16**: Check the criterion to use the bisection method – if  $\gamma$ , used to determine whether the range including the applied displacement where  $F_{r,\text{total}}$  is equal to the design load is found, is true, go to Step **17**; otherwise, go to Step **20**.

Step **17**: Check the criterion to update the parameter  $l$  – if  $F_{r,\text{total}}$  is smaller than the design load, go to Step **18**; otherwise, go to Step **22**.

Step **18**: Update the parameter  $l$ ,  $l = F_{r,\text{total}}$ ; The parameter  $r$  remains unchanged; update the upper bound of the displacement increment; go to Step **19**.

Step **19**: Check the convergence criterion of the whole analysis – if the upper bound of the displacement increment becomes very small, the whole analysis is **finished** and the applied displacement where  $F_{r,\text{total}}$  is equal to the design load is found; otherwise, go to Step **24**.

Step **20**: Check whether the range including the applied displacement where  $F_{r,\text{total}}$  is equal to the design load is found – if  $F_{r,\text{total}}$  is smaller than the design load, the range is not found and go to Step **21**; otherwise, the range is found and go to Step **22**.

Step **21**: Update both  $l$  and  $r$ ; go to Step **7**.

Step **22**: The parameter  $l$  remains unchanged; update the parameter  $r$ ,  $r = F_{r,\text{total}}$ ; update the parameter  $\gamma$ ,  $\gamma = \text{true}$ ; update the upper bound of the displacement increment; go to Step **23**.

Step **23**: Go back to the previous load step. Reduce the load by the current load increment; re-set the displacement field to the saved value; reduce the number of load increments by 1; reduce the load increment by 50%; go to Step **2**.

Step **24**: Reduce the load increment by 50%; if the load increment is larger than its upper bound, re-set it to the value of its upper bound; go to Step **2**.

Here, optimization under the design load  $F_d = 1.5 \times 10^5$  N is conducted. The initial design given in Fig. 5.5(a) is employed, and symmetry control is used. The optimized result is shown in Fig. 5.38. The optimized structure and its postbuckling behaviour are

**Simultaneous Sizing, Layout and Topology Optimization  
for Buckling and Postbuckling of Stiffened Panels**

similar to those in Figs. 5.15(h)-5.15(l) for maximizing  $F_{r,total}$ . Compared with the initial design, the applied displacement under the design load is reduced by 22.8%.

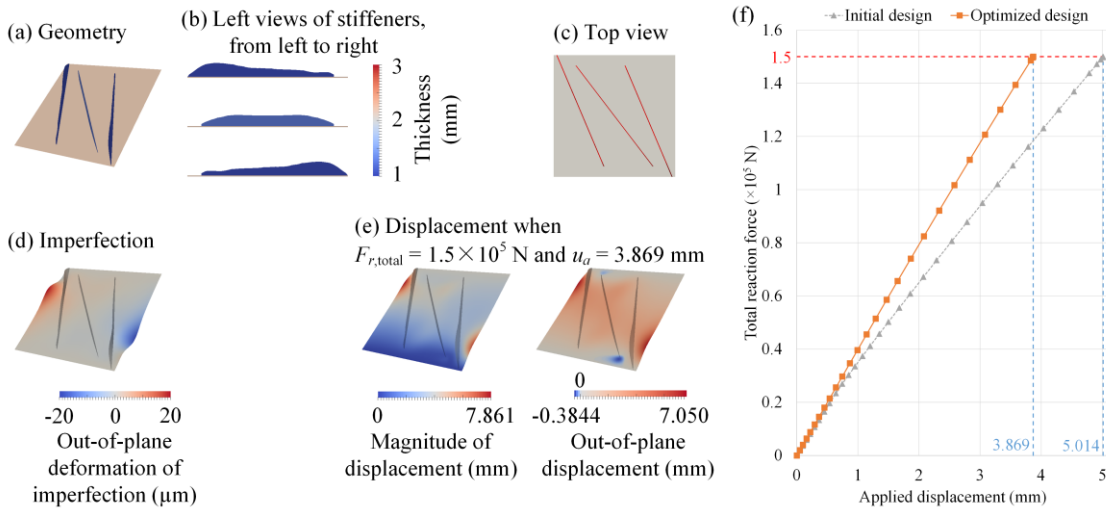


**Figure 5.38 Optimized design minimizing the applied displacement at the design load  $F_d = 1.5 \times 10^5$  N, for the stiffened panel under the design shear displacement.**

#### 5.4.2 Stiffened Panel Loaded by a Shear Load

A stiffened panel of  $0.3 \text{ m} \times 0.3 \text{ m}$  with the loading and boundary conditions shown in Fig. 5.39 is considered for optimization. A shear load  $N_{xx} = 500 \text{ kN/m}$  is applied to the top edge. Two postbuckling optimizations, minimizing  $P_{w,skin}$  and  $P_{in,skin}$  at a given load in Eqs. (5-13a) and (5-13b) with  $p = 6$ , are studied. To investigate the difference between linear buckling and postbuckling optimizations, the maximization of the critical buckling load factor with mass and stiffener spacing constraints is also conducted. To address the convergence issue of linear buckling optimization caused by mode switching, the first several buckling modes are considered. As the  $p$ -norm function has been successfully used to approximate the maximum stress in Chapter 4, it is also applied to linear buckling optimization in this work. The  $p$ -norm function of the inverses of the buckling load factors  $M_P$  is used to approximate the inverse of the critical buckling load factor. The objective maximizing the critical buckling load factor is transformed into the minimization of the  $p$ -norm function value  $M_P$ . The linear buckling optimization formulation is given as:

$$\min_{t,y,\Phi} M_p = \left( \sum_{q=1}^{N_\lambda} \left( \frac{1}{\lambda_q} \right)^p \right)^{\frac{1}{p}}$$

$$s.t. \quad m \leq m_{\max}$$

$$L_l \geq L_{\min}, \quad l = 1, 2, \dots, N_L$$
(5-34)

where  $\lambda_q$  is the buckling load factor for the  $q$ -th mode. The first  $N_\lambda$  buckling modes are considered in the optimization.  $p = 12$  is used for  $M_p$ . For all the three optimizations, the upper bound of the structural mass  $m_{\max} = 0.56$  kg. The lower and upper bounds of the thicknesses of both the skin and the stiffeners are 0.001 m and 0.003 m, respectively.

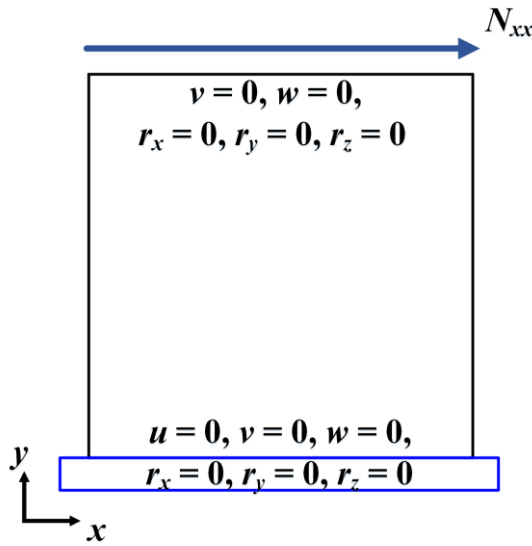


**Figure 5.39 Loading and boundary conditions for the design of a stiffened panel loaded by a shear load.**

In this work the number of stiffeners in the initial design decides the maximum allowable number of stiffeners in the optimized structures. The more stiffeners in the initial configuration, the larger the design space to be searched. In this example initial designs with 3 and 7 uniformly distributed vertical stiffeners, each with a height of 0.03 m, as shown in Fig. 5.40, are employed to investigate their effect on the optimization results. For the optimization employing the 3-stiffener initial design, the lower bound of the stiffener spacing  $L_{\min} = 7.5$  mm; while for the optimization employing the 7-stiffener initial design, the lower bound of the stiffener spacing  $L_{\min} = 3.75$  mm. For both initial designs, the skin and stiffener thicknesses are set to 0.002 m. The skin is discretized with  $80 \times 80$  plate elements, with 8 elements across the height of the

**Simultaneous Sizing, Layout and Topology Optimization  
for Buckling and Postbuckling of Stiffened Panels**

stiffeners. For the postbuckling optimization, the maximum amplitude of the employed imperfection is set to 1% of the skin thickness of the initial design i.e. 20  $\mu\text{m}$ . For the linear buckling optimization, it is not necessary to introduce an imperfection, and the first 10 buckling modes are used.

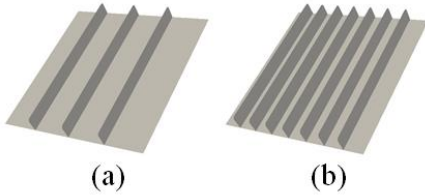


**Figure 5.40 Initial designs with (a) 3 stiffeners and (b) 7 stiffeners, for the design of the stiffened panel under the shear load.**

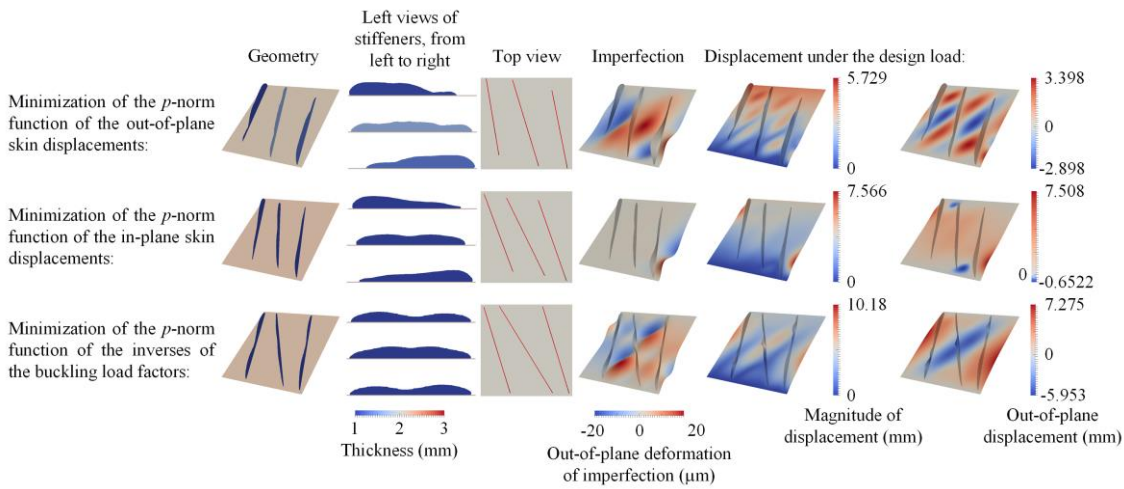


**Figure 5.41 Optimized designs of the stiffened panel under the shear load, employing the 3-stiffener initial design.**

## Chapter 5: Simultaneous Sizing, Layout and Topology Optimization for Postbuckling of Panels with Straight Stiffeners

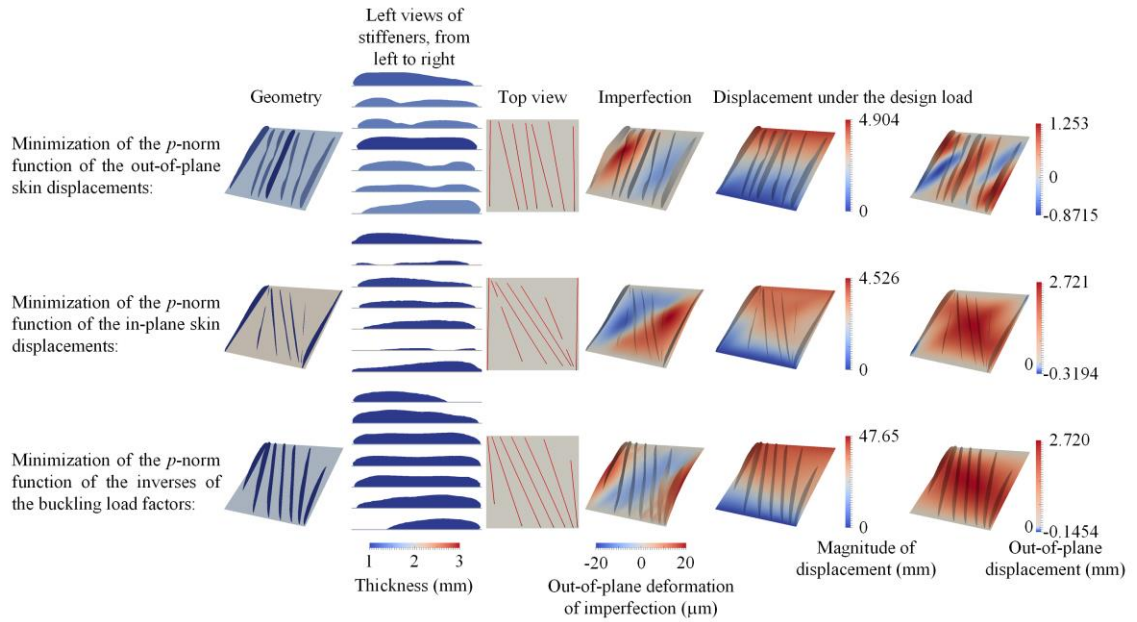


**Figure 5.42** Optimized designs of the stiffened panel under the shear load, employing the 7-stiffener initial design.

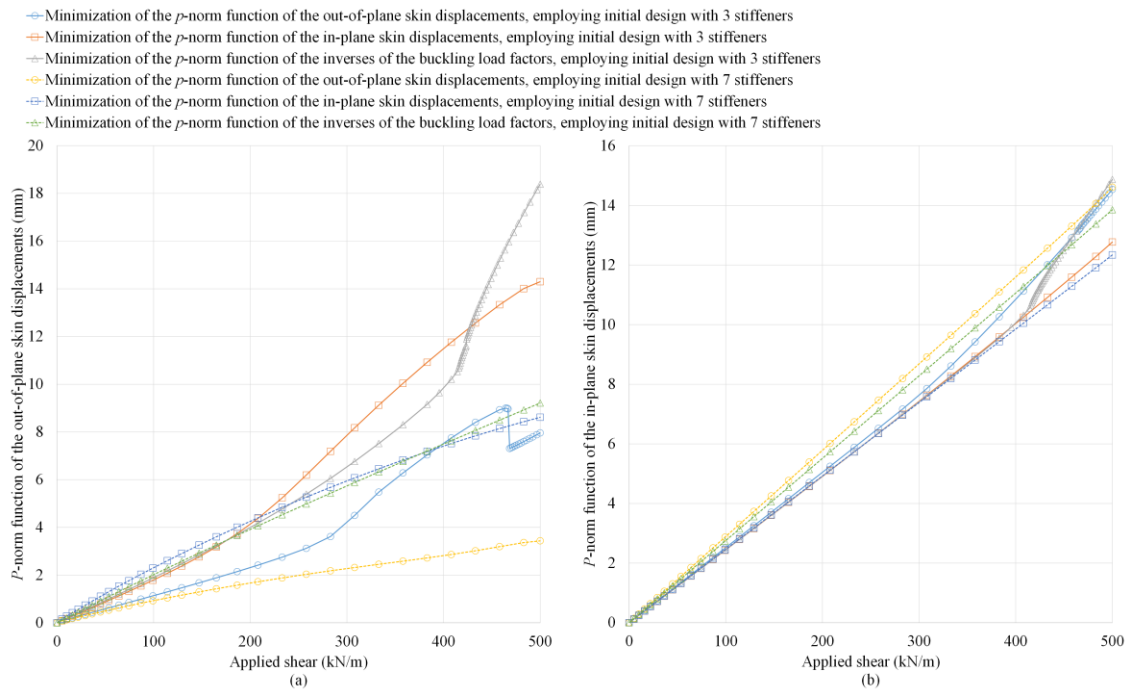


**Figure 5.43** Equilibrium paths for the optimized designs of the stiffened panel under the shear load.

**Table 5.12 Comparison of the optimized designs of the stiffened panel under the shear load.**

Optimization	Employing the initial design with 3 stiffeners			Employing the initial design with 7 stiffeners		
	$P_{w,skin}$ (mm)	$P_{in,skin}$ (mm)	$\lambda_1$	$P_{w,skin}$ (mm)	$P_{in,skin}$ (mm)	$\lambda_1$
Minimizing $P_{w,skin}$ in Eq. (5-13a)	7.961	14.54	0.5949	3.438	14.61	0.9177
Minimizing $P_{in,skin}$ in Eq. (5-13b)	14.30	12.77	0.5805	8.615	12.34	0.8868
Minimizing $M_P$	18.39	14.87	0.9138	9.214	13.85	2.843

The optimized designs and corresponding equilibrium paths for the three optimizations with two different initial designs are shown in Figs. 5.41-5.43. These designs are compared in Table 5.12. For the optimized designs for the minimization of  $P_{w,skin}$  and  $P_{in,skin}$  employing the 3-stiffener initial design in Fig. 5.41, the geometries and buckling modes are similar to those obtained when minimizing  $P_{w,skin}$  and maximizing  $F_{r,total}$  under a shear displacement  $u_a = 5$  mm in Fig. 5.15. For the optimized design minimizing  $P_{w,skin}$ , the stiffeners are again parallel to each other decreasing the unsupported region of the skin. Compared with the other two designs in Fig. 5.41, its stiffeners are higher and thicker. Though mode jumping occurs, global buckling and buckles crossing the stiffeners are avoided, decreasing the out-of-plane skin displacement. For the optimized design minimizing  $P_{in,skin}$ , the stiffeners lean more to the left and the skin is thicker than the other two designs to increase the load-carrying capability and reduce the in-plane skin displacement. For the optimized design minimizing  $M_P$ , it can be observed that the stiffener material distribution depends on the linear buckling shape (which is the same as the shape of the imperfection). For example, the stiffeners have their peak points where the structure buckles in the linear buckling analysis. This however, leads to the middle stiffener offering weak support to the central region of the skin, and the buckling crossing the middle stiffener during postbuckling. Compared with the optimized design minimizing  $M_P$ , the  $P_{w,skin}$  value is decreased by 56.7% when minimizing  $P_{w,skin}$ , and the  $P_{in,skin}$  value is decreased by 14.1% for the optimized design of minimizing  $P_{in,skin}$ . Compared with the other two designs in Fig. 5.41, the critical buckling load factor of the optimized design minimizing  $M_P$  is improved by more than 53.6%.

The optimized designs in Fig. 5.42 employing the 7-stiffener initial design, follow the same trends as those in Fig. 5.41. Since the number of stiffeners in the initial design decides the maximum allowable number of stiffeners in the optimized structures, the design spaces employing the 7-stiffener initial design are larger than those for the 3-stiffener one. It is easier for the optimization employing the 7-stiffener initial design to find a more promising stiffener layout configuration and material distribution in the skin and stiffeners to improve the structural postbuckling behaviours. For the optimized designs minimizing  $P_{w,skin}$ , more material is distributed into the stiffeners when employing the 7-stiffener initial design than for the 3-stiffener one. Unsupported regions of the skin are reduced since more stiffeners are allowed. Though the buckles are found to cross the stiffeners, its  $P_{w,skin}$  value is improved by 56.8%. For the optimized designs minimizing  $P_{in,skin}$ , compared with the 3-stiffener initial design, a more promising stiffener configuration is found with more material allocated to the skin for the one employing the 7-stiffener initial design increasing skin stiffness. Though its  $P_{in,skin}$  value is only improved by 3.37%, its  $P_{w,skin}$  value is improved by 39.8% since there are more stiffeners and fewer unsupported regions on the skin. For the optimized design minimizing  $M_P$  employing the 7-stiffener initial design, its critical buckling load factor is equal to 2.843. As shown in Fig. 5.43, the structure has not buckled under the design load. Even so, its  $P_{w,skin}$  value is worse than both the optimized designs minimizing  $P_{w,skin}$ , and its  $P_{in,skin}$  value is worse than both the optimized designs minimizing  $P_{in,skin}$ .

### 5.4.3 Stiffened Panel Loaded by Compression and Shear Loads

A stiffened panel of 0.3 m × 0.3 m with the loading and boundary conditions shown in Fig. 5.44 is considered for optimization. A compression load  $N_{yy} = 800$  kN/m and a shear load  $N_{xx} = 200$  kN/m are applied to the top edge. Three optimizations, i.e., the minimization of  $P_{w,skin}$  (in Eq. (5-13a)),  $P_{in,skin}$  (in Eq. (5-13b)) and  $M_P$  with mass and stiffener spacing constraints are performed. Initial designs with the 3 and 7 vertical stiffeners in Fig. 5.40 are employed. All the optimization parameters including the upper and lower bounds of the constraints are the same as those in Section 5.4.2 (Stiffened panel loaded in shear).

**Simultaneous Sizing, Layout and Topology Optimization  
for Buckling and Postbuckling of Stiffened Panels**

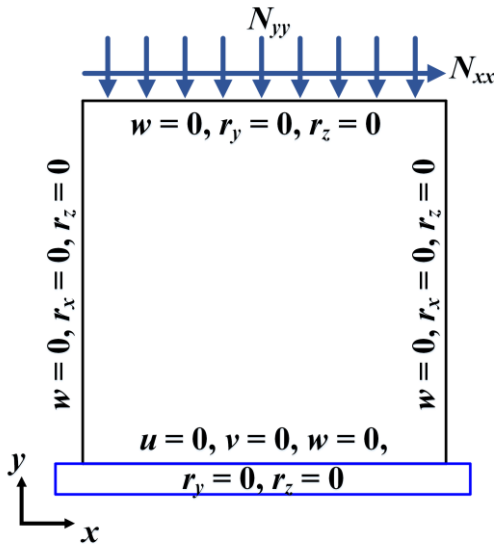


**Figure 5.44 Loading and boundary conditions for the design of a stiffened panel loaded by compression and shear loads.**

The optimized designs and corresponding equilibrium paths for the three optimizations with two different initial designs are shown in Figs. 5.45-5.47 and compared in Table 5.13. For the optimized designs minimizing  $P_{w,skin}$  employing both the 3-stiffener and 7-stiffener initial designs, the stiffeners are more uniformly distributed than for the other two optimizations, to decrease the unsupported regions of the skin. More material is placed on the right-hand-side stiffeners since the right-hand side of the panel is under the largest compression, along with the buckling mode having the largest out-of-plane skin displacements in that region. Compared with the optimized design employing the 3-stiffener initial design, the  $P_{w,skin}$  value for the one employing the 7-stiffener initial design is improved by 39.0%. Though  $P_{in,skin}$  and  $M_P$  are not considered in the optimization of minimizing  $P_{w,skin}$ , they are also improved by 48.3% and 50.4%, respectively.

For the optimized designs minimizing  $P_{in,skin}$  employing both 3-stiffener and 7-stiffener initial designs, all the stiffeners move closer to the right-hand side of the panel to resist the combined compression and shear loads. Compared with the optimized design employing the 3-stiffener initial design, the  $P_{in,skin}$  value for the one employing the 7-stiffener initial design is improved by 38.9%. The  $P_{w,skin}$  and  $M_P$  values are also improved by 45.4% and 55.4%, respectively.

## Chapter 5: Simultaneous Sizing, Layout and Topology Optimization for Postbuckling of Panels with Straight Stiffeners

Compared with the optimized design minimizing  $M_P$  employing the 3-stiffener initial design, the  $P_{w,skin}$  value is improved by 58.7% for the optimized design minimizing  $P_{w,skin}$  employing the 3-stiffener initial design, though its  $P_{in,skin}$  value is 2.59% larger. For the optimized design minimizing  $P_{in,skin}$  employing the 3-stiffener initial design, its  $P_{w,skin}$  and  $P_{in,skin}$  values are improved by 31.5% and 44.8%, respectively.

For the optimized design minimizing  $M_P$  employing the 7-stiffener initial design, its critical buckling load factor is equal to 1.267, and therefore its buckling point is near the design load. As discussed in Section 5.4.1, its structural responses are greatly affected by the employed imperfection. To reduce this influence, an imperfection with a maximum amplitude equal to  $0.2 \mu\text{m}$  is employed for the analysis. Compared with this design, the  $P_{w,skin}$  value is improved by 56.6% for the optimized design of minimizing  $P_{w,skin}$  employing the 7-stiffener initial design, but its  $P_{in,skin}$  value is 5.67% larger. For the optimized design minimizing  $P_{in,skin}$  employing the 7-stiffener initial design, its  $P_{w,skin}$  and  $P_{in,skin}$  values are improved by 35.4% and 32.7%, respectively.

It can be seen from both the examples in Section 5.4.2 and this Section that when more stiffeners are allowed in the optimization, more promising stiffener configurations can be generated and better structural performances can be achieved. Compared with linear buckling optimization, postbuckling optimization is able to provide a design with better postbuckling behaviours of interest.

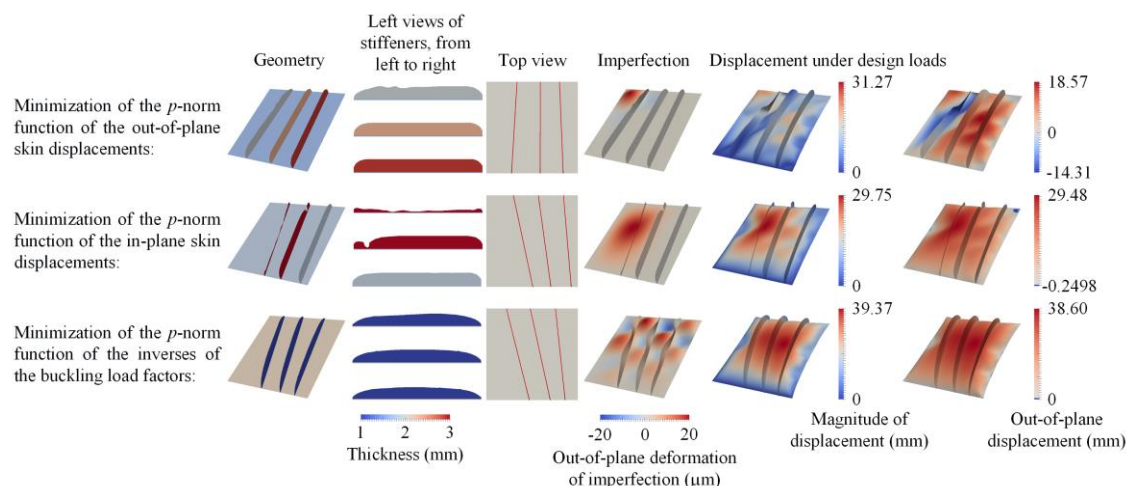


**Figure 5.45 Optimized designs of the stiffened panel under the compression and shear loads, employing the 3-stiffener initial design.**

## Simultaneous Sizing, Layout and Topology Optimization for Buckling and Postbuckling of Stiffened Panels

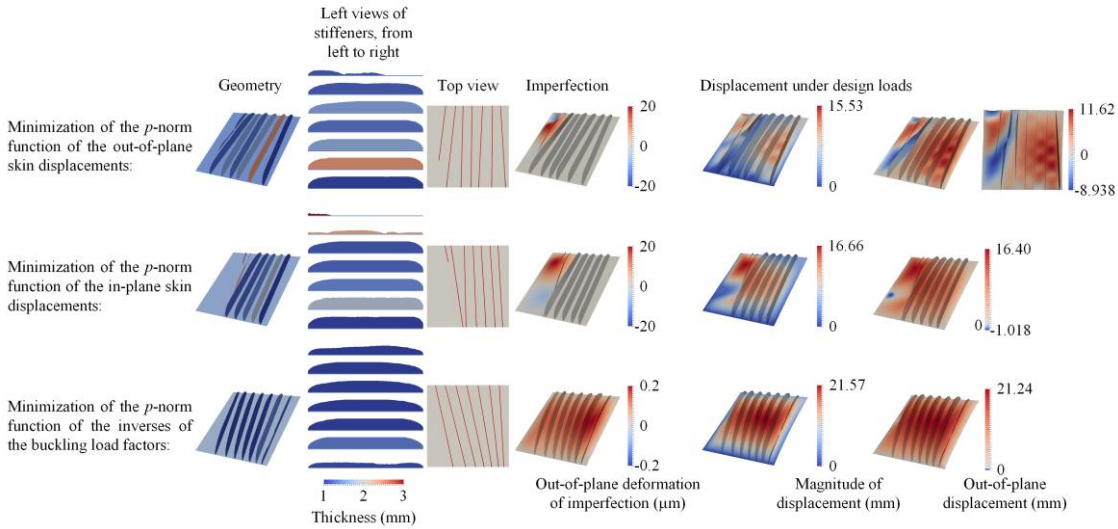


**Figure 5.46** Optimized designs of the stiffened panel under the compression and shear loads, employing the 7-stiffener initial design.

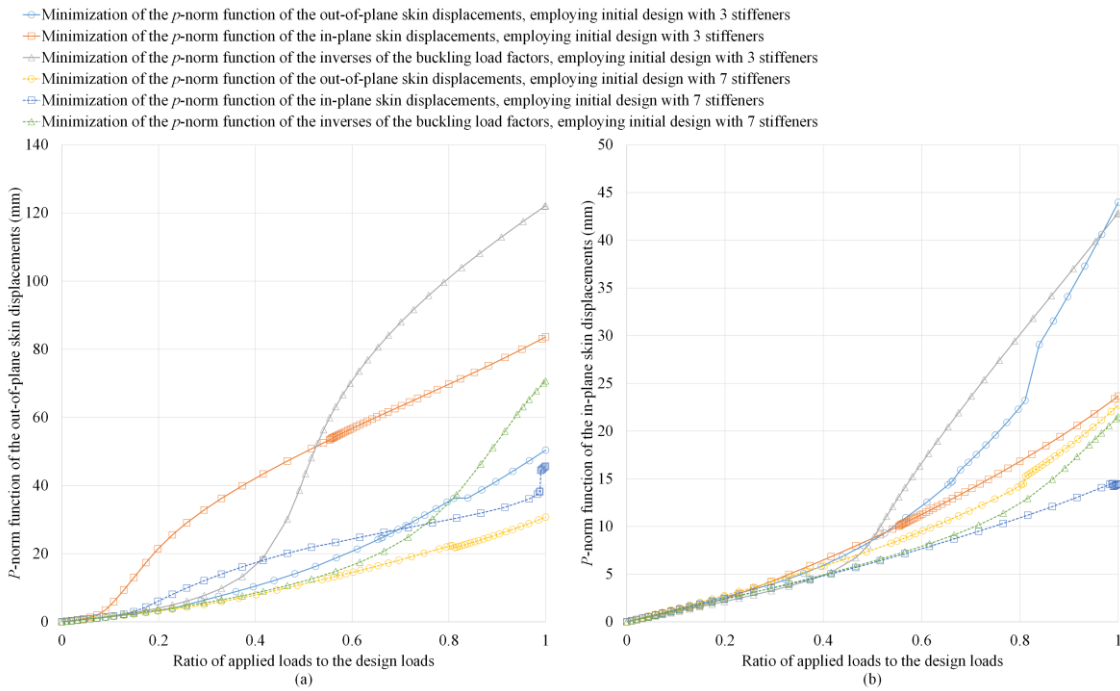


**Figure 5.47** Equilibrium paths for the optimized designs of the stiffened panel under the compression and shear loads.

**Table 5.13 Comparison of the optimized designs of the stiffened panel under the compression and shear loads.**

Optimization	Employing the initial design with 3 stiffeners			Employing the initial design with 7 stiffeners		
	$P_{w,skin}$ (mm)	$P_{m,skin}$ (mm)	$\lambda_1$	$P_{w,skin}$ (mm)	$P_{m,skin}$ (mm)	$\lambda_1$
Minimizing $P_{w,skin}$ in Eq. (5-13a)	50.41	43.98	0.2043	30.73	22.72	0.3073
Minimizing $P_{m,skin}$ in Eq. (5-13b)	83.63	23.66	0.1163	45.68	14.46	0.1807
Minimizing $M_P$	122.1	42.87	0.5870	70.74	21.50	1.267

## 5.5 Conclusion

In this Chapter, postbuckling topology optimization of stiffened panels is investigated for the first time. The computational scheme using the level-set-based topology optimization method, developed in Chapter 3, is used for stiffened panel design. The skin and stiffener thicknesses, and the stiffener layout and internal topologies can be simultaneously optimized. A Newton-Raphson scheme with load/displacement control is used for the FE analysis, where a small imperfection in the form of the first linear buckling mode is imposed on the FE model.

The postbuckling behaviours, i.e., the out-of-plane skin displacement and load-carrying capability, for stiffened panels under force/displacement loading are considered for optimization. A total of five optimization formulations based on different postbuckling indices under load/displacement loading are studied. For the optimizations to decrease the out-of-plane skin displacement, the stiffeners tend to be uniformly distributed on the skin to reduce the unsupported regions; while for the optimizations to improve the load-carrying capability, more material tends to be placed on the skin and the stiffener orientation is more aligned with the direction of maximum compression.

For optimizations at different load levels, i.e., initial postbuckling and moderately deep postbuckling regimes, the effects of imperfection maximum amplitude and direction on structural analysis and optimization are investigated. For optimization at the initial postbuckling regime, the imperfection maximum amplitude and direction greatly affects the deformation amplitude and direction of the buckled structure, respectively. Though

## **Simultaneous Sizing, Layout and Topology Optimization for Buckling and Postbuckling of Stiffened Panels**

similar structural geometries can be found employing imperfections with different maximum amplitudes and directions in optimization, their postbuckling responses can vary considerably. For optimization at the moderately deep postbuckling regime, the influence of the employed imperfection can be alleviated. For the example investigated in this chapter, optimized designs with the same postbuckling behaviours can be obtained from optimizations employing imperfections with different directions.

The convergence of the postbuckling topology optimization is also studied. It is found that mode switching and mode jumping cause oscillations in the convergence curves during optimization. Though these oscillations lead to slow convergence, they do not prevent the structure from being optimized. It is also found that for optimization problems under symmetric loading and boundary conditions, not only does the introduction of unsymmetrical imperfections in the postbuckling analysis cause the optimized structures to be unsymmetrical, but it contributes to mode switching and slow convergence. Symmetry control is developed to alleviate the convergence issue and find better results.

Postbuckling optimization is compared with linear buckling optimization. Based on the optimization formulations, the optimized designs obtained by postbuckling optimization have smaller out-of-plane displacements and/or a better load-carrying capability than the ones obtained from linear buckling optimization.

# 6 SIMULTANEOUS LAYOUT AND TOPOLOGY OPTIMIZATION OF PANELS WITH CURVED STIFFENERS CONSIDERING BUCKLING

In Chapters 3-5, the optimization has been limited to the design of panels stiffened with straight stiffeners. In contrast to panels stiffened with straight stiffeners, Kapania et al. [2] introduced curvilinearly stiffened panels and showed that they have the potential to result in lighter weight designs. However, as discussed in Chapter 2, in the existing works, stiffener curves are usually limited by pre-specified curvilinear functions, e.g. B-splines, as well as the optimization design space. Due to the ability of the level set method to describe variations in topology, being able to increase the design space with the potential to find the global optimum in optimization problems, the optimization of curved stiffeners using the level set method is investigated in this chapter.

This Chapter presents a level-set-based method to simultaneously conduct the layout and topology optimization of panels with curved stiffeners. Specifically, plate elements are used to construct a stiffened panel structure. The level set function (LSF) is then used to describe and freely manipulate the stiffener layout, with curved members allowed. The free-form mesh deformation method with a control mesh is utilized to

adjust the finite element (FE) mesh. The level set method is also used to optimize the internal topologies of the stiffeners. Both mass minimization with buckling constraint and critical buckling load factor maximization with mass constraint are investigated. A semi-analytical sensitivity analysis is performed, and the gradient-based optimizer IPOPT [97] is used. For the buckling-constrained problem, when the  $p$ -norm function and IPOPT are used, an adaptive scaling method is used to ensure the control of the buckling limit. Numerical investigations demonstrate and validate the proposed method.

The remainder of this chapter is organized as follows. In Section 6.1, the geometric and FE models of the curved stiffened panels are presented. Section 6.2 describes the mathematical formulations of the considered problems, the sensitivity analysis and the optimization algorithm. Some numerical examples to test the proposed method are presented in Section 6.3. Conclusions are given in Section 6.4.

## 6.1 Curved Stiffened Panel Model

In this section, the geometric and FE models are described. LSFs are used to represent and optimize both the layout and the internal topologies of the stiffeners. As the stiffener layout changes, a free-form mesh deformation method with a control mesh is used to adjust the FE mesh.

### 6.1.1 Layout Description

The stiffened panel is composed of the skin and stiffeners shown in Fig. 6.1(a). The level set method is used to represent and manipulate the layout of the stiffeners, allowing curved members. Specifically, as shown in Figs. 6.2(a) and 6.2(d), the stiffener curves are defined as the zero level set of an implicit function:

$$\Phi_l(x_l) = 0 \quad x_l \in \Gamma_l \quad (6-1)$$

where  $\Gamma_l$  denotes the stiffener curves.  $\Phi_l(x_l)$  is the implicit function and  $x_l \in \Omega_{d,l}$ , where  $\Omega_{d,l}$  is the design domain corresponding to the panel. Conventionally, the signed distance function is used for the LSF.

**Chapter 6: Simultaneous Layout and Topology Optimization of Panels with Curved Stiffeners Considering Buckling**

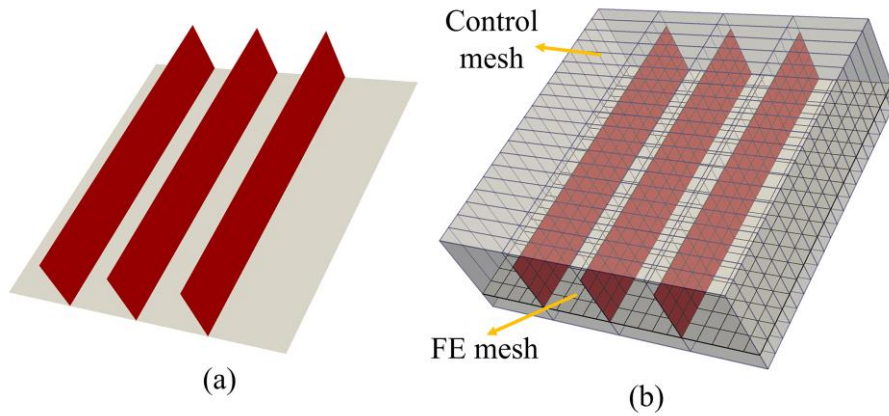


**Figure 6.1** Sample curved stiffened panel and its control and FE meshes: (a) geometric model; (b) control and FE meshes.

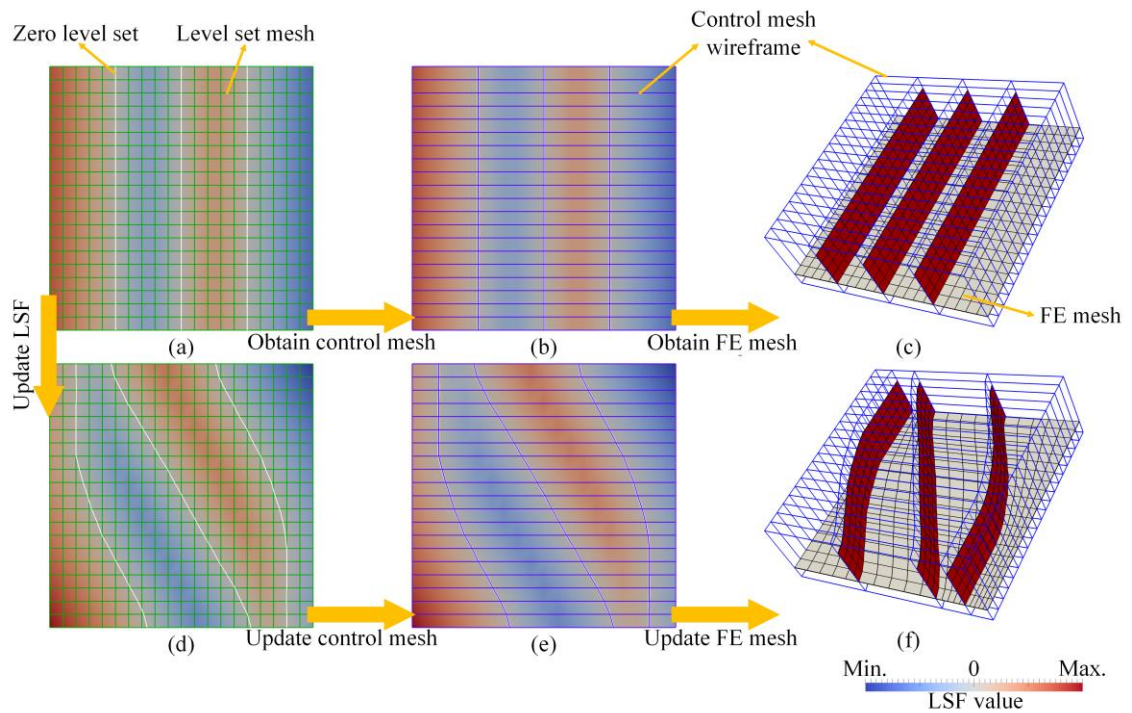


**Figure 6.2** Illustration of the curved stiffener layout represented by the LSF: (a) the LSF, the zero level set and the level set mesh for the initial structure; (b) the LSF, the zero level set and the control mesh wireframe for the initial structure; (c) the initial control mesh wireframe and the FE mesh; (d) the LSF, the zero level set and the level set mesh for the updated structure; (e) the LSF, the zero level set and the control mesh wireframe for the updated structure; (f) the updated control mesh wireframe and the FE mesh.

**Simultaneous Sizing, Layout and Topology Optimization  
for Buckling and Postbuckling of Stiffened Panels**

In the same way as when optimizing the structural boundary to find the best internal topology of a stiffener in Eq. (3-3), the stiffener curves are optimized by iteratively solving the level set equation, Eq. (6-2), to achieve the optimal layout of the stiffeners:

$$\frac{\partial \Phi_l(x_l, t_f)}{\partial t_f} + \nabla \Phi_l(x_l) \cdot V_l(x_l) = 0 \quad (6-2)$$

where  $t_f$  is a fictitious time and  $V_l$  is the velocity vector.

The LSF at each point is updated by solving the following discretized Hamilton-Jacobi equation using an up-wind differential scheme [85]:

$$\Phi_{l,pl}^{k+1} = \Phi_{l,pl}^k - \Delta t_f \left| \nabla \Phi_{l,pl}^k \right| V_{n,l,pl} \quad (6-3)$$

where  $V_{n,l}$  is the normal velocity.  $pl$  is a discrete point in the design domain,  $k$  is the iteration number and  $\left| \nabla \Phi_{l,pl}^k \right|$  is computed for each point using the Hamilton-Jacobi weighted essentially non-oscillatory method (HJ-WENO) [93]. To improve the computational efficiency, the level set update is restricted to points within a narrow band close to the boundary.  $\Phi_{l,pl}$  is chosen to be a signed distance to the boundary within this narrow band. To correct for this effect,  $\Phi_{l,pl}$  is periodically reinitialized to a signed distance function. The fast marching method [85] is used for this re-initialization and velocity extension.

Both the skin and the stiffeners are modeled explicitly with 4-node Mixed Interpolation of Tensorial Components (MITC) plate elements with 6 DOF's per node, comprising a Mindlin-Reissner plate element [91, 92] combined with the plane stress formulation. In order to avoid re-meshing after every update of the stiffener layout, the free-form mesh deformation method with control mesh is extended to the design of panels with curved stiffeners. In Fig. 6.1(b), the control mesh, represented by the blue lines and grey surfaces is illustrated. The intermediate elemental surfaces correspond to the stiffeners, which means that the coordinates in the  $x$  and  $y$  directions of nodes on the control mesh are all located on the stiffener curves represented by the zero level set in Eq. (6-1). As the LSF is updated from Fig. 6.2(a) to Fig. 6.2(d), the nodes on the control mesh are re-located from Fig. 6.2(b) to Fig. 6.2(e). For simplification of implementation, the  $y$  and  $z$  coordinates of the nodes on the control mesh are fixed and only the  $x$  coordinates are allowed to move. Using the free-form mesh deformation method [90], as shown in Figs.

**Chapter 6: Simultaneous Layout and Topology Optimization of Panels with Curved Stiffeners  
Considering Buckling**

6.2(c) and 6.2(f), the FE mesh is deformed to cater to the updated stiffener layout with control mesh:

$$\mathbf{x}_{FE} = \mathbf{N}\mathbf{x}_{control} \quad (6-4a)$$

$$\mathbf{x}_{control}^{k+1} = \mathbf{x}_{control}^k + \mathbf{y} \quad (6-4b)$$

$$\mathbf{x}_{FE}^{k+1} = \mathbf{x}_{FE}^k + \mathbf{z} \quad (6-4c)$$

$$\mathbf{z} = \mathbf{N}\mathbf{y} \quad (6-4d)$$

where  $\mathbf{x}_{FE}$  and  $\mathbf{x}_{control}$  are nodal coordinates on the FE and control meshes, respectively.  $\mathbf{N}$  is the shape function.  $\mathbf{y}$  and  $\mathbf{z}$  represent the changes in the coordinates of the control and FE mesh nodes, respectively. The deformation of the FE mesh can be achieved through Eqs. (6-4c) and (6-4d).

### 6.1.2 Topology Description

The level set method is also used to represent and optimize the internal topologies of the stiffeners with one LSF used to describe the internal topology of each stiffener. The relationship between the LSF values and the resulting structures are shown in Figs. 6.3(b)-6.3(d). The structural boundary is defined as the zero level set of the implicit function  $\Phi_{to}(x_{to})$ :

$$\begin{cases} \Phi_{to}(x_{to}) \leq 0 & x \in \Omega_{to} \\ \Phi_{to}(x_{to}) = 0 & x \in \Gamma_{to} \\ \Phi_{to}(x_{to}) > 0 & x \notin \Omega_{to} \end{cases}, \quad to = 1, 2, \dots, N \quad (6-5)$$

where  $\Phi_{to}$  is the LSF representing the  $to$ -th stiffener, and  $N$  is the number of stiffeners. For the  $to$ -th stiffener,  $\Omega_{to}$  is the domain corresponding to the structure and  $\Gamma_{to}$  is the structural boundary.  $x \in \Omega_{d,to}$ , where  $\Omega_{d,to}$  is the design domain containing the structure,  $\Omega_{to} \in \Omega_{d,to}$ . As in Eq. (3-4), the level set equation can be updated by the discretized Hamilton-Jacobi equation using an up-wind differential scheme in order to optimize the structural boundary.

**Simultaneous Sizing, Layout and Topology Optimization  
for Buckling and Postbuckling of Stiffened Panels**

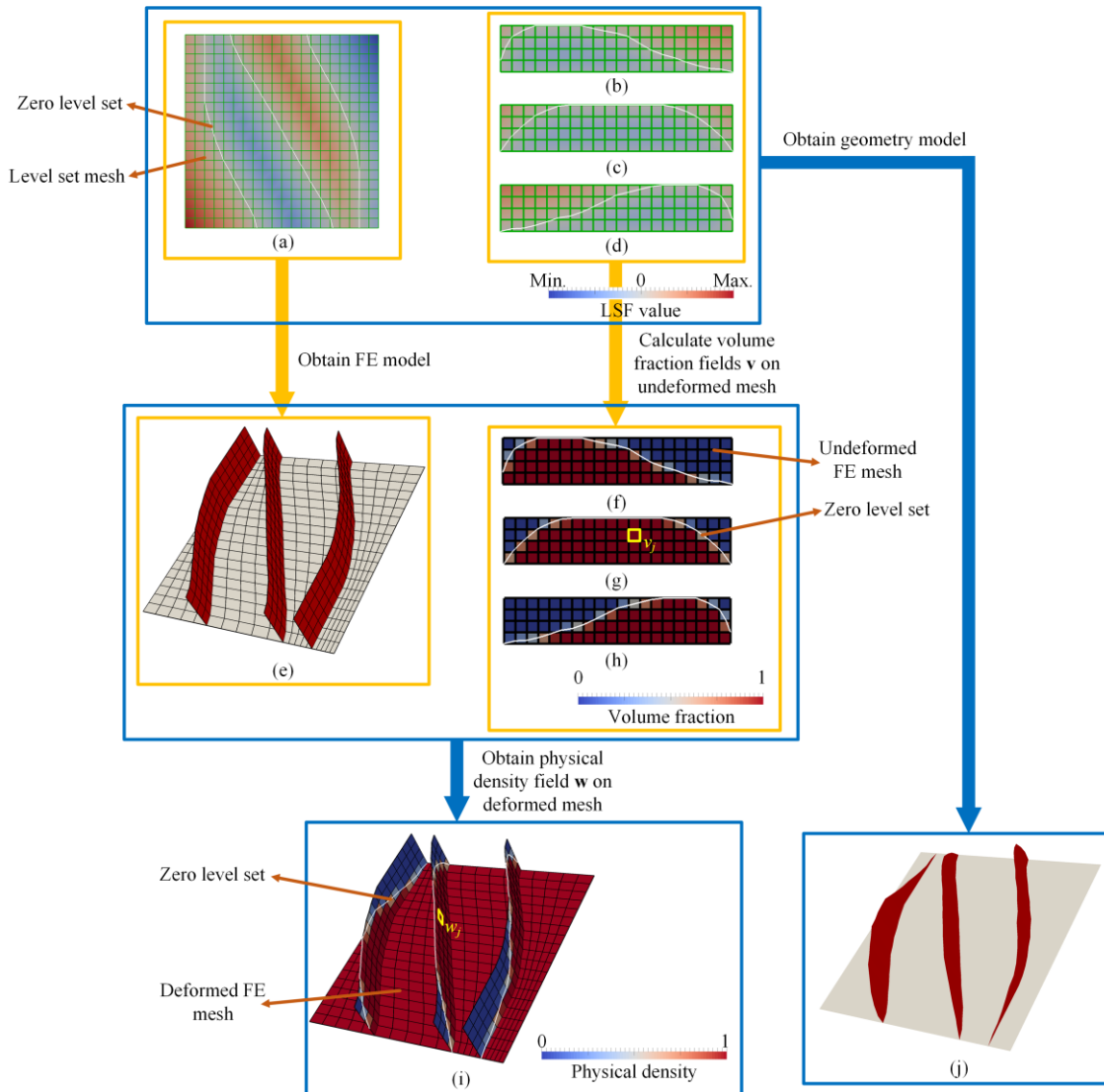


**Figure 6.3** Illustration of how to construct the geometric and FE models of a sample curved stiffened panel using LSFs: (a) the LSF representing the stiffener curves, its zero level set and level set mesh; (b)-(d) the LSFs corresponding to the three stiffeners respectively, their zero level sets and level set meshes; (e) the deformed FE mesh; (f)-(h) the volume fraction fields, zero level sets and undeformed FE meshes corresponding to the three stiffeners; (i) the deformed FE mesh and corresponding physical density field; (j) the geometric model.

As described in Section 3.1.2, the level set mesh has the same mesh size as the FE mesh corresponding to one stiffener, and this is fixed during the optimization in this work. As shown in Figs. 6.3(f)-6.3(h), based on the undeformed mesh, it is easy to calculate the density distribution for each stiffener by calculating the volume fraction field  $\nu$  of solid material in the mesh based on the corresponding level set function values  $\Phi_{i0}$ . Based on

the stiffener layout given by the LSF in Fig. 6.3(a), the deformed FE mesh in Fig. 6.3(e) can be obtained by the method presented in Section 6.1.1. Due to the one-to-one correspondence between the elements of the undeformed and deformed FE meshes, a direct mapping can be used and the physical density distribution  $\mathbf{w}$  for the stiffeners is obtained by  $w_j = v_j$ . The density distribution is  $\mathbf{w} = \mathbf{1}$  for all the elements on the skin, as shown in Fig. 3(i). Meanwhile, the geometry of the curved stiffened panels in Fig. 6.3 (j) can be described through the  $(N + 1)$  LSFs, comprising one for the stiffener layout and  $N$  for internal topologies of  $N$  stiffeners.

It is noted that the level set method has the potential to describe arbitrary stiffener curves. However, since the free-form mesh deformation method with control mesh is utilized to adjust the FE mesh, overlap and intersection between the adjacent stiffeners are not allowed, and thus the stiffener curves are never closed in this work. The end points of the zero level set corresponding to each stiffener curve are placed on the opposite faces of the panel, but the end points of the stiffeners are free to move inside the panel due to topology optimization.

### 6.1.3 Finite Element Model

In the same way as for the FE analysis of a panel with straight stiffeners, the stiffness and geometric stiffness matrices for the  $j$ -th finite element of a curved stiffened panel can be calculated after obtaining the physical density field  $\mathbf{w}$ :

$$K_j = w_j K_j^s(E_s, \rho_s, \nu, t, \mathbf{x}_{FE}) + (1 - w_j) K_j^v(E_v, \rho_v, \nu, t, \mathbf{x}_{FE}) \quad (6-6a)$$

$$K_{g,j} = w_j (\omega_j K_{g,j}^s(E_s, \rho_s, \nu, t, \mathbf{x}_{FE}) + (1 - w_j) K_{g,j}^v(E_v, \rho_v, \nu, t, \mathbf{x}_{FE})) \quad (6-6b)$$

where  $K_j^s$  and  $K_j^v$  represent the stiffness matrices of the  $j$ -th finite element with solid and void phases, respectively.  $K_{g,j}^s$  and  $K_{g,j}^v$  denote the geometric stiffness matrices of the  $j$ -th finite element with solid and void phases, respectively.  $E_s$  and  $\rho_s$  are the Young's modulus and mass density of the solid phase, while  $E_v$  and  $\rho_v$  are the Young's modulus and mass density of the void phase.  $\nu$  and  $t$  are Poisson's ratio and thickness, respectively.

It is noted that, as in previous cases, when axial compression or shear loading is applied on the boundaries of curved stiffened panels with deformed FE meshes, uniform forces

**Simultaneous Sizing, Layout and Topology Optimization  
for Buckling and Postbuckling of Stiffened Panels**

cannot be added directly to the corresponding nodes. As shown in Fig. 6.4, the force applied on the node  $pf$  is calculated as:

$$P_{pf} = \frac{P(L^{pf-1} + L^{pf})}{2} \quad (6-7)$$

where  $P$  is the pressure value per unit length.  $L^{pf-1}$  and  $L^{pf}$  are the lengths of the elemental boundaries with the node  $pf$ , as shown in Fig. 6.4.

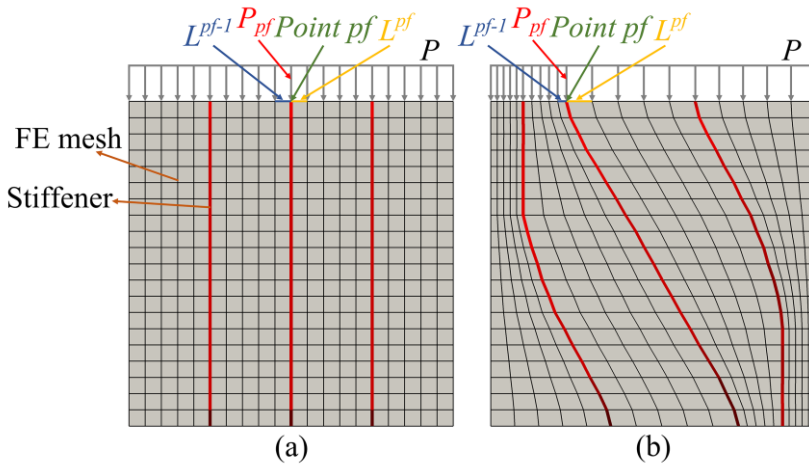


**Figure 6.4 Illustration of the application of pressure: (a) an example with the undeformed FE mesh; (b) an example with the deformed FE mesh.**

The stationary equation (Eq. (6-8a)) and the linear buckling equation (Eq. (6-8b)) are solved using the HSL MA57 solver [94] and ARPACK [95], respectively:

$$\mathbf{K}\mathbf{u} = \mathbf{f} \quad (6-8a)$$

$$(\mathbf{K} + \lambda\mathbf{K}_g(\mathbf{u}))\mathbf{v} = \mathbf{0} \quad (6-8b)$$

where  $\mathbf{K}$ ,  $\mathbf{u}$  and  $\mathbf{f}$  are the structural stiffness matrix, the stationary deflection and the applied load, respectively.  $\mathbf{K}_g$  is the structural geometric stiffness matrix.  $\lambda$  and  $\mathbf{v}$  represent the eigenvalue/eigenvector pair for a given buckling mode.

## 6.2 Problem Formulation and Optimization Method

In this section, the two problems considered in this work are described. To solve these two problems with a gradient-based optimizer, a semi-analytical sensitivity analysis is performed. The optimization methodology used is also presented here.

### 6.2.1 Problem Formulation

Both the problems of mass minimization with buckling constraint and critical buckling load factor maximization with mass constraint are investigated. As the minimum positive buckling load factor, the critical buckling load factor needs to be considered either as an objective or a constraint. In both the problems, the  $p$ -norm function [114] is used as a buckling aggregation function to approximate the inverse of the critical buckling load factor:

$$M_p = \left( \sum_{q=1}^{N_\lambda} (\mu_q)^p \right)^{1/p} \quad (6-9)$$

where  $\mu_q = 1/\lambda_q$ .  $\lambda_q$  is the buckling load factor for the  $q$ -th mode. The first  $N_\lambda$  buckling modes are considered in the optimization. The approximated value  $M_p$  moves closer to the inverse of the actual minimum as the aggregation parameter  $p$  increases.

The optimization problems are formulated as follows.

- 1) Mass minimization with a buckling constraint:

$$\begin{aligned} \min_{\Phi_l, \Phi_{to}} \quad & m(\Phi_l, \Phi_{to}) \\ \text{s.t.} \quad & M_p(\Phi_l, \Phi_{to}) \leq 1/\lambda_{\min} \\ & L_l(\Phi_l) \geq L_{\min}, \quad l = 1, 2, \dots, N_L \\ & A_r(\Phi_l) \geq A_{\min}, \quad r = 1, 2, \dots, N_A \\ & to = 1, 2, \dots, N \end{aligned} \quad (6-10)$$

where  $m$  is the structural mass.  $\lambda_{\min}$  is the lower bound of the critical buckling load factor. In this work, overlap and intersection between the adjacent stiffeners are not allowed, and severely distorted elements are avoided by setting stiffener spacing and element distortion constraints to ensure the accuracy of the finite element analysis (FEA).  $L$  denotes stiffener spacing constraints, and  $L_{\min}$  is their lower bound.  $A$  denotes

**Simultaneous Sizing, Layout and Topology Optimization  
for Buckling and Postbuckling of Stiffened Panels**

element distortion constraints, and  $A_{\min}$  is their lower bound.  $N_L$  and  $N_A$  are the numbers of stiffener spacing and element distortion constraints, respectively. The mass  $m$  is defined by the mass matrix:

$$m = \mathbf{g}^T \mathbf{M} \mathbf{g} \quad (6-11)$$

where the vector  $\mathbf{g}$  contains ones for deflection degrees of freedom along the gravity direction and zeros elsewhere.

The stiffener spacing constraints  $L$  and element distortion constraints  $A$  are evaluated using the element widths and interior angles of the control mesh, which can be calculated through the nodal coordinates  $\mathbf{x}_{\text{control}}$  of the control mesh.

2) Critical buckling load factor maximization with a mass constraint:

$$\begin{aligned} & \min_{\Phi_l, \Phi_{to}} M_p(\Phi_l, \Phi_{to}) \\ & s.t. \quad m(\Phi_l, \Phi_{to}) \leq m_{\max} \\ & \quad L_l(\Phi_l) \geq L_{\min}, \quad l = 1, 2, \dots, N_L \\ & \quad A_r(\Phi_l) \geq A_{\min}, \quad r = 1, 2, \dots, N_A \\ & \quad to = 1, 2, \dots, N \end{aligned} \quad (6-12)$$

where  $m_{\max}$  is the upper bound of the structural mass.

## 6.2.2 Sensitivity Analysis

In order to solve Eqs. (6-10) and (6-12) using a gradient-based optimizer, the sensitivities of the  $p$ -norm function  $M_p$ , the mass  $m$ , the stiffener spacing  $L$  and the element distortion  $A$  are needed. To obtain these sensitivities, a semi-analytical method is used.

### 6.2.2.1 Sensitivity Analysis for Layout Optimization

As shown in Eq. (3-14), the derivative of  $\lambda_q$  with respect to changes in the nodal coordinates of the control mesh  $y_i$  is computed using the adjoint method:

$$\frac{\partial \lambda_q}{\partial y_i} = \frac{\mathbf{u}^{adT} \left( \frac{\partial \mathbf{K}}{\partial y_i} \mathbf{u} - \frac{\partial \mathbf{f}}{\partial y_i} \right) - \mathbf{v}_q^T \left( \frac{\partial \mathbf{K}}{\partial y_i} + \lambda_q \frac{\partial \mathbf{K}_g(\mathbf{u})}{\partial y_i} \right) \mathbf{v}_q}{\mathbf{v}_q^T \mathbf{K}_g(\mathbf{u}) \mathbf{v}_q} \quad (6-13)$$

where  $\mathbf{u}_{ad}$  is the adjoint vector and

$$\lambda_q \mathbf{v}_q^T \frac{\partial \mathbf{K}_g(\mathbf{u})}{\partial \mathbf{u}} \mathbf{v}_q = \mathbf{u}_{ad}^T \mathbf{K} \quad (6-14)$$

It is noted that  $\partial \mathbf{f} / \partial y_i \neq \mathbf{0}$  in Eq. (6-13) because the update of  $\mathbf{y}$  leads to the re-distribution of the force applied to the nodes of the FE mesh via Eq. (6-7).

From Eq. (6-9), the derivative of  $M_p$  with respect to  $y_i$  can be obtained as:

$$\frac{\partial M_p}{\partial y_i} = M_p^{1-p} \sum_{q=1}^{N_s} \left( \mu_q^{p-1} (-\lambda_q^{-2}) \frac{\partial \lambda_q}{\partial y_i} \right) \quad (6-15)$$

Based on Eq. (6-11), the derivative of  $m$  with respect to  $y_i$  can be calculated by:

$$\frac{\partial m}{\partial y_i} = \mathbf{g}^T \frac{\partial \mathbf{M}}{\partial y_i} \mathbf{g} \quad (6-16)$$

The sensitivities of  $\lambda_q$ ,  $M_p$  and  $m$  are analytically derived and given by Eqs. (6-13), (6-15) and (6-16).  $\partial \mathbf{f} / \partial y_i$ ,  $\partial \mathbf{K} / \partial y_i$ ,  $\partial \mathbf{K}_g / \partial y_i$  and  $\partial \mathbf{M} / \partial y_i$  in Eqs. (6-13) and (6-16), as well as the derivatives  $dL_i / dy_i$  and  $dA_i / dy_i$  related to the spacing and element distortion constraints, can then be approximated via the central finite difference method, which is straightforward to implement. In this work, the perturbation is chosen as  $0.0001a_0$ , where  $a_0$  is the initial FE element width. The calculated sensitivities  $\partial g / \partial y_i$  in Eqs. (6-15) and (6-16) have been compared with  $(g(y_{i,0} + \Delta y_i) - g(y_{i,0} - \Delta y_i)) / 2\Delta y_i$ , where  $g$  represents an arbitrary equation, i.e.  $M_p$  and  $m$ . The error in mass sensitivity is within 0.1%, and the errors in buckling sensitivities are within 1% when there is no mode switching for the first few modes, which shows the accuracy of the sensitivity calculation.

As described in Chapters 3-5, during the optimization, the LSFs are always maintained as signed distance functions to ensure a well-behaved boundary. In order to convert an arbitrary LSF to a signed distance function with the same boundary locations, a combination of the marching squares and fast marching algorithms [86] is applied. In order to ensure the signed distance property  $|\nabla \Phi| = 1$  after every update of the LSF, the fast velocity extension algorithm [96] is utilized. The relationship between the changes

**Simultaneous Sizing, Layout and Topology Optimization  
for Buckling and Postbuckling of Stiffened Panels**

to the LSF values  $\Delta\Phi_b$  at the boundary and  $\Delta\Phi$  in the rest of the design domain is determined as:

$$\Delta\Phi = \left[ \frac{\partial\Phi}{\partial\Phi_b} \right] \Delta\Phi_b \quad (6-17)$$

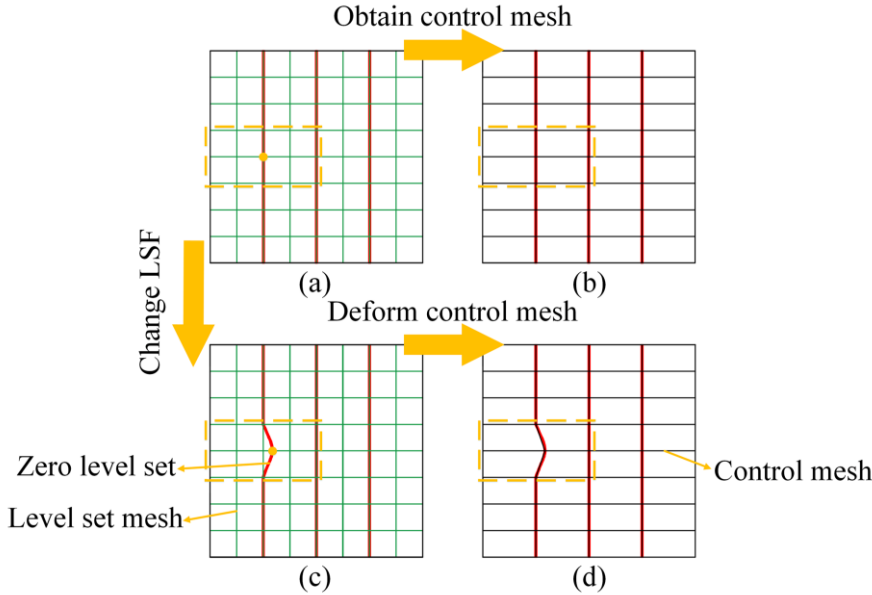


**Figure 6.5 Illustration of how to compute the term of  $\partial y_i / \partial \Phi_{l,b}$ : (a) the zero level set before perturbation and the level set mesh; (b) the zero level set and the corresponding control mesh before perturbation; (c) the zero level set after perturbation; (d) the control mesh, deformed in accordance with the change of the zero level set after perturbation.**

To update the LSF representing the stiffener layout, derivatives with respect to  $y_i$  are further mapped to the level set value of the boundary points  $\Phi_{l,b}$  through the chain rule:

$$\frac{\partial g}{\partial \Phi_{l,b}} = \sum_i \frac{\partial g}{\partial y_i} \frac{\partial y_i}{\partial \Phi_{l,b}} \quad (6-18)$$

where  $g$  is the general function representing the  $p$ -norm function  $M_p$ , the mass  $m$ , the stiffener spacing  $L$  and the element distortion  $A$ . The term  $\partial y_i / \partial \Phi_{l,b}$  is computed by perturbing the level set boundary implicitly, as shown in Fig. 6.5. For a given boundary point of interest, a small perturbation  $\Delta\Phi_{l,b}$  is assigned to its level set value  $\Phi_{l,b}$ . The change in the LSF  $\Delta\Phi_l$  can be obtained via Eq. (6-17). After implementing the marching squares and fast marching algorithms, as shown in Fig. 6.5(c), the new LSF and the

**Chapter 6: Simultaneous Layout and Topology Optimization of Panels with Curved Stiffeners  
Considering Buckling**

corresponding zero level set are achieved. This results in a new  $y_i$ . The control mesh is deformed, which is shown in Fig. 6.5(d). Then using the central finite difference method, the term  $\partial y_i / \partial \Phi_{l,b}$  can be approximated by:

$$\frac{\partial y_i}{\partial \Phi_{l,b}} = \frac{y_i|_{\Phi_{l,b}=\Phi_{l,b}+\Delta\Phi_{l,b}} - y_i|_{\Phi_{l,b}=\Phi_{l,b}-\Delta\Phi_{l,b}}}{2\Delta\Phi_{l,b}} \quad (6-19)$$

where the perturbation  $\Delta\Phi_{l,b}$  is chosen as  $0.001b_{l,0}$ , where  $b_{l,0}$  is the element width of the level set mesh used to describe the stiffener layout.

### 6.2.2.2 Sensitivity Analysis for Topology Optimization

In a similar way to the computation of  $\partial \lambda_q / \partial y_i$  in Eq. (6-13), the derivative of  $\lambda_q$  with respect to the physical density  $w_j$  can be obtained by:

$$\frac{\partial \lambda_q}{\partial w_j} = \frac{\mathbf{u}_{ad}^T \left( \frac{\partial \mathbf{K}}{\partial w_j} \mathbf{u} - \frac{\partial \mathbf{f}}{\partial w_j} \right) - \mathbf{v}_q^T \left( \frac{\partial \mathbf{K}}{\partial w_j} + \lambda_q \frac{\partial \mathbf{K}_g(\mathbf{u})}{\partial w_j} \right) \mathbf{v}_q}{\mathbf{v}_q^T \mathbf{K}_g(\mathbf{u}) \mathbf{v}_q} \quad (6-20)$$

where

$$\lambda_q \mathbf{v}_q^T \frac{\partial \mathbf{K}_g(\mathbf{u})}{\partial \mathbf{u}} \mathbf{v}_q = \mathbf{u}_{ad}^T \mathbf{K} \quad (6-21)$$

Since self-weight is ignored in this work,  $\partial \mathbf{f} / \partial w_j = 0$ , and Eq. (6-20) can be simplified to:

$$\frac{\partial \lambda_q}{\partial w_j} = \frac{\mathbf{u}_{ad}^T \frac{\partial \mathbf{K}}{\partial w_j} \mathbf{u} - \mathbf{v}_q^T \left( \frac{\partial \mathbf{K}}{\partial w_j} + \lambda_q \frac{\partial \mathbf{K}_g(\mathbf{u})}{\partial w_j} \right) \mathbf{v}_q}{\mathbf{v}_q^T \mathbf{K}_g(\mathbf{u}) \mathbf{v}_q} \quad (6-22)$$

From Eq. (6-9), the derivative of  $M_p$  with respect to  $w_j$  can be obtained as:

$$\frac{\partial M_p}{\partial w_j} = M_p^{1-p} \sum_{q=1}^{N_s} \left( \mu_q^{p-1} (-\lambda_q^{-2}) \frac{\partial \lambda_q}{\partial w_j} \right) \quad (6-23)$$

Based on Eq. (6-11), the derivative of  $m$  with respect to  $w_j$  can be calculated by:

**Simultaneous Sizing, Layout and Topology Optimization  
for Buckling and Postbuckling of Stiffened Panels**

$$\frac{\partial m}{\partial w_j} = \mathbf{z}_i^T \frac{\partial \mathbf{M}_i}{\partial w_j} \mathbf{z}_i \quad (6-24)$$

To update the LSFs representing the stiffener internal topologies, the derivatives with respect to  $w_j$  are further mapped to the level set values of the boundary points  $\Phi_{to,b}$  through the chain rule:

$$\frac{\partial g}{\partial \Phi_{to,b}} = \sum_j \frac{\partial g}{\partial w_j} \frac{\partial w_j}{\partial v_j} \frac{\partial v_j}{\partial \Phi_{to,b}} \quad (6-25)$$

where  $\partial w_j / \partial v_j = 1$  because  $w_j = v_j$ . In the same way as for the term  $\partial y_i / \partial \Phi_{l,b}$ , the term of  $\partial v_j / \partial \Phi_{to,b}$  is computed via the implicit perturbation of the level set boundary, which has been described in Section 3.2.2.2.

Using the gradient-based optimization method with the sensitivity information in Eqs. (6-18) and (6-25),  $\Delta \Phi_{l,b}$  and  $\Delta \Phi_{to,b}$  can be obtained. Following this  $\Delta \Phi_l$  and  $\Delta \Phi_{to}$  can be calculated via Eq. (6-17) such that  $|\nabla(\Phi + \Delta \Phi)| = 1$ . It is noted that, since the fast velocity extension algorithm is only first order accurate, the LSFs are re-initialized using the fast marching method after each update in this work.

### 6.2.3 Optimization Algorithm

The IPOPT algorithm [97] is used to solve the optimization problems described in Eqs. (6-10) and (6-12) at each iteration to obtain  $\Delta \Phi_{l,b}$  and  $\Delta \Phi_{to,b}$  in order to update the curved stiffened panels. Linearization of the optimization problems using Taylor's expansion can then be performed as follows.

1) Mass minimization with a buckling constraint:

$$\begin{aligned}
 & \min_{\Delta\Phi_{l,b}, \Delta\Phi_{to,b}} m_0 + \left[ \frac{\partial m}{\partial \Phi_{l,b}} \right]^T \Delta\Phi_{l,b} + \sum_{to=1}^N \left[ \frac{\partial m}{\partial \Phi_{to,b}} \right]^T \Delta\Phi_{to,b} \\
 \text{s.t. } & M_{p,0} + \left[ \frac{\partial M_p}{\partial \Phi_{l,b}} \right]^T \Delta\Phi_{l,b} + \sum_{to=1}^N \left[ \frac{\partial M_p}{\partial \Phi_{to,b}} \right]^T \Delta\Phi_{to,b} \leq \frac{1}{\lambda_{\min}} \\
 & L_{l,0} + \left[ \frac{dL_l}{d\Phi_{l,b}} \right]^T \Delta\Phi_{l,b} \geq L_{\min}, \quad l = 1, 2, \dots, N_L \\
 & A_{r,0} + \left[ \frac{dA_r}{d\Phi_{l,b}} \right]^T \Delta\Phi_{l,b} \geq L_{\min}, \quad r = 1, 2, \dots, N_A \\
 & -\gamma_1 \leq \Delta\Phi_{l,b} \leq \gamma_1 \\
 & -\gamma_2 \leq \Delta\Phi_{to,b} \leq \gamma_2 \\
 & to = 1, 2, \dots, N
 \end{aligned} \tag{6-26}$$

2) Critical buckling load factor maximization with a mass constraint:

$$\begin{aligned}
 & \min_{\Delta\Phi_{l,b}, \Delta\Phi_{to,b}} M_{p,0} + \left[ \frac{\partial M_p}{\partial \Phi_{l,b}} \right]^T \Delta\Phi_{l,b} + \sum_{to=1}^N \left[ \frac{\partial M_p}{\partial \Phi_{to,b}} \right]^T \Delta\Phi_{to,b} \\
 \text{s.t. } & m_0 + \left[ \frac{\partial m}{\partial \Phi_{l,b}} \right]^T \Delta\Phi_{l,b} + \sum_{to=1}^N \left[ \frac{\partial m}{\partial \Phi_{to,b}} \right]^T \Delta\Phi_{to,b} \leq m_{\max} \\
 & L_{l,0} + \left[ \frac{dL_l}{d\Phi_{l,b}} \right]^T \Delta\Phi_{l,b} \geq L_{\min}, \quad l = 1, 2, \dots, N_L \\
 & A_{r,0} + \left[ \frac{dA_r}{d\Phi_{l,b}} \right]^T \Delta\Phi_{l,b} \geq L_{\min}, \quad r = 1, 2, \dots, N_A \\
 & -\gamma_1 \leq \Delta\Phi_{l,b} \leq \gamma_1 \\
 & -\gamma_2 \leq \Delta\Phi_{to,b} \leq \gamma_2 \\
 & to = 1, 2, \dots, N
 \end{aligned} \tag{6-27}$$

where  $M_{p,0}$ ,  $m_0$ ,  $L_{l,0}$  and  $A_{r,0}$  are the values at the current iteration.  $\gamma_1$  and  $\gamma_2$  are the move limits for  $\Delta\Phi_{l,b}$  and  $\Delta\Phi_{to,b}$ , respectively.

The proposed method is illustrated in Fig. 6.6.

## Simultaneous Sizing, Layout and Topology Optimization for Buckling and Postbuckling of Stiffened Panels

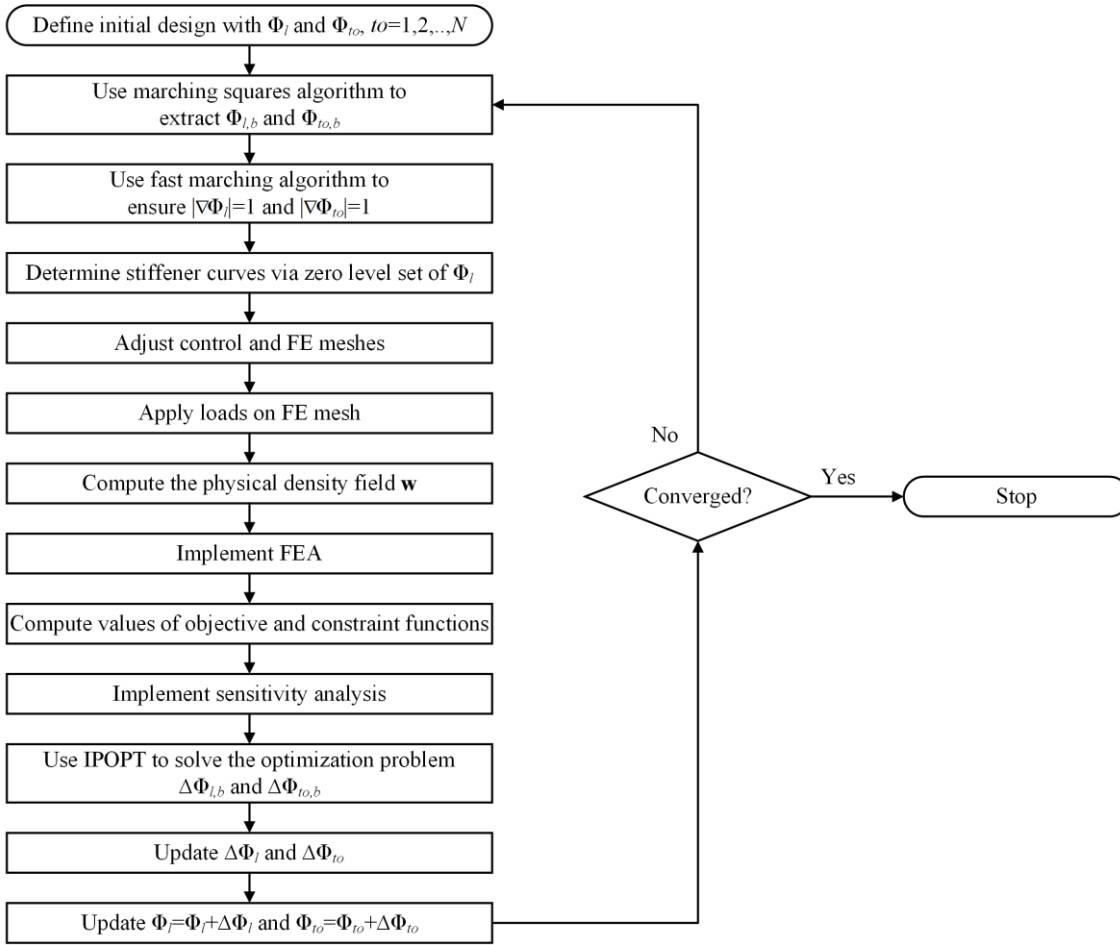


**Figure 6.6** Flowchart of the proposed method for the design of curved stiffened panels.

### 6.3 Numerical Examples

In this section, two numerical examples are presented to demonstrate the application of the proposed method for the simultaneous layout and topology optimization of curved stiffened panels. The Young's modulus of the solid material is  $E_s = 73$  GPa and the Young's modulus of the void phase is  $E_v = 10^{-6} \times 73$  GPa. The density is  $\rho_s = 2795$  kg/m<sup>3</sup> for the solid material and  $\rho_v = 0$  for the void phase. The Poisson's ratio is  $\nu = 0.33$ . The thicknesses of both the skin and the stiffeners is  $t = 0.002$  m.

#### 6.3.1 Mass Minimization with Buckling Constraint

For buckling-constrained problems, the  $p$ -norm function  $M_p$  cannot be applied directly to enforce a constraint on the inverse of the minimum positive buckling load factor. This is because, in Eq. (6-9), a finite  $p$  needs to be chosen for numerical stability, which

**Chapter 6: Simultaneous Layout and Topology Optimization of Panels with Curved Stiffeners  
Considering Buckling**

leads to the  $p$ -norm function value being greater than the inverse of the minimum. An adaptive scaling constraint [61, 114] similar to that for stress-constrained problems is adopted to make the  $p$ -norm function value closer to the inverse of the critical buckling load factor:

$$\alpha_1 M_p \leq \frac{1}{\lambda_{\min}} \quad (6-28)$$

where  $\alpha_1^k = \frac{1}{\lambda_1^k M_p^k}$  at the  $k$ th iteration.

When IPOPT is used to solve the problem described by Eq. (6-28), the buckling constraint is approximated as:

$$\alpha_1 [M_p^k]_{\text{approximation}} = \alpha_1 \left( M_p^{k-1} + \left[ \frac{\partial M_p}{\partial \Phi_{l,b}} \right]_{k-1}^T \Delta \Phi_{l,b,k-1} + \sum_{to=1}^N \left[ \frac{\partial M_p}{\partial \Phi_{to,b}} \right]_{k-1}^T \Delta \Phi_{to,b,k-1} \right) \leq \frac{1}{\lambda_{\min}} \quad (6-29)$$

Using IPOPT, only the constraint in Eq. (6-29) is satisfied at each iteration of the optimization. However, since only first-order sensitivity information is used and higher-order sensitivity information is ignored, the prediction of the  $p$ -norm function  $[M_p^k]_{\text{approximation}}$  from Eq. (6-29) is not sufficiently accurate and may be slightly smaller than the real one  $M_p^k$ . This may lead to the violation of the actual buckling constraint  $\lambda_1 \geq \lambda_{\min}$ . Therefore, an additional adaptive scaling constraint scheme is introduced and Eq. (6-28) is re-written as:

$$\alpha_1 \alpha_2 M_p \leq \frac{1}{\lambda_{\min}} \quad (6-30)$$

where  $\alpha_2^k = \frac{M_p^k}{[M_p^k]_{\text{approximation}}}$ .

The mass minimization problem with buckling constraint at each iteration in Eq. (6-26) can therefore be re-written as:

**Simultaneous Sizing, Layout and Topology Optimization  
for Buckling and Postbuckling of Stiffened Panels**

$$\begin{aligned}
 & \min_{\Delta\Phi_{l,b}, \Delta\Phi_{to,b}} \quad m_0 + \left[ \frac{\partial m}{\partial \Phi_{l,b}} \right]^T \Delta\Phi_{l,b} + \sum_{to=1}^N \left[ \frac{\partial m}{\partial \Phi_{to,b}} \right]^T \Delta\Phi_{to,b} \\
 \text{s.t.} \quad & M_{p,0} + \left[ \frac{\partial M_p}{\partial \Phi_{l,b}} \right]^T \Delta\Phi_{l,b} + \sum_{to=1}^N \left[ \frac{\partial M_p}{\partial \Phi_{to,b}} \right]^T \Delta\Phi_{to,b} \leq \frac{1}{\alpha_1 \alpha_2 \lambda_{\min}} \\
 & L_{l,0} + \left[ \frac{dL_l}{d\Phi_{l,b}} \right]^T \Delta\Phi_{l,b} \geq L_{\min}, \quad l = 1, 2, \dots, N_L \\
 & A_{r,0} + \left[ \frac{dA_r}{d\Phi_{l,b}} \right]^T \Delta\Phi_{l,b} \geq L_{\min}, \quad r = 1, 2, \dots, N_A \\
 & -\gamma_1 \leq \Delta\Phi_{l,b} \leq \gamma_1 \\
 & -\gamma_2 \leq \Delta\Phi_{to,b} \leq \gamma_2 \\
 & to = 1, 2, \dots, N
 \end{aligned} \tag{6-31}$$

A stiffened panel with the loading and boundary conditions shown in Fig. 6.7 is considered for optimization. The bottom edge of the panel is fixed, and a shear load  $P = 300$  kN/m is applied on the top edge. The initial design, which comprises a  $0.3 \text{ m} \times 0.3 \text{ m}$  skin and 7 vertical stiffeners, each with a height of  $0.03 \text{ m}$  is shown in Fig. 6.8. The FE mesh comprises  $80 \times 80$  plate elements for the skin, with 8 elements along the height of each of the stiffeners. Eight LSFs are used, comprising one representing the stiffener curves and seven for the internal topologies of the stiffeners. The first 50 buckling modes are considered in the optimization. For the  $p$ -norm function, the aggregation parameter  $p = 12$  is used. The lower bound of the critical buckling load factor  $\lambda_{\min} = 1$ . The lower bound of the stiffener spacing  $L_{\min} = 15 \text{ mm}$ .

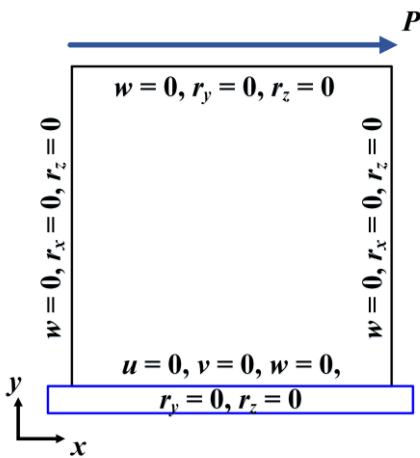


**Figure 6.7 Loading and boundary conditions for the design of a stiffened panel under shear loading.**

**Chapter 6: Simultaneous Layout and Topology Optimization of Panels with Curved Stiffeners Considering Buckling**

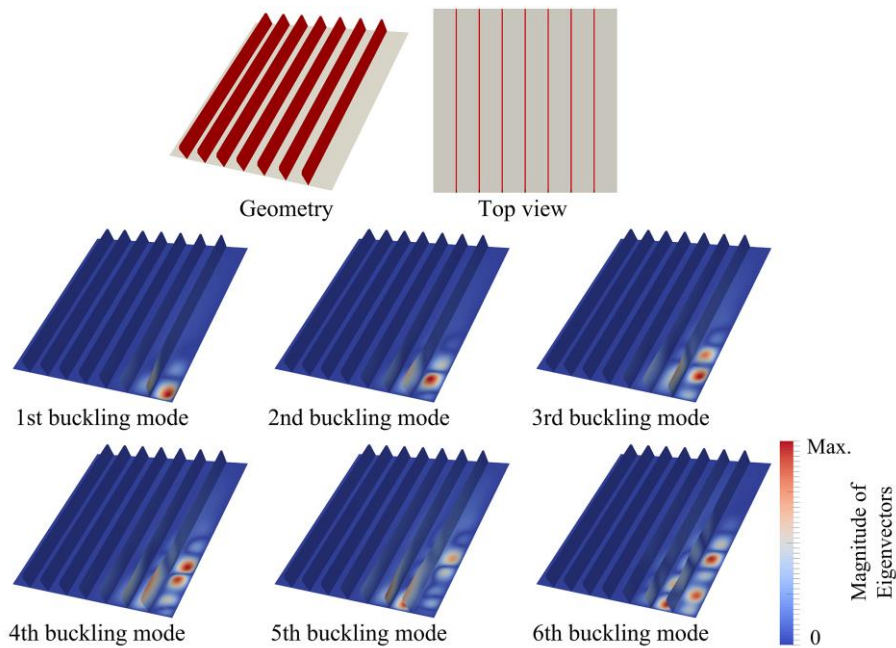


**Figure 6.8 Initial design with 7 vertical stiffeners,  $m = 0.855$  kg, and its first 6 buckling modes under shear loading,  $\lambda_1 = 1.141$ ,  $\lambda_2 = 1.459$ ,  $\lambda_3 = 1.702$ ,  $\lambda_4 = 1.903$ ,  $\lambda_5 = 2.089$ ,  $\lambda_6 = 2.155$ .**

The optimized design is shown in Fig. 6.9. Compared with the initial design, the mass is decreased by 34.1%. Despite this, the critical buckling load factor  $\lambda_1 = 1.008$  and the buckling constraint is satisfied. It can be observed that, by using topology optimization, the number of stiffeners and the internal topology, height and width of each of them are optimized. From the initial design and corresponding buckling modes in Fig. 6.8, it can be seen that buckling tends to occur towards the right-hand side of the panel under the given load case since this is the area where the greatest compression due to in-plane bending occurs. In order to increase the stiffness in these regions, the three stiffeners which remain are moved to the right-hand side of the structure. It can also be seen that for each stiffener in the optimized design, the height of the central part of the stiffeners is greater than that at the ends, to increase out-of-plane stiffness in this unsupported region (the ends are prevented from deflecting out of plane) and defer overall buckling modes.

**Simultaneous Sizing, Layout and Topology Optimization  
for Buckling and Postbuckling of Stiffened Panels**

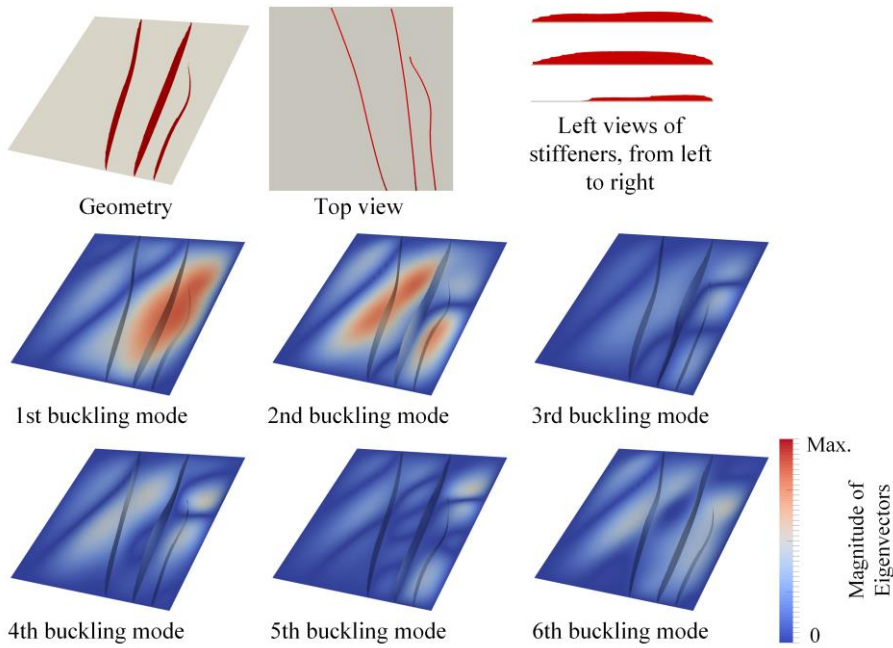


**Figure 6.9** Optimized design for mass minimization with buckling constraints, considering the initial design with 7 vertical stiffeners,  $m = 0.563$  kg, and its first 6 buckling modes under shear loading,  $\lambda_1 = 1.008$ ,  $\lambda_2 = 1.077$ ,  $\lambda_3 = 1.102$ ,  $\lambda_4 = 1.122$ ,  $\lambda_5 = 1.246$ ,  $\lambda_6 = 1.256$ .

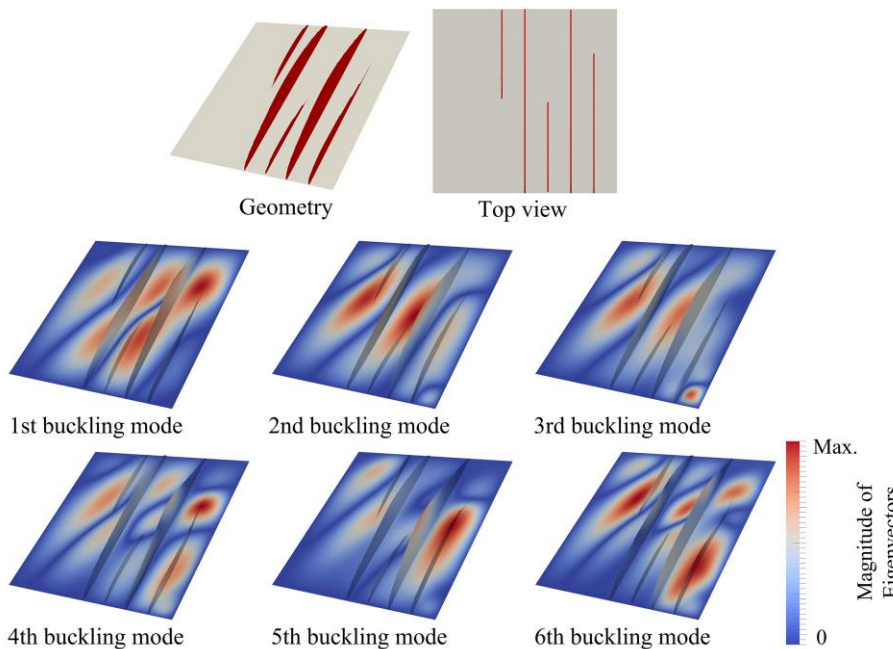


**Figure 6.10** Optimized design without the layout optimization for mass minimization with buckling constraints, considering the initial design with 7 vertical stiffeners,  $m = 0.594$  kg, and its first 6 buckling modes under shear loading,  $\lambda_1 = 1.000$ ,  $\lambda_2 = 1.039$ ,  $\lambda_3 = 1.064$ ,  $\lambda_4 = 1.170$ ,  $\lambda_5 = 1.182$ ,  $\lambda_6 = 1.293$ .

## Chapter 6: Simultaneous Layout and Topology Optimization of Panels with Curved Stiffeners Considering Buckling

An optimization where the layout design variables are excluded, is also performed. The same initial design with 7 vertical stiffeners shown in Fig. 6.8 is used. The result is presented in Fig. 6.10. Here, the layout of the stiffeners is frozen, with only the number and topologies of the stiffeners optimized. The mass of the optimized design in Fig. 6.9 with simultaneous layout and topology optimization is 0.563 kg, while the optimized design in Fig. 6.10 without the layout design variables is 0.594 kg, a 5.4% difference. In comparison with the optimized design in Fig. 6.9, more stiffeners with greater height are required in the optimized design in Fig. 6.10. In terms of the mass of the stiffeners, there is a 50.9% difference between the two optimized designs. This shows that simultaneous layout and topology optimization allows a further significant reduction in the panel's weight.

To investigate the influence of the initial configuration, the optimization problem is also solved considering initial designs with different numbers of stiffeners. The maximum number of iterations is 1500. The initial designs are shown in Figs. 6.11, 6.13 and 6.15. The corresponding results are given in Figs. 6.12, 6.14 and 6.16, respectively. The differences between their masses are within 0.54%. It can be observed that, three stiffeners remain in the optimized designs in Figs. 6.12 and 6.14, while there are four stiffeners left in the optimized designs in Fig. 6.16. When the maximum number of iterations is extended to 2500 for the optimization considering the initial design with 11 vertical stiffeners, it is found in Fig. 6.17 that the extra stiffener is removed. However, the mass is only reduced by 0.53%, compared to that of the optimized design using 1500 iterations. Considering the computational cost, it may not be worth continuing to optimize the structure after 1500 iterations. It can be also observed that all the optimized designs follow the same trends. The remaining stiffeners are moved to the right-hand side of the panel to increase the stiffness in the bottom right-hand region of the panel. Therefore, even though initial designs with different numbers of stiffeners are selected, the proposed method has the potential to find promising results within the corresponding limited design space.

**Simultaneous Sizing, Layout and Topology Optimization  
for Buckling and Postbuckling of Stiffened Panels**

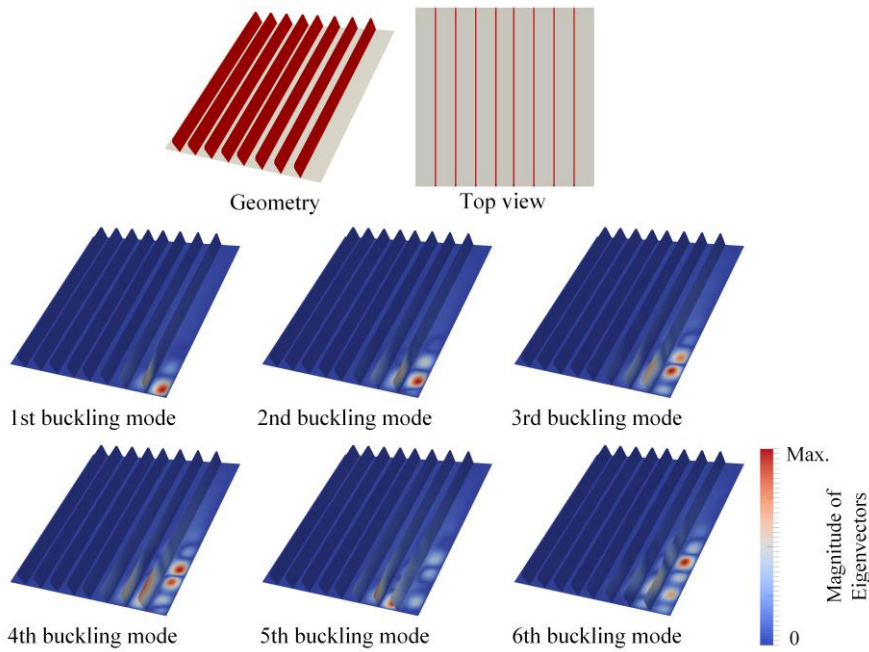


**Figure 6.11** Initial design with 8 vertical stiffeners,  $m = 0.905$  kg, and its first 6 buckling modes under shear loading,  $\lambda_1 = 1.364$ ,  $\lambda_2 = 1.744$ ,  $\lambda_3 = 2.027$ ,  $\lambda_4 = 2.255$ ,  $\lambda_5 = 2.412$ ,  $\lambda_6 = 2.522$ .

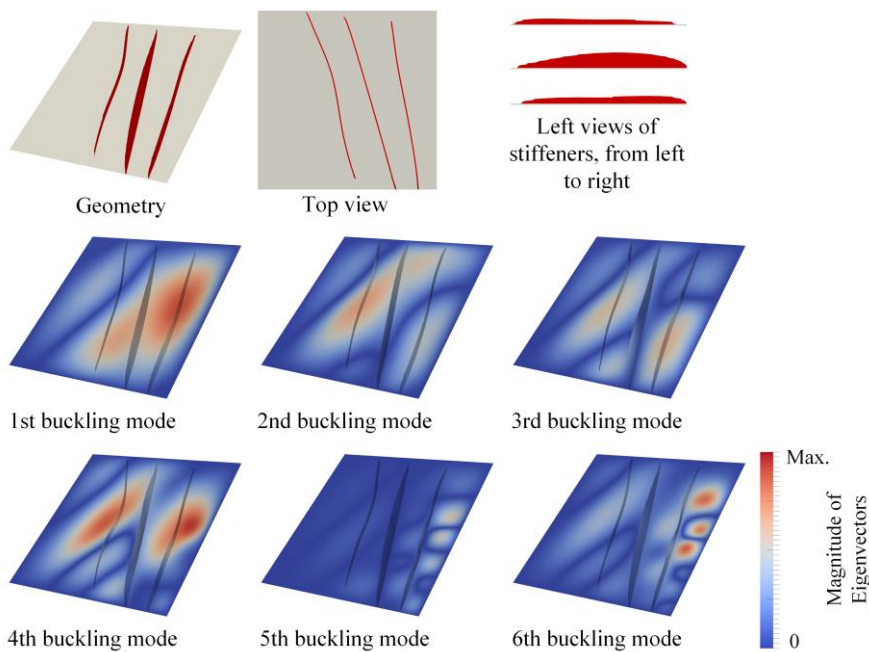


**Figure 6.12** Optimized design for mass minimization with buckling constraints, considering the initial design with 8 vertical stiffeners,  $m = 0.564$  kg, and its first 6 buckling modes under shear loading,  $\lambda_1 = 1.002$ ,  $\lambda_2 = 1.061$ ,  $\lambda_3 = 1.119$ ,  $\lambda_4 = 1.190$ ,  $\lambda_5 = 1.248$ ,  $\lambda_6 = 1.253$ .

Chapter 6: Simultaneous Layout and Topology Optimization of Panels with Curved Stiffeners Considering Buckling

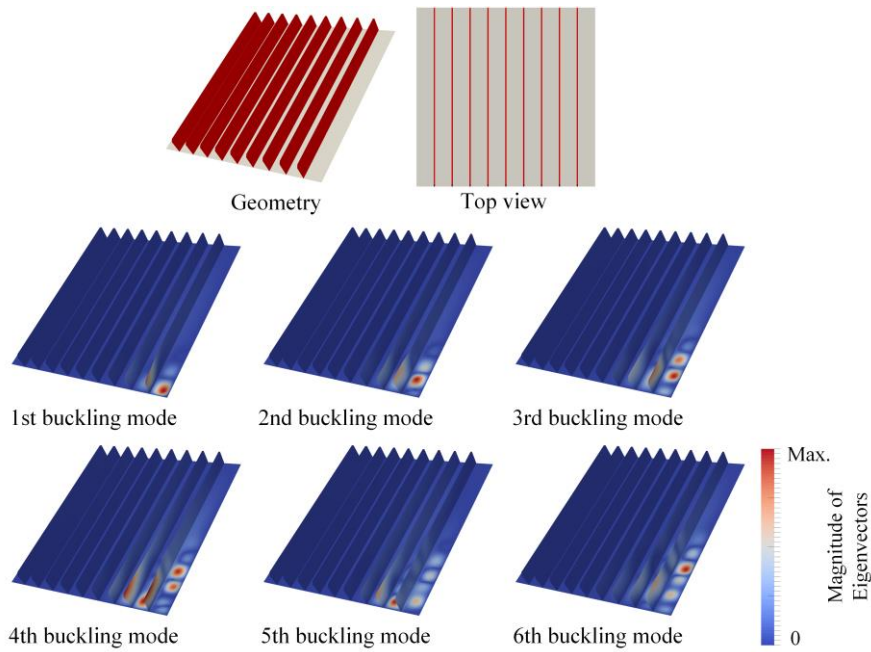


Figure 6.13 Initial design with 9 vertical stiffeners,  $m = 0.955$  kg, and its first 6 buckling modes under shear loading,  $\lambda_1 = 1.667$ ,  $\lambda_2 = 2.134$ ,  $\lambda_3 = 2.475$ ,  $\lambda_4 = 2.731$ ,  $\lambda_5 = 2.837$ ,  $\lambda_6 = 3.046$ .

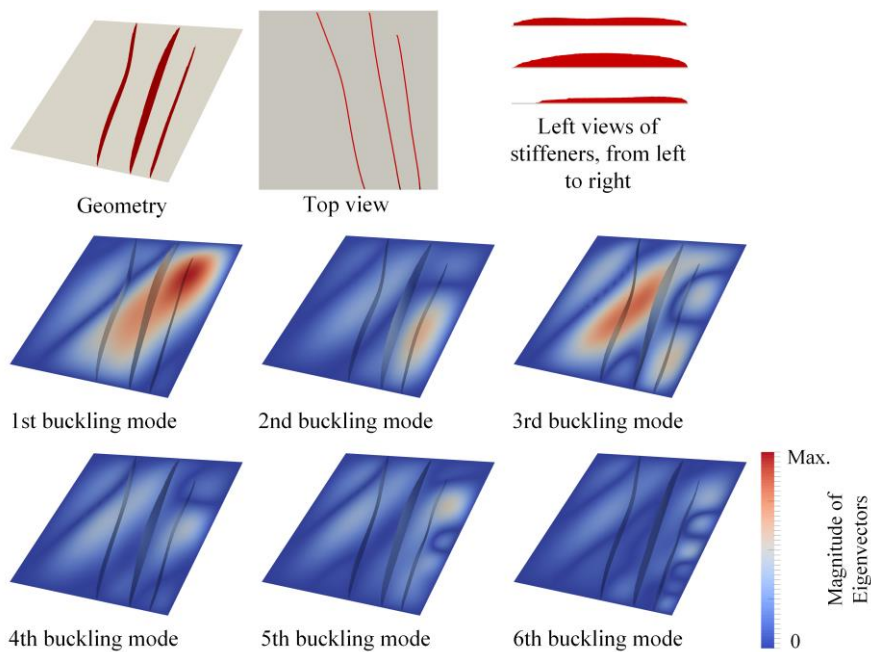
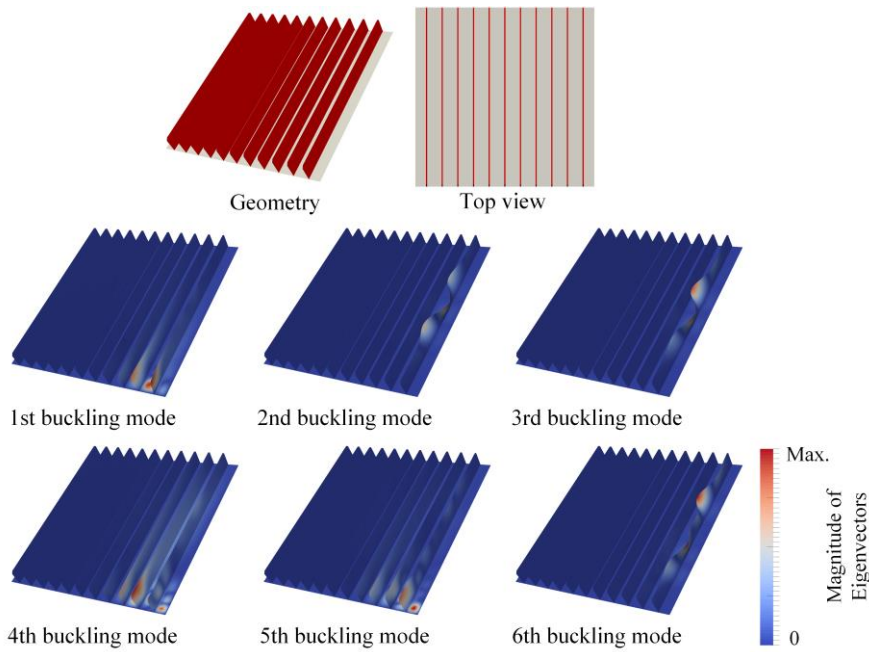
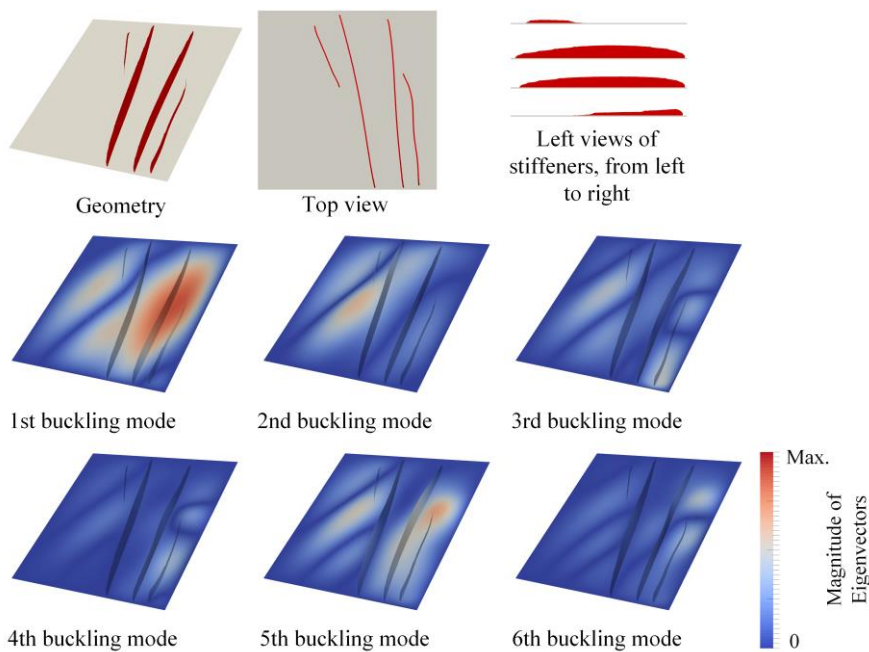


Figure 6.14 Optimized design for mass minimization with buckling constraints, considering the initial design with 9 vertical stiffeners,  $m = 0.565$  kg, and its first 6 buckling modes under shear loading,  $\lambda_1 = 1.008$ ,  $\lambda_2 = 1.058$ ,  $\lambda_3 = 1.108$ ,  $\lambda_4 = 1.196$ ,  $\lambda_5 = 1.298$ ,  $\lambda_6 = 1.316$ .

**Simultaneous Sizing, Layout and Topology Optimization  
for Buckling and Postbuckling of Stiffened Panels**



**Figure 6.15** Initial design with 11 vertical stiffeners,  $m = 1.056$  kg, and its first 6 buckling modes under shear loading,  $\lambda_1 = 3.153$ ,  $\lambda_2 = 3.2322$ ,  $\lambda_3 = 3.2325$ ,  $\lambda_4 = 3.848$ ,  $\lambda_5 = 3.992$ ,  $\lambda_6 = 4.193$ .



**Figure 6.16** Optimized design at 1500th iteration for mass minimization with buckling constraints, considering the initial design with 11 vertical stiffeners,  $m = 0.562$  kg, and its first 6 buckling modes under shear loading,  $\lambda_1 = 1.006$ ,  $\lambda_2 = 1.047$ ,  $\lambda_3 = 1.099$ ,  $\lambda_4 = 1.145$ ,  $\lambda_5 = 1.163$ ,  $\lambda_6 = 1.216$ .

## Chapter 6: Simultaneous Layout and Topology Optimization of Panels with Curved Stiffeners Considering Buckling

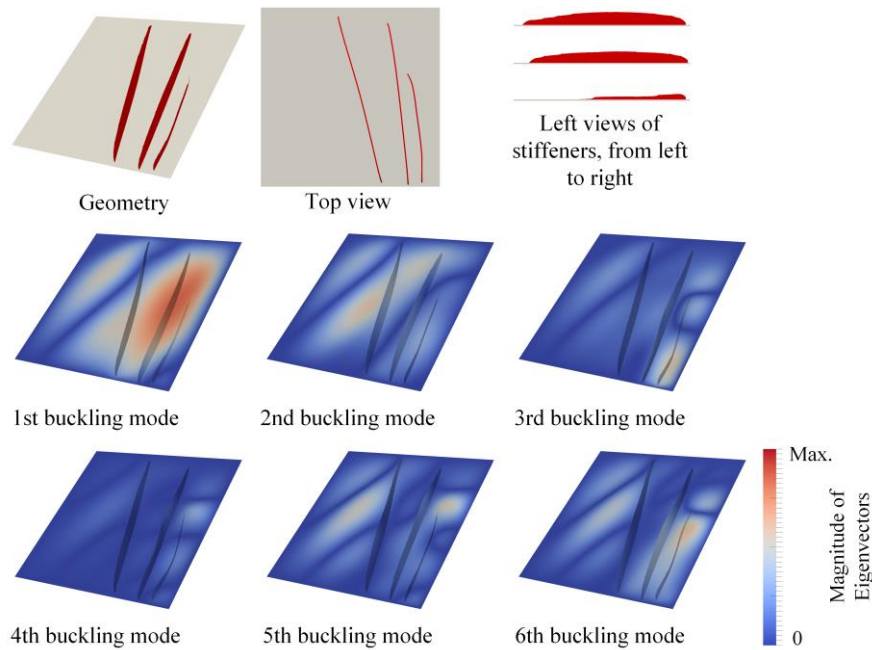


**Figure 6.17** Optimized design at 2500th iteration for mass minimization with buckling constraints, considering the initial design with 11 vertical stiffeners,  $m = 0.559$  kg, and its first 6 buckling modes under shear loading,  $\lambda_1 = 1.003$ ,  $\lambda_2 = 1.085$ ,  $\lambda_3 = 1.142$ ,  $\lambda_4 = 1.163$ ,  $\lambda_5 = 1.220$ ,  $\lambda_6 = 1.254$ .

### 6.3.2 Critical Buckling Load Factor Maximization with Mass Constraint

A stiffened panel with the same loading and boundary conditions as in Fig. 6.7 is considered for the optimization of critical buckling load with mass constraint. The same initial design with 7 vertical stiffeners shown in Fig. 6.8 is used. All the FEA and optimization parameters are the same as those in Section 6.3.1. The upper bound of the stiffener mass is set to 17% of the initial design, i.e., the upper bound of the structural mass  $m_{max} = 0.563$  kg which is that of the optimized design obtained from the mass minimization with a buckling constraint.

The optimized design is shown in Fig. 6.18. Its mass is 0.563 kg. The mass constraint is satisfied. The stiffener layout is optimized, and the redundant material is removed. The geometries of the optimized design in this optimization problem and the one obtained by mass minimization with a buckling constraint in Fig. 6.9 are compared in Fig. 6.19. It can be seen that both the topology and the layout of the two results are almost same. However, there are minor differences in the stiffener curves and heights causing the buckling load factors in Fig. 6.9 to be a little larger (within 3%) than the ones in

**Simultaneous Sizing, Layout and Topology Optimization  
for Buckling and Postbuckling of Stiffened Panels**

Fig.6.18. It is noted that, since both the topology optimization problems of mass minimization with buckling constraint and critical buckling load factor maximization with mass constraint are highly nonlinear, many local optima exist. Therefore, the similarity between the results in Figs. 6.9 and 6.18 demonstrates that the optimization methodology proposed in this work shows a reasonable level of reliability.

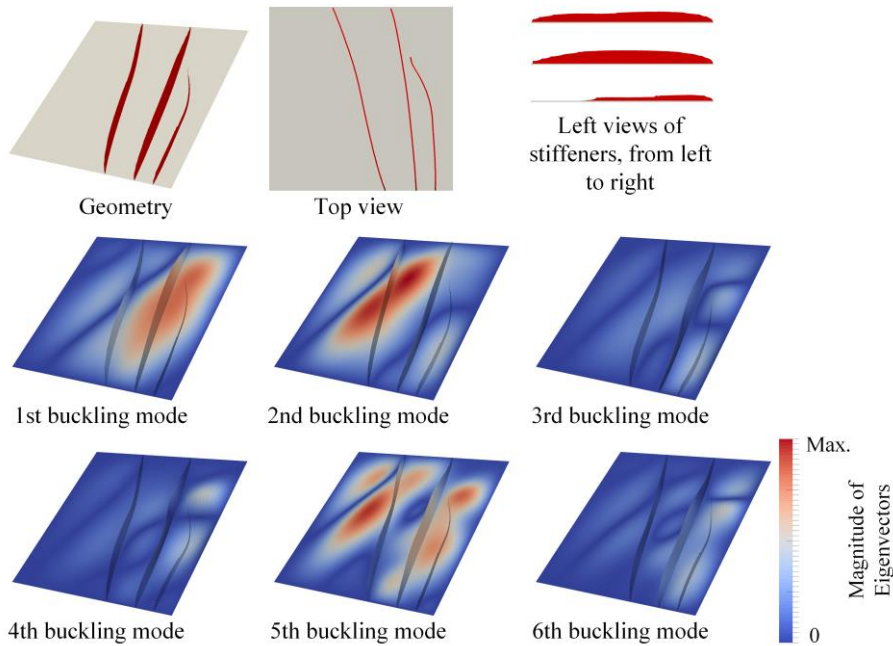


**Figure 6.18 Optimized design for critical buckling load factor maximization with a mass constraint, considering the initial design with 7 vertical stiffeners,  $m = 0.563$  kg, and its first 6 buckling modes under shear loading,  $\lambda_1 = 1.000$ ,  $\lambda_2 = 1.060$ ,  $\lambda_3 = 1.094$ ,  $\lambda_4 = 1.119$ ,  $\lambda_5 = 1.210$ ,  $\lambda_6 = 1.242$ .**

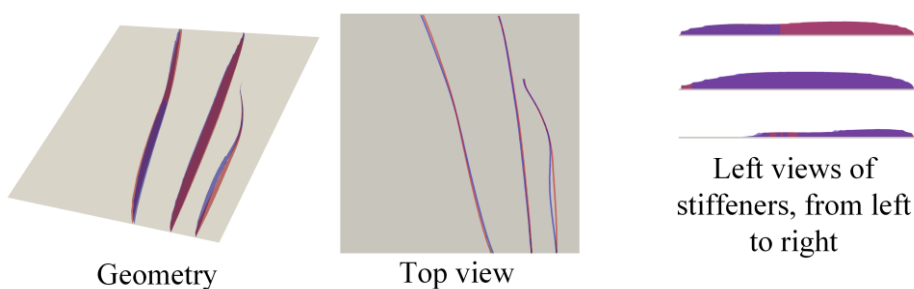


**Figure 6.19 Comparison of the geometries of the optimized designs in Figs. 6.9 (blue,  $m = 0.563$  kg and  $\lambda_1 = 1.008$ ) and 6.18 (red,  $m = 0.563$  kg and  $\lambda_1 = 1.000$ ).**

## Chapter 6: Simultaneous Layout and Topology Optimization of Panels with Curved Stiffeners Considering Buckling

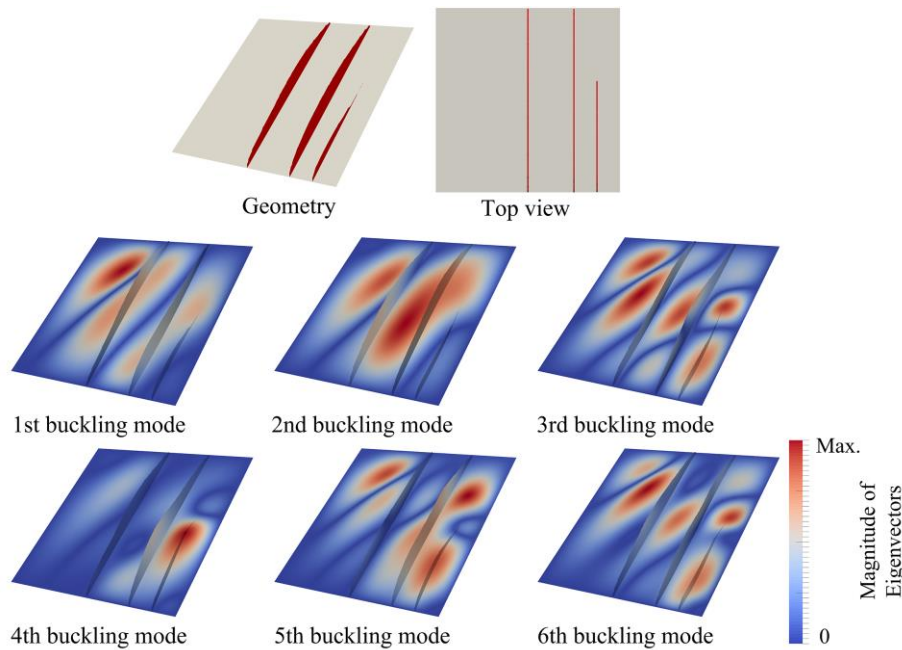


**Figure 6.20** Optimized design without the layout optimization for critical buckling load factor maximization with a mass constraint, considering the initial design with 7 vertical stiffeners,  $m = 0.563$  kg, and its first 6 buckling modes under shear loading,  $\lambda_1 = 0.691$ ,  $\lambda_2 = 0.717$ ,  $\lambda_3 = 0.805$ ,  $\lambda_4 = 0.823$ ,  $\lambda_5 = 0.884$ ,  $\lambda_6 = 0.958$ .

An optimization in which the layout design variables are excluded is also performed. The initial design with 7 vertical stiffeners shown in Fig. 6.8 is used. The result is presented in Fig. 6.20. Compared with the optimized design in Fig. 6.18 based on simultaneous layout and topology optimization, the optimized design in Fig. 6.20 with topology optimization only, has a worse buckling performance. There is a 30.9% difference in the critical buckling load factors. This shows the simultaneous layout and topology optimization can be effective in improving the buckling performance.

### 6.3.3 Comparison with the Optimization of Panels with Straight Stiffeners

To compare the optimized designs with curved and straight stiffeners, the simultaneous layout and topology optimization for the minimization of the mass of a panel with straight stiffeners under buckling constraints is conducted. As for the optimization of curved stiffened panels, the initial design in Fig. 6.8 is utilized and the first 50 buckling modes are considered in the optimization. The optimized design is given in Fig. 6.21. Its mass is 0.557 kg, which is 1.07% lighter than that of the design in Fig. 6.9. This

### Simultaneous Sizing, Layout and Topology Optimization for Buckling and Postbuckling of Stiffened Panels

conflicts with the statement that panels stiffened with curved stiffeners have the potential to result in lighter weight designs than those with straight stiffeners [2].

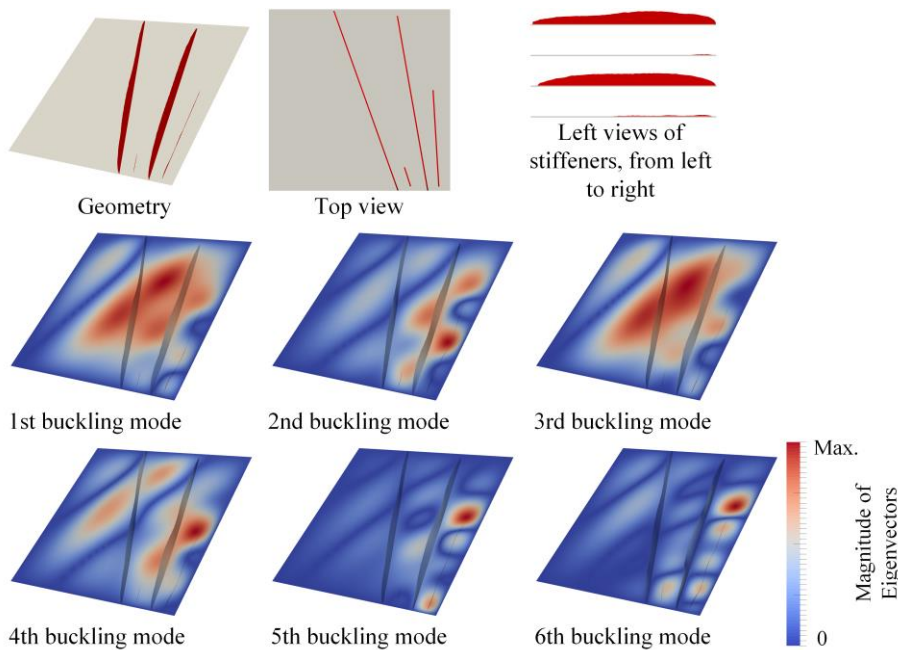


**Figure 6.21 Optimized design with straight stiffeners for mass minimization with buckling constraints, considering the initial design with 7 vertical stiffeners,  $m = 0.557$  kg, and its first 6 buckling modes under shear loading,  $\lambda_1 = 1.001$ ,  $\lambda_2 = 1.012$ ,  $\lambda_3 = 1.014$ ,  $\lambda_4 = 1.022$ ,  $\lambda_5 = 1.070$ ,  $\lambda_6 = 1.162$ .**

To investigate why this happens, the optimization formulation and algorithm are studied first. The optimization defined in Eq. (6-31), introduces hundreds of constraints since the stiffener spacing and element distortion constraints are local constraints and therefore need to be measured at every element on the control mesh. In this work, to decrease this large number of constraints, threshold values are set for stiffener spacing and element distortion constraints. Only when these values are exceeded are the constraints added to the optimization. Even so although only a small number of constraints exist at the beginning of the optimization, this can increase to more than one hundred as the optimization proceeds and stiffener spacing and element distortion constraints become active. To check whether a large number of constraints could be making it difficult for the optimizer to find a promising solution, the  $p$ -norm function with an adaptive scaling scheme is also applied to stiffener spacing and element distortion constraints, so that only three constraints, i.e.,  $p$ -norm functions for buckling, stiffener spacing and element distortion, are included in the optimization. The

optimization for the curved stiffened panel is repeated with the seven-vertical-stiffener initial design in Fig. 6.8, and the optimized design is given in Fig. 6.22. Using three significant numbers, the same mass as that of the design in Fig. 6.9 is found. This shows the robustness of the proposed algorithm, and that a large number of constraints are not the reason a worse design is obtained with curved stiffeners than with straight stiffeners. To further investigate this problem, the optimization of curved stiffened panels is repeated using Eq. (6-31), taking the optimized design with straight stiffeners in Fig. 6.21 as the initial design. The optimized design is shown in Fig. 6.23. Its mass is 0.54% smaller than that of the design in Fig. 6.21. This shows that the proposed parameterization has the capability to describe a panel with curved stiffeners having a better performance than the optimized design with straight stiffeners. However, many local optima exist for this problem, which agrees with the observation in [2]. In this work, using the gradient-based optimizer, IPOPT, a worse local optimum is found when the initial design with 7 vertical stiffeners is employed.

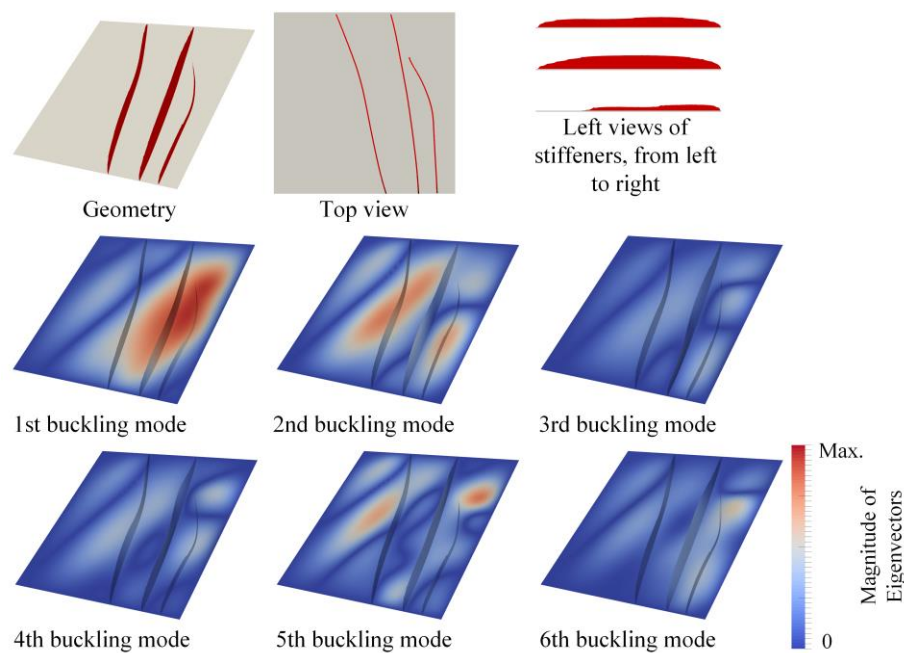


**Figure 6.22** Optimized design with curved stiffeners for mass minimization with  $p$ -norm buckling, stiffener spacing and element distortion constraints, considering the initial design with 7 vertical stiffeners,  $m = 0.563$  kg, and its first 6 buckling modes under shear loading,  $\lambda_1 = 1.007$ ,  $\lambda_2 = 1.065$ ,  $\lambda_3 = 1.083$ ,  $\lambda_4 = 1.119$ ,  $\lambda_5 = 1.237$ ,  $\lambda_6 = 1.244$ .

**Simultaneous Sizing, Layout and Topology Optimization  
for Buckling and Postbuckling of Stiffened Panels**

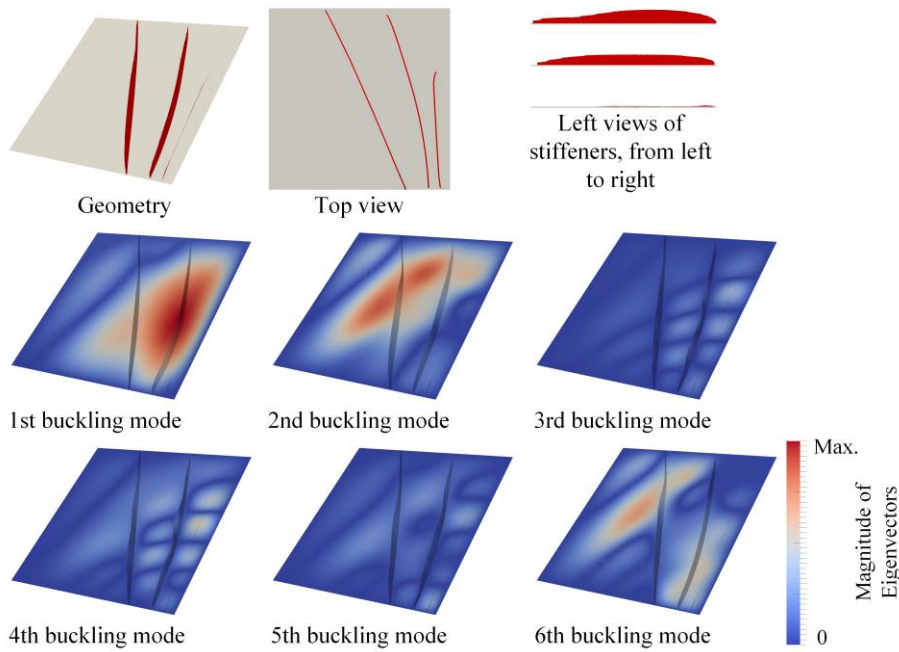


**Figure 6.23 Optimized design with curved stiffeners for mass minimization with buckling constraints, considering the optimized design with straight stiffeners in Fig. 6.21 as the initial design,  $m = 0.554$  kg, and its first 6 buckling modes under shear loading,  $\lambda_1 = 1.002$ ,  $\lambda_2 = 1.118$ ,  $\lambda_3 = 1.140$ ,  $\lambda_4 = 1.150$ ,  $\lambda_5 = 1.203$ ,  $\lambda_6 = 1.241$ .**

Postbuckling analyses are implemented for the optimized designs in Figs. 6.21 and 6.23, where imperfections based on critical buckling modes are introduced and their maximum amplitudes are set to  $20 \mu\text{m}$ . Their postbuckling behaviours are shown in Fig. 6.24. It can be found that although the difference in the critical buckling load factors of these two designs is within 0.1%, the maximum out-of-plane and in-plane skin displacements of the optimized design with curved stiffeners in Fig. 6.23 are respectively 1.30% and 2.37% better than those with straight stiffeners in Fig. 6.21 when the shear load  $P = 300$  kN/m corresponding to the critical buckling load, is applied. When the shear load is increased to twice the critical buckling load,  $P = 600$  kN/m, the maximum out-of-plane and in-plane skin displacements of the optimized design with curved stiffeners in Fig. 6.23 are 2.10% and 7.14% better than those with straight stiffeners in Fig. 6.21, respectively. This shows that curved stiffened panels might have more advantages in the postbuckling regime.

## Chapter 6: Simultaneous Layout and Topology Optimization of Panels with Curved Stiffeners Considering Buckling

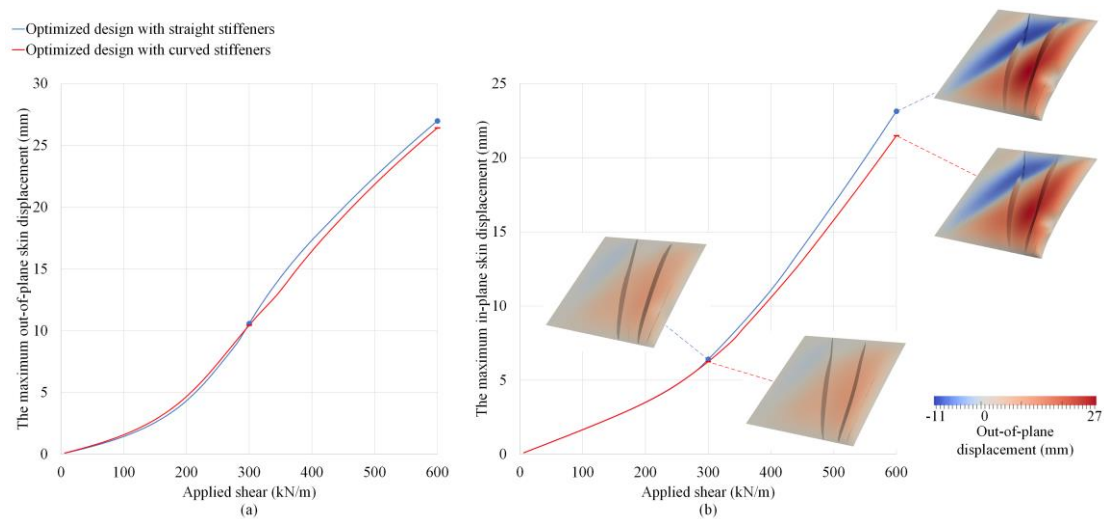


**Figure 6.24** Comparison of postbuckling behaviours between the optimized design with curved stiffeners in Fig. 6.23 and the optimized design with straight stiffeners in Fig. 6.21.

### 6.4 Conclusions

This chapter presents a level-set-based method for simultaneous layout and topology optimization of curved stiffened panels. To the best of the authors' knowledge, this work is the first to investigate the simultaneous layout and topology optimization of panels with curved stiffeners using a gradient-based approach. The construction and update of the geometric and finite element models using the level set method and a free-form mesh deformation method are described in detail. Both the problems of mass minimization with buckling constraint and critical buckling load factor maximization with mass constraint are studied. A sensitivity analysis is presented, and the optimization algorithm is outlined. The numerical results show the presented method is able to efficiently solve the two stiffened panel design problems. The stiffener layout is optimized, redundant stiffeners are removed, and the material in the remaining stiffeners is redistributed to satisfy all the constraints. For the buckling-constrained problem, when the  $p$ -norm function and the gradient-based optimizer IPOPT are used, the presented method is able to satisfy the buckling constraints with an adaptive scaling method. However, many local optima exist for this problem. Though a curved stiffened panel having a better performance than the optimized design with straight stiffeners, can be described by the proposed method, it might not be found using the gradient-based optimizer. The postbuckling behaviours of optimized designs with curved and straight

**Simultaneous Sizing, Layout and Topology Optimization  
for Buckling and Postbuckling of Stiffened Panels**

stiffeners are also investigated, showing that curved stiffened panels may be superior in the postbuckling regime.

# 7 CONCLUSIONS AND FURTHER WORK

This chapter gives some concluding remarks. The main contributions of this thesis are outlined. Suggestions for future research are also provided.

## 7.1 Summary and Main Contributions

This thesis is focused on the development of a level set topology optimization method to simultaneously optimize the size, layout and topology of stiffened panels against buckling and postbuckling. This method employs plate elements to model stiffeners which are parametrized by multiple implicit level set functions (LSFs) thus optimizing the shape (straight or curved, and internal topology) and size of each stiffener, simultaneously with the orientation and number of the stiffeners and the skin thickness. By using 2D plate elements, the mesh density can be several orders of magnitude less than for an equivalent mesh of 3D continuum elements.

A level-set-based topology optimization parameterization for panels stiffened with straight stiffeners is proposed, in Chapter 3. The weight minimization of stiffened panels simultaneously optimizing size, layout and topology under buckling constraints, employing a gradient-based algorithm, is investigated for the first time.

- The proposed parameterization allows the simultaneous sizing, layout and topology optimization of panels with straight stiffeners, using a gradient-based algorithm. Specifically, sizing variables are included to optimize the skin

### Simultaneous Sizing, Layout and Topology Optimization for Buckling and Postbuckling of Stiffened Panels

thickness and the thickness of each stiffener. The positions, rotations and spacing of the stiffeners are all represented and manipulated using the coordinates of their two ends. The level set method is employed to represent and optimize the internal topologies of the stiffeners. One LSF is used to describe the internal topology of each stiffener. When all the material in a stiffener is removed, this stiffener is deleted. In this way, the number of stiffeners can be changed and optimized, without introducing an integer variable.

- A control mesh with a free-form mesh deformation method is developed to adaptively deform the FE mesh to cater for the updated stiffener layout. Re-meshing after every update of the stiffener layout is thus avoided. Since the relationship between the movement of stiffeners and the deformation of the FE mesh has been established, the sensitivities of the objective and constraint functions with respect to the layout variables can be easily calculated, enabling the application of the gradient-based optimizer.
- The effectiveness of the parameterization and optimization algorithm has been demonstrated through numerical investigations minimizing the structural weight with buckling constraints:
  - Through the optimization, the number of stiffeners is optimized and the redundant stiffeners in the initial design are removed. The layout and internal topologies of the remaining stiffeners are optimized as well as the thicknesses of the skin and stiffeners. Compared with the initial design, the weight of the optimized design is decreased whilst ensuring buckling constraints are satisfied.
  - The effect of buckling modes is investigated. Increasing the number of buckling modes in constraints can improve the convergence of the optimization. However, it is observed that the global panel buckling modes which cross the stiffeners, tend to occur in the lower buckling modes, while the local modes which occur between the stiffeners correspond to the stiffener layout and tend to appear in the higher buckling modes. As the stiffened panel, particularly the stiffener layout, is optimized, additional first buckling modes, not be found in the higher

modes in the previous optimization iteration begin to appear. Therefore, employing too many buckling modes in the constraints may not help with the convergence. To ensure convergence and computational efficiency, an appropriate number of buckling modes needs to be chosen.

- By solving optimization problems employing initial designs with different thickness distributions, stiffener layouts and topologies, and numbers of stiffeners, it is found that whilst the optimization is initial-design-dependent and has several local optimal solutions with similar structural performances, the proposed method can reliably find useful design candidates within the given design space.
- The benefit of simultaneously conducting sizing, layout and topology optimization for the design of stiffened panels is quantified, by comparing optimized designs resulting from this process with those obtained from sizing optimization, sizing and layout optimization, topology optimization, sizing and topology optimization, and layout and topology optimization.
- The difference between buckling-driven and stiffness-driven designs is investigated, by comparing buckling-based and stiffness-based optimizations. When structural stiffness is considered, more material is prone to be distributed on the skin, along with corresponding changes to stiffener configurations. This can lead to heavier designs.

The level-set-based optimization method is extended for both stress and buckling failure criteria, enabling the weight minimization of stiffened panels simultaneously optimizing size, layout and topology, in Chapter 4.

- A modified free-form mesh deformation method is developed. The free-form mesh deformation method presented in Chapter 3 can cause inaccuracies in the stress computation of a stiffened panel and hence the optimizer being misdirected to decrease the maximum stress primarily by deforming the FE mesh and moving the stiffeners. In order to minimize the effect of the mesh deformation on the stress computation, the free-form mesh deformation method is modified to maintain the size of the FEs in the regions where the maximum

## Simultaneous Sizing, Layout and Topology Optimization for Buckling and Postbuckling of Stiffened Panels

stress can occur during optimization. Numerical investigations show the effectiveness of the modified free-form mesh deformation method for both stress and buckling computation.

- Weight minimization subject to stress and buckling constraints is investigated. The local stress constraints, i.e., the von Mises stresses at the bottom, middle and top surfaces of each finite element in a structure, are aggregated into a global constraint using a  $p$ -norm function. Numerical investigations demonstrate that the developed method is able to effectively solve the optimization problem:
  - Minimum weight designs can be obtained while satisfying the stress and buckling constraints.
  - The influences of the stress and buckling constraints on the optimized solutions are investigated. Increasing the stress upper bound whilst maintaining the same buckling constraints, leads to the thickness and the stiffness of the skin being decreased. Correspondingly, more stiffeners are needed to resist the buckling and ensure the buckling constraint is satisfied. Increasing the lower bound of the buckling load factors with the same stress constraints, leads to more stiffeners tending to remain in the optimized design while the skin thickness remains almost unchanged. This shows that the impact of the buckling constraints on the stiffeners is greater than that on the skin.
  - The effect of the aggregation parameter in the  $p$ -norm stress function on the optimized design is investigated. It is observed that when the aggregation parameter is low, the optimization may converge to a local optimum. Nevertheless, for the presented example, when the aggregation parameter takes values between 6 and 24, acceptable optimized designs can be obtained with only small differences in their weights.
  - The benefit of simultaneously conducting sizing, layout and topology optimization for the design of stiffened panels for weight minimization with stress and buckling constraints is also quantified, by comparing its optimized design with those obtained from sizing optimization, sizing

## Chapter 7: Conclusions and Further Work

and layout optimization, topology optimization, sizing and topology optimization, and layout and topology optimization.

The simultaneous sizing, layout and topology optimization for postbuckling of stiffened panels is investigated for the first time, in Chapter 5.

- The level-set-based topology optimization method developed in Chapter 3 is extended for postbuckling optimization. A small imperfection in the form of the first linear buckling mode is imposed on the finite element model for the postbuckling analysis which uses the Newton-Raphson scheme. A modified automatic load incrementation scheme is developed to ensure the accuracy of the solution for the postbuckling analysis and handle the convergence challenges caused by mode jumping.
- Stiffened panels under force/displacement loading are considered for optimization. Out-of-plane skin deformation and load-carrying capability are considered to assess the postbuckling behaviours of the stiffened panels. A range of performance metrics, i.e., the total reaction force under a given displacement and the applied displacement at a given design load for stiffened panels under displacement loading, and the maximum in-plane skin displacement at a given load for those under force loading, are used to evaluate the load-carrying capability. A total of five optimization formulations based on different postbuckling metrics are studied.
- Numerical examples demonstrate the application of the proposed method. Compared with the initial design, the postbuckling behaviour of interest can be effectively improved in the optimized design. Optimizations considering different postbuckling metrics lead to different optimized designs. For the optimizations to decrease the out-of-plane skin displacement, the stiffeners tend to be uniformly distributed on the skin to reduce width of the unsupported regions; while for the optimizations to improve the load-carrying capability, more material tends to be placed on the skin and the stiffener orientation is more aligned with the direction of maximum compression.
- The selection of an appropriate imperfection, mode jumping and mode switching all present challenges for postbuckling optimization of stiffened

## Simultaneous Sizing, Layout and Topology Optimization for Buckling and Postbuckling of Stiffened Panels

panels. Their effects on optimization in both the initial postbuckling and moderately deep postbuckling regimes are investigated:

- Both the postbuckling analysis and optimization of stiffened panels can be sensitive to the imperfection introduced in the FE model, especially for those in the initial postbuckling regime. Using the imperfection with the smallest amplitude necessary to create a continuous path at the bifurcation point is observed to cause the minimum effect on the overall structural behaviour. For a stiffened panel design under symmetric loading and boundary conditions, the introduction of an asymmetric imperfection based on the critical buckling mode can result in an asymmetrical displacement field and sensitivity distribution. Therefore, a local optimum, and an asymmetrical design would be obtained. Symmetry control is developed to enforce the generation of a symmetrical design in this case, with the optimized designs having better postbuckling behaviours than those without using symmetry control.
- Both mode switching and mode jumping cause different buckling modes at the design loading between the adjacent optimization iterations. This results in discontinuities in the optimization, causing oscillations and slowing the convergence. Nevertheless, they do not prevent stiffened panels from being optimized. During the optimization, structures can be continuously optimized to achieve better postbuckling performance.
- Through numerical investigations, it is also found that when more stiffeners are allowed to exist in the optimized structures, designs having more promising postbuckling behaviours can be obtained. Compared with linear buckling optimization, postbuckling optimization is able to provide a design with better postbuckling behaviours of interest.

The simultaneous layout and topology optimization of panels with curved stiffeners, employing a gradient-based approach, is investigated for the first time, in Chapter 6:

- A level-set-based method for simultaneous layout and topology optimization of curved stiffened panels, is developed. Here, the level set method is used for both the description and optimization of stiffener

curves and internal topologies. The free-form mesh deformation method with control mesh is employed to adjust the FE mesh after every update of the stiffener layout.

- Both the problems of mass minimization with a buckling constraint and critical buckling load factor maximization with a mass constraint are studied. In both of these formulations, the  $p$ -norm function is used as a buckling aggregation function to approximate the inverse of the critical buckling load factor, and is considered either as a constraint or the objective. For the buckling-constrained problem, an adaptive scaling method is used to ensure the control of the buckling limit. Numerical investigations demonstrate and validate the proposed method. However, for the same initial designs, the optimized design with curved stiffeners is worse than the one with straight stiffeners. Through numerical investigations, it can be shown that the proposed parameterization has the capability to describe a panel with curved stiffeners which has a better performance than the optimized design with straight stiffeners. However, since the optimization problem is highly nonlinear, many local optima exist. This can cause an inferior local optimum to be found.
- By comparing two optimized designs stiffened by curved and straight stiffeners but having quite closed weights and critical buckling load factors, it is found that the postbuckling behaviour of the design with curved stiffeners is better than the one with straight stiffeners. This shows that curved stiffened panels may have advantages in the postbuckling regime.

### 7.2 Suggestions for Further Work

Based on the works and investigations in this thesis, several suggestions for future research are provided below.

- Since free-form mesh deformation with a control mesh is utilized to adaptively adjust the FE mesh, the intersection between adjacent stiffeners is not allowed in the works in this thesis. This results in a reduced design space being able to be searched. Allowing an intersection between stiffeners during the optimization

## Simultaneous Sizing, Layout and Topology Optimization for Buckling and Postbuckling of Stiffened Panels

would bring some difficulties in meshing the structures and calculating layout sensitivities, for example, how to use sensitivity information to account for the introduction and removal of the intersections between stiffeners.

- In this thesis, optimization for postbuckling performance under a mass constraint is investigated. It is easy for the mass constraint to be satisfied during optimization. For most iterations, the optimization starts with a feasible solution. However, when the weight minimization with postbuckling constraints is investigated, unexpected infeasible solutions can occur during optimization due to sudden and significant changes in postbuckling behaviours caused by mode switching and mode jumping. This may cause challenges to the optimizer in finding a feasible design. The optimization of stiffened panels, enabling weight minimization under postbuckling constraints, could be explored in future work.
- In both the optimization of panels with straight and curved stiffeners, it has been found that the optimization problem is initial-design-dependent when using a gradient-based algorithm and has several local optimal solutions. This can lead to only a local optimum being found, which may be substantially inferior to the achievable performance via the global optimum, especially in the case of the design of curved stiffened panels. Gradient-free methods have the potential to jump out of these local solutions and find the global optimum. However, they scale poorly with large numbers of design variables being necessary for the simultaneous sizing, layout and topology optimization of stiffened panels. Therefore, ways to effectively and robustly find a global optimum in the simultaneous sizing, layout and topology optimization of stiffened panels, need to be investigated in future work.
- In this thesis, only linear buckling optimization is investigated for curved stiffened panels. As the numerical investigations in Chapter 6 show that curved stiffened panels may be superior in a postbuckling regime, there is a need to investigate postbuckling optimization of curved stiffened panels, and compare the optimized designs with those with straight stiffeners to have a better understanding of the field of stiffened panel design.

# 8 REFERENCES

- [1] N. Aage, E. Andreassen, B.S. Lazarov, O. Sigmund, Giga-voxel computational morphogenesis for structural design, *Nature*, 550 (2017) 84-86.
- [2] R. Kapania, J. Li, H. Kapoor, Optimal design of unitized panels with curvilinear stiffeners, in: *AIAA 5th ATIO and 16th Lighter-Than-Air Sys Tech. and Balloon Systems Conferences*, 2005, pp. 7482.
- [3] O.K. Bedair, Influence of stiffener location on the stability of stiffened plates under compression and in-plane bending, *International journal of mechanical sciences*, 39 (1997) 33-49.
- [4] S. Nagendra, R. Haftka, Z. Gürdal, J. Starnes Jr, Design of a blade-stiffened composite panel with a hole, *Composite Structures*, 18 (1991) 195-219.
- [5] S. Nagendra, D. Jestin, Z. Gürdal, R.T. Haftka, L.T. Watson, Improved genetic algorithm for the design of stiffened composite panels, *Computers & Structures*, 58 (1996) 543-555.
- [6] L. Lamberti, S. Venkataraman, R.T. Haftka, T.F. Johnson, Preliminary design optimization of stiffened panels using approximate analysis models, *International Journal for Numerical Methods in Engineering*, 57 (2003) 1351-1380.
- [7] B. Colson, M. Bruyneel, S. Grihon, C. Raick, A. Remouchamps, Optimization methods for advanced design of aircraft panels: a comparison, *Optimization and Engineering*, 11 (2010) 583-596.

**Simultaneous Sizing, Layout and Topology Optimization  
for Buckling and Postbuckling of Stiffened Panels**

- [8] M. Bhatia, R.K. Kapania, D. Evans, Comparative study on optimal stiffener placement for curvilinearly stiffened panels, *Journal of Aircraft*, 48 (2011) 77-91.
- [9] S.B. Mulani, W.C. Slemple, R.K. Kapania, EBF3PanelOpt: An optimization framework for curvilinear blade-stiffened panels, *Thin-Walled Structures*, 63 (2013) 13-26.
- [10] A.Y. Tamijani, S.B. Mulani, R.K. Kapania, A framework combining meshfree analysis and adaptive kriging for optimization of stiffened panels, *Structural and Multidisciplinary Optimization*, 49 (2014) 577-594.
- [11] X. Ni, B. Prusty, A. Hellier, Buckling and post-buckling of isotropic and composite stiffened panels: A review on optimisation (2000-2015), *International Journal of Maritime Engineering*, 158 (2016).
- [12] S. Gurav, R. Kapania, Development of framework for the design optimization of unitized structures, in: 50th AIAA/ASME/ASCE/AHS/ASC Structures, Structural Dynamics, and Materials Conference 17th AIAA/ASME/AHS Adaptive Structures Conference 11th AIAA No, 2009, pp. 2186.
- [13] D. Locatelli, S.B. Mulani, R.K. Kapania, Parameterization of curvilinear spars and ribs for optimum wing structural design, *Journal of Aircraft*, 51 (2014) 532-546.
- [14] B.K. Stanford, C.V. Jutte, C.A. Coker, Aeroelastic sizing and layout design of a wingbox through nested optimization, *AIAA Journal*, 57 (2019) 848-857.
- [15] S. De, M. Jrad, R.K. Kapania, Structural optimization of internal structure of aircraft wings with curvilinear spars and ribs, *Journal of Aircraft*, 56 (2019) 707-718.
- [16] S. Nagendra, Z. Gürdal, R. Haftka, J. Starnes Jr, Buckling and failure characteristics of compression-loaded stiffened composite panels with a hole, *Composite structures*, 28 (1994) 1-17.
- [17] O. Park, R.T. Haftka, B.V. Sankar, J.H. Starnes Jr, S. Nagendra, Analytical-experimental correlation for a stiffened composite panel loaded in axial compression, *Journal of aircraft*, 38 (2001) 379-387.

## Chapter 8: References

- [18] R. Vitali, R.T. Haftka, B.V. Sankar, Multi-fidelity design of stiffened composite panel with a crack, *Structural and Multidisciplinary Optimization*, 23 (2002) 347-356.
- [19] R. Vitali, O. Park, R.T. Haftka, B.V. Sankar, C.A. Rose, Structural optimization of a hat-stiffened panel using response surfaces, *Journal of aircraft*, 39 (2002) 158-166.
- [20] J.E. Herencia, R.T. Haftka, P.M. Weaver, M.I. Friswell, Lay-up optimization of composite stiffened panels using linear approximations in lamination space, *AIAA journal*, 46 (2008) 2387-2391.
- [21] M.P. Bendsøe, N. Kikuchi, Generating optimal topologies in structural design using a homogenization method, *Computer methods in applied mechanics and engineering*, 71 (1988) 197-224.
- [22] M.P. Bendsøe, Optimal shape design as a material distribution problem, *Structural optimization*, 1 (1989) 193-202.
- [23] O. Sigmund, A 99 line topology optimization code written in Matlab, *Structural and multidisciplinary optimization*, 21 (2001) 120-127.
- [24] E. Andreassen, A. Clausen, M. Schevenels, B.S. Lazarov, O. Sigmund, Efficient topology optimization in MATLAB using 88 lines of code, *Structural and Multidisciplinary Optimization*, 43 (2011) 1-16.
- [25] M.Y. Wang, X. Wang, D. Guo, A level set method for structural topology optimization, *Computer methods in applied mechanics and engineering*, 192 (2003) 227-246.
- [26] G. Allaire, F. Jouve, A.-M. Toader, Structural optimization using sensitivity analysis and a level-set method, *Journal of computational physics*, 194 (2004) 363-393.
- [27] J.A. Sethian, A. Wiegmann, Structural boundary design via level set and immersed interface methods, *Journal of computational physics*, 163 (2000) 489-528.
- [28] P.D. Dunning, H.A. Kim, Introducing the sequential linear programming level-set method for topology optimization, *Structural and Multidisciplinary Optimization*, 51 (2015) 631-643.

**Simultaneous Sizing, Layout and Topology Optimization  
for Buckling and Postbuckling of Stiffened Panels**

- [29] Y.M. Xie, G.P. Steven, A simple evolutionary procedure for structural optimization, *Computers & structures*, 49 (1993) 885-896.
- [30] X. Huang, M. Xie, *Evolutionary topology optimization of continuum structures: methods and applications*, John Wiley & Sons, 2010.
- [31] B. Stanford, P. Beran, M. Bhatia, Aeroelastic topology optimization of blade-stiffened panels, *Journal of Aircraft*, 51 (2014) 938-944.
- [32] S. Townsend, H.A. Kim, A level set topology optimization method for the buckling of shell structures, *Structural and Multidisciplinary Optimization*, 60 (2019) 1783-1800.
- [33] W. Zhao, K. Singh, R. Kapania, Thermo-mechanical buckling of curvilinearly stiffened variable angle tow laminated panels, in: *22nd AIAA International Space Planes and Hypersonics Systems and Technologies Conference*, 2018, pp. 5165.
- [34] M. Lillico, R. Butler, G. Hunt, A. Watson, D. Kennedy, F. Williams, Optimum design and testing of a post-buckled stiffened panel, in: *41st Structures, Structural Dynamics, and Materials Conference and Exhibit*, 2000, pp. 1659.
- [35] A. Watson, C. Featherston, D. Kennedy, Optimization of postbuckled stiffened panels with multiple stiffener sizes, in: *48th AIAA/ASME/ASCE/AHS/ASC Structures, Structural Dynamics, and Materials Conference*, 2007, pp. 2207.
- [36] C. López, O. Bacarreza, A. Baldomir, S. Hernández, M. H Ferri Aliabadi, Reliability-based design optimization of composite stiffened panels in post-buckling regime, *Structural and Multidisciplinary Optimization*, 55 (2017) 1121-1141.
- [37] F.S. Liguori, G. Zucco, A. Madeo, D. Magisano, L. Leonetti, G. Garcea, P.M. Weaver, Postbuckling optimisation of a variable angle tow composite wingbox using a multi-modal Koiter approach, *Thin-Walled Structures*, 138 (2019) 183-198.
- [38] P. Arendsen, H. Thuis, J. Wiggenraad, Optimization Of Composite Stiffened Panels With Postbuckling Constraints, *WIT Transactions on Engineering Sciences*, 4 (1994).
- [39] C. Bisagni, L. Lanzi, Post-buckling optimisation of composite stiffened panels using neural networks, *Composite Structures*, 58 (2002) 237-247.

## Chapter 8: References

- [40] R. Rikards, H. Abramovich, J. Auzins, A. Korjakins, O. Ozolinsh, K. Kalnins, T. Green, Surrogate models for optimum design of stiffened composite shells, *Composite Structures*, 63 (2004) 243-251.
- [41] L. Lanzi, V. Giavotto, Post-buckling optimization of composite stiffened panels: Computations and experiments, *Composite structures*, 73 (2006) 208-220.
- [42] J.-H. Kang, C.-G. Kim, Minimum-weight design of compressively loaded composite plates and stiffened panels for postbuckling strength by genetic algorithm, *Composite structures*, 69 (2005) 239-246.
- [43] K. Swingler, *Applying neural networks: a practical guide*, Morgan Kaufmann, 1996.
- [44] Z. Waszczyszyn, L. Ziemiański, Neural networks in mechanics of structures and materials—new results and prospects of applications, *Computers & Structures*, 79 (2001) 2261-2276.
- [45] M.F. Hussain, R.R. Barton, S.B. Joshi, Metamodeling: radial basis functions, versus polynomials, *European Journal of Operational Research*, 138 (2002) 142-154.
- [46] T. Krishnamurthy, Response surface approximation with augmented and compactly supported radial basis functions, in: 44th AIAA/ASME/ASCE/AHS/ASC structures, structural dynamics, and materials conference, 2003, pp. 1748.
- [47] W. Liu, S. Batill, Gradient-enhanced response surface approximations using kriging models, in: 9th AIAA/ISSMO symposium on multidisciplinary analysis and optimization, 2002, pp. 5456.
- [48] H.S. Chung, J. Alonso, Design of a low-boom supersonic business jet using cokriging approximation models, in: 9th AIAA/ISSMO symposium on multidisciplinary analysis and optimization, 2002, pp. 5598.
- [49] K. Liang, Z. Li, Postbuckling analysis and optimization of composite laminated panels using a novel perturbation-based approximation FE method, *Thin-Walled Structures*, 160 (2021) 107398.

**Simultaneous Sizing, Layout and Topology Optimization  
for Buckling and Postbuckling of Stiffened Panels**

- [50] O. Bacarreza, M. Aliabadi, A. Apicella, Robust design and optimization of composite stiffened panels in post-buckling, *Structural and Multidisciplinary Optimization*, 51 (2015) 409-422.
- [51] V. Tvergaard, Imperfection-sensitivity of a wide integrally stiffened panel under compression, *International Journal of Solids and Structures*, 9 (1973) 177-192.
- [52] D. Bushnell, C. Rankin, E. Riks, D. Bushnell, C. Rankin, E. Riks, Optimization of stiffened panels in which mode jumping is accounted for, in: *38th Structures, Structural Dynamics, and Materials Conference*, 1997, pp. 1141.
- [53] M.M. Neves, O. Sigmund, M.P. Bendsøe, Topology optimization of periodic microstructures with a penalization of highly localized buckling modes, *International Journal for Numerical Methods in Engineering*, 54 (2002) 809-834.
- [54] P.D. Dunning, E. Ovtchinnikov, J. Scott, H.A. Kim, Level-set topology optimization with many linear buckling constraints using an efficient and robust eigensolver, *International Journal for Numerical Methods in Engineering*, 107 (2016) 1029-1053.
- [55] X. Gao, H. Ma, Topology optimization of continuum structures under buckling constraints, *Computers & Structures*, 157 (2015) 142-152.
- [56] C.R. Thomsen, F. Wang, O. Sigmund, Buckling strength topology optimization of 2D periodic materials based on linearized bifurcation analysis, *Computer Methods in Applied Mechanics and Engineering*, 339 (2018) 115-136.
- [57] M. Bruyneel, B. Colson, A. Remouchamps, Discussion on some convergence problems in buckling optimisation, *Structural and Multidisciplinary Optimization*, 35 (2008) 181-186.
- [58] R. Dienemann, A. Schumacher, S. Fiebig, Considering Linear Buckling for 3D Density Based Topology Optimization, in: *International Conference on Engineering Optimization*, Springer, 2018, pp. 394-406.
- [59] F. Ferrari, O. Sigmund, Revisiting topology optimization with buckling constraints, *Structural and Multidisciplinary Optimization*, 59 (2019) 1401-1415.

## Chapter 8: References

- [60] F. Ferrari, O. Sigmund, J.K. Guest, Topology optimization with linearized buckling criteria in 250 lines of Matlab, *Structural and Multidisciplinary Optimization*, 63 (2021) 3045-3066.
- [61] C. Le, J. Norato, T. Bruns, C. Ha, D. Tortorelli, Stress-based topology optimization for continua, *Structural and Multidisciplinary Optimization*, 41 (2010) 605-620.
- [62] G. Cheng, P. Pedersen, On sufficiency conditions for optimal design based on extremum principles of mechanics, *Journal of the Mechanics and Physics of Solids*, 45 (1997) 135-150.
- [63] P. Duysinx, M.P. Bendsøe, Topology optimization of continuum structures with local stress constraints, *International journal for numerical methods in engineering*, 43 (1998) 1453-1478.
- [64] M. Bruggi, On an alternative approach to stress constraints relaxation in topology optimization, *Structural and multidisciplinary optimization*, 36 (2008) 125-141.
- [65] S.J. Moon, G.H. Yoon, A newly developed qp-relaxation method for element connectivity parameterization to achieve stress-based topology optimization for geometrically nonlinear structures, *Computer Methods in Applied Mechanics and Engineering*, 265 (2013) 226-241.
- [66] R. Yang, C. Chen, Stress-based topology optimization, *Structural optimization*, 12 (1996) 98-105.
- [67] P. Duysinx, O. Sigmund, New developments in handling stress constraints in optimal material distribution, in: *7th AIAA/USAF/NASA/ISSMO symposium on multidisciplinary analysis and optimization*, 1998, pp. 4906.
- [68] Y. Luo, M.Y. Wang, Z. Kang, An enhanced aggregation method for topology optimization with local stress constraints, *Computer Methods in Applied Mechanics and Engineering*, 254 (2013) 31-41.
- [69] A. Verbart, M. Langelaar, F.v. Keulen, A unified aggregation and relaxation approach for stress-constrained topology optimization, *Structural and Multidisciplinary Optimization*, 55 (2017) 663-679.

**Simultaneous Sizing, Layout and Topology Optimization  
for Buckling and Postbuckling of Stiffened Panels**

- [70] A. Verbart, M. Langelaar, N. Van Dijk, F. Van Keulen, Level set based topology optimization with stress constraints and consistent sensitivity analysis, in: 53rd AIAA/ASME/ASCE/AHS/ASC Structures, Structural Dynamics and Materials Conference 20th AIAA/ASME/AHS Adaptive Structures Conference 14th AIAA, 2012, pp. 1358.
- [71] R. Picelli, S. Townsend, C. Brampton, J. Norato, H.A. Kim, Stress-based shape and topology optimization with the level set method, *Computer methods in applied mechanics and engineering*, 329 (2018) 1-23.
- [72] L. Xia, L. Zhang, Q. Xia, T. Shi, Stress-based topology optimization using bi-directional evolutionary structural optimization method, *Computer Methods in Applied Mechanics and Engineering*, 333 (2018) 356-370.
- [73] L. Krog, A. Tucker, M. Kemp, R. Boyd, Topology optimisation of aircraft wing box ribs, in: 10th AIAA/ISSMO multidisciplinary analysis and optimization conference, 2004, pp. 4481.
- [74] K. Maute, M. Allen, Conceptual design of aeroelastic structures by topology optimization, *Structural and Multidisciplinary Optimization*, 27 (2004) 27-42.
- [75] B.K. Stanford, P.D. Dunning, Optimal topology of aircraft rib and spar structures under aeroelastic loads, *Journal of Aircraft*, 52 (2015) 1298-1311.
- [76] B.K. Stanford, Aeroelastic wingbox stiffener topology optimization, *Journal of Aircraft*, 55 (2018) 1244-1251.
- [77] W. Dorn, Automatic design of optimal structures, *J. de Mecanique*, 3 (1964) 25-52.
- [78] S. Slesongsom, S. Bureerat, New conceptual design of aeroelastic wing structures by multi-objective optimization, *Engineering Optimization*, 45 (2013) 107-122.
- [79] W. Yang, Z. Yue, L. Li, P. Wang, Aircraft wing structural design optimization based on automated finite element modelling and ground structure approach, *Engineering optimization*, 48 (2016) 94-114.

## Chapter 8: References

- [80] X. Ding, K. Yamazaki, Stiffener layout design for plate structures by growing and branching tree model (application to vibration-proof design), *Structural and Multidisciplinary Optimization*, 26 (2004) 99-110.
- [81] X. Ding, K. Yamazaki, Adaptive growth technique of stiffener layout pattern for plate and shell structures to achieve minimum compliance, *Engineering Optimization*, 37 (2005) 259-276.
- [82] X. Dong, X. Ding, M. Xiong, Optimal layout of internal stiffeners for three-dimensional box structures based on natural branching phenomena, *Engineering Optimization*, 51 (2019) 590-607.
- [83] X. Dong, X. Ding, G. Li, G.P. Lewis, Stiffener layout optimization of plate and shell structures for buckling problem by adaptive growth method, *Structural and Multidisciplinary Optimization*, 61 (2020) 301-318.
- [84] W. Zhang, Y. Liu, Z. Du, Y. Zhu, X. Guo, A moving morphable component based topology optimization approach for rib-stiffened structures considering buckling constraints, *Journal of Mechanical Design*, 140 (2018).
- [85] J.A. Sethian, *Level set methods and fast marching methods: evolving interfaces in computational geometry, fluid mechanics, computer vision, and materials science*, Cambridge university press, 1999.
- [86] S. Osher, R. Fedkiw, K. Piechor, *Level set methods and dynamic implicit surfaces*, in, American Society of Mechanical Engineers Digital Collection, 2004.
- [87] N.P. Van Dijk, K. Maute, M. Langelaar, F. Van Keulen, Level-set methods for structural topology optimization: a review, *Structural and Multidisciplinary Optimization*, 48 (2013) 437-472.
- [88] D. Locatelli, S.B. Mulani, R.K. Kapania, Wing-box weight optimization using curvilinear spars and ribs (SpaRibs), *Journal of Aircraft*, 48 (2011) 1671-1684.
- [89] W. Zhao, R.K. Kapania, BLP optimization of composite flying-wings with sparibs and multiple control surfaces, in: 2018 AIAA/ASCE/AHS/ASC Structures, Structural Dynamics, and Materials Conference, 2018, pp. 2150.

**Simultaneous Sizing, Layout and Topology Optimization  
for Buckling and Postbuckling of Stiffened Panels**

- [90] T.W. Sederberg, S.R. Parry, Free-form deformation of solid geometric models, *ACM SIGGRAPH Computer Graphics*, 20 (1986) 151-160.
- [91] K.J. Bathe, E.N. Dvorkin, A four-node plate bending element based on Mindlin/Reissner plate theory and a mixed interpolation, *International Journal for Numerical Methods in Engineering*, 21 (1985) 367-383.
- [92] D. Chapelle, K.-J. Bathe, *The finite element analysis of shells-fundamentals*, Springer Science & Business Media, 2010.
- [93] G.-S. Jiang, D. Peng, Weighted ENO schemes for Hamilton--Jacobi equations, *SIAM Journal on Scientific computing*, 21 (2000) 2126-2143.
- [94] H. HSL, *A collection of Fortran codes for large scale scientific computation*, 2002, 2002.
- [95] R.B. Lehoucq, D.C. Sorensen, C. Yang, *ARPACK users' guide: solution of large-scale eigenvalue problems with implicitly restarted Arnoldi methods*, SIAM, 1998.
- [96] D. Adalsteinsson, J.A. Sethian, The fast construction of extension velocities in level set methods, *Journal of Computational Physics*, 148 (1999) 2-22.
- [97] A. Wächter, L.T. Biegler, On the implementation of an interior-point filter line-search algorithm for large-scale nonlinear programming, *Mathematical programming*, 106 (2006) 25-57.
- [98] M. Cavazzuti, A. Baldini, E. Bertocchi, D. Costi, E. Torricelli, P. Moruzzi, High performance automotive chassis design: a topology optimization based approach, *Structural and Multidisciplinary Optimization*, 44 (2011) 45-56.
- [99] J.-H. Zhu, W.-H. Zhang, L. Xia, Topology optimization in aircraft and aerospace structures design, *Archives of Computational Methods in Engineering*, 23 (2016) 595-622.
- [100] M. Baandrup, O. Sigmund, H. Polk, N. Aage, Closing the gap towards super-long suspension bridges using computational morphogenesis, *Nature Communications*, 11 (2020) 1-7.

## Chapter 8: References

- [101] M. Wallin, A. Dalklint, D. Tortorelli, Topology optimization of bistable elastic structures—An application to logic gates, *Computer Methods in Applied Mechanics and Engineering*, 383 (2021) 113912.
- [102] M. Wallin, N. Ivarsson, D. Tortorelli, Stiffness optimization of non-linear elastic structures, *Computer Methods in Applied Mechanics and Engineering*, 330 (2018) 292-307.
- [103] A. Dalklint, M. Wallin, D.A. Tortorelli, Eigenfrequency constrained topology optimization of finite strain hyperelastic structures, *Structural and Multidisciplinary Optimization*, 61 (2020) 2577-2594.
- [104] P. Bulson, *The Stability of Flat Plates*, Chatto and Windus Ltd, London, 1970.
- [105] F. Wang, B.S. Lazarov, O. Sigmund, J.S. Jensen, Interpolation scheme for fictitious domain techniques and topology optimization of finite strain elastic problems, *Computer Methods in Applied Mechanics and Engineering*, 276 (2014) 453-472.
- [106] H. Deng, L. Cheng, X. Liang, D. Hayduke, A.C. To, Topology optimization for energy dissipation design of lattice structures through snap-through behavior, *Computer Methods in Applied Mechanics and Engineering*, 358 (2020) 112641.
- [107] A. Pica, R. Wood, E. Hinton, Finite element analysis of geometrically nonlinear plate behaviour using a Mindlin formulation, *Computers & Structures*, 11 (1980) 203-215.
- [108] A. Sheikh, M. Mukhopadhyay, Geometric nonlinear analysis of stiffened plates by the spline finite strip method, *Computers & structures*, 76 (2000) 765-785.
- [109] D. Bushnell, Optimization of composite, stiffened, imperfect panels under combined loads for service in the postbuckling regime, *Computer Methods in Applied Mechanics and Engineering*, 103 (1993) 43-114.
- [110] A. Faggiani, B.G. Falzon, Optimization strategy for minimizing damage in postbuckling stiffened panels, *AIAA journal*, 45 (2007) 2520-2528.
- [111] Z. Wu, G. Raju, P.M. Weaver, Optimization of postbuckling behaviour of variable thickness composite panels with variable angle tows: Towards “Buckle-Free” design concept, *International Journal of Solids and Structures*, 132 (2018) 66-79.

**Simultaneous Sizing, Layout and Topology Optimization  
for Buckling and Postbuckling of Stiffened Panels**

[112] V.N. Van Do, K.-H. Chang, C.-H. Lee, Post-buckling analysis of FGM plates under in-plane mechanical compressive loading by using a mesh-free approximation, *Archive of Applied Mechanics*, 89 (2019) 1421-1446.

[113] K. Sze, X. Liu, S. Lo, Popular benchmark problems for geometric nonlinear analysis of shells, *Finite elements in analysis and design*, 40 (2004) 1551-1569.

[114] R. Picelli, S. Townsend, C. Brampton, J. Norato, H. Kim, Stress-based shape and topology optimization with the level set method, *Computer methods in applied mechanics and engineering*, 329 (2018) 1-23.